A multi–parameter study of iceberg calving and the retreat of *Haupapa*/Tasman Glacier, South Island, New Zealand

A thesis presented in partial fulfilment of the requirements for the degree of

Doctor of Philosophy in Geography

at Massey University, Palmerston North, New Zealand

Robert Campbell Dykes

2013

Key words: Tasman Glacier, iceberg calving, freshwater, debris–cover, icequake, seismicity, remote sensing.

Abstract

Iceberg calving is an efficient ablation process which introduces mechanical instability to glacier systems and can cause a non–linear climatic response. This thesis quantifies the calving retreat of the freshwater–terminating Tasman Glacier and the coeval expansion of Tasman Lake, at a range of temporal and spatial scales. Tasman Glacier is the longest glacier (*c.* 23 km) in New Zealand, and lies east of the Main Divide of the Southern Alps, extending from a névé at 2400 m to an ice–contact lake at *c.* 727 m. Although 20th century warming caused down–wastage, it remained at its Little Ice Age terminus until the late 20th century. Since then, calving retreat has occurred, allowing a large proglacial lake to form. Remote sensing datasets, namely satellite imagery, time–lapse photography, and passive seismic recording were used to observe and characterise retreat and calving style and magnitude at inter–annual, sub–annual, and intra–event time–scales.

Between 2000 and 2013 Tasman Glacier has retreated *c.* 6 km, corresponding to an average decrease in ice surface loss at the terminus of 0.37 km^2 a^{-1}, through a combination of melting of the lower glacier and iceberg calving. However, an order of magnitude increase in retreat occurred since 2006 with peak retreat rates in excess of 1.5 km^2 a^{-1}. This retreat has seen a continuation of accelerated ice loss since the formation of Tasman Lake in the late 1980s. A four–stage model for the transition between melt and calving regimes refined in this study has indicated that the processes and factors that contribute to the development of a proglacial lake at the termini of debris–covered glaciers worldwide are similar, although they act over different time–scales depending on glacier dynamics and climate regimes.

At a sub–annual time–scale calving events between October 2011 and November 2012 were identified at a rate of 0.94 events d^{-1}, with significant seasonal differences, in that the number of calving events increased during the ablation season. Calving events driven by thermo–erosional notching at the waterline were the most frequent of all calving events, followed by events initiated by over–steepening of the subaerial ice cliff, then sub–aqueous and buoyancy–driven calving events. Buoyancy–driven calving events were of the largest magnitude, and had the greatest effect on glacier retreat. Such events are initiated by a combination of glacier thinning, increased water–depth at the terminus, terminus geometry, subaqueous melt and calving, perturbations in lake level and near–field earthquakes.

The increase in calving frequency during spring and summer 2011/12 was directly related to the increase in thermo–erosional notch events. Correlation of calving frequency, lake level and lake temperature time–series data reveals that the frequency changes are related to the stability in lake level and elevated lake temperatures. This indicates that although calving retreat rate has increased, low–magnitude calving events are the most frequent, but low frequency, high magnitude buoyancy–driven events have had the greatest influence on net glacier retreat.

Calving events at Tasman Glacier emit seismic signals similar to those found at other calving margins globally. All calving events generated seismic signals that had emergent onsets with weak frequencies above 5 Hz, followed by a high amplitude phase with frequency content between 1 and 5 Hz and a protracted coda. The study highlighted relationships between calved iceberg size and seismic parameters (e.g., signal duration, peak amplitude and integrated amplitude) that can be used to remotely assess the frequency, style and magnitude of calving events. It was shown that seismic waveforms, signal duration, and energy indicate order–of–magnitude differences in calving event size and style. However, due to the continuum of spatial and temporal scales over which calving operates, seismic signals are generally too variable to completely substitute direct observational data. Signal analysis algorithms analogous to those used in volcano seismology have been developed for the automatic detection of iceberg calving and were thoroughly tested against independent observational datasets. The algorithms and thresholds can be readily deployed in future seismic studies of dynamic ice margins at freshwater–terminating glaciers.

Acknowledgements

This project would not have been possible without the support, guidance and encouragement of a number of people. I would firstly like to express my appreciation to my supervisors, Dr Gert Lube for allowing me to drag him away from volcanoes and introduce him to the wonders of glaciers, as well as stepping into the breach towards the end; Dr Martin Brook for introducing me to glaciology and Tasman Glacier; and Dr Mark Bebbington for providing invaluable assistance and guidance on all things statistical.

I wish to thank the following organisations for providing financial support throughout the course of research: Massey University (Vice–Chancellor's Doctoral Scholarship), Massey University School of People, Environment, and Planning (Graduate Research Fund), and Massey University Institute of Agriculture and Environment. The New Zealand Alpine Club (NZAC) also provided field accommodation.

My research would not have been possible without the time and expertise of a number of people, and I would like to acknowledge their contribution: Dr Ian Fuller and David Feek for field assistance on Tasman Lake, Graeme Slatter for making my days on the glacier shorter by providing me with alternate transport options and an ear to talk to at the end of the day, Dennis Callesen for keeping me up to date on everything going on at Tasman whilst I wasn't there and for being eternally interested in my research, Amelia Hitchcock for introducing me to a different way of looking at Tasman Glacier and providing a side project to get distracted with, Grant Pearson and Chas and Katrina Tanner for making my stays at Unwin Lodge all the better, Daniel Farley for assisting with the development of field equipment, and Friederike von Schilppe for providing invaluable assistance with analysing seismic data and introducing me the joys of Python. Satellite imagery was supplied by Dr Wolfgang Rack via the GLIMs project and Dr Stefan Winkler provided recent oblique aerial photographs of Tasman Glacier and Tasman Lake. Logistical support provided by the pilots and staff at HeliLine when transporting equipment to and from Tasman Lake and Tasman Glacier was much appreciated. Meridian Energy Ltd. and NIWA for supplying climate data. Ray Bellringer, Shirley Slatter and the other staff at the Department of Conservation/*Te Papa Atawhai* for allowing research in the *Aoraki*/Mount Cook National Park. Many thanks also goes to Glacier Explores and Tasman Valley 4WD and Argo Tours, for always being willing to give me a ride up the valley and out on Tasman Lake. In particular, I would like to thank Bede Ward and the other boat drivers for making any time on and off the water enjoyable.

Special thanks also go to the postgraduate students and staff of the Massey University Geography Programme for their support and encouragement whilst completing this project. I would especially like to thank Dr John Appleby and Dr Clare Robertson for assisting in the field and making our voyages on Tasman Lake entertaining. To Dr Alastair Clement for helping me out with any problems I had and Dr Jane Richardson for always lending an ear to talk too with any frustrations I may have had along the way.

To my family, thank you for giving me the support and freedom to find my own way no matter what it was. I would not be where I am without your constant encouragement and willingness to help. Finally, to Tash, for always being there when I needed you.

Contents

List of Figures xi
List of Tables xxv
Chapter 1: Introduction 1
1.1 Background 1
1.2 Aims, scope and objectives 3
1.3 Thesis structure 5
Chapter 2: Literature Review 7
2.1 Introduction 7
2.2 Glacier mass balance 7
2.3 Supraglacial debris–cover and proglacial lake formation 9
2.3.1 Asymmetric glacial advance 10
2.3.2 Downwasting and thermokarst erosion 11
2.3.3 Supraglacial ponds 12
2.3.4 Proglacial lake development 13
2.3.5 Proglacial lake hazards 14
2.4 Calving margins 15
2.4.1 Dry calving 16
2.4.2 Tidewater glaciers 16
2.4.3 Freshwater (lacustrine) glaciers 17
2.4.4 Ice shelves 17
2.5 Calving Processes 18
2.5.1 Fracturing and crevassing of ice 19
2.5.2 Processes leading to calving 22
2.5.2.1 Surface velocity gradients 22
2.5.2.2 Force imbalance at the terminus 23
2.5.2.3 Melt associated with proglacial water bodies 24
2.5.2.4 Torque induced buoyant forces 26
2.5.3 Calving mechanisms 28
2.5.3.1 Calving hierarchy 29
2.5.4 Calving laws and models 30
2.5.4.1 Empirically derived ‘calving rate functions’ 32
2.5.4.2 Height above buoyancy model 34

2.5.4.3 Theoretical process based calving models 37
2.5.4.4 Fracture scale calving law 43
2.6 Calving–generated seismicity 44
2.6.1 Characteristics of calving–generated icequakes 45
2.6.2 Source mechanisms 46
2.6.2.1 Ice fracture and crevassing 46
2.6.2.2 Resonance within a fluid filled crack 46
2.6.2.3 Iceberg detachment and rotation 47
2.6.2.4 Fracturing of ice melange and wave action 48
2.6.2.5 Ice–water interaction 49
2.7 Summary and conclusions 50
Chapter 3: Study Area *Haupapa*/Tasman Glacier 53
3.1 Introduction 53
3.2 Regional Setting 53
3.3 Climate 55
3.4 Tasman Glacier 55
3.4.1 Mass balance 57
3.4.2 Debris–cover 58
3.4.3 Ice velocity 60
3.4.4 Downwasting and lake formation 61
3.5 Tasman Lake 63
3.6 Glaciers of the *Aoraki*/Mount Cook Region 65
3.6.1 Hooker Glacier 65
3.6.2 Mueller Glacier 65
3.6.3 Murchison Glacier 66
3.6.4 Godley Valley glaciers 66
3.7 Summary and conclusions 67
Chapter 4: The calving retreat of Tasman Glacier 69
4.1 Introduction 69
4.2 Methods 70
4.2.1 Terminus and lake mapping 70
4.2.2 Bathymetry 71
4.3 Results 71
4.3.1 Spatio–temporal changes of Tasman Glacier: 2000–2013 71
4.3.2 Lake area 75
4.3.3 Tasman Glacier: 1957–2012 78
4.3.4 Tasman Lake bathymetry and water depth at the terminus 79

4.4 Discussion 82
4.4.1 Synthesis of Tasman Glacier calving retreat 83
4.4.1.1 Lake formation and growth: 1950s–1990 83
4.4.1.2 Calving retreat: 1990–2006 84
4.4.1.3 Terminus disintegration: 2006–2007 85
4.4.1.4 Calving retreat: 2007–2013 88
4.4.2 Terminus flotation and retreat 90
4.4.3 Thresholds of retreat at Tasman Glacier 93
4.4.4 Glaciers of the Aoraki/Mount Cook National Park and a model for proglacial lake evolution 95
4.5 Conclusions 97
Chapter 5: Analysis of sub–annual retreat and iceberg calving at Tasman Glacier, 2011–2012 99
5.1 Introduction 99
5.2 Background 99
5.3 Methods 100
5.3.1 Terminus and lake mapping 101
5.3.2 Water–level and temperature 102
5.3.3 Climate 103
5.3.4 Direct record of individual calving events 104
5.3.4.1 Timing of calving 107
5.3.4.2 Calving regions 108
5.3.4.3 Vertical extent of calving 108
5.3.4.4 Mechanisms of calving 110
5.3.4.5 Calving magnitude and volume 111
5.4 Results 113
5.4.1 Terminus geometry change 113
5.4.2 Temporal distribution of calving 116
5.4.3 Mechanisms of calving 120
5.4.4 Vertical extent of calving 122
5.4.5 Regional distribution of calving 124
5.4.6 Diurnal distribution of calving 127
5.4.7 Event magnitude and volumes 129
5.4.8 Climate and lake characteristics 132
5.4.8.1 Rainfall 132
5.4.8.2 Air temperature 134
5.4.8.3 Lake level 135
5.4.8.4 Lake temperature 135

5.5 Discussion 136
5.5.1 Comparison between the retreat of Tasman Glacier and identified calving events 136
5.5.2 Temporal patterns in calving events 137
5.5.2.1 Thermo–erosional notch calving 138
5.5.2.2 Over–steepening calving 140
5.5.2.3 Buoyancy–driven calving 141
5.5.2.4 Subaqueous calving 145
5.5.3 Regional patterns of calving and retreat 146
5.5.3.1 Western embayment 147
5.5.3.2 Southern ice cliff 149
5.5.3.3 Eastern embayment 151
5.5.4 Diurnal variations in calving 152
5.5.5 Factors contributing to calving 153
5.5.5.1 Climate and meltwater 153
5.5.5.2 Waterline melt and notching 154
5.5.5.3 Terminus structure and geometry 154
5.5.5.4 Basin morphology 156
5.5.6 Comparison with previous research 156
5.5.6.1 Previous research at Tasman Glacier 156
5.5.6.2 Frequency of calving events 157
5.5.6.3 Seasonal distribution of calving events 157
5.6 Conclusion 158
Chapter 6: Statistical analysis of sub–annual iceberg calving at Tasman Glacier, 2011–2012 161
6.1 Introduction 161
6.2 Calving volumes 162
6.2.1 Distribution of volumes 162
6.2.2 Volume as a function of time 163
6.3 Time dependent model for calving rate 165
6.4 Analysis of Calving Style 168
6.4.1 Correlations between successive events 168
6.4.2 Style–time dependence 171
6.5 Discussion 172
6.5.1 Calving event volumes 172
6.5.2 Temporal variability in iceberg calving 174
6.5.3 Clustering of events 176
6.5.4 Wider implications and model improvements 177
6.6 Conclusions 178

Chapter 7: Seismic detection of calving events at a lake–calving glacier, Tasman Glacier 181
7.1 Introduction 181
7.2 Background 181
7.3 Methods 183
7.3.1 Time–lapse photography 183
7.3.2 Seismic recordings 183
7.4 Analysis 185
7.4.1 Calving events 185
7.4.2 Examples of calving–generated seismic signals 187
7.4.2.1 Subaerial calving 187
7.4.2.2 Buoyancy–driven calving 193
7.4.2.3 Subaqueous calving 194
7.4.3 Common characteristics of calving–generated icequakes 195
7.4.3.1 Signal form 196
7.4.3.2 Frequency content 199
7.4.3.3 Signal duration 199
7.4.3.4 Integrated amplitude 200
7.4.3.5 Filtered response 201
7.4.3.6 Comparison of calving seismicity at a single location 203
7.4.4 STA/LTA trigger 205
7.5 Discussion 209
7.5.1 Calving–induced icequakes 209
7.5.1.1 Subaerial events 210
7.5.1.2 Buoyancy and subaqueous events 212
7.5.2 Seismic monitoring of iceberg calving 213
7.5.2.1 Iceberg magnitude and seismic characteristics 213
7.5.2.2 Automatic detection of calving icequakes 215
7.6 Conclusion 217
Chapter 8: Buoyancy–driven calving at Tasman Glacier 219
8.1 Introduction 219
8.2 Background 219
8.3 Methods 220
8.4 Description of calving events 220
8.4.1 August 2010 220
8.4.2 December 2010 223
8.4.3 February 2011 224
8.4.4 January and April 2012 227

8.4.5 February 2013 227
8.5 Discussion 229
8.5.1 Subaqueous ice cliff loss and buoyancy–driven calving 229
8.5.2 Buoyancy–driven calving and lake level fluctuations 230
8.5.3 Coseismic triggering of buoyancy–driven calving events 232
8.5.4 Flotation and buoyancy–driven calving at freshwater and tidewater glaciers 234
8.6 Conclusions 235
Chapter 9: Synthesis 237
9.1 Introduction 237
9.2 Conceptual model of calving at Tasman Glacier, 2000–2013 237
9.2.1 Terminus dynamics and calving pre–2006 238
9.2.2 Present terminus dynamics and calving processes 239
9.3 Future response of Tasman Glacier 241
9.4 Comparison of calving at Tasman Glacier with calving margins globally 245
9.4.1 Comparison of the evolution of Tasman Glacier with debris–covered glaciers globally 245
9.4.2 Comparison of calving frequencies and magnitudes 247
Chapter 10: Conclusions 249
10.1 Objectives revisited 249
10.2 Future work 252
10.3 Concluding remarks 253
References 255
Appendix A: Contents of the DVD 269
Appendix B: Coverage and sources of satellite imagery 271
Appendix C: Geophones and data loggers 273

List of Figures

Figure 2.1: Schematic representations of accumulation and ablation zones for a valley glacier.. 8

Figure 2.2: Supraglacial debris–cover and calving have had a significant impact on glacier mass balance of Tasman Glacier. Tasman Lake is in the foreground, with Aoraki/Mount Cook visible in the upper left of the photograph (photo: S. Winkler, 2007) 8

Figure 2.3: Schematic diagram demonstrating the evolution of a debris–covered tongue over multiple mass–balance cycles, showing net debris accumulation and glacier expansion. AD and TD refer to ablation– and transport dominant conditions, respectively (Kirkbride, 2000). 10

Figure 2.4: Supraglacial pond and exposed englacial conduit (arrowed) on the surface of the debris–covered Tasman Glacier. The clean ice walls at the margin of the supraglacial pond and surrounding area exposed due to backwasting and the gravitational reworking of debris. 13

Figure 2.5: Sequence of proglacial lake development at a debris–covered glacier due to the (1) downwasting and (2) coalescing of supraglacial ponds, (3) eventually leading to subaqueous calving and (4) rapid retreat of the glacier (Kirkbride, 1993). 15

Figure 2.6: Schematic diagram showing the three principal modes of crack propagation from Benn et al. (2007b). Arrows indicate direction of applied force. Mode I is the development of a fracture due to tensile stresses. Mode II occurs when a fracture develops along a shear plan and the fracture walls remain in contact and sliding past each other. Mode III describes the tearing of an ice body, with propagation occurring at right angles to the original parallel shearing. 20

Figure 2.7: Diagram showing the factors that affect the crevasse development and propagation via Mode I (Figure 2.6) fracture. (A) Tensile and compressive forces are matched limiting the depth of penetration. (B) Water within the crevasse increases pressure at the fracture tip, allowing the crevasse to penetrate to greater depths (Benn and Evans 2010). 21

Figure 2.8: Common crevasse patterns found in valley glaciers. (A) Chevron crevasses from due to lateral shear. (B) Transverse crevasses develop with a slightly curved form due to a combination of extending glacier flow and lateral shear. (C) Splaying crevasses develop due to lateral shear stress and longitudinal shear stress as a result of compressive flow (after Nye, 1957; Benn and Evans 2010). 22

Figure 2.9: Illustration demonstrating the imbalance of horizontal cryostatic and hydrostatic forces at a grounded calving margin. 24

Figure 2.10: Thermo–erosional notche forming at the terminus of Tasman Glacier. (A) shows the significance of stable lake level in notch formation at the *c.* 20 m high ice cliff. (B) The extensive development of notches along the ice cliff is shown (black arrow) and the importance of crevasses (white arrows) on calving due to notch development. 26

Figure 2.11: Diagram of the key parameters the affect terminus flotation as defined in equation (2.3). (A) Ice thickness (h_i) exceeds flotation thickness (h_f) resulting in stability of the terminus. (B) Ice thickness at the terminus is below flotation thickness due to thinning or increased water depth, leading to flotation and retreat until h_i equals h_f. 27

Figure 2.12: Illustration of iceberg calving mechanisms from grounded termini (adapted from van der Veen, 2002). See text for explanation. 29

Figure 2.13: Conceptual model of a calving continuum. See text for explanation (Haresign, 2004).....30

Figure 2.14: Schematic diagram of the mass flux in (Q_{in}) and calving flux (Q_c) at a calving terminus. Key variables in determining mass flux and major processes resulting in the loss ice at the terminus (adapted from Motyka et al. (2003a) and O'Neel et al. (2003)). 31

Figure 2.15: Conceptual illustration from Hughes (2002) showing bending shear bands for (A) and grounded land based ice cliff with the vertical velocity gradient inducing forwards bending causing slip along shear bands, and (B) slab calving from the subaerial ice cliff resulting in the formation of a subaqueous ice foot at a water terminating glacier. 38

Figure 2.16: Illustration of an ice ledge and the forces acting at a water terminating glacier according to Hughes (2002). 38

Figure 2.17: The cyclical pattern of tidewater glacier advance (A) and retreat (B). (A) Slow advance of the glacier occurs behind a moraine shoal (positions 1–3). (B) After an initial climate forcing that alters water level at the terminus (4), retreat of the glacier will occur as water depth increases down the moraine shoal (5) until (6) it either reaches equilibrium or retreats out of the water (adapted from Warren, 1992) 41

Figure 2.18: Calving in response to longitudinal strain rates. Surface crevasses propagate downward to a depth, d, in response to the velocity gradient $\partial U_B/\partial x$, where calving is assumed to occur when $d = h_w$ (Benn et al., 2007a). 43

Figure 2.19: Schematic diagram showing the bottom (A and C) and (B) top out rotation and scrapping of calved icebergs at floating (A and B) and grounded (C) termini (adapted from Amundson et al., 2010).....48

Figure 2.20: Schematic diagram of a calved ice block entering a proglacial water–body and potential the potential seismogenic mechanisms. After the iceberg 'slams' (A) in the proglacial water body it transfers its momentum to the water, decelerating the iceberg (B) and causing a cavity to form above it. This cavity begins to collapse (C), eventually pinching off (D). A Worthington jet (E) is often formed after the cavity pinch off and complete submergence of the iceberg. Illustration adapted from Gekle and Gordillo (2010), and Bartholomaus et al. (2012). 49

Figure 3.1: Map of the *Aoraki*/Mount Cook National Park showing the glaciers discussed throughout the thesis and their locations. Topographic data sourced from the LINZ Topo50 database. 54

Figure 3.2: (A) Satellite mosaic (Worldview 2– 15/4/10 and 19/2/10), of Tasman Glacier and the surrounding area showing the extent of LIA glaciation. (B) and (C) are photographs looking up to the head of Tasman Glacier, and up the Hochstetter icefall respectively. Location of major flow units discussed in text also shown: (1) Hochstetter icefall, (2) upper Tasman Glacier, (3) Rudolf Glacier, (4) Darwin Glacier, and (5) Ball Glacier. Dotted line in (B) indicates the area of rock lost from *Aoraki*/Mt Cook on the 14 December 1991 (Photos: S. Winkler). 56

Figure 3.3: Graph showing the deviation of the EOSS away from the mean ELA (ELA_0) of Tasman Glacier between 1977 and 2011. ELA_0 for Tasman Glacier is 1810 m (Willsman et al., 2012). 58

Figure 3.4: Photograph showing exposed sections of clean ice and the debris thickness on the lower terminus of Tasman Glacier. Arrowed boulder is approximately 1 m in diameter. 59

Figure 3.5: The terminus of Tasman Glacier showing the up–glacier extension of the debris–covered area since 1890. The bare–ice area is shaded, lakes are shown in black. The rest of the glacier surface is debris–covered. The 1991 map shows the area of a large rock

avalanche deposit which fell on the glacier on 14 December, 1991. Arrows indicate locations of contemporary outwash streams (Kirkbride, 1993). 60

Figure 3.6: Aerial photograph of the Tasman Glacier, 25 February 1964. A number of small supraglacial sink–holes are evident on the lower and true left of the glacier. Also noticeable is a tongue of clean ice sourced from the Hochstetter Glacier on the upper section of the glacier (New Zealand Department of Lands and Survey photo 3724/24). 62

Figure 3.7: Tasman Lake bathymetric change between 1995 (Watson, 1995) and 2002 (Röhl, 2005). 64

Figure 4.1: Spatial changes of Tasman Glacier between 2000 and the end of 2012 digitised from ASTER imagery. Each panel describes the plan form change of the glacier between three image dates with the final image reproduced as the base image in the following sequence. White indicates Tasman Lake and supraglacial ponds when evident on the surface of the glacier at the start of each image period. Dates reported as month/year. See Table 4.1 for date and area information. 72

Figure 4.2: (A) Retreat rates (black squares are u_{ave} and gray diamonds are u_{max}) and (B) changes in terminus length (T_L) of Tasman Glacier between 2000 and 2013. Retreat rates highlight the variability of glacier retreat over the study period and the sharp increase in retreat between 2006 and 2007. The dramatic the shortening of the terminus in contact with Tasman Lake in 2007 indicates that retreat of the glacier is being centred over a smaller area. See Table 4.1 for values. 75

Figure 4.3: Lake area (squares) and volume (circles) for Tasman Lake since its initial formation in the late 1950s. Grey squares and circles are area and volume information from previous studies. See Table 4.2 for explanation of sources. 77

Figure 4.4: Bathymetry of Tasman Lake in 2008. The change in surface area of Tasman Lake between 2008 and 2013 is also shown. 77

Figure 4.5: Graph of the increase in surface area of Tasman Lake between 1957 (time zero on x–axis) and 2012, showing the three phases of retreat. Also shown are the best fit linear and power–law functions for the three phases discussed in the text. The red arrow indicates the large shift in lake area that occurred between 2006 and 2007. 78

Figure 4.6: Terminus positions of Tasman Glacier between 2000 and 2013 overlaid on Tasman Lake bathymetry (20 m contour interval) from 2008. Also shown is the centre line of Tasman Glacier along which the long profile in Figure 4.7 is derived. Supraglacial ponds on the lower glacier are not shown. 80

Figure 4.7: (A) Long profile of Tasman Lake along the former centre line of Tasman Glacier from the southern margin moraine dam, with terminus positions derived from satellite imagery. Rapid shoaling towards the terminus in 2008 evident in Figure 4.6 is not shown as terminus position has retreated past this point. Dotted line indicates the inferred water–depth calculated by terminus uplift. (B) Distance along centre line in Figure 4.6 and (C) water depth (squares) at those locations. Also shown in (C) is the subaerial freeboard height (h_s) below which flotation of the glacier is initiated. Hollow points indicate estimated water depths and freeboard height..... 81

Figure 4.8: Photographs of large calving event in August 2010 initiated by flotation and buoyancy of the terminus. The sequence of photographs shows the terminus prior to (A) and mid (B) uplift. (C) Shows the post calving geometry. Uplift and flotation occurred over a 30 day period (Photos: G. Pearson)..... 82

Figure 4.9: Bathymetric map of Tasman Lake with the position of the Tasman Glacier terminus and the extent of supraglacial ponds in April 2000 and January 2006. In general, pond growth is in the region of greatest water depth of Tasman Lake in 2008. 86

Figure 4.10: Oblique aerial photography of the terminus of Tasman Glacier in (A) March 2007 showing the state of the terminus immediately prior to breakup (Photo: S. Winkler) and (B) February 2008 after breakup. Note that several large and coherent icebergs have already calved from the terminus in (A) and that a large number of icebergs were preserved over the following year. 87

Figure 4.11: False colour ASTER image of Tasman Lake at the start of April 2007 showing the disintegration of the lower section of the Tasman Glacier terminus pictured in Figure 4.10A. The presence of white icebergs within the region of the former terminus indicates that calving has taken place in the days prior to image acquisition. 88

Figure 4.12: Photographs of large calving events at Tasman Glacier that was initiated by flotation and buoyancy of the terminus in February 2009. Note that the icebergs have rotated as they calved from the terminus..... 89

Figure 4.13: Photograph showing the terminus of Tasman Glacier in May 2012. Note that no supraglacial ponds are present on the lower glacier tongue as well as the increase in glacier slope present from *c.* 700 m (white dotted line) up glacier from the terminus. It was along this line that the calving occurred in February 2013. Also note the depression present running along the centre of the glacier (black dotted line) and the presence of transverse crevasses at the terminus (arrowed). 90

Figure 4.14: (A) Surface area of glacial lakes in the Mount Cook National Park between 1955 and 2013. Data for Tasman Lake is shown in Table 4.1, with the data for the all other glacier lakes from a combination of data sources compiled by Robertson (2012): Mueller (Watson, 1995; Röhl, 2005; Robertson, 2012), Hooker (Warren and Kirkbride, 1998; Robertson, 2012), Murchison (Robertson, 2012), Classen (Robertson, 2012), Grey/Maud (Warren and Kirkbride, 1998; Robertson, 2012), and Godley (Warren and Kirkbride, 1998; Robertson, 2012). (B) The percentage of lake growth with respect to time the six proglacial lakes between 1955 and 2013 is shown so a comparison between lakes is possible. 100 % refers to the last surface area of the proglacial lake reported. . 95

Figure 4.15: Stages of lake growth proposed by Robertson (2012) for lakes within the *Aoraki*/Mount Cook National Park. Once ponds have formed (stage 1) and coalesced (stage 2) on a downwasting debris–covered terminus, expansion of the proglacial lake (stage 3) takes place through a series of steady (3a), rapid/accelerating (3b) and decelerating (3c) sub–stages. Finally stability is attained due to basin morphology and glacier dynamics (stage 4). 97

Figure 5.1: Map showing an example of how retreat of the terminus of Tasman Glacier was calculated by measuring the perpendicular distance between image dates (*L*) at a spacing of 50 m along the initial terminus position. Also shown are the three regions that are used to analyse spatial variations in retreat; WE is western embayment, EE is eastern embayment and SI is southern ice cliff (see section 5.4.3.2 for more detail). . 102

Figure 5.2: Location of Tasman Glacier and Tasman Lake showing the surrounding glaciated region (light grey) and the position of the time–lapse camera, water level logger and automatic weather stations at Mount Cook Village and Rose Ridge. Major ridgelines are highlighted by dotted lines. Proglacial lakes are shown in dark grey. 103

Figure 5.3: (A) Photograph showing the position of the time–lapse camera set atop the unstable western lateral moraine (star). The camera was later moved from this position as the section under the power supply box collapsed into Tasman Lake. (B) Photograph of the time–lapse camera setup on the western lateral moraine..... 104

Figure 5.4: Sequential images from the time–lapse camera showing the visible loss of ice (circled) from the southern ice cliff on 24/04/12. The waves emanating from the epicentre of calving suggest that calving has recently taken place and aid in locating the calving event..... 106

Figure 5.5: Photograph taken by the author of the terminus of Tasman Glacier on 28/04/12 after a series of calving events over multiple days (including the event shown in Figure 5.4). Note the newly exposed blue ice indicating recent calving in the centre of the ice cliff (circled) compared to the un–calved white ice along the rest of the ice cliff. 106

Figure 5.6: Deep blue basal ice present immediately after a large subaqueous calving event on 02/04/2012. 106

Figure 5.7: Cropped time–lapse images showing calving events occurring (A) simultaneous to the photograph, and (B) immediately before the image was taken. The spray of water and particles emanating from the point of calving can clearly be seen in (A), indicating image capture and calving occurring simultaneously. Waves emanating from the epicentre of calving shown in (B) suggest calving has taken place in the minute prior to image capture. 108

Figure 5.8: Photo of the terminus of Tasman Glacier on 13/12/12 showing each of the three spatial regions set using obvious natural breaks in aspect. 108

Figure 5.9: Diagram showing the five categories of vertical extent used in this study. Upper and lower refer to the upper and lower half of the subaerial ice cliff, respectively. Full–height is the entire subaerial ice cliff, whereas full–depth calving events comprise the loss of a height greater than the subaerial ice cliff height. Subaqueous refers to calving from the subaqueous section of the ice cliff or "ice foot"..... 109

Figure 5.10: Image showing icebergs ranging in colour from deep blue (basal ice) through to primarily white/dirty icebergs after a full–depth calving event at 13:05 29/04/12..... 109

Figure 5.11: Examples of pre–calving terminus geometry and morphology for (A) Over–steepening of the subaerial ice cliff, (B) thermo–erosional notching undercutting the ice cliff at or below the waterline, (C–E) buoyancy induced calving, (F–G) subaqueous calving. 111

Figure 5.12: Distribution of volume measurements for the example events (crosses) in each magnitude increment (log–log scale). The mean for each event is also shown (grey circles) Volume up to magnitude 6 are based on ten example events for each magnitude. The limited number of data points for magnitude 1 and 2 events is an artefact of the resolution to which event dimensions could be determined (*c.* 5 m). Power–law fit and regression equation is also shown. 113

Figure 5.13: Changes in the terminus of Tasman Glacier between March 2011 and June 2012 from ASTER satellite imagery. Dark grey area on the lower terminus in March 2011 is a supraglacial pond. WE, is western embayment. SI, is southern ice cliff. EE, is eastern embayment. 114

Figure 5.14: Time–lapse images taken at the beginning and end of the study, as well as at approximately the same time as satellite imagery used in Figure 5.13. Note that the pointing angle and location of the camera was changed between some images..... 116

Figure 5.15: Calving events grouped by month showing the distribution of events for the entire data, regions and mechanism of calving. 'All' refers to the entire dataset, 'EE' is eastern embayment, 'SI' is southern ice cliff and 'WE' is western embayment. 'B' is buoyancy–driven calving, 'N' is thermo–erosional notch calving, 'O' is over–steepening calving, and 'SA' is subaqueous calving. 117

Figure 5.16: Plot showing the daily totals (dots) of calving events at Tasman Glacier. Also shown are the 5–day (grey line) and 30–day (black line) running mean across the entire study period. Grey bars represent days that the camera was not operational. The 5–day running mean shows the variability in calving over the study period, while the 30–day running mean indicates the general increase in the number of calving events during January and the start of February 2012. 119

Figure 5.17: Graph showing the total number of calving events for each of the four mechanisms identified in this study. O is over–steepening calving, N is thermo–erosional notch calving, B is buoyancy–driven calving, and SA is subaqueous calving. 120

Figure 5.18: The number of calving events per day graphed by the mechanism of calving. Also shown are the 5–day (grey line) and 30–day (black line) running mean across the entire study period. Grey bars represent days that the camera was not operational due to factors such as interruption of the power supply. Note the periods of elevated activity able to be identified in over–steepening (O) and thermo–erosional notch (N) driven calving event graphs highlighting the grouping of events with respect to time. In contrast, buoyancy (B) and subaqueous (SA) events were less common. 122

Figure 5.19: Daily distribution of the vertical extent of the calved sections of the ice cliff. Also shown are the 5–day (grey line) and 30–day (black line) running mean across the entire study period. Grey bars represent days that the camera was not operational. See section 5.4.3.3 for explanation of extents. 123

Figure 5.20: The distribution of 30–day running means for the different vertical sections of the ice cliff by the mechanism of calving. Grey bars indicate periods where the camera was not operational. Due to the parameters selected, notching events could only occur at the lower section and full–height of the ice cliff, while over–steepening events (O) could occur throughout the subaerial section of the ice cliff. N is notching events, B is buoyancy events, and SA is subaqueous events (see section 5.4.3.4). 124

Figure 5.21: The number of calving events per day within each of the three regions. Also shown are the 5–day (grey line) and 30–day (black line) running mean across the entire study period. Grey bars represent days that the camera was not operational. The number of calving events increases during January and February 2012 in both the western embayment (WE) and southern ice cliff (SI). However, increases are more pronounced in the western embayment. Limited calving was observed along the eastern embayment (EE) due to the limited view of the time–lapse camera. 126

Figure 5.22: The distribution of the 30–day running mean calving frequencies by the four mechanisms used in this study along the western embayment ice cliff (WE), the southern ice cliff (SI), and the eastern embayment (EE). Grey bars indicate periods where the camera was not operational. Note that in the western embayment total calving frequency and notch driven calving mirror each other. Vertical black lines indicate the two largest volume calving events to occur 127

Figure 5.23: The distribution of calving events by the time of day that they occurred, showing the distribution of events for the entire data (All), regions (western embayment (WE), southern ice cliff (SI), and eastern embayment (EE)) and mechanism (over–steepening (O), notch (N), buoyancy (B), and subaqueous (SA) calving) of calving. The 78 calving events recorded during night time hours are not shown. 128

Figure 5.24: The distribution of magnitudes (A) and inferred volumes (B) for the identified calving events between October 2011 and November 2012. 130

Figure 5.25: The distribution of calving events within each magnitude class for (A) all calving events, (B) notch (N) and over–steepening (O) calving events, and (C) buoyancy–driven (B) and subaqueous (SA) calving events. See Table 5.2 for estimated volumes of each magnitude increment. 131

Figure 5.26: Cumulative percentage plot of volume (black line) and the number of events (grey line) throughout the study period. Large steeps in the percentage of volume lost over the study period are associated with high magnitude buoyancy and subaqueous calving events. 131

Figure 5.27: Monthly rainfall (bars) and mean air temperature (lines) at MCV (dark grey bars and circles) and RR (light grey bars and squares) AWS. October 2011 and November

2012 are incomplete months, with only 3 and 20 days (respectively) of data included. 133

Figure 5.28: Daily rainfall (grey bars) and maximum air temperature (solid black line) at Mount Cook Village (A) for the period 27 October 2011 to 3 May 2012. (B) Lake level (black line) and lake temperature (grey line) for Tasman Lake over the concurrent period of time as A and B is also shown to highlight the dynamic link between rainfall, air temperature, lake level and lake temperature..... 133

Figure 5.29: Diurnal distribution of mean hourly air temperature at MCV between 27 October 2011 and 20 November 2012. 134

Figure 5.30: Diurnal fluctuations in relative lake level of Tasman Glacier over a seven day period in December 2011. 135

Figure 5.31: Comparison plots between (top) lake level (black line) and temperature (grey line) and the (bottom) 30–day running means for each of the four calving mechanism between October 2011 and November 2012. Grey bars signify days the camera was not operational. 138

Figure 5.32: Calving due to formation of a thermo–erosional notch at the waterline. (A) Example of a thermo–erosional notch event from the southern ice cliff. Note the undercut nature of the ice cliff prior to calving. (B) The undercut calved section has become isolated and undercut due to calving from the surrounding area and formation of chevron crevasses near the terminus..... 140

Figure 5.33: Over–steepening calving event in (A) the western embayment and (B) the southern ice cliff. The section of the terminus that calved in (A) was over–steepened after a large calving event removed the section in front in the hours prior to this calving event. ... 141

Figure 5.34: The high magnitude buoyancy–driven calving events observed throughout the study period occurring along (A) the entire width of the terminus overnight of 30/04/12 and (B) from the eastern section of the southern ice cliff on 29/04/12. The resulting icebergs have a mixture of white ice through to deep blue icebergs indicating that calving has occurred throughout the majority of the ice column. The dotted line indicates the calved section in the upper image. Image quality is degraded for the 30/01/12 event due to scratches on the lens. 142

Figure 5.35: The development of surface crevasses immediately up glacier prior to the calving event on 29/04/12 (shown in Figure 5.34). Black arrows indicate the region in which crevasses formed throughout the month of April after a subaqueous calving event. White box indicates the area shown in the close up images on 29/04/12 and 02/05/12. White arrow indicates an exposed thermo–erosional notch present prior to the calving event. Note the highly irregular surface present in the 02/05/12 image highlighting the potential for large events to increase smaller over–steepening calving. 144

Figure 5.36: Lower magnitude buoyancy–induced calving events on the (A) 03/01/12 and (B) 05/01/12, indicating that buoyant forces affect calving at a range of spatial scales. ... 145

Figure 5.37: Image sequence showing a subaqueous calving event in the area in front of the southern ice cliff. Note the deep blue icebergs that emanated from the 146

Figure 5.38: The numbered icebergs indicate the potential presence of a subaqueous ice ‘foot’ within the western embayment and the absence of one along the southern ice cliff. The inability of either of the icebergs to enter the eastern and western embayment indicates that those sections are ice cored, whereas the close proximity of the icebergs to the southern ice cliff indicate a near vertical ice cliff. The height of each iceberg is ~ 20 m. 148

Figure 5.39: View of the southern ice cliff showing transverse crevasses (dotted white line) developed at the terminus of Tasman Glacier indicating flow direction and the presence of extensive flow towards the southern ice cliff. 150

Figure 5.40: Overflow (arrowed) of meltwater into Tasman Lake that regularly develops throughout the day from the diurnal melt cycle within the western embayment of Tasman Glacier. 152

Figure 5.41: Images of the Tasman Glacier terminus in December 2011 (A) and November 2012 (C), with interpretation of identifiable crevasses, (B) and (D) respectively. Note the highly complex arrangement of structures that appear to cut across each other, indicating that not only flow velocity, but also terminus geometry plays an important control on the development of crevasses. Square and dotted line on the glacier surface indicates the approximate position of a bolder and ridge in the two images. 155

Figure 6.1: Cumulative calving frequency (normalised to 1) against logarithm of volume fitted with a variety of distributions. Only a gamma distribution gives a satisfactory fit to the observed volume distribution. 162

Figure 6.2: PDF converted to calving volume using the gamma distribution shown in Figure 6.1. Botch linear (A) and log (B) volumes scales are shown to highlight the overall distribution of calving event volumes. Note that the long tail (very large volumes) is not shown in A. 164

Figure 6.3: Local linear regression of log(volume) against time in days since the start of the observation period. Time zero refers to the first day of the study period, 27 October 2011. Note the overall increase in mean event volumes during winter months (approximately 214 to 310 days) when compared to the rest of the dataset. 164

Figure 6.4: Comparison plots of the observed calving rate with the stationary rate (A) and exponential intervals (B) from the fitted model of calving occurrences at Tasman Glacier. The compensator used is Poisson. 166

Figure 6.5: Variations in (A) lake temperature and (B) lake level (depth) between 27 October 2011 and 22 November 2012. The fitted proportional hazard model for all styles of calving events is shown in C. 167

Figure 6.6: Plot showing the influence of lake temperature and lake depth on calving rate. 167

Figure 6.7: The modelled (Equation (6.3)) survival probability (Prob(R>*r*)) of calving occurrences (i.e. the probability that the time between events is > *r*) for a variety of lake temperatures (T (ºC) = 1, 3, 6) and lake levels (D (m) = 0, 1, 3, 6). The reference curve (grey dotted line) is the modelled survival probability given a Poisson process (Equation (6.4)). 169

Figure 7.1: Map of the lower Tasman Glacier and Tasman Lake. The location of the broadband seismometer (BB), two geophones (GD and GU, Appendix C) and the time–lapse camera positions over the survey period. Background image is a false colour ASTER (Advanced Spaceborne Thermal Emission and Reflection) image taken on 26 February 2012. Topographic contour interval is 200 m and is from LINZ NZTopo Database (www.linz.govt.nz). 185

Figure 7.2: Temporal distribution of calving event magnitudes (A) and estimated volumes (B) at the Tasman Glacier terminus between 22 February and April 30 2012. See section 5.4.3.5 for information on magnitude scale and volume estimation. 186

Figure 7.3: Example of an unfiltered seismic waveform recorded on the vertical channel of BB showing two separate calving–generated seismic signals generated by calving at the same location between image pairs. Arrows indicate the two separate sections that calved between images. Time zero is UTC 24/04/2012 22:42:30. 187

Figure 7.4: Pre and post time–lapse images (A) of a subaerial calving event at the Tasman Glacier terminus, unfiltered vertical component of the seismic waveform (B), absolute of values seismic data (C), and spectrogram of the unfiltered waveform (D). Circles in the pre– and post–calving images in (A) indicate the calved section, with arrows representing the extent of waves emanating from the location of calving. The calving event had an iceberg size (magnitude) of 1 (*c.* 125 m^3) and originated from the lower section of the subaerial ice cliff that had become over–steepened. Maximum ground velocity (B) in the vertical component was 1.9 μm s^{-1}. The onset and end timing of calving (blue vertical lines in C) was calculated based on the deviation of the signal away from the background noise using a running mean of absolute values of the seismic waveform (red line in C). Calving was considered to have ended when the running average had returned to the onset value. Absolute values of the seismic data also show the gradual onset of calving and highlights the 'step' in icequake amplitude (grey diamond) discussed in the text. The spectrogram (D) of the event was computed showing the log of spectral amplitude between 0.5 and 30 Hz, as a function of time. Warm (reddish) colours define high spectral amplitudes; cold (bluish) colours represent lower amplitudes and background. Time zero is UTC 07/04/2012 00:23:50, with calving onset at 00:23:52.6. 188

Figure 7.5: A–D sows the same data types as in Figure 7.4, except for a iceberg magnitude 3 (*c.* 2700 m^3) calving event from the upper section of the subaerial ice cliff that had become over–steepened prior to calving (circled in A). The calving event had a gradual onset up until a step in amplitude (grey diamond). Maximum vertical ground velocity was 4.6 μm s^{-1}. Time zero is UTC 22/02/2012 00:29:14, with calving onset (first blue vertical line) at 00:29:15.8. 189

Figure 7.6: A–D show the same data types is in Figure 7.4, except for a iceberg magnitude 4 (*c.* 7300 m^3) calving event of the entire height of the subaerial ice cliff that had become over–steepened prior to calving (circled in A). The calving event had a gradual onset up until a step in amplitude (grey diamond). Maximum vertical ground velocity was 8.4 μm s^{-1}. Time zero is UTC 14/03/2012 05:54:50, with calving onset at 05:54:53.0. 190

Figure 7.7: Magnitude 2 (*c.* 1200 m^3) notch–driven calving event from the subaerial ice cliff in the western embayment. A–D are the same data types shown in Figure 7.4. The circled section in A1–2 is the location of calving. Time zero is at UTC 03/03/2012 04:59:22 and the start of the calving event is at 04:59:25.0 (first blue line in C). Maximum vertical ground velocity was 4.1 μm s^{-1}. 191

Figure 7.8: Magnitude 3 (*c.* 2700 m^3) notch–driven calving event from the subaerial ice cliff in the western embayment. A–D are the same data types shown in Figure 7.4. The circled section in A1–2 is the location of calving. Time zero is at UTC 02/04/2012 04:39:47 and the start of the calving event is at 04:39:50.8 (first blue line in C). Maximum vertical ground velocity was 6.2 μm s^{-1}. 192

Figure 7.9: A–D are the same data types shown in Figure 7.4 for a magnitude 5 (*c.* 13500 m^3) calving event of the entire height of the subaerial ice cliff that was undercut by a thermo–erosional notch prior to calving (circled in A). The calving event again had a gradual onset up until a step in amplitude (grey diamond). Maximum vertical ground velocity was 24 μm s^{-1}. Time zero is UTC is 21/03/2012 01:24:07, with calving onset at 01:24:09.0. 193

Figure 7.10: Magnitude 14 (1.4×10^6 m^3) buoyancy–driven calving event on the eastern section of the southern ice cliff. A–D are the same data types shown in Figure 7.4. The calving event had a long (*c.* 10 s) onset, increasing steadily over a 5 second period (B) to the first peak in seismic amplitude. In total, five peaks and an extended period of elevated seismic amplitudes occurred throughout the calving event, with a secondary event present after amplitudes had returned to background levels (second blue line in B). High spectral amplitudes in the low frequency 1–3 Hz range dominate the spectrogram of the

calving event (D), although high frequency signals (up to 20 Hz) are present throughout. Maximum vertical ground velocity was 51.5 μm s^{-1}. Time zero is UTC 29/04/2012 01:07:30, with calving onset at 01:07:42.0 (first blue vertical line in C).. 194

Figure 7.11: Magnitude 12 (1.0×10^6 m^3) subaqueous calving event originating from the base of the southern ice cliff. (A) The pre– (A1), mid– (A2), and post–calving (A3) time–lapse images of the subaqueous calving event. The entire vertical seismic waveform is shown in (B), with inserts (C) and (D) showing the seismic data of two separate periods of activity between the mid– (A2) and post–calving (A3) images. Time zero in (B) is UTC 02/04/2012 05:47:56. Maximum vertical ground velocity across the entire seismic waveform (B) was 23 μm s^{-1}. The data presented in C1–3 and D1–3 is the same as shown in Figure 7.4A–C. Inset boxes (C) and (D) start at 05:47:56 and 05:51:08, respectively. Both periods of activity have long (*c.* 20 s) onsets prior to the first major peak in amplitude. 195

Figure 7.12: Example icequakes generated by subaerial calving identified from the time–lapse imagery record. Seismograms were recorded on the vertical channel and have been filtered between 1 and 5 Hz. The amplitude of all the example icequakes have been normalised, with the relative amplitude of each icequake (in μm s^{-1}) indicated by the height of the vertical bar on the left of the seismogram. The grey diamond indicates the sudden increase (or 'step') in seismic amplitude discussed in section 7.5.1. 197

Figure 7.13: Five example icequakes generated by buoyancy or subaqueous calving from the terminus of Tasman Glacier. Seismograms were recorded on the vertical channel and have been filtered between 1 and 5 Hz. The top seismogram is the buoyancy event described in section 7.4.2.2, with the four other calving events subaqueous. The second and third examples are the two successive events in described in section 7.4.2.3. Vertical black bars to the left of the seismic waveforms show the relative maximum amplitude (in μm s^{-1}) of each event. 198

Figure 7.14: Graphs of unfiltered seismic waveform maximum amplitudes (in μm s^{-1}), magnitude, and mechanism of calving. Event maximum amplitude generally increased between magnitude 1 (*c.* 300 m^3 of ice) and 2 (*c.* 1200 m^3 of ice) events, with great scattering of seismic amplitudes between magnitude 3 (*c.* 2700 m^3 of ice) and 6 (*c.* 17000 m^3 of ice). Higher magnitude events (12 and 14) did not necessarily have higher seismic amplitudes, but did tend to be greater than lower magnitude events. Over–steepening (O) and notch–driven (N) events were confined to magnitudes 1 to 6, with buoyancy (B) and subaqueous (SA) calving events typically higher in magnitude. Regression equations and R^2 are also shown for All, N and O events. 198

Figure 7.15: Graphs of the duration (in seconds) of seismic waveform, magnitude, and mechanism of calving events from the time–lapse imagery. Event durations generally increased marginally between magnitude 1 (*c.* 300 m^3 of ice) and 6 (*c.* 17000 m^3 of ice), although there is some scattering within each magnitude increment. Higher magnitude events (12 and 14) were longer than lower magnitude events. Over–steepening (O) and notch–driven (N) events were confined to magnitude 1 to 6 events, with buoyancy (B) and subaqueous (SA) calving events typically higher in magnitude and longer in duration. 200

Figure 7.16: Graphs (log–log scale) of integrated amplitude and magnitude (calving size) of calving–generated seismic waveforms. There is scatter of integrated amplitude data, although there is a general increasing trend with respect to magnitude. Over–steepening (O) and notch–driven (N) events were confined to magnitude 1 to 6 events, with buoyancy (B) and subaqueous (SA) calving events typically higher in magnitude. The magnitude 14 buoyancy–driven event is several orders of magnitude greater than all other events. Power–law best fits are shown for All, N, and O events. Linear and power–law regression equations and R^2 are also shown for All, N and O events. 201

Figure 7.17: Graphs of the 1–5 and 1–3 Hz filtered seismic waveform maximum amplitudes (in μm s^{-1}), magnitude and mechanism of calving. Over–steepening (O), notch–driven (N) and subaqueous and buoyancy (SA/B) events are shown in separate graphs, with 'All' referring to all events. Regression equations and R^2 are also shown for All, N and O events. 202

Figure 7.18: Graphs (log–log scale) of integrated amplitude and magnitude (calving size) of calving–generated seismic waveforms filtered between 1–5 Hz and 1–3 Hz. 'All' refers to all events, with over–steepening (O) and notch–driven (N) events in separate graphs. Subaqueous and buoyancy events are presented in the same graph (SA/B). Regression equations (power–law and linear) and R^2 are also shown for All, N and O events. 203

Figure 7.19: Photograph of the terminus of Tasman Glacier on 02/05/2012 showing the western embayment (WE), eastern embayment (EE), and southern ice cliff (SI). SI–E represents the eastern section of the southern ice cliff along which seismic parameters are compared with calving magnitude. 203

Figure 7.20: Graphs showing the comparison between magnitude and (A) duration, (B) maximum amplitude, and (C) integrated amplitude (log–log scale). Regression equations and R^2 are shown for each graph. 204

Figure 7.21: Graphs showing the 1–5 Hz and 1–3 Hz filtered comparison of the subset of calving events between iceberg magnitude and maximum amplitude or integrated amplitude (log–log scale) described in section 7.4.3.6. Linear fit, regression equation and R^2 are shown for maximum amplitude. Power–law fit and equation as well as linear regression equation and R^2 is shown for integrated amplitude. 205

Figure 7.22: Example of the recursive STA/LTA event detector triggering for a magnitude 4 over–steepening calving event. (A) The unfiltered seismic waveform with the timing of the trigger threshold being exceeded (red line) and when the event has returned to near background levels (blue line). (B) The STA/LTA ratio over time showing background levels and the triggering of the event once the threshold of 10 has been met. STA and LTA window lengths are 3 and 40 seconds, respectively. Time zero is UTC 24/04/2012 22:50:30. Note that there is a lag between the onset of the event and the threshold being exceeded..... 206

Figure 7.23: The timing and duration of events that exceeded the recursive STA/LTA trigger threshold for the day UTC 24 April 2012. The light grey area indicates night time hours where the time–lapse camera was non operational and no manually identified events occurred. There is no evidence that occurred along the western embayment and southern ice cliff from the time–lapse images bracketing night time hours. 207

Figure 7.24: Seismic event identified by the STA/LTA trigger during night time hours. The seismic waveform is shown in (A), with the STA/LTA ratio in (B). The spectrogram of the event is shown in (C), with warm (reddish) colours high spectral amplitudes; cold (bluish) colours represent lower amplitudes and background The signal form and frequency content is similar to buoyancy or subaqueous calving events, although there is no evidence for such calving events to have occurred between image pairs in Figure 7.23. Time zero is UTC 24/04/2012 11:56:10. Maximum amplitude in (A) is 3.8 μm s^{-1}. 208

Figure 7.25: Triggered seismic event identified by the STA/LTA event detector. A–C show the same information as described for Figure 7.24. Signal form and frequency content is different to this identified in section 7.4.3. Time zero is UTC 24/04/2012 16:33:30. Maximum seismic amplitude in (A) is 4.4 μm s^{-1}. 208

Figure 7.26: Seismic event that triggered the STA/LTA event detector. A–C is the same as Figure 7.24. The event has a frequency content different to calving events and has

sudden onset unlike the relatively gradual onset of calving events (e.g., Figure 7.22) Time zero is UTC 24/04/2012 02:16:10. Maximum amplitude in (A) is 2.9 μm s^{-1}. ... 209

Figure 7.27: Cropped time–lapse image on 17/02/2012 showing the splash of water associated with the entry of the calved iceberg into the proglacial water–body. It is this entry into the proglacial water–body and the collapse of a cavity formed by the decelerating ice block that is considered to be the primary source of seismic energy during subaerial calving. 211

Figure 8.1: Oblique photographs and morphological maps of Tasman Glacier depicting the sequence of events leading up to, and post, calving during August 2010. (A) 22 April. terminus geometry pre–flotation. (B) 20 August, mid–flotation geometry. Black arrows indicate tilted thermo–erosional notches and white arrows indicate the hinge point of calving failure. (C) 22 August. Post calving terminus geometry (sources: D. Callesen and G. Pearson). 221

Figure 8.2: Photograph of a section of the calving terminus of Tasman Glacier showing uplifted thermo–erosional notches (arrowed) on 9 August 2010 prior to the 22 August calving event. Maximum height of notches is *c.* 25 m above the waterline in the central section of the terminus. Note the extensive snow cover over the lower glacier surface..... 222

Figure 8.3: Daily rainfall (bars) at MCV and Tasman Lake level (solid line) between July and August 2010. Dotted vertical line indicates calving event. 223

Figure 8.4: Photographs of the Tasman Glacier terminus in the days after the 19 December 2010 calving event. Circle in (A) denotes the area that calved. Evidence for the uplift of the terminus is provided by the exposed thermo–erisional notches above the waterline in (B) (source: D. Callesen). 223

Figure 8.5: Daily rainfall (bars) at MCV and Tasman Lake level (solid line) between December 2010 and January 2011. Dotted vertical line indicates calving event..... 224

Figure 8.6: Timeline of the 22 February 2011 calving event at Tasman Glacier, showing the timing of earthquakes and the S–wave arrival time at Tasman Glacier as well as the pre– (A), during (B–C), and post–calving (D) images. The approximate dimensions of the calved iceberg are shown in B (source: C. and S. Walter). 224

Figure 8.7: Still images from video of calving at the terminus of Tasman Glacier on 22 February 2011. Water level in the ponds behind the terminus can be observed to drop (B) from their initial level (A), increasing again mid–event (C), before lowering again to a level below their original level (D). Dotted black line in B shows the original pond level, with the white dotted line indicating the calved section. Arrow in C indicates ice particles that have sprayed onto the glacier surface (source: C. and S. Walter). 225

Figure 8.8: Map showing the location of Tasman Glacier, Christchurch, and the epicentre (triangle) of the M_L 6.3 earthquake. Also shown is the location of the McQueen's Valley (MQZ) Fox Glacier (FOZ) seismic station. 226

Figure 8.9: Waveform data of the M_L 6.3 Christchurch earthquake at (A) MQZ and (B) FOZ seismic stations. The same amplitude scale is used in (A) and (B). Seismic data retrieved from www.geonet.org.nz. 226

Figure 8.10: Lake–level of Tasman Lake and rainfall data from MCV. Dotted vertical indicates the calving event on 22 February 2011. 227

Figure 8.11: Photograph of the terminus region of Tasman Glacier event on 31 January 2012227

Figure 8.12: Oblique photographs of the terminus of Tasman Glacier before calving on 18/02/2013 (A) and after calving (B) 23/02/2013. Dotted line in (A) indicates the position of the terminus after calving. The single large iceberg formed during this calving event can be seen near the terminus of Tasman Glacier in (B) (source: G. Slatter). 228

Figure 8.13: Rainfall data from MCV. Dotted vertical indicates the calving event on 22 February 2011. 228

Figure 8.14: Diagram showing the effect that losing a section of the subaqueous ice cliff can have on the flotation thickness of the glacier. (A) Ice thickness (h_i) exceeds flotation thickness (h_f) resulting in stability of the terminus. (B) Ice thickness at the terminus is below flotation thickness due loss of the subaqueous section of the ice cliff, leading to flotation and retreat until h_i equals h_f. 230

Figure 8.15: Schematic diagram of the processes of buoyancy driven calving for the two described calving events at Tasman Glacier on 22 August (Process 1) and 19 December 2012 (Process 2). In both cases the glacier is subjected to upward buoyant forces (1). Process 1 follows the description of the 22 August calving event where several fluctuations in lake level (2i) damaged the ice at the hinge point until calving was initiated as lake level decreased (2ii). Process 2 describes the 19 December calving event where an increase in (2i) lake level lead to calving (3) due to upward buoyant forces..... 232

Figure 8.16: Vertical depth of crack propagation described in the scenario of fracture propagation from the surface of the glacier during the three earthquakes. Dotted line indicates glacier thickness..... 234

Figure 9.1: Schematic diagram of processes and mechanisms of calving that have contributed to the retreat of Tasman Glacier. Black arrows indicate external inputs into the terminus, with grey arrows indicating melt processes and dotted arrows showing water movement. Numbers 1–3 refer to three potential states Tasman Glacier has been in during retreat between 2000 and 2013. Inset (A) provides greater detail on long term controls of notch–driven calving. Note calving processes (e.g., over–steepening and notch–driven calving) can occur at any time and location along the ice cliff and are not necessarily associated with the hypothesised states. 238

Figure 9.2: Photo showing vertical notches that have formed on a large iceberg that calved from the terminus of Tasman Glacier on 22 February 2011. Black line indicates the original orientation of the iceberg running east to west along the terminus of Tasman Glacier. Dotted white line indicates the waterline along the former subaerial ice cliff, with the white line highlighting the perpendicular orientation of notches extensively formed along the ice cliff. Solid black line is approximately 250 m in length..... 241

Figure 9.3: Long profile of Tasman Lake along the former centre line of Tasman Glacier from the southern margin moraine dam, with terminus positions derived from satellite imagery. Terminus positions throughout the observed retreat and predicted retreat are shown to indicate the potential rate of glacier retreat. Dates past 2013 below the level of Tasman Lake are based on linear regression equation for post 2007 shown in Figure 4.5. Terminus positions dates above the lake level are based on the power–law regression post 2007 shown in Figure 4.5. 242

Figure 9.4: Photograph of Tasman Glacier and Tasman Lake in February 2007 showing the approximate location of the 2013 terminus position and the potential terminus position where basin topography intercepts current lake level. The position of the confluences of Ball Glacier (A) and the Hochstetter ice fall (B) with Tasman Glacier are also shown. (Source: S. Winkler, 2007). 244

Figure 9.5: Comparison between the growth of Tasman Lake and proglacial lakes in the Himalaya throughout the 20th century (lake areas from Thompson et al. (2012), after Komori et al. (2008); Sakai et al. (2009b)). 246

Figure C.1: Photograph showing the geophone and data logger during a pre–deployment test during fieldwork carried out at Hooker Glacier in November 2009. 273

List of Tables

Table 2.1: Relationship between calving rate (u_c) and water depth (h_w). u_c is width averaged calving speed (ma^{-1}), h_w and h_{max} are the average and maximum water depth at the calving front (m), and c is a coefficient. 33

Table 4.1: Summary of changes in glacier area, terminus retreat, terminus length and supraglacial pond area for Tasman Glacier between 2000 and 2013 based off ASTER satellite imagery. Glacier area includes supraglacial ponds that were present at the time of image capture..... 73

Table 4.2: Changes in the surface area and volume of Tasman Lake since its inception. Area and volume information between 2000 and 2013 are from this study, with data prior to 2000 retrieved from previous studies..... 76

Table 5.1: Overview of the time–lapse image record for Tasman Glacier, showing the start and end date between survey periods, number of days of operation, and sampling interval. 105

Table 5.2: Estimated iceberg volumes and errors for the perceived size of individual calving events. Several classes of magnitude were not observed throughout the study period and therefore do not have an estimate of volume. 112

Table 5.3: Retreat data of Tasman Glacier from ASTER satellite imagery for the three ice cliff regions used in this study, indicating the regional variability of retreat between March 2011 and January 2013. Positive values represent up–valley retreat, whereas negative values indicate the down–valley movement of the terminus (i.e. advance of the glacier). 114

Table 5.4: Summary of calving events by month, showing the total number of events as well as a breakdown of calving events by the region they took place, and the mechanism of calving..... 118

Table 5.5: Table showing the breakdown of calving events by region and mechanism by the hour within which a calving event took place..... 129

Table 5.6: Monthly climate data for AWS located in Mount Cook Village and Rose Ridge... 132

Table 6.1: Contingency table showing chi–square test results to determine the independence of calving styles for buoyancy (B), notch (N), over–steepening (O), and subaqueous (SA) calving events. Expected counts are reported below observed counts, with chi–square contributions printed below expected counts..... 170

Table 6.2: Contingency table of chi–square test results to determine the independence of calving styles grouping buoyancy and subaqueous events (B/SA. Notch (N) and over–steepening (O) calving events remain separate. Expected counts are reported below observed counts, with chi–square contributions printed below expected counts..... 170

Table 6.3: Contingency table showing chi–square test results to determine whether there is any style–time dependence. Buoyancy (B), notch (N), over–steepening (O) and subaqueous (SA) calving events are compared approximately to time bins 0 to 68 days, 68 to 103 days, 103 to 156 days, 156 to 227 days, and 227 days onwards to have approximately equal numbers of total events in each. Expected counts are reported below observed counts, with chi–square contributions printed below expected counts. 171

Table 6.4 Contingency table showing chi–square test results to determine whether there is any style–time dependence, with buoyancy and subaqueous events grouped (B/SA). Notch

(N) and over–steepening (O) calving events remain separate, with time bins the same as Table 6.3. Expected counts are reported below observed counts, with chi–square contributions printed below expected counts. 172

Table 7.1: Table showing the duration of calving events in seconds by the mechanism of calving. Mean, minimum, and maximum duration is shown to highlight the similarity of durations between over–steepening (O) and notch–driven (N) events, and buoyancy (B) and subaqueous (SA) events. 200

Table 7.2: Number of events that exceed the STA/LTA threshold for 24 April 2012, all of April 2012 and for all data recorded by BB. 207

Table B.1: The date, types, coverage, and cloud cover for satellite images used throughout the study. Advanced Spaceborne Thermal Emission and Reflection Radiometer (ASTER) imagery was sourced from Wolfgang Rack at the University of Canterbury, New Zealand via the Global Land Ice Measurements from Space (GLIMS) project. Where cloud cover is indicated, the clouds present did not hinder identification of the terminus of Tasman Glacier. 271

Chapter 1: Introduction

1.1 Background

Calving margins are characterised as regions of a glacier where the dominant process of ablation is the loss of ice through the calving of blocks of ice. As such, calving margins can be found within almost every glacial environment, ranging from tens of metres to the entire terminus of a glacier. The loss of mass via calving from water–terminating margins represents one of the major components of ice sheet (e.g., Hagen et al., 2003; Benn et al., 2007b; Moon and Joughin, 2008) and glacier (e.g., Meier and Post, 1987; Kirkbride and Warren, 1999; Warren and Aniya, 1999; van der Veen, 2002; Nick and Oerlemans, 2006; Benn et al., 2007b) mass balance. Globally this accounts for ~ 70 % (*c.* 2400 × 10^{12} kg–per year water equivalent) of mass lost from glaciers (Houghton et al., 2001), and allows for the rapid transfer of mass from the cryosphere to oceans (van der Veen, 2002). As a result, calving margins can contribute disproportionately (e.g., Pfeffer et al., 2008; Nick et al., 2013) to global mean sea level rise (SLR). This is due to their advance or retreat often being controlled by factors other than equilibrium line altitude (ELA), such as proglacial geometry, proglacial water–body characteristics, and presence/absence of a shoal at the terminus. However, climate signals can drive calving glaciers into significant disequilibrium causing them to respond rapidly (Meier, 1997) by decoupling them from climate fluctuations (Oerlemans and Nick, 2006). Such processes are thought to have had a significant impact on large ice sheets that developed during the Pleistocene (Hughes, 2002; Zweck and Huybrechts, 2003; Mangerud et al., 2004; Siegert and Dowdeswell, 2004; Stokes and Clark, 2004).

The current understanding of calving processes at water–terminating glaciers and its impact on future SLR is poor (Amundson et al., 2008; Pfeffer et al., 2008; Nick et al., 2013). For example, calving processes are not included in the Intergovernmental Panel on Climate Change (IPCC) fourth assessment estimate of SLR (0.18-0.6 m; IPCC, 2007), potentially resulting in a significant underestimation of future SLR (Rahmstorf, 2007; Amundson et al., 2008). Calving processes remain one of the least understood of all glacial processes due to a combination of (1) the multivariate nature of calving and (2) the inherent dangerous and difficult nature of studying such dynamic environments (Benn et al., 2007b). This has seen a wide variety of studies being carried out at outlet, tidewater, and freshwater glaciers globally, in an attempt to fully understand calving at wide range of margins. Such studies have typically quantified calving by

documenting long–term fluctuations in terminus position to imply a calving rate, although process–based models have also been developed to account for the variability of calving. Indeed, several models (or 'calving laws') have been proposed that seek to relate calving to independent parameters, either empirically–or physically–based. However, debate has continued over the exact controls on iceberg calving at water–terminating glaciers (van der Veen, 2002; Benn et al., 2007b). Varying results have materialised from studies of water–terminating glaciers, with a number of conflicting hypotheses proposed to explain the mechanisms of calving (e.g. Brown et al., 1982; Funk and Rothlisberger, 1989; van der Veen, 1996, 2002; Vieli et al., 2002; Warren and Kirkbride, 2003; Benn et al., 2007a) often developed from the same dataset (Meier, 1994; van der Veen, 1996; Meier, 1997; van der Veen, 2002). Recently, several new and innovative techniques have been utilised to overcome inherent survey dangers, and gain a greater understanding of the connections between glacier dynamics and calving mechanisms. In particular, the use of passive geophysical techniques coupled with automated external monitoring systems and direct field measurements to link calving events to underlying glaciological dynamics has emerged (e.g., Qamar, 1988; O'Neel et al., 2007; Amundson et al., 2008; Richardson et al., 2010; Walter et al., 2010; Bartholomaus et al., 2012). Through the use of passive geophysical techniques (such as seismometers and lake–based hydrophones), these signals can be identified and linked to calving events and glacier dynamics, providing a safe mechanism for quantifying the extent and mechanisms of calving at water–terminating glaciers (O'Neel et al., 2007).

The impact of calving on glacier dynamics is not only critical to understanding the response of tidewater and outlet glaciers globally, but also in the retreat of freshwater–terminating glacier systems that have developed within over–deepened basins formed during and post Little Ice Age (LIA). Such active calving margins at the termini of terrestrial valley glaciers have formed due to *in situ* melting and development of proglacial lakes as the glacier retreats along an over–deepened basin. The formation of such proglacial lakes has the effect of decoupling the glacier system from solely a climate forcing (Kirkbride and Brazier, 1998; Warren and Aniya, 1999), to a regime where the calving of icebergs and associated processes dominate glacier mass balance (Benn et al., 2007b). Such a transition from melt–dominated to calving–dominated ablation regime has been observed at glaciers in Norway (Laumann and Wold, 1992), the European Alps (Funk and Rothlisberger, 1989; Huggel et al., 2004), Alaska (Motyka et al., 2003b; Boyce et al., 2007), Patagonia (Warren and Aniya, 1999; Naruse and Skvarca, 2000; Warren et al., 2001), the Himalayas (Sakai et al., 2009b; Bolch et al., 2012) and New Zealand (Kirkbride, 1993; Warren and Kirkbride, 2003; Dykes et al., 2011; Robertson et al., 2013).

The transition from purely melt–dominated ablation to calving–dominated is particularly important for glaciers covered in extensive debris–cover (Kirkbride, 1993; Kirkbride and Warren, 1999; Sakai, 2012), as debris–covered glaciers are often significantly out of phase with climate (i.e. have not retreated in response to decreased mass accumulation), compared to non–debris–covered glaciers that fluctuate readily with climate (Kirkbride and Brazier, 1998; Chinn et al., 2012). Once such a transition has occurred, rapid retreat of debris–covered glaciers often takes place as ice lost via calving exceeds ice supply to the terminus by several orders of magnitude (Kirkbride, 1993). Despite the importance of lake development and the resulting glacial retreat due to calving, the current understanding of lake development and evolution remains relatively incomplete. Several studies have begun to expand the current knowledge of proglacial lake development (Kirkbride, 1993; Robertson, 2012; Sakai, 2012). However, further research is required to understand the ongoing effects that such lake development has on the evolution and retreat of freshwater calving termini. Of particular importance is characterising not only the long–term trends in calving, but also how variations in calving at a sub–annual scale can affect long–term retreat.

1.2 Aims, scope and objectives

The primary aim of this study is to improve the current understanding of calving processes at retreating, and debris–covered calving margins. This is in order to better understand how calving has (and will continue) to affect glacier mass balance and retreat of *Haupapa*/Tasman Glacier, *Aoraki*/Mount Cook National Park, New Zealand. Tasman Glacier (New Zealand's longest glacier) is a debris–covered, freshwater–terminating glacier which provides an excellent natural laboratory for studying calving mechanisms and the impact of calving on glacier retreat. Previous studies undertaken at Tasman Glacier have sought to identify the processes of proglacial lake formation (e.g. Kirkbride, 1993; Hochstein *et al.*, 1995; Watson, 1995; Purdie and Fitzharris, 1999; Röhl, 2005) and how the water–glacier interaction is conditioning glacier retreat (e.g. Kirkbride and Warren, 1999; Röhl, 2005). From these studies, information has been used to add to the global dataset on water–terminating glaciers (e.g. Warren et al., 1995b; Warren and Kirkbride, 2003; Haresign, 2004; Chinn et al., 2012). However, little research has been conducted on the recent retreat of Tasman Glacier and the impact that iceberg calving processes have had on conditioning glacier retreat since the inception of Tasman Lake. In particular, there have been no detailed studies on the impact of calving at Tasman Glacier since it has entered a phase of accelerated retreat and terminus disintegration, during the early 21st century (post–2006).

Therefore, the focus of this study is to quantify and describe the contemporary retreat of Tasman Glacier at varying temporal scales (inter–annual, sub–annual, and intra–event). It is envisaged that this will improve the understanding of how debris–covered glaciers transition between a melt–dominated to a calving–dominated regime, and the ongoing effects that calving processes have on conditioning retreat. In particular, iceberg calving at a temporal resolution greater than previously studied at Tasman Glacier will be investigated to improve the understanding of calving processes at such margins that are currently under–represented in global datasets (e.g., sub–annual and intra–event). To quantify the effect and natural variability of iceberg calving on driving the retreat of debris–covered freshwater terminating glacier, the following key questions are posed at the onset of this study:

1. What are the long–term kinematic (decadal) characteristics of glacier retreat since the initial formation of Tasman Lake, and how can they be explained?
2. How does the contemporary phase of retreat (2000–2013) of Tasman Glacier compare with previous phases of retreat and what forces current changes in ice loss behaviour?
3. What is the natural variability in magnitude, frequency and style of iceberg calving at freshwater–terminating glaciers and is there any time–dependent pattern to them?
4. What is the relative impact of high–frequency, low–magnitude and low–frequency, high–magnitude calving on the overall ice loss budget and is the occurrence of small and large calving events linked?
5. Do external parameters directly control iceberg calving and can they be used to model and forecast the probability of calving events?
6. Can seismic methods, successfully applied to calving margins at tidewater glaciers, be deployed at freshwater–terminating glaciers to reliably detect and possibly quantify the frequency, magnitude and style of iceberg calving?

In order to provide answers to the above questions, five main research approaches have been followed:

1. Quantify the time resolved retreat of Tasman Glacier since the initial formation of Tasman Lake until present (2013) by analysing available satellite imagery datasets.
2. Establish the first sub–annual dataset of the frequency distribution, magnitude, and styles of calving at a freshwater–terminating glacier, to quantify the spatial and temporal variability of iceberg calving.
3. Apply statistical modelling to identify temporal patterns in the occurrence, style and magnitude of calving events, and to derive the probability of calving as a function of external parameters.
4. Investigate the ability for passive seismic techniques to remotely detect and characterise calving events at a freshwater–terminating glacier.

1.3 Thesis structure

This thesis is divided into analysis of calving at three main temporal scales (inter–annual, sub–annual, and intra–event) to quantify the extent to which calving has affected the retreat of Tasman Glacier, and to identify how the glacier has responded to the evolution of Tasman Lake. To do this, a succinct literature review is presented in chapter 2 to provide the reader with an introduction to the key themes of the thesis, with the study area of Tasman Glacier and the surrounding landscape discussed in chapter 3. In chapter 4 the retreat of Tasman Glacier since the inception of Tasman Lake is quantified, focussing on the role of calving processes on conditioning contemporary retreat. Chapter 5 presents data to characterise the spatial and temporal distribution of iceberg calving at Tasman Glacier at a sub–annual scale. This is followed by chapter 6, in which a statistical analysis is applied to the observed temporal distribution of calving events to further understand the controls of calving at a sub–annual time scale. Chapter 7 identifies and describes individual calving events at Tasman Glacier through the use of seismic instruments and time–lapse photography to further understand the intra–event dynamics of calving events. Chapter 8 combines multiple datasets to identify and describe the processes involved in initiating high–magnitude, low–frequency, buoyancy–driven calving events at Tasman Glacier. A synthesis is presented in chapter 9 which incorporates the main findings from each chapter to describe how calving at Tasman Glacier has varied since the inception of Tasman Lake as well as the potential glacier response in the near future. Concluding the thesis (chapter 10), the main aims of the thesis are considered and future research directions identified. Throughout the thesis there is some repetition of key information so that each chapter is presented as a coherent piece of work that is intended to be submitted as stand–alone journal articles, as well to provide a clear indication of how the data and information presented relates to Tasman Glacier and research globally.

Chapter 2: Literature Review

2.1 Introduction

The following chapter is organised so that it provides a review of research on the development of lake–calving glaciers such as Tasman Glacier and the processes and mechanisms which affect calving margins. The first section (2.3) discusses the effects that supraglacial debris–cover can have on providing the preconditions for the development of a proglacial lake. The second section (2.4) introduces the different types of calving glacier margins at which calving processes play an important part in the loss of ice from the glacier system. The processes and mechanisms of iceberg calving are then summarised and discussed to provide an overview of the current understanding (section 2.5). Section 2.6 introduces and discusses glacier–generated seismic signals, with a focus on those generated by calving events. Finally, a summary of the main findings of the literature review concludes the chapter.

2.2 Glacier mass balance

The inputs and outputs of snow, ice, and meltwater in a glacier system govern glacier movement and dynamics. Mass is gained through the *accumulation* of snow (and other forms of ice) on the glacier surface. The progressive layering and compaction of snow over successive years eventually leads to the formation of glacier ice as the volume of air in pores is reduced. Once ice has formed, *ablation* removes mass (either snow or ice) from the glacier system. Ablation refers to all processes that remove mass from the glacier system, including wind ablation, dry calving (ice avalanching), iceberg calving, melting and associated runoff, evaporation and sublimation (Benn and Evans 2010). Each form of ablation occurs at a range of temporal and spatial scales, contributing to ice mass lost within the glacier system. In general, however, a glacier is typically categorised into two zones (Figure 2.1): the accumulation zone (where accumulation exceeds ablation) and ablation zone (where ablation exceeds accumulation). The altitude at which mass lost through ablation is equivalent to mass gained through accumulation is the equilibrium line altitude (ELA).

The mass balance of a glacier can be significantly affected by altering how mass is lost from the glacier system, either by enhancing or reducing ablation. A decrease in ablation can occur due

to the extensive presence of supraglacial debris–cover over the lower glacier surface, which insulates the underlying ice. In contrast, the calving (or the mechanical loss of ice) from water–terminating glaciers and ice sheets significantly increases ablation compared to ice melt alone (van der Veen, 2002; Benn et al., 2007b). Ice calved from the terminus can range from individual crystals to large tabular icebergs hundreds of square kilometres across (Hanson and Hooke, 2000). This potentially leads to large deficits in glacier mass balance, altering the dynamics of a glacier and its response to climatic inputs (Kirkbride and Brazier, 1998; Benn et al., 2007b). These two processes affecting ablation can occur in isolation or, in combination can lead to the development of lake–calving glaciers. Such a combination of processes has taken place at Tasman Glacier resulting in both a reduction in ablation due to debris–cover, and an increase in ablation loss at the terminus associated with calving (Figure 2.2).

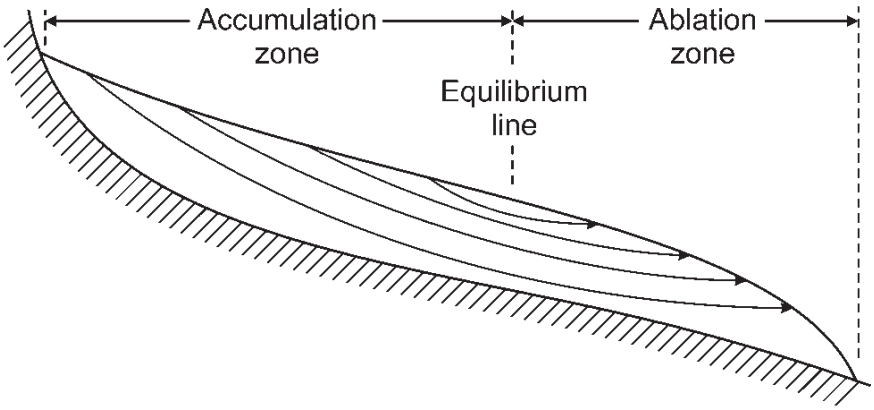

Figure 2.1: Schematic representations of accumulation and ablation zones for a valley glacier.

Figure 2.2: Supraglacial debris–cover and calving have had a significant impact on glacier mass balance of Tasman Glacier. Tasman Lake is in the foreground, with Aoraki/Mount Cook visible in the upper left of the photograph (photo: S. Winkler, 2007)

2.3 Supraglacial debris–cover and proglacial lake formation

Supraglacial debris significantly influences the ablation rates and ice dynamics of a glacier (Nakawo and Young, 1981; Benn et al., 2003). Supraglacial debris–covered glaciers are common throughout the world in regions with high topographic relief, where rock type and tectonic setting allow for the supply of debris to a glacier surface (Nakawo and Young, 1981; Kirkbride, 1989; Lundstrom et al., 1993; Glasser et al., 2003; Röhl, 2005; Bolch et al., 2007). Debris–cover forms due to the accumulation of extraglacial material derived from snow–rock avalanches, low magnitude–high frequency rock–falls, debris–flows, and to a lesser extent atmospheric precipitation (e.g. dust and volcanic material) and aerosols (microparticles). The net result of extraglacial debris supplied to the surface of a glacier is that debris moves down–glacier, coalescing and thickening at the glacier terminus (Drewry, 1986; Hambrey, 1994). A thin debris–cover (< *c.* 2 cm) greatly increases the rate of ice ablation due to the lower albedo of rock surfaces compared with ice (Østrem, 1959; Singh et al., 2000; Benn et al., 2003; Nicholson and Benn, 2006). In contrast, thicker (> *c.* 2 cm), continuous, debris–covers can have the opposite effect, insulating ice from ablation by shielding it from short and long–wave radiation (Nakawo and Young, 1981; Nakawo and Rana, 1999; Lejeune et al., 2013). This insulating effect has been identified on glaciers globally, with varying critical thicknesses (defined as the thickness at which sub–debris ablation rate is equivalent to the ablation of adjacent bare ice) identified at different altitudes and latitudes (Reznichenko et al., 2010).

Supraglacial debris–cover substantially affects the patterns of ablation and ice flow (Benn and Evans 2010) of the affected glacier, significantly altering its mass balance and ultimately its response to changes in regional and global climates. For debris–free (clean ice) glaciers, changes in ice volume (as a result of variations in accumulation and ablation) result in fluctuations of a glacier's terminus. In contrast, debris–covered glaciers often have a dampened response to changes in climate due to the accumulation of debris throughout the ablation zone (Benn et al., 2003). In general, the increase in ablation with decreasing elevation is described in terms of a glaciers *ablation gradient* (Schytt, 1967), which is often reduced or reversed (Rogerson et al., 1986; Kirkbride, 1989; Naito et al., 2000) on the lower reaches of debris–covered glaciers. In some cases this can cause the ablation zone to enlarge (Benn and Evans 2010), or result in the advance or thickening (i.e. volume increase) of the glacier to accommodate for accumulation (Kirkbride, 1989, 2000; Naito et al., 2000; Benn et al., 2003; Vacco et al., 2010).

2.3.1 Asymmetric glacial advance

If debris–cover is retained for an extended period of time, debris–covered glaciers can expand coeval with the retreat of debris–free glaciers (Kirkbride, 2000). An asymmetric response to climatic warming, where debris–cover insulates a glacier from melting associated with a warming climate and results in ice persisting during periods of negative mass balance (Kirkbride and Warren, 1999; Nakawo and Rana, 1999; Naito et al., 2000). During periods of positive mass balance (i.e. *transport–dominant* conditions), increased ice flow and decreased ablation decrease debris–cover by efficiently transporting and concentrating debris at the terminus. In contrast, reduced flow and increased ablation under negative mass balance conditions results in the upstream spread of debris–cover as greater amounts of debris become exhumed (i.e. *ablation dominant* conditions). Figure 2.3 demonstrates the accumulation of supraglacial material via this process over several mass balance cycles. After an initial 'wedge' is formed (unit 1) and consolidated at the terminus by fast flow, melt–out of debris replaces debris on the lower glacier (unit 2). Under transport–dominant conditions units 1 and 2 thicken towards the terminus, insulating underlying ice. As long as marginal deposition does not exceed debris supply, then thickening of debris–cover at the terminus will continue (units' 3–5 *et seq*) over multiple mass balance cycles (Kirkbride, 2000).

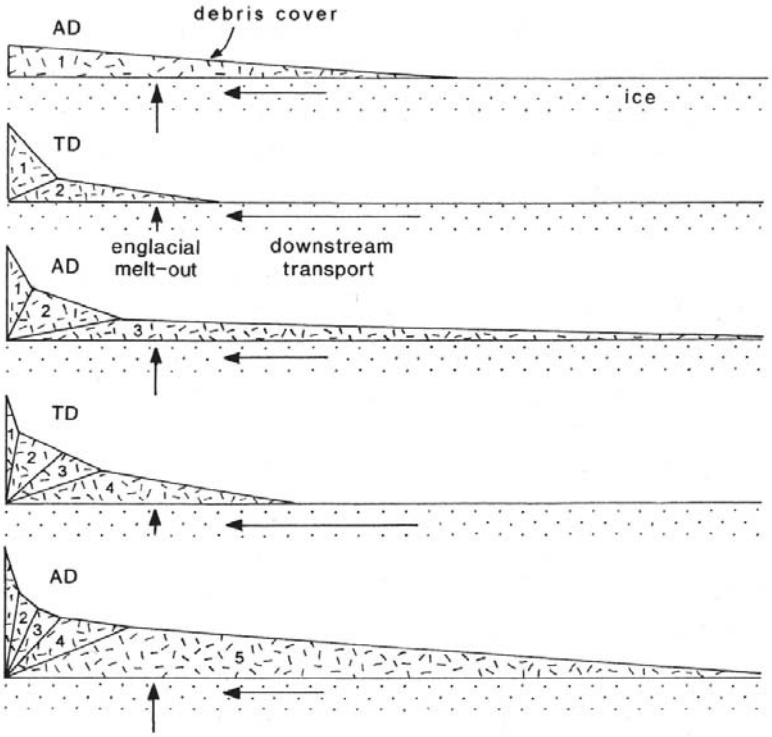

Figure 2.3: Schematic diagram demonstrating the evolution of a debris–covered tongue over multiple mass–balance cycles, showing net debris accumulation and glacier expansion. AD and TD refer to ablation– and transport dominant conditions, respectively (Kirkbride, 2000).

The Southern Alps of New Zealand provide an excellent example of this asymmetric response to climate, with the maritime glaciers (such as the Franz Josef and Fox Glaciers) situated on the western flanks of the Alps responding rapidly to changes in climatic input throughout the past century (Purdie et al., 2008). This has been represented by periods of advance and retreat visible in changes in terminus position over decades. Indeed, the response time of Fox Glacier to a change in climate input has been estimated as being between 9 and 20 years (Purdie et al., 2008). In contrast, the termini of the debris–covered glaciers of the *Aoraki*/Mount Cook region, situated on the eastern flank of the Southern Alps, have not fluctuated as markedly throughout this period of time (Kirkbride, 1993). This difference is primarily due to the presence of the insulating debris–cover on the glaciers of the *Aoraki*/Mount Cook region (Hambrey and Ehrmann, 2004).

2.3.2 Downwasting and thermokarst erosion

A secondary effect of supraglacial debris–cover on glacier dynamics is the progressive 'downwasting' (defined as the net lowering of the glacier surface by ablation and ice flow (Chinn et al., 2012)) of glacier margins associated with glacier thinning (Posamentier, 1977; Kirkbride, 1993; Hochstein et al., 1995). Such glaciers often become overextended after sustained periods of advance due to the accumulation of supraglacial debris (Chinn et al., 2012). As a result, stagnation of the glacier system occurs owing to a decrease in accumulation (associated with extended periods of negative mass balance), or where accumulation is unable to sustain advance (Benn et al., 2003). If ice supplied to the terminus during periods of intervening positive mass balance is not significant enough to compensate for *in situ* melt under supraglacial debris, downwasting of the glacier surface will take place instead of glacier retreat. During this process, debris becomes redistributed, leading to differential ablation and the eventual exposure of clean ice.

As *in situ* melting occurs, the long–profile gradient of the glacier lowers in response to decreased ice flux, often resulting in a gradient of less than 2°, providing the preconditions for the formation of *thermokarst erosion* (Healy, 1975; Kirkbride, 1993) and supraglacial ponds (Clayton, 1964; Reynolds, 2000). The downwasting of debris–covered glaciers results in the exposure of clean ice as englacial and subglacial melt lower the glacier surface, redistributing supraglacial debris. The redistribution of supraglacial debris–cover exposes greater areas of relatively clean ice (Benn and Evans 2010). On the newly exposed ice faces, subaerial ablation increases, owing to the loss of the insulating rock layer (Purdie and Fitzharris, 1999; Naito et al., 2000). A positive feedback effect is then created as the melting of exposed ice results in the further redistribution of supraglacial debris exposing an even greater proportion of clean ice to subaerial ablation (Richardson and Reynolds, 2000). The result of this process is the formation

of pseudokarst landforms (such as tunnels, caves, sinking streams, ponds, etc.), caused by thermokarst erosion (Clayton, 1964; Healy, 1975; Kirkbride, 1993).

Progressive downwasting and the formation of thermokarst erosion during periods of stagnation provide an important component in the formation of supraglacial ponds and the eventual formation of proglacial lakes (Clayton, 1964; Kirkbride, 1993). These lakes are generally constrained by post–Last Glacial Maximum (LGM) outwash gravels and late Holocene Little Ice Age (LIA) moraines (Gellatly, 1984, 1985; Winkler, 2000, 2005). The formation of lake–terminating margins has further decoupled these glaciers from changes in climate, with a transition from primarily melt–dominated ablation to calving dominated–ablation appearing to over–ride subsequent climatic inputs (Kirkbride and Brazier, 1998; Kirkbride and Warren, 1999).

2.3.3 Supraglacial ponds

Supraglacial ponds are formed via the pooling of meltwater, and the collapse of englacial water channels (e.g. Kirkbride, 1993; Sakai et al., 2000; Benn et al., 2001). Thermokarst sinkholes develop on debris–covered glaciers where meltwater ponds form in depressions caused by water– and debris– filled crevasses. Enhanced melting over the water–ice interface (Röhl, 2008) occurs due to increased heat transfer, caused by conduction and convection of heat from the relatively warmer surface water of supraglacial ponds (Sakai et al., 2000) and the exposed surrounding ice. This accelerates backwasting, leading to the formation of ice cliffs (Figure 2.4). Undercutting of the ice cliff due to increased heat transfer (Röhl, 2006, 2008) leads to the calving of ice blocks at the pond margins, causing the pond to expand. If connected with the englacial drainage network, pond expansion continues via thermokarst erosion (Etzelmuller, 2000), exploiting lines of weakness created by the englacial channels (Kirkbride, 1993), eventually penetrating to the englacial base water level (Röhl, 2008). As a result, warmer pond water routed through conduits can lead to channel enlargement, and subsequent channel roof collapse. This results in a positive–feedback, where multiple ponds form along englacial channels, accelerating ablation rates (Sakai et al., 2000). In contrast, the growth of perched supraglacial ponds (i.e. ponds disconnected from the englacial drainage network) is limited to intermittent pond drainage (Benn et al., 2001).

The formation of supraglacial ponds on debris–covered glaciers is primarily a function of the surface gradient, which is in turn controlled by glacier flow, allowing the pooling of meltwater caused by negative mass balance conditions (Reynolds, 2000; Benn et al., 2001; Röhl, 2008). Reynolds (2000) identifies that on slopes of >10º no ponding can occur due to complete drainage, with small, intermittent, ponds developing with surface slopes of 6–10º. Between 2–

6º, ponding is more substantial, but still transient, with slopes of <2º providing the preconditions for large–scale ponding, and subsequent proglacial lake development.

Figure 2.4: Supraglacial pond and exposed englacial conduit (arrowed) on the surface of the debris–covered Tasman Glacier. The clean ice walls at the margin of the supraglacial pond and surrounding area exposed due to backwasting and the gravitational reworking of debris.

2.3.4 Proglacial lake development

Numerous studies have documented lake formation via downwasting and supraglacial pond formation, expansion, and coalescing throughout Alaska (Reid and Callender, 1965), Patagonia (Aniya and Wakao, 1997), the Himalayas (Chikita et al., 1999; Reynolds, 2000; Benn et al., 2001; Komori, 2008; Fujita et al., 2009; Sakai et al., 2009a; Sakai, 2012), and New Zealand (Kirkbride, 1993; Hochstein et al., 1995; Robertson et al., 2013). For example, in the Southern Alps of New Zealand 20th century downwasting has led to the formation of Tasman Lake, as well as the Godley, Maud, and Classen lakes at the head of the Godley Valley, via the formation and coalescence of supraglacial ponds throughout the latter half of the 20th century (Kirkbride, 1993; Robertson, 2012). Subaqueous calving of the ice–cored sections of these lakes and the initiation of calving retreat in the mid–1970s (Godley, Maud and Classen glaciers) and 1980s (Tasman Glacier) have resulted in the retreat of the associated glaciers (Kirkbride, 1993; Dykes et al., 2011; Robertson, 2012). The formation and coalescing of supraglacial lakes at the termini of many Himalayan glaciers during the latter half of the 20th century (e.g., Komori, 2008; Sakai et al., 2009b; Sakai, 2012) further demonstrates how important ice–contact lake development is in affecting glacier dynamics, specifically glacier response to changes in climate.

The process of proglacial lake formation at the termini of debris–covered glaciers occurs as a result of the thinning and downwasting of the terminus due to the decreased supply of ice (Kirkbride, 1993; Komori, 2008; Sakai, 2012). At the termini of debris–covered glaciers, with a surface gradient <2º (Kirkbride, 1993; Reynolds, 2000), multiple supraglacial ponds form due to the pooling of meltwater and expand via the mechanical calving of lake margins and accelerated melting of exposed clean ice cliffs (Röhl, 2008). As supraglacial ponds expand (both in plan–

form and penetrating downwards through the ice column to the englacial base water level), a positive feedback occurs resulting in the rapid expansion of supraglacial ponds (Röhl, 2008), particularly where englacial conduits and crevasses provide a loci of lake development (Kirkbride, 1993; Benn et al., 2001). Adjacent ponds coalesce to form a single, large, ice–floored lake (Chikita et al., 1999; Reynolds, 2000). Subaqueous calving of the floor of the lake is initiated (Duck and Mcmanus, 1985; Kirkbride, 1993; Robertson et al., 2012), causing the lake water to penetrate downwards to underlying sediment (be it bedrock or moraine material). At this point full calving of the glacier terminus begins, with the consequence rapid retreat of the glacier up–valley (Kirkbride, 1993; Sakai, 2012).

Kirkbride (1993) classifies the development of lakes via this process into two main thresholds. Threshold 1 (Figure 2.5, Stage 1 and 2) relates to the initial development and expansion of supraglacial ponds, with threshold 2 encompassing the transition to a straight transverse ice cliff and the resulting calving retreat (Figure 2.5, Stage 3 and 4). Kirkbride (1993) primarily developed this model of lake formation from the evolution of Tasman Glacier and other glaciers of the *Aoraki*/Mount Cook National Park, New Zealand, through the mid 20th century. Recent observed changes in Tasman Glacier (e.g., Strong, 2008; Quincey and Glasser, 2009; Dykes et al., 2011) and other glaciers of the *Aoraki*/Mount Cook National Park (e.g., Robertson, 2012; Robertson et al., 2013) suggest that this model may need to be updated to include the post–calving retreat evolution of proglacial lakes (Robertson, 2012). However, the model as it stands does provide a framework within which lake development has been described in several glacial settings, such as the Himalayas (e.g., Komori, 2008; Sakai et al., 2009b; Sakai, 2012).

2.3.5 Proglacial lake hazards

The primary hazards associated with proglacial lakes are glacial lake outburst floods (GLOFs) and their associated debris flows down–valley (Cenderelli and Wohl, 2003; Kershaw et al., 2005; McKillop and Clague, 2007b; Benn et al., 2012). Catastrophic floods originating from proglacial lakes threaten lives and property in many parts of the world (Richardson and Reynolds, 2000) including the Himalayas (Kattelmann, 2003; Benn et al., 2012), British Columbia (McKillop and Clague, 2007a), the Swiss Alps (Huggel et al., 2004), and New Zealand (Allen et al., 2009b). The major cause of GLOFs is the sudden drainage of a proglacial lake due to drainage routes becoming blocked or the disintegration of unconsolidated moraines (McKillop and Clague, 2007b). However, GLOFs can also be caused by the avalanching of ice and/or sediment from the surrounding landscape into a proglacial lake. If enough water is displaced, the resulting waves can overtop the bounding moraines (Kershaw et al., 2005; Harrison et al., 2006; McKillop and Clague, 2007b; Canassy et al., 2011). Common sources of avalanched material include surrounding mountain ranges, valley walls, and lateral moraines

(Blair, 1994; Quincey et al., 2005; Allen et al., 2009b). For example, rock avalanches are a common hazard identified within the *Aoraki*/Mount Cook National Park (e.g., McSaveney, 2002; Cox et al., 2008; Cox and Allen, 2009; Reznichenko et al., 2011), representing one of the more likely initiating mechanisms of GLOFs (Allen et al., 2009b).

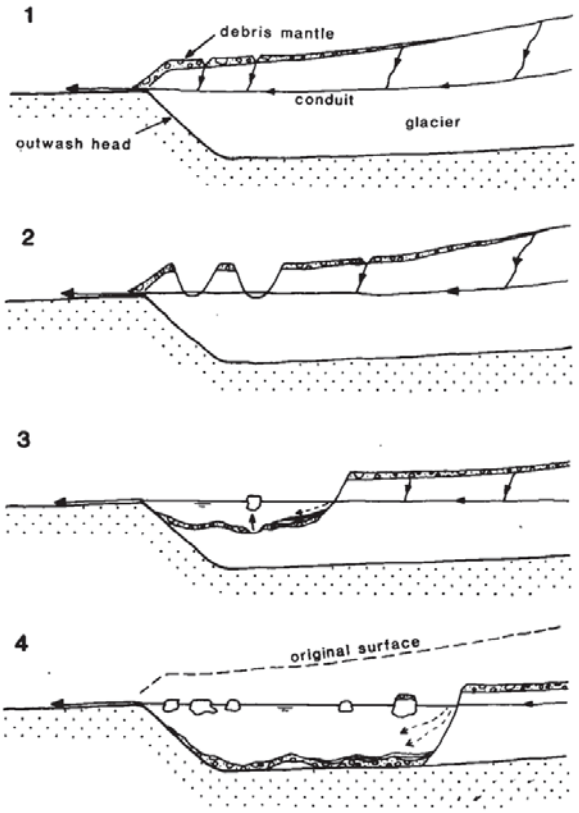

Figure 2.5: Sequence of proglacial lake development at a debris–covered glacier due to the (1) downwasting and (2) coalescing of supraglacial ponds, (3) eventually leading to subaqueous calving and (4) rapid retreat of the glacier (Kirkbride, 1993).

2.4 Calving margins

There are four main types of calving margins have been described to account for all settings within which ice is lost through calving. These range from areas of glaciers where *dry calving* occurs, to *tidewater* and *freshwater* (*lacustrine*) margins, where a glacier terminates into either the sea or lake respectively. The calving of ice from *ice shelves* represents the fourth setting from which calving occurs. Typically the term “calving margin” refers to water–terminating glacier margins, which are generally classified according to the previously mentioned type of calving margin. However, it is important to note that although one type of calving margin might be characterised by a specific type of calving mechanism, calving of all types can occur at all calving margins (Benn et al., 2007b).

2.4.1 Dry calving

Dry calving (or ice avalanching) is characterised as the loss of ice from a section of a glacier that occurs as a result of local stress concentrations (Hughes, 1989; Hughes and Nakagawa, 1989). Dry calving is most commonly found at the margins of glaciers that terminate at, or above, a steep slope (including at the termini of water–terminating glacier). Ice that detaches from the glacier falls down the slope coming to rest at a lower altitude, with the ice either melting *in situ* or becoming incorporated into the glacier system below (Benn and Evans 2010). Limited modelling of dry calving has taken place primarily as a result of the limited effect that it has on glacier ablation compared to more substantial ablative processes (such as iceberg calving and surface melting). Work by Pralong et al. (2003) and Pralong and Funk (2005) on the process of serac formation and calving due to local stress concentrations, and Hughes (1989), Hughes and Nakagawa (1989), and Kenneally and Hughes (2002) on dry calving as a result of bending shear at the terminus of Deception Island, Antarctica, represent some of the only theoretical studies to have looked at dry calving.

2.4.2 Tidewater glaciers

Tidewater glaciers have classically been defined as glaciers that extend into the sea, where icebergs are discharged from an ice cliff (van der Veen, 1999). Found in temperate and polar latitudes, tidewater glaciers are typically located at the margins of ice caps, for example the outlet glaciers of the Greenland ice sheet (e.g., Jakobshavn Isbrae), and large ice fields such as those found in Glacier Bay, Alaska (e.g., Columbia Glacier). More specifically, tidewater glaciers are characterised by their high flow velocities, pervasively crevassed surfaces (related to their high flow velocities), and comparatively high magnitude of calving events (van der Veen, 1996; Venteris, 1999; Vieli et al., 2001; van der Veen, 2002; Benn et al., 2007b). Furthermore, all temperate tidewater glaciers are grounded at the terminus, except locally for short durations (Meier and Post, 1987; van der Veen, 1996). However, recent evidence (e.g., Walter et al., 2010) has suggested that tidewater glaciers may in fact be able to sustain floating termini for extended periods of time (e.g., years). Polar tidewater glaciers, on the other hand, can sustain floating margins similar to ice shelves (van der Veen, 1999). Based on the above description several authors (e.g., Venteris, 1999; Mottram, 2008) have identified that tidewater glaciers represent a theoretical ‘type’ of calving margin, and not simply a description of the physical setting within which a glacier terminates, noting that some freshwater–terminating glaciers, such as Glaciar San Rafael, Patagonia, also demonstrate similar characteristics to their sea–terminating counterparts (Venteris, 1999). In this and the following sections (in accordance with the bulk of published literature), tidewater glaciers will refer to grounded tidewater glaciers based on their glacier dynamics and characteristics.

2.4.3 Freshwater (lacustrine) glaciers

Glaciers that extend into freshwater (lacustrine) proglacial water–bodies lose mass through the calving of icebergs similar to their tidewater counterparts (Benn et al., 2007b). In general, freshwater calving margins are distinctive in their setting from tidewater glaciers, but as noted above, similar calving mechanisms and responses to changes in glacier dynamics can be found between the two (e.g. Venteris, 1999). However, freshwater–terminating glaciers are typically smaller and slower moving, and as such the dominant calving mechanism is not always controlled by glacier dynamics, but often melt associated with the proglacial water body characteristics (Warren and Kirkbride, 2003; Haresign and Warren, 2005; Röhl, 2008). Reinforcing the difference between freshwater and tidewater glaciers is the order of magnitude difference in the rate of mass lost via calving between the two (Haresign and Warren, 2005; Benn et al., 2007b). This has been confirmed by multiple studies of freshwater terminating glaciers in New Zealand, Patagonia, and Alaska that have identified calving rates significantly lower than their tidewater counterparts (e.g., Pelto and Warren, 1991; Warren et al., 1995b; Skvarca et al., 2002; Motyka et al., 2003b; Warren and Kirkbride, 2003).

Freshwater–terminating glaciers may develop through a number of processes (Benn et al., 2007b). As described above (section 2.3.4) proglacial lakes may develop due to the downwasting and retreat of debris–covered glaciers, with water pooling behind an outwash head or moraine (Kirkbride, 1993; Sakai, 2012). Moraine–dammed lakes can also from in the absence of supraglacial debris–cover where water pools in the void between the retreating glacier and lateral or frontal moraines (Clague and Evans, 2000; McKillop and Clague, 2007b; Komori, 2008; Sakai, 2012). As mentioned above (section 2.3.5), such proglacial lakes can pose a significant hazard (McKillop and Clague, 2007b; Benn et al., 2012) if water overtops the moraine dam or if the moraine dam fails, causing glacial lake outburst floods (GLOFs). Freshwater–terminating glaciers may also form as a glacier retreats through an overdeepened glacially–excavated trough (Warren and Aniya, 1999).

2.4.4 Ice shelves

Ice shelves represent the fourth glaciological setting from which ice is lost through calving. In general, ice shelves can be categorised into three main types (Benn and Evans 2010): (a) the floating margins of outlet or valley glaciers (such as found at the outlet glaciers of the Greenland Ice Sheet); (b) locally grounded floating ice sheets fed by surface accumulation and bottom freezing (sea ice shelves); and (c) large floating ice shelves by a combination of glacier inflow, surface accumulation and bottom freezing (such as the Ross Ice Shelf). Due to the fractured and

brittle nature of temperate ice (Meier and Post, 1987; van der Veen, 1996), ice shelves are only found within polar environments, except locally and for short periods of time at some temperate tidewater glaciers. Calving from ice shelves typically occurs as very low frequency, extremely high magnitude events, with large sections of ice shelves (often several hundred kilometres in length) calving through the intersection of rifts (MacAyeal et al., 2003; Bassis et al., 2005). Such rifts are thought to develop as a result of either tidal flexure (e.g. Schmeltz et al., 2002), storm–generated transoceanic waves (e.g. MacAyeal et al., 2006; Squire, 2007), or local fracturing caused by changes in ice dynamics (e.g. Larour et al., 2004; Bassis et al., 2005) such as water filling ice rifts causing penetration downwards to sea level (e.g. Scambos et al., 2000).

Calving accounts for up to 77% of ablation from the Antarctic ice sheet (Jacobs et al., 1992), and approximately 56% from the Greenland ice sheet (Reeh, 1994). Increased iceberg calving from the Antarctic Peninsula due to regional warming could initiate the rapid disintegration of the West Antarctic Ice Sheet (MacAyeal et al., 2003). Such ice sheet disintegration, resulting in a potential global sea level rise of up to 7 m, would severely impact coastal communities around the world along with global climate change (Vaughan and Doake, 1996; van der Veen, 2002). Hence, understanding calving processes and rates represents a critically important parameter feature of global environmental change. The processes acting at the margins of ice shelves are distinct from tidewater and freshwater glaciers as they occur at persistently floating termini. Primarily two types of calving processes operate: (1) bending of the floating ice shelf inducing frequent low–magnitude (relative to the size of ice shelves) calving events as a result of force imbalances; and (2), the episodic rift formation and calving of significantly high–magnitude calving events (MacAyeal et al., 2003; Joughin and MacAyeal, 2005). As ice shelves represent a separate type of calving margin with distinct processes they are not discussed in any great detail in the following sections.

2.5 Calving Processes

As iceberg calving from terrestrial water–terminating glaciers and outlet glaciers and ice shelves of the Antarctic and Greenland ice sheets is becoming more significant in a global context (Rignot and Kanagaratnam, 2006), understanding calving mechanisms and predicting glacier response to external inputs is of increasing importance (Benn et al., 2007b). This section outlines the current understanding of calving mechanisms, and the underlying processes that affect these calving processes. Included in this discussion is an overview of selected calving models that have been proposed to quantify and predict calving rates and processes at different calving margins.

2.5.1 Fracturing and crevassing of ice

Iceberg calving and associated processes are in principle a function of fracture formation (crevassing) and propagation in response to applied stresses (van der Veen, 1998b; Benn et al., 2007b). The development of crevasses within the terminal zone of water–terminating glaciers therefore plays a key role in the location, magnitude and timing of calving by providing pre–existing or new lines of weakness along which calving is initiated (Benn et al., 2007b; Mottram and Benn, 2009). As a result, the temporal distribution of calving is related to the development of fractures in the ice, the rate at which they enlarge, how deep they can penetrate, and whether they are preferentially orientated to initiate calving.

Glacier ice is typically represented in models as a visco–elastic medium (Bamber and Payne, 2004; Mottram, 2008). However, once an applied stress (tensile or compressive) exceeds the fracture strength of ice, brittle fracture occurs instead of plastic deformation. In theory, fractures and crevasses develop perpendicular to the principle direction of stress. However, this does not always occur, with crevasses often rotated due to changes in glacier flow and the complex arrangement of forces applied to an ice body (Cuffey and Paterson, 2010).

Three principle modes of fracture formation for ice have been identified (Figure 2.6), based on linear elastic fracture mechanics (Benn et al., 2007b). These are *tensile cracking* (Mode I), *sliding* (Mode II), and *tearing* (Mode III). As the name suggests Mode I fractures occur due to tensile stress causing the walls of the fracture to pull apart. Fracture development along a shear plane, where the walls stay in contact, is Mode II (sliding). Mode III describes the propagation of fracture at right angles to the parallel shearing which initiates fracture development. If a combination of modes occurs to initiate and propagate crevasses, it is called *mixed mode fracture*. Historically, only Mode I fracturing has been considered in models of glacier ice deformation (van der Veen, 1998b, a; Benn et al., 2007b).

Once initiated, crevasses can either propagate through an ice body or be closed due to compressive forces. Compressive forces are applied due to glacier flow changing the orientation of the crevasse and the direction of applied stress, or where tensile stresses are matched or offset by compressive forces of the overlying ice body (Benn et al., 2007b; Benn and Evans 2010). Several studies (see Benn et al. (2007b) for overview) have sought to model the process of fracture growth (e.g., Iken, 1977; Kenneally and Hughes, 2002; Pralong and Funk, 2005) and depth (e.g., Nye, 1957; Benn et al., 2007b), as the rate and depth of propagation of crevasses is considered by many authors to be the rate–controlling factor at many calving margins (Kenneally and Hughes, 2002; Pralong and Funk, 2005).

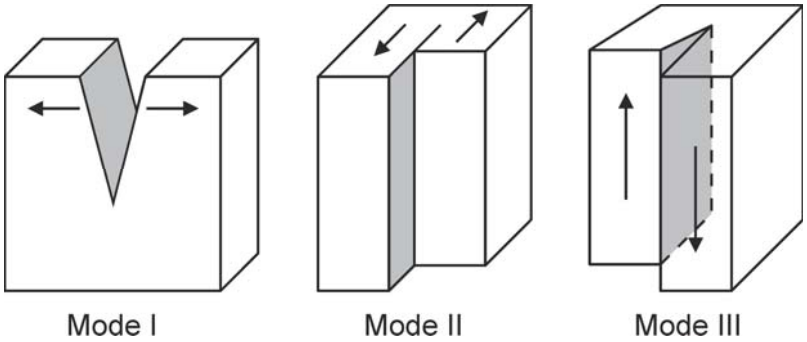

Figure 2.6: Schematic diagram showing the three principal modes of crack propagation from Benn et al. (2007b). Arrows indicate direction of applied force. Mode I is the development of a fracture due to tensile stresses. Mode II occurs when a fracture develops along a shear plan and the fracture walls remain in contact and sliding past each other. Mode III describes the tearing of an ice body, with propagation occurring at right angles to the original parallel shearing.

The depth of a crevasse at the terminus, in particular, plays a significant role in calving by isolating blocks of ice to an extent that calving is inevitable. The point at which this occurs is typically assumed to be the point at which the crevasse intercepts with the waterline (Benn et al., 2007b). As a crevasse penetrates through an ice body tensile stress at the tip of the fracture is eventually counteracted by the weight of the ice, limiting crevasse depth (Figure 2.7A). Based on this assumption Nye (1957) derived a formula to calculate crevasse depth (d) for a given strain rate:

$$d = \frac{2}{\rho_i g}\left(\frac{\dot{\varepsilon}}{\mathrm{A}}\right)^{\frac{1}{\mathrm{n}}} \tag{2.1}$$

where ρ_i is ice density, g is gravitational acceleration, A and n are flow law parameters, and ε̇ is longitudinal strain rate. However, several authors (Weertman, 1973; Robin, 1974; van der Veen, 1998b; Alley et al., 2005; Benn et al., 2007b; Hart et al., 2011) have noted that the presence of water within a crevasse can have a significant impact on crevasse depth. This is due to cryostatic compressive forces (weight of ice) being opposed by the pressure of water as well as tensile stresses (Figure 2.7B). As a result, Benn et al. (Benn et al., 2007a; Benn et al., 2007b) have modified Equation (2.1) to incorporate water pressure within a crevasse:

$$d = \frac{2}{\rho_i g}\left[\left(\frac{\dot{\varepsilon}}{A}\right)^{\frac{1}{\mathrm{n}}} + (\rho_\mathrm{w} g d_\mathrm{w})\right] \tag{2.2}$$

where d_w represents the water depth in the crevasse and ρ_w is water density in the crevasse. As water pressure acts in the same direction as tensile stresses, crevasses will penetrate deeper with the presence of water. If enough water is present they have the potential for penetrating indefinitely through an ice body. The presence of water within a crevasse is particularly important for calving as water can enter from the proglacial water body. This can cause an

increase in the propagation of crevasses that have developed due to processes acting at the terminus (section 2.5.2).

The orientation of crevasses near the terminus has a significant influence on the geometry of calving margins. In valley glaciers, tensile and shear stresses applied due to glacier flow and lateral drag lead to the development of several common patterns of crevasses (Figure 2.8). They are chevron, transverse and splaying crevasses. Such crevasse patterns can be advected passively to the terminus region or develop due to near–terminus stresses. For example, transverse crevasses commonly develop at the termini of tidewater glaciers due to the simple shear along valley margins and longitudinal extension near the centre, which is often mirrored in the geometry of the calving margin (see Figure 6A in Benn et al. (2007b)).

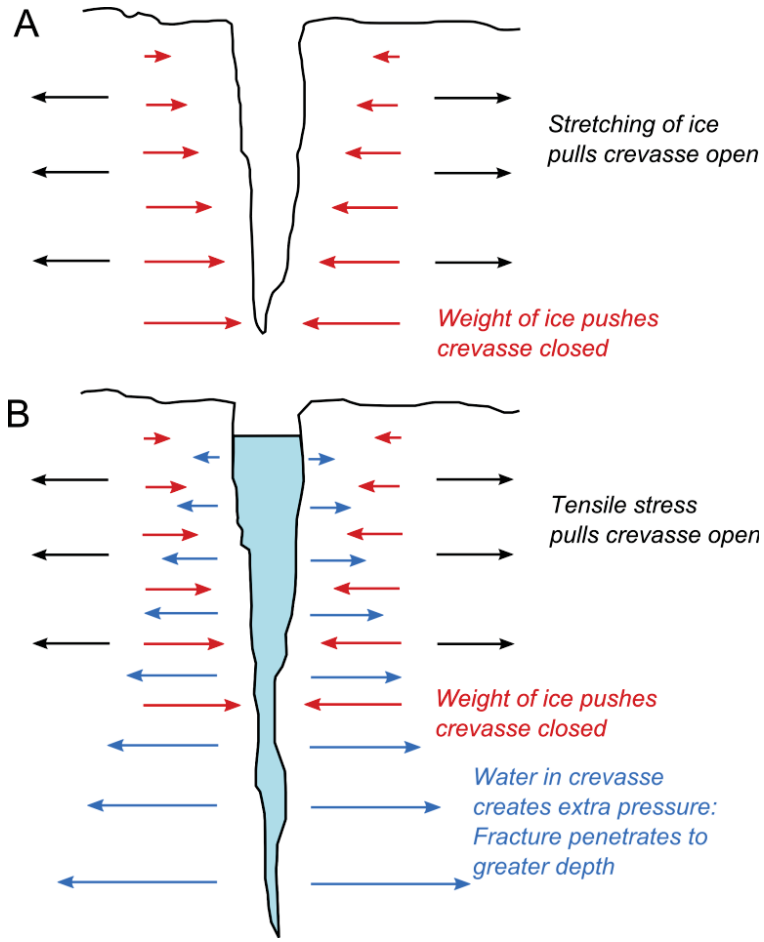

Figure 2.7: Diagram showing the factors that affect the crevasse development and propagation via Mode I (Figure 2.6) fracture. (A) Tensile and compressive forces are matched limiting the depth of penetration. (B) Water within the crevasse increases pressure at the fracture tip, allowing the crevasse to penetrate to greater depths (Benn and Evans 2010).

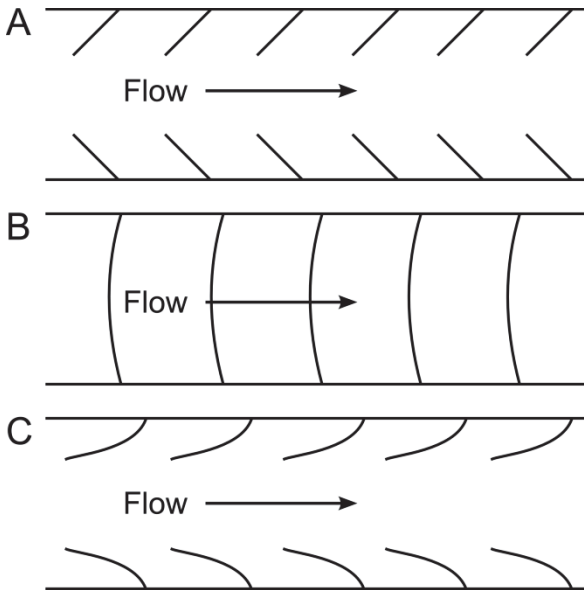

Figure 2.8: Common crevasse patterns found in valley glaciers. (A) Chevron crevasses from due to lateral shear. (B) Transverse crevasses develop with a slightly curved form due to a combination of extending glacier flow and lateral shear. (C) Splaying crevasses develop due to lateral shear stress and longitudinal shear stress as a result of compressive flow (after Nye, 1957; Benn and Evans 2010).

2.5.2 Processes leading to calving

Given that calving of icebergs from water–terminating glaciers is the result of the development and propagation of crevasses, the processes that induce stress at the terminal zone provide a key control on calving. Benn et al. (2007b) have identified four processes that are thought to alter or induce enough stress within the terminus region to enhance and control crevassing and calving. Changes in the stress regime are thought to occur due to: (1) high surface velocity gradients resulting in longitudinal stretching, (2) force imbalances at the terminus, (3) melt associated with the proglacial water–body, and (4) torque induced by buoyant forces. These processes are elaborated on in the following sections.

2.5.2.1 Surface velocity gradients

Increased surface velocity at the termini of calving margins observed by a number of authors (e.g., Krimmel and Vaughn, 1987; Rott et al., 1998; Venteris, 1999; Vieli et al., 2000) is thought to occur as a result of increased basal motion. A decrease in basal drag occurs as effective pressure at the base of a glacier approaches zero (Vieli et al., 2000; O'Neel et al., 2005), and has been argued (e.g., van der Veen, 1996) to arise as the terminus of the glacier approaches flotation. Tensile stress resulting from high longitudinal and transverse surface velocity gradients cause the fracturing of ice and the propagation of crevasses if longitudinal strain–rates are sufficiently high (Meier and Post, 1987; Venteris, 1999; Vieli et al., 2000; Benn et al., 2007b). Such crevasses provide preferential lines of weakness at the terminus (Powell, 1983)

that facilitate structural failure and the calving of ice (Dowdeswell, 1989; Warren, 1992). The result of high surface velocity gradients can be clearly seen by the pervasively crevassed surfaces and high rates of mass loss via calving evident at the termini of tidewater glaciers (Benn et al., 2007b). It should be noted, however, that such increase in velocity at the termini are not universal, with a number of glaciers demonstrating a decrease in velocity towards the terminus, presumably indicating a decoupling of the glacier from the bed (Benn et al., 2007b). For example, O'Neel et al. (2001) identified a marked decrease in strain–rates within 200 m of the terminus of Le Conte Glacier, Alaska, indicating that the glacier was potentially at, or in excess of, the point of flotation.

Water–filled crevasses penetrate downwards through a glacier without limit (section 2.5.1). As a result, crevasses that form due to longitudinal stretching associated with high velocity gradients facilitate calving events once they penetrate to a depth in line with the proglacial water body level. The point at which this occurs will therefore define the position of the terminus. As such, the velocity distribution at the terminus (causing initial crevassing), the height of the subaerial ice cliff (determining the height through which crevasses have to penetrate), and whether meltwater is stored in surface crevasses (Benn et al., 2007a; 2007b), all provide key controls over the loss of ice due to calving and the position of the terminus.

2.5.2.2 Force imbalance at the terminus

Originally proposed by Reeh (1968) in relation to floating termini and ice shelves, local force imbalances between cryostatic and hydrostatic forces (Figure 2.9) at the terminus is considered an important control on calving events. Cryostatic pressure above the waterline is effectively unopposed by atmospheric pressure, unlike below the waterline where hydrostatic force is exerted by the water column. Tensile and shear stress develops at the glacier terminus, extending up–glacier to a maximum distance equal to approximately the ice thickness. The result is the formation of crevasses within this zone, providing lines of weakness, from which low magnitude, high frequency calving events result. A similar process is thought to operate at grounded tidewater and lacustrine calving margins, with the added effect of the development of an overhanging subaerial ice cliff resulting from deformation along forward bending shear bands (Hughes and Nakagawa, 1989; Hughes, 1992, 2002; Kenneally and Hughes, 2002).

Calving events resulting from force imbalances further alter glacier geometry causing greater force imbalances at the glacier terminus, subsequently causing further fracturing. A positive feedback is created whereby the magnitude of calving events controls the position of the glacier terminus by regulating changes in glacier geometry and force imbalances at glacier termini (Reeh, 1968; Hughes, 2002). The position of the glacier terminus in this situation is therefore

controlled by the length of the calving cycle, and the time between successive calving events. As a result, a longer calving cycle will result in glacier advance, whilst a shorter calving cycle will result in retreat. Calving in this situation is therefore governed primarily by calving margin geometry and ice rheology, which act upon longitudinal velocity gradients.

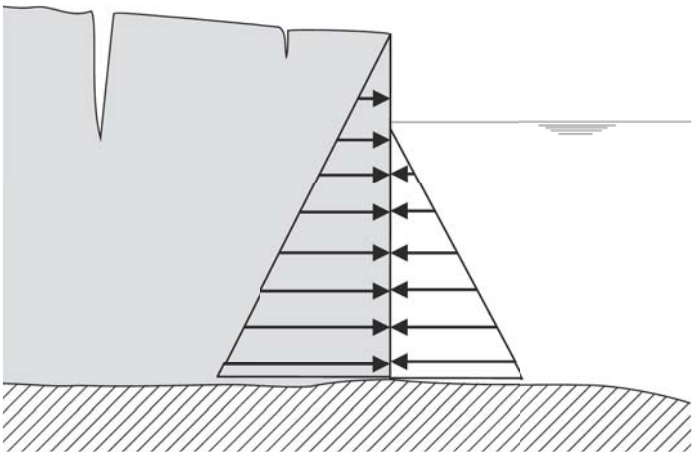

Figure 2.9: Illustration demonstrating the imbalance of horizontal cryostatic and hydrostatic forces at a grounded calving margin.

2.5.2.3 Melt associated with proglacial water bodies

Melt along the ice cliff of calving margins can have a significant effect on altering the localised stress regime and driving calving (Hanson and Hooke, 2000; Vieli et al., 2002; O'Leary and Christoffersen, 2012). The loss of ice as a result of melting associated with an ice–contact proglacial water body occurs via two main processes: (1) melting along the subaqueous portion of an ice cliff, and (2) mechanical calving associated with waterline melt.

2.5.2.3a Subaqueous melt

Subaqueous and waterline melt at calving margins is an important control of retreat for both tidewater and freshwater–terminating glaciers (Warren et al., 1995a; Vieli et al., 2002; Warren and Kirkbride, 2003). The current understanding of subaqueous melt rates and their potential impact on calving processes is limited (Eijpen et al., 2003; Motyka et al., 2003a; Haresign and Warren, 2005; O'Leary and Christoffersen, 2012), with numerous methods having been applied to determine subaqueous melt rates, utilising both melt rates from iceberg (e.g., Weeks and Campbell, 1973; Mathews and Quinlan, 1975; Josbergerm and Neshyba, 1980; Russell-Head, 1980), field (e.g., Motyka et al., 2003a; Haresign and Warren, 2005), laboratory (e.g., Eijpen et al., 2003), and modelling–based studies (e.g., O'Leary and Christoffersen, 2012). From these studies the fundamental controls on melt rates along the subaqueous portion of an ice cliff appear to be (1) temperature and salinity, and (2) forced convection from glacial and non–

glacial sources in the associated proglacial water body (Eijpen et al., 2003; Haresign and Warren, 2005; Röhl, 2006).

At margins that have high calving rates, subaqueous melt has generally been assumed not to play a significant role in mass loss (Laumann and Wold, 1992; Hochstein et al., 1998; Fitzharris et al., 1999), accounting for one or two orders of magnitudes less than calving (Syvitski, 1989). However, recent estimates of the effect of subaqueous melting at calving margins have indicated that it may play a greater role in mass loss then previously suspected. For example, Motyka et al. (2003a) estimated that up to 57 % of total ice loss from the tidewater LeConte Glacier (Alaska), was the direct result of subaqueous melt. Similar results have been found at tidewater glaciers in Greenland (Rignot et al., 2010; Sutherland and Straneo, 2012; Xu et al., 2012; Sciascia et al., accepted). Increased subaqueous melt may also play a role in glacier thinning (e.g., Trüssel et al., 2013), resulting in an increase in buoyancy forces at the terminus. However, as yet there is no consensus around the calculation of subaqueous melt rates and their impact on glacier mass balance and changes in the geometry of calving margins. In particular, there have been very few studies at freshwater margins (e.g., Hochstein et al., 1998; Röhl, 2008; Robertson, 2012) limiting the understanding of the contribution of mass loss from freshwater margins.

2.5.2.3b Waterline melt and thermo–erosional notch formation

Melting at the waterline of calving margins often results in the formation of a horizontal notch in the ice cliff if left for a significant length of time (Figure 2.10). As the *thermo–erosional* notch develops it alters the stress regime of the overlying ice, creating shear and tensile stresses, and resulting in the destabilisation of the subaerial ice cliff (Iken, 1977; Kirkbride and Warren, 1997; Benn et al., 2001; Röhl, 2006). The subsequent evolution of a notch is in turn affected by cliff geometry, debris supply (limiting water temperature and currents within notches), and water–level fluctuations (Sakai et al., 2000; Röhl, 2006). The process of notch formation results from the complex interaction of these factors, with no one factor proving to be correlated significantly to notch formation (Röhl, 2006). The spatial variation and importance of thermal undercutting relies upon the above factors, particularly thermal stratification in the water body, as melt distributed over a large vertical water depth will not form thermo–erosional notches as effectively as melt localised over a narrow vertical range (Benn et al., 2007b). The resulting calving events exploit pre–existing lines of weakness at the glacier terminus (such as crevasses or englacial thrust plains (Röhl, 2005)) to produce ‘full–height’ slab calving or smaller, lower angle, waterline calving events (Figure 2.10).

The impact of thermo–erosional notch formation at calving margins varies significantly with glacier speed (Haresign and Warren, 2005). At slow glacier speeds, subaqueous and waterline melt (as a cause of direct mass loss or resulting in mechanical calving) dominates mass loss at the terminal ice cliff, controlling the rate of retreat. However, at faster glacier speeds the significance of subaqueous and waterline melting decreases as calving associated with changes in ice dynamics control retreat (Haresign and Warren, 2005). For example, at fast flowing glaciers such as Glaciar León and Glaciar Ameghino, Patagonia, the rate of waterline melt and notch formation is slow, and thus does not affect calving from the highly crevassed glaciers (Warren and Aniya, 1999; Haresign and Warren, 2005). In contrast, at the relatively slow–moving glaciers of New Zealand, waterline melt and notch formation is more important for controlling calving (Purdie and Fitzharris, 1999; Röhl, 2006) over short timescales.

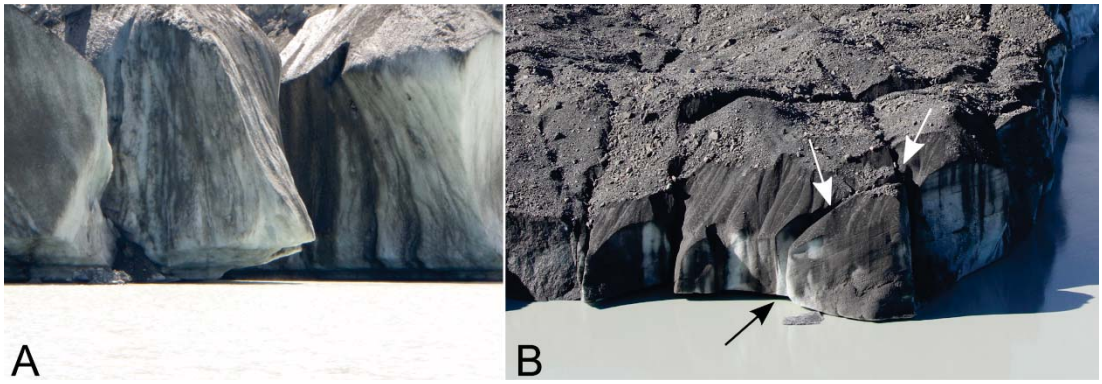

Figure 2.10: Thermo–erosional notche forming at the terminus of Tasman Glacier. (A) shows the significance of stable lake level in notch formation at the *c.* 20 m high ice cliff. (B) The extensive development of notches along the ice cliff is shown (black arrow) and the importance of crevasses (white arrows) on calving due to notch development.

2.5.2.4 Torque induced buoyant forces

2.5.2.4a Buoyancy of the terminal zone

Buoyancy of the terminus at calving margins occurs as a result of thinning associated with longitudinal stretching and subaerial melt altering the stress regime of the terminus, decreasing ice overburden pressure. The result of this decrease in ice overburden pressure is that basal drag decreases to zero (Warren et al., 2001; O'Neel et al., 2005) resulting in an increase in ice velocity (e.g. O'Neel et al., 2005) and an increase in torque arising from buoyancy forces acting at the terminus (van der Veen, 1996; Warren et al., 2001). Calving results as the fractured, temperate ice which retreating glaciers are composed of, approaches near zero tensile strength at (or near) the point of flotation (Meier and Post, 1987; van der Veen, 1996; O'Neel et al., 2003; O'Neel et al., 2005). Consequently, any processes (such as high basal water pressures and lake level fluctuations) move the glacier away from hydrostatic equilibrium and lead to large bending forces at the terminus (Warren et al., 2001; Boyce et al., 2007). If upward–bending

forces in the terminal zone are not accommodated, then tensile stress at the glacier bed develops basal crevasses, ultimately resulting in buoyancy–driven–calving of large sections of ice at the point of failure (Warren et al., 2001). The point at which this occurs is defined as the flotation thickness, h_f (Warren et al., 2001; Boyce et al., 2007; Benn and Evans 2010):

$$h_f = \frac{\rho_w}{\rho_i} h_{\mathrm{w}} \tag{2.3}$$

where ρ_w is the density of sea or freshwater (1030 or 1000 kg m^{-3}), ρ_i is the density of glacier ice (917 kg m^{-3}), and h_{w} is water depth. h_f provides a critical thickness of the terminus (Figure 2.11), past which retreat of the glacier occurs until h_f is again exceeded (van der Veen, 1996, 2002).

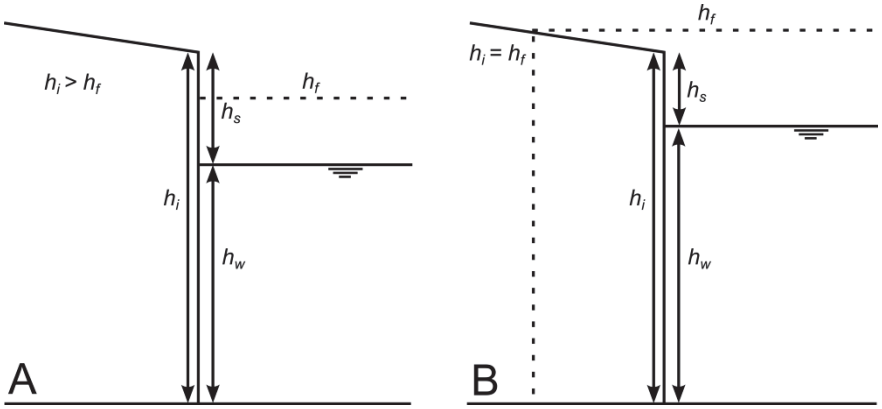

Figure 2.11: Diagram of the key parameters the affect terminus flotation as defined in equation (2.3). (A) Ice thickness (h_i) exceeds flotation thickness (h_f) resulting in stability of the terminus. (B) Ice thickness at the terminus is below flotation thickness due to thinning or increased water depth, leading to flotation and retreat until h_i equals h_f.

Observations from temperate tidewater calving margins (e.g., Meier and Post, 1987; van der Veen, 1996; O'Neel et al., 2003; O'Neel et al., 2005) have supported this idea, demonstrating that tidewater glaciers cannot support floating termini except locally for short periods of time, with calving occurring at the point of flotation (Meier and Post, 1987; van der Veen, 1996). However, at slower flowing freshwater glaciers, buoyancy of the terminus (or sections of it) have been observed (e.g., Naruse and Skvarca, 2000; Warren et al., 2001; Boyce et al., 2007; Trüssel et al., 2013). Buoyancy at lacustrine termini is thought to occur if bending stresses are applied over a significant length of time for internal deformation to accommodate flotation (Warren et al., 2001; Boyce et al., 2007). Once at the point of flotation, calving events and terminus breakup result from relatively small, rapidly applied perturbations in proglacial water level (Boyce et al., 2007). For tidewater glaciers, these perturbations are typically provided by tidal motion, which immediately destabilise the buoyant ice cliff. In comparison, such

perturbations at freshwater calving margins are caused by, for example, meltwater discharge or rainfall. Slow perturbations at freshwater calving margins may therefore allow for viscoelastic deformation rather than calving failure (Boyce, 2006). Boyce et al. (2007) demonstrated this with the example of Mendenhall Glacier, Alaska, where flotation of a section of the glacier was sustained over a two–year period by ice creep and lateral support of grounded ice near bedrock margins.

2.5.2.4b Subaqueous calving

Subaerial calving of the fashion described above (and shown in Figure 2.12A–B) can subsequently lead to the development a subaqueous ice 'foot', or ice ramp, protruding (Figure 2.12D) from a grounded glacier (Motyka, 1997; Hunter and Powell, 1998; Robertson et al., 2012). Such an ice foot remains due to thermal stratification occurring in the ice contact water body producing differential melting between the upper, warmer layer (the epilimnion) and the lower, cooler bottom layer (the hypolimnion), as well as an apron debris–cover (Hunter and Powell, 1998). Torque arising from buoyancy differences between the ice foot and water, and the opening of bottom crevasses (e.g., van der Veen, 1998a), results in the subaqueous calving (Figure 2.12D) of ice from the ice 'foot' (Motyka, 1997; Hunter and Powell, 1998). Such calving events often produce large icebergs (>100 m^3) that can surface hundreds of meters from the calving face (Warren et al., 1995a; Motyka, 1997). Recent research (e.g., O'Neel et al., 2003) has indicated that subaqueous calving is often preceded by subaerial calving events at a short time lag. This indicates that increased buoyant forces are applied to the subaqueous portion of the ice cliff as subaerial ice loss decreases ice overburden pressure. Although subaqueous calving has been well documented (e.g., Warren et al., 1995a; Motyka, 1997; Hunter and Powell, 1998; O'Neel et al., 2007), its effect is often neglected in studies at calving margins due to the difficulty in quantifying the rate and timing of events (Robertson et al., 2012).

2.5.3 Calving mechanisms

Four basic mechanisms of iceberg calving from grounded water–terminating glaciers have been identified by authors (e.g., Reeh, 1968; Hughes, 1989; Kirkbride and Warren, 1997; Motyka, 1997; Warren et al., 2001; Röhl, 2006; Benn et al., 2007b) to describe calving events (Figure 2.12): (A) spall (or flake) and larger slab calving, caused by differences in local stress concentrations causing the over–steepening of the subaerial ice cliff; (B) the formation of thermo–erosional notch at the water line destabilising the ice cliff (Kirkbride and Warren, 1997; Röhl, 2006); (C) buoyancy–driven calving of large tabular icebergs exploiting pre–existing lines of weakness (Warren et al., 2001; Boyce et al., 2007); and (D) subaqueous calving of a glacier ice 'foot' (Motyka, 1997; Hunter and Powell, 1998; Robertson et al., 2012). These four

mechanisms can be attributed to the underlying processes acting at the calving margin discussed in section 2.5.2. Changes in ice dynamics as a result of high velocity gradients and force imbalances at the terminus, resulting in crevasse formation, provide initial lines of weakness from which spall (or flake) and slab calving result (Figure 2.12A). Subaqueous melt and waterline melt–induced calving (Figure 2.12B) along with buoyancy–driven calving (Figure 2.12C, D) are superimposed on changes in ice dynamics further exploiting lines of weakness (Benn et al., 2007b).

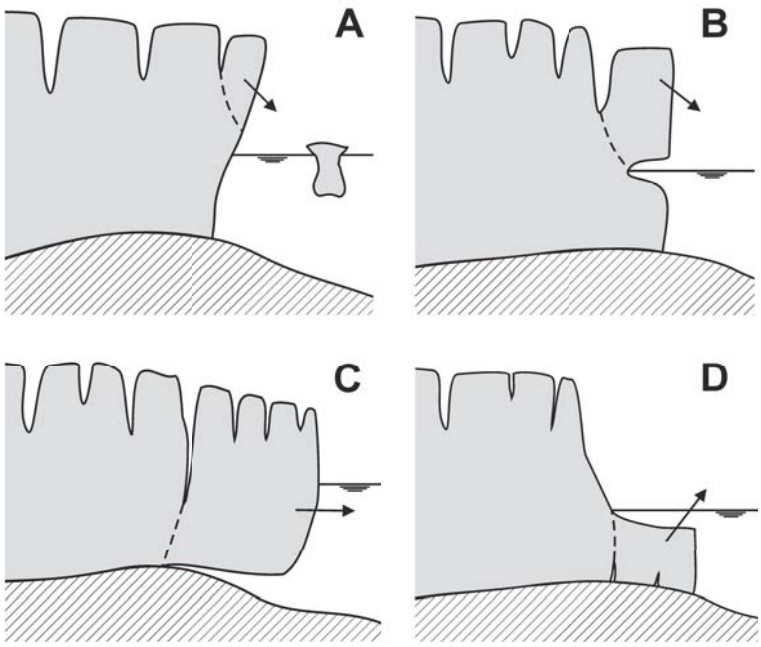

Figure 2.12: Illustration of iceberg calving mechanisms from grounded termini (adapted from van der Veen, 2002). See text for explanation.

2.5.3.1 Calving hierarchy

Due to the complex nature of iceberg calving, a hierarchy has been proposed within which calving processes and mechanisms operate (Benn et al., 2007b). As presented above, the first order control on calving is changes in ice dynamics, such as longitudinal strain rates caused by large–scale velocity gradients and large force imbalances at unsupported ice cliffs. Such changes in longitudinal strain rates and force imbalances control the formation and propagation of surface crevasses, providing lines of weakness from which calving events result (Benn et al., 2007a). Calving events resulting from thermo–erosional notch–driven calving, make up the second order controls on calving as they are superimposed on changes in ice dynamics. Buoyancy–driven calving also represents a second order calving mechanism as it is controlled primarily by the position of the grounding line and thickness of the glacier, which is in turn controlled by the aforementioned mechanisms.

Alternatively, calving has been conceptualised as a continuum where the relative importance of each mechanism varies depending on ice velocity (Figure 2.13). Proposed by Haresign (2004), the continuum identifies that at slower ice velocities over–steepening by ice flow and undercutting by waterline melt dominate calving, whereas at higher velocities, longitudinal stretching and buoyant forces become rate–controlling. Although longitudinal stretching and buoyant forces operate at all speeds, the impact of over–steepening by force imbalance at the terminus and undercutting by waterline melt becomes negligible at higher velocities. This fits with observed results from fast and slow–flowing glaciers alike. Indeed, the rate–controlling calving mechanism at the fast–flowing outlet glaciers of Alaska and Greenland is controlled primarily by calving as a result of their pervasively crevassed calving margins (e.g., Meier and Post, 1987; van der Veen, 2002; O'Neel et al., 2007; Joughin et al., 2008a; Nettles et al., 2008). By comparison, at the relatively slow–moving glaciers of New Zealand, the rate–controlling mechanism appears to be undercutting by waterline melt (e.g., Kirkbride and Warren, 1997; Purdie and Fitzharris, 1999; Röhl, 2006).

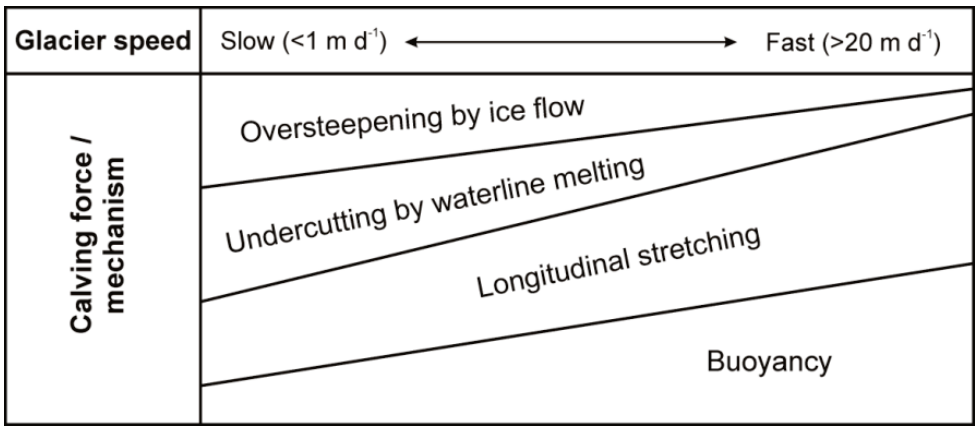

Figure 2.13: Conceptual model of a calving continuum. See text for explanation (Haresign, 2004).

2.5.4 Calving laws and models

A number of calving models have sought to quantify calving rates, and produce over–arching "calving laws" that can accurately describe and predict calving from water–terminating glaciers. However, due to the inherently difficult (and dangerous) nature of measuring such dynamic systems a number of compounding factors remain poorly quantified. As a result, there is currently no consensus on the processes, or underlying factors, that control the rate of ice calving at water–terminating glaciers (van der Veen, 1996; Hanson and Hooke, 2000; van der Veen, 2002; Benn et al., 2007b), with a wide range of studies being carried out on calving margins around the world. Such studies typically account for calving from the terminus by calculating the calving rate (the volume of ice lost per unit time per vertical unit area (Paterson,

1994), which is equal to the difference between ice velocity and change in terminus position over time (Vieli et al., 2001)), u_c (m a^{-1}), of a glacier:

$$u_c = u_i - \frac{\Delta L}{\Delta t} \tag{2.4}$$

where u_i is ice velocity (typically vertically averaged), L is glacier length, and t is time. In general, surface melt is implicitly included in the calculation of calving rate as it is considered negligible compared to ice loss as a result of calving processes. However, at slow moving freshwater glaciers, where surface melt accounts for a large proportion of total ice loss at the terminus, authors have excluded surface melt from calving rates (e.g., Warren and Kirkbride, 2003; Röhl, 2006). Alternatively, calving rate can also be expressed in relation to mass flux per unit width (Motyka et al., 2003a; Benn et al., 2007b):

$$Q_c + Q_m = Q_{in} - Q_{out} \tag{2.5}$$

where Q_c is calving flux, Q_m is melting, Q_{in} is ice flux into the terminus, and Q_{out} is the rate of change of the terminus (Figure 2.14). This equation can then be recast to calculate Q_c in terms of volume flux (m^3 a^{-1}):

$$Q_c = Q_{in} - \frac{\Delta V}{\Delta t} \tag{2.6}$$

where the rate of volume change at the terminus is $\Delta V/\Delta t$. In this equation Q_c implicitly includes both calving and subaqueous melt at the terminus (Motyka et al., 2003a; O'Neel et al., 2003).

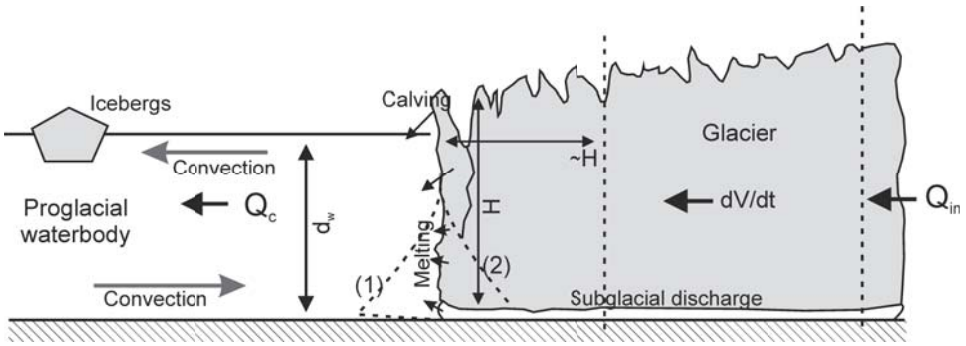

Figure 2.14: Schematic diagram of the mass flux in (Q_{in}) and calving flux (Q_c) at a calving terminus. Key variables in determining mass flux and major processes resulting in the loss ice at the terminus (adapted from Motyka et al. (2003a) and O'Neel et al. (2003)).

The relationship between calving and glacier dynamics has been the focus of study and debate due to the apparent linkages between glacier thinning, acceleration and retreat, and increased calving found at retreating water–terminating glaciers (van der Veen, 2002). Whether this

increase in retreat is the cause, or result, of increased calving has led to the so called "master versus slave debate". Where increased calving losses occur as a result of changes in glacier dynamics (glacier thinning/acceleration), calving is seen as the 'slave' to glacier dynamics (van der Veen, 1996; Venteris et al., 1997; van der Veen, 2002). In contrast, where increased calving triggers acceleration in glacier flow and thinning, calving is considered the 'master' in triggering increased calving losses and retreat (Hughes, 1986; Meier and Post, 1987; Meier, 1994; Hughes, 1996; Meier, 1997; Howat et al., 2005). This distinction between increased calving as the 'master' or 'slave' of terminus position has polarised researchers, with each hypothesis being developed from the same dataset derived for Columbia Glacier, Alaska. Both relationships appear to explain a similar proportion of observed data for Columbia Glacier and have empirical support from other studies. However, given the complex nature of calving and its interaction with glacier dynamics a causal relationship between the two is unclear (Benn et al., 2007b) and likely to be an oversimplification with both factors feeding back into one another. The result of this uncertainty has been a plethora of models and laws to understand calving and its interaction with glacier dynamics.

As a result, several methods have been employed to solve Equation (2.4). In one approach, changes in calving rate and ice velocity as control the retreat of the terminus. In another, changes in terminus position are controlled by geometric factors, with calving rate varying in response to ice velocity and terminus position. The first approach derives empirically based calving rate functions from independent variables (e.g., Brown et al., 1982; Sikonia, 1982; Funk and Rothlisberger, 1989), whereas the second approach focuses on changes in terminus position and dynamics to predict calving rates (e.g., van der Veen, 1996; Vieli et al., 2001; van der Veen, 2002; Vieli et al., 2002). Process–based models represent a third method with which calving mechanisms and processes have been quantified. Such models focus on the physical mechanisms (such as fracture mechanics and stress distribution at the terminus) involved in the calving of icebergs.

2.5.4.1 Empirically derived 'calving rate functions'

Initial attempts to quantify calving rates have seen authors attempt to correlate them with measured independent external variables, the most noteworthy being the relationship between water–depth and calving rate. Brown et al. (1982) first quantified the correlation between water depth at the calving margin and calving rate for Alaskan tidewater glaciers, with water depth governing calving rate (Funk and Rothlisberger, 1989; Hanson and Hooke, 2000). Following Brown et al. (1982) a number of authors (e.g., Funk and Rothlisberger, 1989; Pelto and Warren, 1991; Warren et al., 1995a; Warren and Kirkbride, 2003) have elaborated on this idea by identifying a variety of empirically based linear relationships with the form:

$$u_c = ch_w \quad (2.7)$$

where, u_c is width–averaged calving rate , h_w is water depth, and c is a constant.

Linear regression applied to a number of datasets has produced several different relationships between u_c and h_w for tidewater and freshwater calving–glaciers (Table 2.1). The most recent attempt for freshwater–terminating glaciers by Warren and Kirkbride (2003) incorporated a total of 21 glaciers, from Patagonia (Warren et al., 1995b), Svartisheibreen, Norway (Kennett et al., 1997), Glacier Ameghino, Argentina (Warren, 1999), and six New Zealand glaciers (Warren and Kirkbride, 2003), producing Equation (2.14). However, the relationship described by Warren and Kirkbride (2003) is questionable, as shallower, less realistic, proglacial water depths are reported in their study (Dykes and Brook, 2010). Considering that subaqueous processes act on the entire submerged portion of the glacier terminus, the measurement of h_w should take into account the average total depth of the glacier terminus not just to a subaqueous foot, which is apparently the case in this study. Furthermore, studies have also indicated that this linear relationship between calving rate and water depth does not hold true over long–term datasets (e.g., Robertson et al., 2013). Nevertheless, the difference between Warren and Kirkbride's (2003) coefficients and Pelto and Warren's (1991), for freshwater and tidewater glaciers respectively, does highlight the difference in rates of retreat between tidewater and freshwater glaciers. However, it has recently been shown that there could be just as much variation between glacial regions and even between glaciers within the same mountain zone (Haresign, 2004).

Table 2.1: Relationship between calving rate (u_c) and water depth (h_w). u_c is width averaged calving speed (ma^{-1}), h_w and h_{max} are the average and maximum water depth at the calving front (m), and c is a coefficient.

Equation	Coefficent (c)	Glacier type	Source	Equation
$u_c = ch_w$	27.1 a^{-1}	12 tidewater glaciers	Brown et al. (1982)	(2.8)
$u_c = ch_w + 70$	8.33 a^{-1}	22 tidewater glaciers	Pelto and Warren (1991)	(2.9)
$u_c = ch_w + 12$	1.9 a^{-1}	5 freshwater glaciers	Funk and Rothlisberger (1989)	(2.10)
$u_c = ch_w$	2.5 ± 0.5 a^{-1}	14 freshwater glaciers	Warren et al. (1995b)	(2.11)
$u_c = ch_{max}$	1.8 ± 0.5 a^{-1}	14 freshwater glaciers	Warren et al. (1995b)	(2.12)
$u_c = ch_w$	3.62 a^{-1}	19 freshwater glaciers	Skvarca et al. (2002)	(2.13)
$u_c = ch_w + 17.4$	2.3 a^{-1}	21 freshwater glaciers	Warren and Kirkbride (2003)	(2.14)

The water depth model has been criticised from a number of sources, which have identified the u_c/h_w correlation as being spurious (e.g., van der Veen, 2002). Calving rates are typically given as annually–averaged data (m a^{-1}), which appears to predict calving rates at this timescale quite well. However, this is not always the case, with calving rate actually accelerating at some glaciers (e.g., Columbia Glacier, Alaska) as the glacier retreated into shallower waters (Hanson and Hooke, 2000). The water depth model also breaks down at shorter timescales (e.g., seasonally) as fluctuations in calving rate occur at a near constant water depth (Sikonia, 1982; Krimmel, 1997; Meier, 1997; van der Veen, 2002; Benn et al., 2007b). For example, during the initial retreat of Columbia Glacier, Alaska, seasonal variations in calving rate occurred (with the lowest calving rates occurring in winter and early spring (Krimmel, 1997)), whilst water depth remained relatively constant throughout (Sikonia, 1982; Krimmel, 1997; Meier, 1997; van der Veen, 2002).

An equally important criticism of the u_c/h_w correlation is that as $\Delta L/\Delta t$ is typically smaller than u_i, a correlation between ice velocity and calving rate exists (van der Veen, 2002). This is, however, implicit as ice velocity is used as a proxy for ice flux into the calving front, and therefore coeval fluctuations would be expected. The example of the Columbia Glacier has again been used to describe the relationship between glacier velocity and calving rate, with van der Veen (2002) finding a strong correlation (r^2 = 0.94) between the two variables. This correlation between glacier velocity and calving rate was identified during the retreat of the Columbia Glacier, with similar relationships having been identified for other Alaskan glaciers in the study by Brown et al. (1982). The implication of this is that as ice velocity is dependent on a large number of factors (such as basal water pressure, valley/glacier geometry, and longitudinal strain rates) there must be underlying factors affecting calving.

As a result of this analysis, a number of authors (e.g., Pelto and Warren, 1991; van der Veen, 1996; Hanson and Hooke, 2000; van der Veen, 2002) have speculated that the strong correlation that exists between u_c/h_w actually represents a dynamically linked third (unspecified) variable that has not yet been conclusively identified (Hanson and Hooke, 2000). This is based on the assumption that as no physical mechanism has been found to explain the correlation between the two, there must be a third hidden variable which would explain the relationship. As yet this has not occurred. However, the water–depth model has provided the basis from which other studies have built on.

2.5.4.2 Height above buoyancy model

Ice cliff height in excess of flotation was first proposed by Sikonia (1982) as a possible factor influencing calving termini. However, it was not until van der Veen (1996, 2002) that the impact

of ice cliff height was considered as a rate–controlling factor of calving margin retreat. The height–above–buoyancy model, as described by van der Veen (1996), focuses on terminus position, controlled by ice velocity and local geometric factors, not by the calving rate as in the water depth model.

Underpinning the height–above–buoyancy model is the observation that fractured (temperate) ice, which retreating tidewater glaciers are typically composed of, approaches zero tensile strength near flotation (Meier and Post, 1987; van der Veen, 1996; O'Neel et al., 2003; O'Neel et al., 2005). As a result, such glaciers cannot sustain floating ice tongues, with calving initiated as a glacier reaches the point of flotation, resulting from thinning (as a result of longitudinal stretching or a decrease in effective pressure associated with high basal water pressure) or changes in bed topography (van der Veen, 1996, 2002). Once flotation is reached, glacier retreat continues until the ice cliff height exceeds the flotation thickness, or to a point where effective pressure becomes positive or equivalent (O'Neel et al., 2003). The point at which the critical thickness threshold, H_o is met is governed by the densities of water and ice, and depth of water at the calving margin:

$$H_{\mathrm{c}} = \frac{p_w}{p_i} h_w + H_o \tag{2.15}$$

where, H_{o} represents the minimum thickness above flotation that can be supported by the glacier, h_w water depth, and p_{i} and p_{w} the density of ice and the proglacial water body respectively. van der Veen (2002), for example, uses a value of H_0 = *c.* 50 m for Columbia Glacier, Alaska, with thinning below this critical ice cliff height resulting in the destabilisation of the terminus. Such an observation that appears to hold true for the 17 km retreat of Columbia Glacier, documented between 1976 and 1993.

More recently, Vieli et al. (2001; 2002) have modified the height–above–buoyancy model, substituting the thickness in excess of flotation, H_{o}, for a fraction of the flotation thickness of the terminus $(1 + q)$:

$$H_{\mathrm{c}} = \frac{p_w}{p_i}(1 + q)h_w \tag{2.16}$$

For example, at Columbia Glacier a value of q= 0.15 yields H_0 = *c.* 50 m. The advantage of using the modified flotation criterion is that it is more applicable to a larger number of glaciers which do not have the same characteristics as the fast–flowing tidewater glaciers from which the initial model was developed (Vieli et al., 2001). To this end, the model reproduces qualitatively

similar behaviour to some calving margins (Benn et al., 2007b), such as the modelled retreat of Hansbreen Glacier, Svalbard (Vieli et al., 2002).

The major advantage of the height–above–buoyancy model is that it removes geometric factors from the calculation of calving rates. Therefore, it does not try to establish a calving law but simply a boundary condition within which calving will be initiated. The apparent correlation between water depth and calving rate is therefore the result of the boundary condition of ice cliff thickness being met. As a result, the height–above–buoyancy model provides a heuristic boundary condition for calving to occur, however there are limitations. The first is that although the model explains longer term changes in calving from grounded termini, it does not explain the presence of calving from termini which are far from the threshold thickness. Secondly, it does not allow for the condition of floating ice shelves, which are well in excess of flotation. The use of this model is, therefore, similar to that of the water depth model in that it provides another quantified relationship that does not holistically describe the response of all calving margins to changes in ice dynamics.

As a result of a number of these limitations a modified version of this calving model has been proposed by Amundson and Truffer (2010) that builds on the previously proposed models. In their model the pre– (H_0) and post– (H_1) calving terminus thicknesses are given two unknown but related functions, with the ratio between the two influencing the size and timing between calving events. For grounded glaciers, floating glaciers and unstable ice shelves a ratio of 1, 0.98 and < 0.9 respectively, have been proposed. This means that the calving rate at a glacier is influenced by processes which affect this ratio. Processes include: ice thickness, thickness gradient, strain rates, crevasse spacing, proximity to flotation, fluctuations in the proglacial water–body and melting at the terminus. Of these factors, crevasse spacing may play a significant role in the timing and magnitude of calving events by providing the nuclei for calving events (Benn et al., 2007a). Where crevasse spacing is large for slow moving grounded termini, flotation of the glacier would be needed prior to calving. In comparison, at fast–flowing glaciers with smaller crevasse spacing, calving occurs more frequently due to decreased distance between the ice cliff and the first crevasse. This does not limit the ability of fast flowing glaciers to develop floating margins where the difference between ice thickness and crevasse depth is large. Amundson and Truffer (2010) suggest that although it is difficult to measure H_0, if crevasse spacing is large then Equation (2.3) will hold true.

2.5.4.3 Theoretical process based calving models

2.5.4.3a Lameller calving

Early modelling work by Iken (1977) sought to identify and define the process of calving using finite element analysis of fracture propagation of an undercut serac at a grounded calving margin. In this model the propagation of a fracture that develops at the glacier surface behind the terminus, due to differential ice flow between the glacier surface and base of the subaerial ice cliff, was simulated in relation to the evolution of the changing stress field and evolving ice block geometry. This model shows that as the fracture propagates downwards the ice block rotates forward increasing tensile stress at the fracture tip, and further increasing fracture depth. This produces an overhanging ice block that eventually calves as it becomes isolated due to the growth of the crevasse. Such processes have been observed at several calving margins (e.g., Benn et al., 2001). Although Iken's (1977) model provides a good explanation for the processes acting at an undercut ice cliff, it is necessarily simplistic and does not take into account other processes and calving types that act at calving margins.

2.5.4.3b Bending shear

Hughes (1989, 1992, 2002), Hughes and Nakagawa (1989), and Kenneally and Hughes (2002) have suggested an alternate process–based theoretical model that was born out of the analysis of stress and strain patterns at the terminal ice cliff on Deception Island, Antarctica. Originally proposed by Hughes (1989, 1992) and Hughes and Nakagawa (1989), bending shear, caused by basal drag as the top of the ice cliff moves faster than the base, is thought to control calving from a land terminating vertical ice cliff. An overhang and the formation of curved shear bands parallel to the ice cliff (Figure 2.15A), similar to the pages of a book bent around its spine, develops as a result of this process. Bending creep and eventual fracture along these pre–existing shear bands (based on the bending beam theory) eventually cause 'slab' calving.

Despite the fact that calving controlled by bending shear was based on a polar, cold–based glacier, the authors argue that this mechanism could be applied to all environments where calving occurs (Hughes and Nakagawa, 1989). However this is obviously not the case, as calving along the entire ice cliff height (as predicted by Hughes (1992)) does not typically occur, with subaqueous ledges (or ice feet) often protruding from the ice cliff (e.g. Motyka, 1997; Hunter and Powell, 1998). As a result, Hughes (2002) and Kenneally and Hughes (2002) re–evaluated the bending shear model to incorporate fracture mechanics to describe the development of crevasses immediately behind a water–terminating terminus. The crevassing in Hughes' (2002) model relies upon the elastic bending of the subaerial ice cliff as a result of local force imbalances between cryostatic and hydrostatic forces (Figure 2.16), causing higher

velocities at the top of the ice cliff, and over–steepening of the subaerial ice cliff. Shear bands created by the forward bending of the ice cliff provide lines of weakness from which crevasses are formed. Calving results as support along the shear bands is lost, and the 'crushing stress' at the base of the subaerial ice cliff is exceeded.

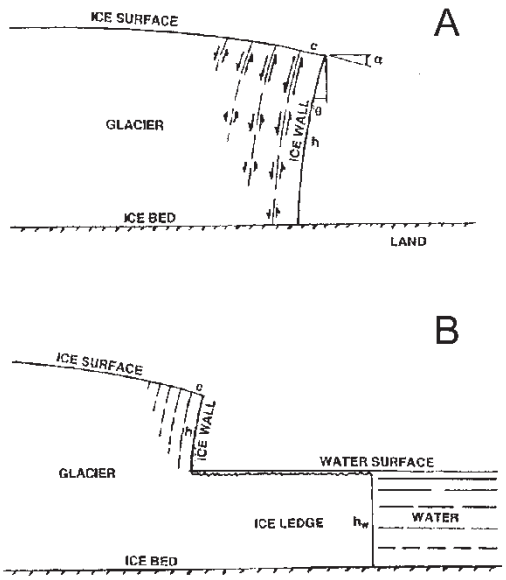

Figure 2.15: Conceptual illustration from Hughes (2002) showing bending shear bands for (A) and grounded land based ice cliff with the vertical velocity gradient inducing forwards bending causing slip along shear bands, and (B) slab calving from the subaerial ice cliff resulting in the formation of a subaqueous ice foot at a water terminating glacier.

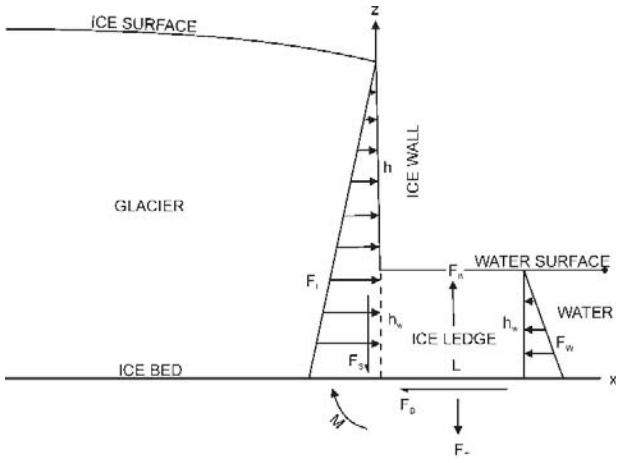

Figure 2.16: Illustration of an ice ledge and the forces acting at a water terminating glacier according to Hughes (2002).

Although this refined model is superior to Hughes (1989, 1992) and Hughes and Nakagawa's (1989) original model of ice cliff evolution, Hughes (2002) and Kenneally and Hughes (2002) still base their calculation of slab calving rate, u_c, on the bending shear mechanism studied on Deception Island. The authors propose that u_c for slabs from the ice cliff should be calculated by balancing the forces and moments acting on the slab (Hughes, 2002):

$$u_c = \left(\frac{3\rho_I g_x}{2\eta c^2}\right) h_s^4 + \left(\frac{2\rho_I g_z}{5\eta c^3}\right) h_s^5 - \left(\frac{\rho_I g_z}{\eta c}\right) h_s^3$$
$$= \left(\frac{3\rho_I g h_s^4}{2\eta c^2}\right) \sin\theta + \left(\frac{2\rho_I g h_s^5}{5\eta c^3} - \frac{\rho_I g h_s^3}{\eta c}\right) \cos\theta \quad (2.17)$$

where, g is gravitational acceleration, h_s is ice height above land or water, η is effective ice viscosity, c is the distance from the ice wall to the crevasse along which the slab calves, and θ is the forward bending angle of the ice wall (Kenneally and Hughes, 2002). The resultant slab calving above the waterline, predicted by Hughes (2002), allows for the formation of a subaqueous ice foot (Figure 2.15b) at grounded calving margins. Such an ice foot is developed as a result of hydrostatic forces opposing cryostatic forces along the subaqueous ice cliff (Figure 2.16), unlike the force imbalance at the subaerial ice cliff. Once an ice foot has developed, buoyant forces act to induce calving by the formation of bottom crevasses (see Figure 2.12D).

A more holistic model of calving and glacier response to external factors has also been put forward. In line with the effect that high velocity gradients have on calving, Hughes (1986) proposed the "Jakobshavns effect" for the rapid retreat of fast flowing tidewater glaciers based on the retreat of Jakobshavn Isbræ, Greenland. An increase in glacier flow caused by surface melt increasing basal water pressure is thought to result in longitudinal stretching. This results in greater crevassing at the terminus, enhancing calving. This then allows more summer melt to penetrate and lubricate the base of a glacier. A positive feedback system is created where increased surface velocities result in increased crevassing and calving. In this situation calving would increase until the glacier retreats to a topographic pinning point. If no pinning point exists then glacier retreat would continue to retreat until either the glacier retreats out of the water or, in the case of outlet glaciers, the ice sheet collapses. This idea is similar to the proposed cyclical nature of retreat for tidewater glaciers described in section 2.5.4.3d.

2.5.4.3c Stress distribution at the terminus

The multivariate nature of calving is considered by Hanson and Hooke (2000, 2003) to represent the presence of currently unspecified variables. The authors use a finite element model of stress distribution at the terminus, incorporating water depth, longitudinal strain and temperature, to identify if there is any physical basis for the water depth/calving rate relationship. Their results show a zone of high velocity just below the water line leads to the development of an overhanging ice cliff. The tendency of a glacier to develop such an overhang will also increase as the glacier's thickness increases, due to an increase in velocity gradients. A zone of high tensile stresses (high longitudinal deviatoric stress) located just back from the ice cliff also results in extensive crevassing, which commonly present at calving termini. The uneven

distribution of hydrostatic and cryostatic forces acting on either side of the ice cliff, causing high tensile stresses at the surface, would also lead to high tensile stresses at the base of the calving face, resulting in the formation of bottom crevasses (e.g. van der Veen, 1998a) and associated subaqueous calving.

Hanson and Hooke's (2000) interpretations have been debated by van der Veen (2002) on two counts. First, the affect that an overhang has on calving is not as significant as the authors propose, with the velocity difference between the base of the glacier and at the waterline far too low to entirely account for the apparent relationship between water depth and calving rate (van der Veen, 2002). Secondly, longitudinal deviatoric stress calculated at the base may not initiate bottom fracture (van der Veen, 1998a), as indicated by Hanson and Hooke (2000). Indeed, van der Veen (1998a) identifies that this criterion for bottom fracture at grounded termini only occurs if the glacier is very near flotation, primarily due to increases in basal water pressure. Nevertheless, Hanson and Hooke's (2000, 2003) modelled results remain important as they represent the first attempt to fully incorporate the distribution of stresses into calving models (Mottram, 2008). This demonstrates the importance of basal sliding speed, surface profile, subaerial ice cliff height, lateral shape, presence or absence of crevasses, and ice rheology on the development of an overhang, and presumably also calving (Hanson and Hooke, 2003).

2.5.4.3d Advance–retreat cycling and sediment dynamics

The terminus position of a tidewater glacier typically demonstrates a cyclical from of slow advance followed by periods of rapid retreat (Meier and Post, 1987; van der Veen, 1996; Pfeffer, 2007). The cause of the advance phase has been suggested by several authors (e.g., Powell, 1983; Syvitski, 1989; Hallet et al., 1996; Nick and Oerlemans, 2006; Oerlemans and Nick, 2006) to result from an interaction of the ice–water–sediment systems. The supply of sediment to a tidewater glacier terminus leads to the development of a large submarine terminal moraine shoal that reduces the effective water depth at the glacier front. This permits the slow advance (Figure 2.17A) of the glacier, as the forward movement of the terminal moraine regulates water depth (as material is eroded from the ice proximal side and deposited on the ice distal slope), and therefore calving rate is based on the water depth model (Warren, 1992; Oerlemans and Nick, 2006). In this situation the terminal moraine is also thought to provide sufficient back pressure by buttressing the calving front (Fischer and Powell, 1998; Venteris, 1999), stabilising the grounding line.

Following the period of slow advance, any perturbations altering terminus dynamics, such as thinning associated with enhanced ablation or a rise in the ELA, and causing a loss of contact with the terminal moraine can result in the collapse and retreat of the terminus. Once retreat has

been initiated a positive feedback system is developed where thinning propagates upstream as a result of increased glacier flow, caused by a decrease in basal drag as the glacier approaches flotation, and resulting in a drawdown of ice from the névé (e.g. Meier and Post, 1987; Pfeffer, 2007). Retreat of the glacier continues as longitudinal stretching associated with increased glacier flow and flotation of the terminus occurs, resulting from thinning, and increases calving. Glacier retreat continues until a stable position is again attained at a shallower water depth (Figure 2.17B), often at a topographic pinning point such as a valley constriction or valley head.

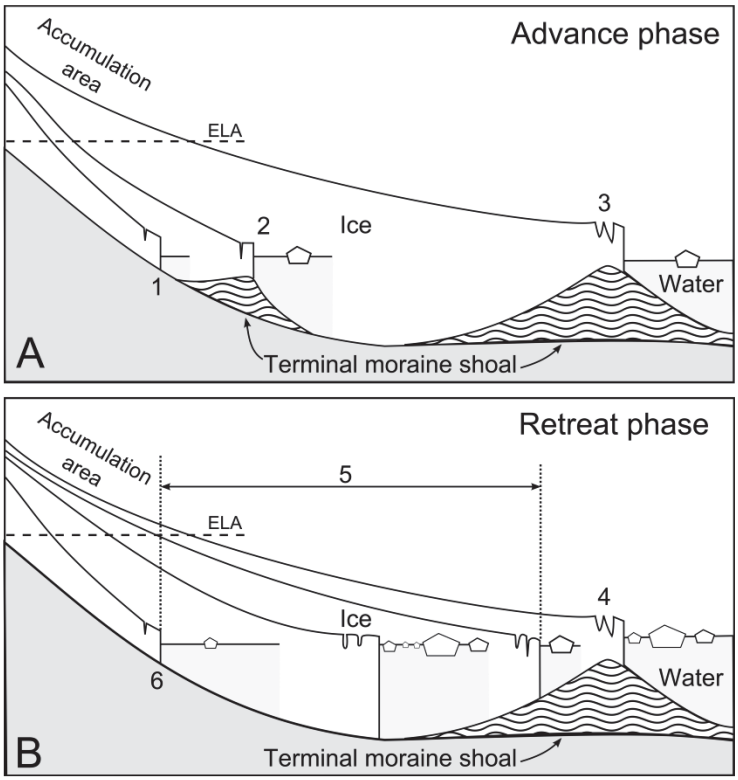

Figure 2.17: The cyclical pattern of tidewater glacier advance (A) and retreat (B). (A) Slow advance of the glacier occurs behind a moraine shoal (positions 1–3). (B) After an initial climate forcing that alters water level at the terminus (4), retreat of the glacier will occur as water depth increases down the moraine shoal (5) until (6) it either reaches equilibrium or retreats out of the water (adapted from Warren, 1992)

Modelling of the advance–retreat cycle phase by Oerlemans and Nick (2006) indicates that through this process tidewater glaciers can advance over large depressions, however, once a critical point is met retreat rates can be as high as 10 km in 50 years. The result is a highly non–linear retreat cycle that is suggested to be initiated by long–term mass balance deficits, but once initiated is ultimately controlled by the complex interaction of a series of factors (such as bed topography, sediment supply, and ice dynamics) that decouples the retreat of tidewater glaciers from climate (Oerlemans and Nick, 2006; Pfeffer, 2007). Observations of tidewater glaciers from Alaska, such as those found in Glacier Bay, seem to demonstrate this cyclical nature, with a number of glaciers rapidly retreating after a long period of stability (e.g., Columbia Glacier),

whereas others have remained stable and even advanced during the same period (e.g., Harvard Glacier). However, only elements of this cycling have been found within glacier systems outside of Alaskan tidewater glaciers, resulting in some authors (e.g., Warren, 1992) questioning whether the cyclical oscillations are simply an amplification/dampening of climate signals and not an independent cycle.

2.5.4.3e Crevasse depth calving criterion

Benn et al. (2007a) have proposed a calving model that seeks to link the physical characteristics of glacier termini to the prediction of calving. This calving criterion has been born out of the inability of the previously mentioned calving models to produce calving rate functions that are directly related to physical principles. Their calving criterion seeks to quantify first order control (i.e. ice dynamics) on calving from which secondary processes act (i.e. waterline melt and buoyant forces). Calving primarily occurs following fracture propagation and the formation of crevasses in ice, which provides a pattern of weaknesses from which calving then proceeds. It follows that calving models should, therefore, focus on fracture mechanics as the calving occurs when transverse crevasses propagate downward to the level of the proglacial water body (Figure 2.18). Benn et al. (2007a) define this point as:

$$x = L \text{ where } d(x) = h(x) \tag{2.18}$$

where d is crevasse depth, x is the horizontal coordinate parallel to glacier flow, positive downstream, L is glacier length and h is freeboard above proglacial water level (Figure 2.18).

Crevasses are formed out of the variation in flow speed and longitudinal strain rate at the terminus. Crevasse depth is calculated using Nye's (1957) equation of Mode I (Figure 2.6) surface fracture (Equation (2.1)). This provides an explanation for crevasse formation and propagation, but does not take into account water partially or completely filling the crevasse. Benn et al. (2007a) have modified Equation (2.1) to include the effect of water pressure (Equation (2.2) and combined this equation with three glacier sliding models to directly relate the importance of ice velocity on the formation of crevasses and therefore calving rates. The importance of ice velocity is related to the delivery of ice to the calving front, therefore controlling calving flux, and the direct relationship between ice velocity and longitudinal strain rates. With crevasse propagation directly related to these factors, the authors argue that crevasse propagation therefore represents a first order control on calving termini.

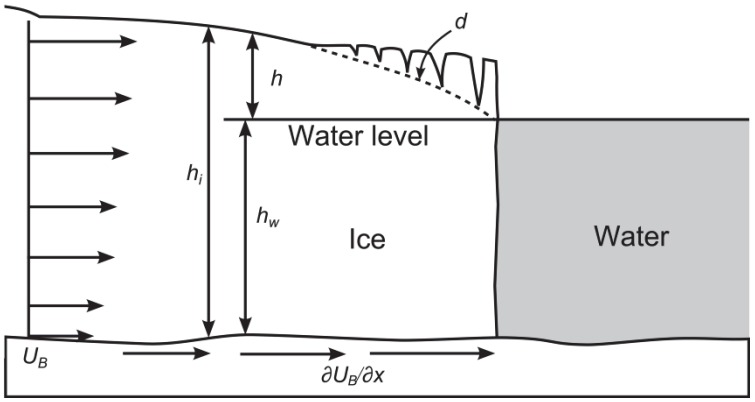

Figure 2.18: Calving in response to longitudinal strain rates. Surface crevasses propagate downward to a depth, *d*, in response to the velocity gradient $\partial U_B/\partial x$, where calving is assumed to occur when $d = h_w$ (Benn et al., 2007a).

The criterion proposed by Benn et al. (2007a) only represents a two–dimensional model of calving from a margin, limiting its implementation. Otero et al. (2010) have further expanded the calving criterion by developing a three–dimensional version that incorporates a full–Stokes model of glacier dynamics. Their results indicate that the original calving criterion is improved by their extensions and that it can accurately predict the calving front of an example glacier, Johnsons Glacier, Antarctica. However, limitations still exist in the applicability of the criterion in both forms due to problems with the flow models and surface velocity distribution. Also, the models only relate to first–order controls on calving (stretching associated with surface velocity gradients (section 2.5.2.1)). Second order processes also acting on calving margins are therefore neglected, leading to potential over–estimations of glacier length (Benn et al., 2007a). Nevertheless, the calving criterion provides a more robust form of parameters for predicting calving. Further research into physical mechanisms, such as crevasse propagation, could provide the key to greater understanding of the controls on calving glaciers.

2.5.4.4 Fracture scale calving law

The proliferation of attempts to derive universal calving laws from semi–empirical datasets has not yet led to a single, unified, calving law. To develop such a unified calving law that is applicable to all glaciological and environmental regimes (e.g., ice shelf, tidewater, freshwater), Bassis (2011) uses the theoretical method of mesoscopic fracture theory to develop a macroscopic calving law. This is rooted in the assumption that iceberg calving is inherently linked with ice fracture and should therefore include fracture physics within its underpinning. As a result, Bassis (2011) uses a modified differential master equation (see Bassis (2011) for a full explanation) that describes the rate of change of probability, to generate an equation that is able to describe the variability of terminus position at a macroscopic level (both temporally and spatially). This theoretical approach to calving laws has the advantage in that it is not tied to any

specific theory of fracture mechanics (e.g., Benn et al., 2007a), iceberg calving mechanisms (e.g., Iken, 1977; Brown et al., 1982; van der Veen, 2002), or glaciological setting (e.g., Alley et al., 2008). However, this could also be considered a disadvantage as it has no observational underpinning. Nevertheless, Bassis (2011) indicates that it does have the ability to reproduce a range of calving styles, from low magnitude events through to the detachment of large tabular icebergs from ice shelves. For the proposed model, greater testing and validation against datasets from glaciers is needed, as well as formulating a physical theory to describe model outputs, so that it can be successfully integrated into future modelling of calving margins.

2.6 Calving–generated seismicity

Studies have shown that glaciers generate energetic seismic signals, broadly termed *icequakes* (Neave and Savage, 1970; Wolf and Davies, 1986; Qamar, 1988; O'Neel et al., 2007). Icequakes were originally identified by Rothlisberger (1955), Crary (1955) and Hatherton and Evison (1962), although it was not until Neave and Savage (1970) that the emission of icequakes were systematically described and linked to glaciological mechanisms. Following these initial descriptions, several mechanisms for icequake production have been hypothesised. These include: surface crevassing (e.g., Neave and Savage, 1970; Cichowicz, 1983; Roux et al., 2008), stick–slip basal sliding (e.g., Anandakrishnan and Bentley, 1993; Anandakrishnan and Alley, 1997; Bindschadler et al., 2003), motion along–glacier shear zones (e.g., Górski, 1997), fluid–driven crack propagation (e.g., Métaxian et al., 2003; O'Neel et al., 2007), hydraulic transients in subglacial conduits (e.g., St Lawrence and Qamar, 1979), iceberg harmonic tremor (IHT; e.g., MacAyeal et al., 2008) and calving at the glacier front (e.g., Qamar, 1988; O'Neel et al., 2007). As a result, the generation of seismic signals by glaciers has become an increasingly important field of study due to its potential to passively, and remotely, identify source mechanisms of a number of glaciological phenomena.

In particular, characterising seismic signals generated by calving events has been identified as an effective and important technique for study as it removes some of the inherent dangers and difficulties historically encountered by researchers at calving margins (Benn et al., 2007b; O'Neel et al., 2007). As a result, a large body of literature (e.g., Qamar, 1988; O'Neel et al., 2007; Amundson et al., 2008; Tsai et al., 2008; MacAyeal et al., 2009; Richardson et al., 2010; Walter et al., 2010; Chen et al., 2011; Bartholomaus et al., 2012; Richardson et al., 2012; Veitch and Nettles, 2012; Walter et al., 2012) has emerged over the last decade to characterise calving–generated seismic signals so that they can be differentiated from other glaciological phenomena. Studies have recorded calving seismicity across a continuum of scales ranging from the detachment of small seracs (e.g., O'Neel et al., 2007; Bartholomaus et al., 2012), to the full ice

thickness calving of tabular icebergs (e.g., Warren et al., 2001; Amundson et al., 2008) and the episodic rifting of ice shelves (e.g., MacAyeal et al., 2003; Bassis et al., 2005). At the largest spatial scales, full–thickness kilometre–sized icebergs (Tsai et al., 2008; Amundson, 2010) have been recorded on global seismic networks up to earthquake magnitudes of M_L 5 (Ekström et al., 2003; Tsai and Ekström, 2007), leading them to be described as *glacial earthquakes* (see Nettles and Ekström (2010) for summary). However, such calving events and associated glacial earthquakes are rare and have only been identified near the termini of several Greenland outlet glaciers (e.g., Veitch and Nettles, 2012) and Antarctic ice shelves (e.g., Chen et al., 2011). This has led authors to seek alternate seismogenic sources for icequakes associated with calving at smaller scales and mechanisms.

2.6.1 Characteristics of calving–generated icequakes

Due to the energetic nature of calving, several studies (e.g., Qamar, 1988; O'Neel et al., 2007; Bartholomaus et al., 2012; Walter et al., 2012) have shown that iceberg calving events across a range of sizes generate seismic energy. The first description of calving as a potential source mechanism for icequakes was by Hatherton and Evison (1962), although, it was not until Qamar (1988) linked the emission of low–frequency seismic signals to calving events at Columbia Glacier, Alaska, that iceberg calving was established as a source mechanism for low–frequency icequakes (O'Neel et al., 2007). Qamar (1988) identified that: (1) virtually every iceberg calving event observed produced a low–frequency seismic event, (2) the duration of the seismic event corresponded to the duration of the calving, and (3) the emergence of icebergs rising out to the water was also accompanied by low–frequency seismic signals. Recently, greater attention has focussed on calving–generated seismic signals, which has led to significant advances in understanding the calving signals (e.g., O'Neel et al., 2007; Amundson et al., 2008; Richardson et al., 2010; Bartholomaus et al., 2012). From these studies, several characteristics have been identified which differentiate calving seismograms from those generated by earthquakes, crevasses, and basal motion. Calving event signals are typically emergent with cigar–shaped envelopes, monochromatic, long–lived (2–1000 s), have weak high frequency (>10 Hz) content at their onset, dominated by lower (1–5 Hz) frequencies and can have multiple high amplitude spikes (Qamar, 1988; O'Neel et al., 2007; Richardson et al., 2010; Bartholomaus et al., 2012). This classification of calving–generated low–frequency icequakes is important as it aids in the isolation of source mechanisms of calving events, by relating the timing and duration of calving events to corresponding glaciological dynamics, with these characteristics observed to occur during calving events at multiple glaciers globally.

2.6.2 Source mechanisms

Through the integrated use of passive seismic observations, terrestrial time–lapse photography, weather data, and qualitative observational records of calving events, substantial advances in the understanding of calving–generated icequakes has occurred in recent years (e.g., O'Neel et al., 2007; Amundson et al., 2008; Tsai et al., 2008; Bartholomaus et al., 2012). However, there is currently no consensus as to what mechanism during the calving process is associated with the release of seismic energy (Bartholomaus et al., 2012). This is unsurprising, as a complex arrangement of mechanisms occurs simultaneously throughout the calving process. Potential sources described in the literature include ice fracture (e.g., Neave and Savage, 1970; Cichowicz, 1983; Roux et al., 2008; Walter et al., 2009; West et al., 2010); fluid–driven crack resonance and other hydraulic transients (e.g., Métaxian et al., 2003; O'Neel et al., 2007); the overturning and scraping of icebergs on the glacier and proglacial foreland (e.g., Amundson et al., 2008; Tsai et al., 2008); grinding and fracturing within an ice mélange that occurs during the detachment of icebergs (e.g., Amundson et al., 2010); and the interaction between icebergs and the surface of the proglacial water body post–calving (e.g., Bartholomaus et al., 2012). The following sections highlight the main characteristics of source mechanisms associated with calving–generated seismic signals.

2.6.2.1 Ice fracture and crevassing

The fracturing of ice and crevasse development is an energetic process which releases seismic energy across a range of frequencies between 10 and 100 Hz (Neave and Savage, 1970; Cichowicz, 1983; Métaxian et al., 2003; O'Neel et al., 2007; Dalban Canassy et al., 2012). Icequakes associated with ice fracture are generally impulsive, have short durations (< 1 second), and are localised within the upper 20 to 30 m of a glacier (Neave and Savage, 1970; Métaxian et al., 2003; Roux et al., 2008; Dalban Canassy et al., 2012), with swarms of such icequakes observed in densities of 2–10 events/s for durations of 1–15 s (Neave and Savage, 1970; Walter et al., 2008). Such swarms were associated with the sequential ‘cracking’ and connection of pre–existing flaws in the ice, generated by an increase in tensile stress within the crevasse zone, forming crevasses (Neave and Savage, 1970; Roux et al., 2008). Additional icequakes may also be associated with the deepening and lengthening of original cracks as shear stress increases. The typical waveform characteristics of ice fracture rules it out as the sole source mechanism for the bulk of energy released during calving events. However, they are thought to play a part during calving onset (Bartholomaus et al., 2012).

2.6.2.2 Resonance within a fluid filled crack

The narrow frequency band (1–3 Hz) of calving–generated icequakes has led authors to suggest an alternative source mechanism that involves the resonance of water within a crack instead of

hydraulic transient. Within this process cracks or fractures in the ice are enlarged due to the presence of fluid. As the crack grows, resonance of the crack walls develops and propagates (Métaxian et al., 2003; Stuart et al., 2005; O'Neel and Pfeffer, 2007), creating the observed frequencies for a given crack geometry. O'Neel and Pfeffer (2007) indicate that a variety (infinite) of crack geometries are able to reproduce the narrow band of frequencies (1–3 Hz) observed for calving events. Furthermore, as the spectral composition is uniform regardless of calving event size, the fault rupture size may be similar across all events, indicating that larger events are made up of a series of small ruptures rather than a single large rupture. These smaller ruptures occur after a critical (but small) rupture destabilises a larger section of ice. Similar ruptures are thought to also occur within the basal zone of glaciers (e.g., Métaxian et al., 2003).

2.6.2.3 Iceberg detachment and rotation

Seismograms of calving events have been associated with the rotation of full–thickness (up to kilometre–sized) icebergs and the resulting interaction (scraping) between the iceberg and the glacier terminus or sea or lake floor (Amundson et al., 2008; Joughin et al., 2008a; Tsai et al., 2008; Amundson et al., 2012). Icequakes (or glacial earthquakes at larger scales) are generated as icebergs overturn and rotate during calving due to hydrostatic imbalances (Figure 2.19). The rotation and break–up of icebergs post–calving contributes to the release of energy and the generation of icequakes through the transfer of momentum to the surrounding water–body. However, it is the scraping of the rotating iceberg when they come into contact with either the terminus or the former glacier bed and surrounding margins that has been hypothesised to account for the bulk of energy released (Amundson et al., 2008; Tsai et al., 2008; Amundson et al., 2010).

Such calving events have been observed at numerous Greenland outlet glaciers that are retreating into deeper water (Amundson et al., 2008; Joughin et al., 2008a; Joughin et al., 2008b; Amundson et al., 2010) and to a lesser extent the smaller tidewater glaciers of Alaska (Walter et al., 2010). Such large calving events are preceded by the thinning of glaciers to the point of flotation, allowing for the development of rifts in the glacier surface and basal crevasses to penetrate the full thickness of the glacier. It is this process of iceberg calving and rotation that has been hypothesised (Amundson et al., 2008; Tsai et al., 2008) to account for large–scale (e.g., kilometre–scale) events that have been recorded on global seismic networks up to earthquake magnitudes of M_L 5 (e.g., Ekström et al., 2003; Tsai and Ekström, 2007).

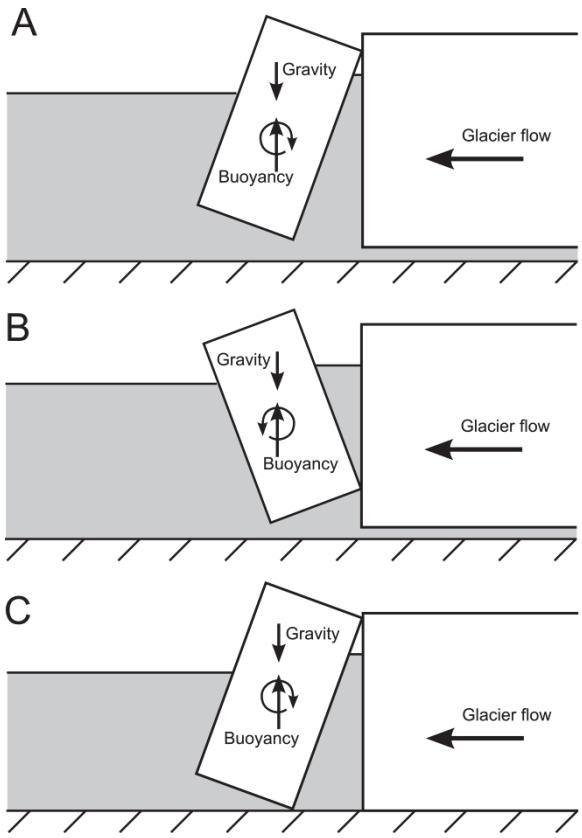

Figure 2.19: Schematic diagram showing the bottom (A and C) and (B) top out rotation and scrapping of calved icebergs at floating (A and B) and grounded (C) termini (adapted from Amundson et al., 2010).

2.6.2.4 Fracturing of ice melange and wave action

The presence of an ice mélange bounding a glacier terminus has been shown to have an effect on not only the calving of icebergs from termini, but also the seismic response of calving events (Amundson et al., 2010). The transfer of momentum due to the rotation of calved icebergs causes the development of waves within the ice mélange that can exceed 1 metre in height. It is the combination of the transfer of waves through the ice mélange and fracturing of ice within it that contributes to the overall seismicity of calving events. For example, Amundson et al. (2010) attributed the long (> 10 minutes) protracted coda of calving events at Jakobshavn Isbræ to the movement and breakup of ice mélange, with seismicity not returning to background levels until the ice mélange stiffens and stops moving. At glaciers without an ice mélange, the development of waves in the proglacial water–body can have the same effect of transferring momentum and seismic energy as the mélange, although they will decay at a faster rate as they will reach equilibrium faster (Amundson et al., 2010). It is this wave action that has also been hypothesised to account for the emergent onset of large calving events (Amundson et al., 2008).

2.6.2.5 Ice–water interaction

At smaller scales, recent work by Batholomaus et al. (2012) has indicated that the dominant 1–5 Hz frequencies generated by calving events are associated with the interaction between the calved section of ice and the proglacial water body. Utilising synchronised video of the terminus and seismograms (Welty et al., 2013) the authors identified that a major 'step' in seismic amplitude within the 1–5 Hz frequency range occurs when an ice block that is calved from the subaerial ice cliff impacts with the water (Figure 2.20). Peak seismic amplitudes following this step coincided with the emergence of high velocity jets after the submergence of the entire ice block. As a result, Bartholomaus et al. (2012) has suggested that seismicity associated with calving events is generated at some point during this process. Four possible mechanisms may account for observed seismicity. They are: (1) the deceleration of the ice block as it enters the proglacial water–body and the resulting transfer momentum; (2) the formation of an air cavity above the descending ice block (Figure 2.20B); (3) cavity wall collapse (Figure 2.20C); or (4), the eventual pinching off of the cavity (Figure 2.20D). The result of this cavity closure is the formation of Worthington jets (Gekle and Gordillo, 2010) that are emitted from the centre of the collapsing cavity (Figure 2.20E). Modelling of processes 2 and 4 suggest that they are able to generate forces over time–scales expected for the generation of 1–5 Hz seismic signals (Bartholomaus et al., 2012). In contrast, processes 1 and 3 are also able to generate significant forces but over millisecond time–scales. As a result, all processes may play a role in generating seismic signals associated with calving, but the deceleration and cavity pinch off represent more realistic source mechanisms.

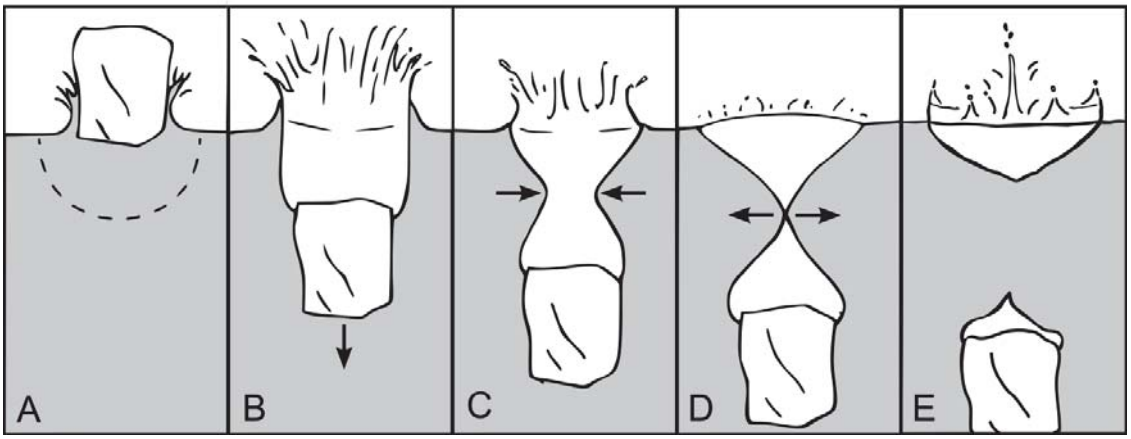

Figure 2.20: Schematic diagram of a calved ice block entering a proglacial water–body and potential the potential seismogenic mechanisms. After the iceberg 'slams' (A) in the proglacial water body it transfers its momentum to the water, decelerating the iceberg (B) and causing a cavity to form above it. This cavity begins to collapse (C), eventually pinching off (D). A Worthington jet (E) is often formed after the cavity pinch off and complete submergence of the iceberg. Illustration adapted from Gekle and Gordillo (2010), and Bartholomaus et al. (2012).

2.7 Summary and conclusions

In summary, the effect of debris–cover, proglacial lake development, and iceberg calving on glacier dynamics and the generation of seismic signals from glaciers and calving events have been discussed. In particular, it has been found that:

- Glacier downwasting due to the presence of supraglacial debris–cover and sustained periods of decreased ice supply play an important role in altering glacier mass balance and the development and expansion of supraglacial ponds.
- Proglacial lake development at the termini of debris–covered glaciers is controlled by (1) the transition of a glacier from melt under debris to the formation and expansion of supraglacial ponds, and (2) a transition to a calving dominated ablation regime.
- There is limited understanding of the dynamics of valley glaciers after the development of a proglacial lake.
- Calving has a significant effect on glacier and ice sheet mass balance, affecting their responses to changes in climate.
- Understanding the processes and mechanisms that control calving is important for quantifying mass loss from glaciers and ice caps, and the incorporation of iceberg calving into predicting future eustatic sea–level rise (SLR).
- Due to the multivariate nature of calving, understanding of the key processes and mechanisms involved remains unresolved.
- The formation and development of fractures (crevasses) is thought to play an important role in conditioning the timing and size of iceberg calving events.
- Four key processes alter the stress regime at calving margins, inducing ice fracture: (1) high surface velocity gradients resulting in longitudinal stretching, (2) force imbalances at the terminus, (3) melt associated with the proglacial water–body, and (4) torque induced by buoyant forces.
- The calving of icebergs can be classified into four different types of events: (1) over–steepening of the subaerial ice cliff caused by differences in local stress concentrations; (2) melt at the water line destabilising the ice cliff; (3) buoyancy–driven calving; and (4) subaqueous calving of an ice ‘foot’.
- A range of empirical relationships and process based models have been developed to form a universally acceptable calving law, with varying degrees of success.
- To better understand calving processes and their effects on the future evolution of unstable calving margins a greater number of observational datasets are needed.
- The recording of “icequakes” generated from glaciers represents a method to passively and remotely document glaciological processes (such as iceberg calving) that have been historically difficult and dangerous to quantify.

- Calving events have been shown to generate seismic signals that are long–lived, have emergent onsets and protracted coda, and are dominated by 1–5 Hz frequencies.
- Suggested source mechanisms for calving–generated icequakes include: ice fracture, fluid–driven crack resonance, the overturning and scraping of icebergs on the glacier and proglacial foreland, grinding and fracturing within an ice mélange, and the interaction between icebergs and the surface of the proglacial water body post calving.

From this review, it is established that there is a need to expand the current understanding of the dynamics and calving processes of glaciers that terminate in proglacial lakes. In order to achieve this, a greater number of studies at glaciers terminating in proglacial lakes are required to provide a larger dataset from which models of calving and its future contribution to SLR can be determined. Tasman Glacier provides an ideal field site to observe the above processes on account of the continued retreat and iceberg calving. This analysis will be undertaken at varying temporal and spatial scales, enhancing the understanding of glaciers that terminate into proglacial lakes, as well as shedding light on the processes that affect water–terminating calving glaciers in general. In particular, exploring calving processes via passive seismological techniques provides an opportunity to identify intra–event processes to aid the understanding of processes operating during calving events.

Chapter 3: Study Area

Haupapa/Tasman Glacier

3.1 Introduction

Haupapa/Tasman Glacier (43°30 S, 170°20 E) is a compound valley glacier system located within the *Aoraki*/Mount Cook National Park of the Southern Alps, New Zealand (Figure 3.1). It is the longest and largest of all glaciers found within New Zealand, and as a result has received the greatest research attention dating back to the early 19th century (Kirkbride and Warren, 1999). In this chapter, Tasman Glacier and the surrounding landscape are discussed to introduce the physical setting within which the glacier is located, and the key characteristics of the glacier that have controlled its evolution and present state. Particular emphasis throughout this chapter is given to the evolution of Tasman Glacier throughout the 19th and 20th centuries and how this has led to accelerated glacial retreat since the formation of Tasman Lake. An in–depth analysis of the development and expansion of Tasman Lake throughout the late 20th century (1950–onwards) is reserved for chapter 4, with only the general characteristics of lake development introduced here.

3.2 Regional Setting

Tasman Glacier is located on the eastern side of the Main Divide of the Southern Alps (Figure 3.1). Rapid uplift (*c.* 8–10 mm a^{-1}) of the Southern Alps (Simpson et al., 1994; Cox and Findlay, 1995; Tippett and Kamp, 1995) has resulted in the formation of a number of peaks in excess of 3000 m, the highest of which is *Aoraki*/Mt Cook (3754 m). The region's geology is dominated by greywacke and argillite of the Torlesse group that has been severely deformed due to folding and faulting of the Pacific plate (Cox and Findlay, 1995; Cox and Barrell, 2007; Allen et al., 2009a). This sector of the Pacific plate represents a hanging–wall sequence, which is typically more pervasively fractured than footwall sequences, giving rise to a high susceptibility of failure (Cox and Barrell, 2007; Allen et al., 2009b), often resulting in large rock avalanches (McSaveney, 2002; Allen et al., 2011). As a result of the fractured and unstable nature of the surrounding mountain peaks, several glaciers (including Tasman Glacier) within the *Aoraki*/Mount Cook National Park are covered in a thick debris–cover (Figure 3.2) that has affected their mass balance and response to climate fluctuations (Kirkbride, 1993; Chinn, 1996).

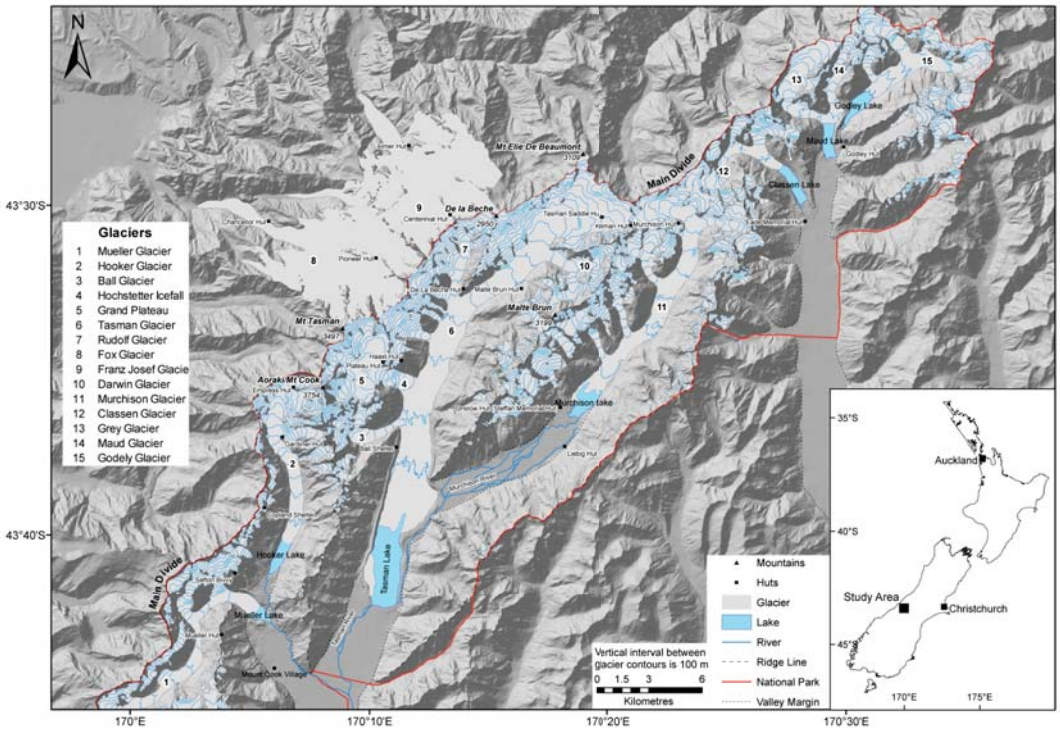

Figure 3.1: Map of the *Aoraki*/Mount Cook National Park showing the glaciers discussed throughout the thesis and their locations. Topographic data sourced from the LINZ Topo50 database.

3.3 Climate

Regional climate is dominated by prevailing southwesterly airflow from the Tasman Sea. This results in orographically–enhanced precipitation caused by the Southern Alps as warm–moist air is forced upwards by the large mountain chain, creating a 'rain shadow' effect (Chamberlain et al., 1999; Lamont et al., 1999). The moist air cools and condenses on the western side of the Southern Alps resulting in high precipitation rates on the West Coast (>12 000 mm a^{-1}), west of the Main Divide (Griffiths and McSaveney, 1983). Significantly lower precipitation rates (as low as 1000 mm a^{-1}) are found on the eastern side of the Main Divide (Lamont et al., 1999). At Tasman Glacier, precipitation varies from approximately 7 m a^{-1} in the upper reaches of Tasman Glacier to around 3 to 5 m a^{-1} at Mount Cook Village (Figure 3.1), with monthly rainfall peaking during spring months (Röhl, 2006; Purdie et al., 2011a). Mean annual temperature at Mount Cook Village is 11 ºC, with maximum temperatures occurring in January and February (Purdie et al., 2011a).

3.4 Tasman Glacier

Tasman Glacier covers an area of approximately 95 km^2, or 220 km^2 if its tributary glaciers are included (Hochstein et al., 1995), and extends 22 km southwards from the Main Divide down the Tasman Valley to 715 m a.s.l., where it terminates into Tasman Lake. The lower tongue of the glacier is *c.* 1–2 km wide, has a very low gradient (<1.5°), and has a debris thickness ranging from 1–2 m (Kirkbride, 1989; Röhl, 2005). Downwasting of the glacier surface throughout the 19th and 20th centuries due to the extensive debris–cover has resulted in *in situ* melting instead of retreat from Tasman Glacier's Little Ice Age (LIA) maximum (Kirkbride, 1993; Chinn et al., 2012). As a result, the lower glacier is flanked by large lateral and terminal moraines which are remnants of LIA advances (Figure 3.2A and Figure 2.2). Underlain by *c.* 200m of compacted till and outwash gravels (Hochstein et al., 1995), the glacier has formed a large ice–contact adverse slope (outwash head) that has provided the preconditions for proglacial lake development. Since the formation of Tasman Lake in the early 1980's due to the coalescing of thermokarst ponds on the lower glacier (Kirkbride, 1993; Hochstein et al., 1995; Kirkbride and Warren, 1999), Tasman Glacier has retreated by a combination of the incorporation of additional thermokarst ponds on the lower glacier (Röhl, 2008; Dykes et al., 2011), subaqueous and subaerial melting (Hochstein et al., 1995; Kirkbride, 1995b; Röhl, 2005; Robertson et al., 2012), and iceberg calving (Purdie and Fitzharris, 1999; Röhl, 2006; Dykes et al., 2011; Robertson et al., 2012).

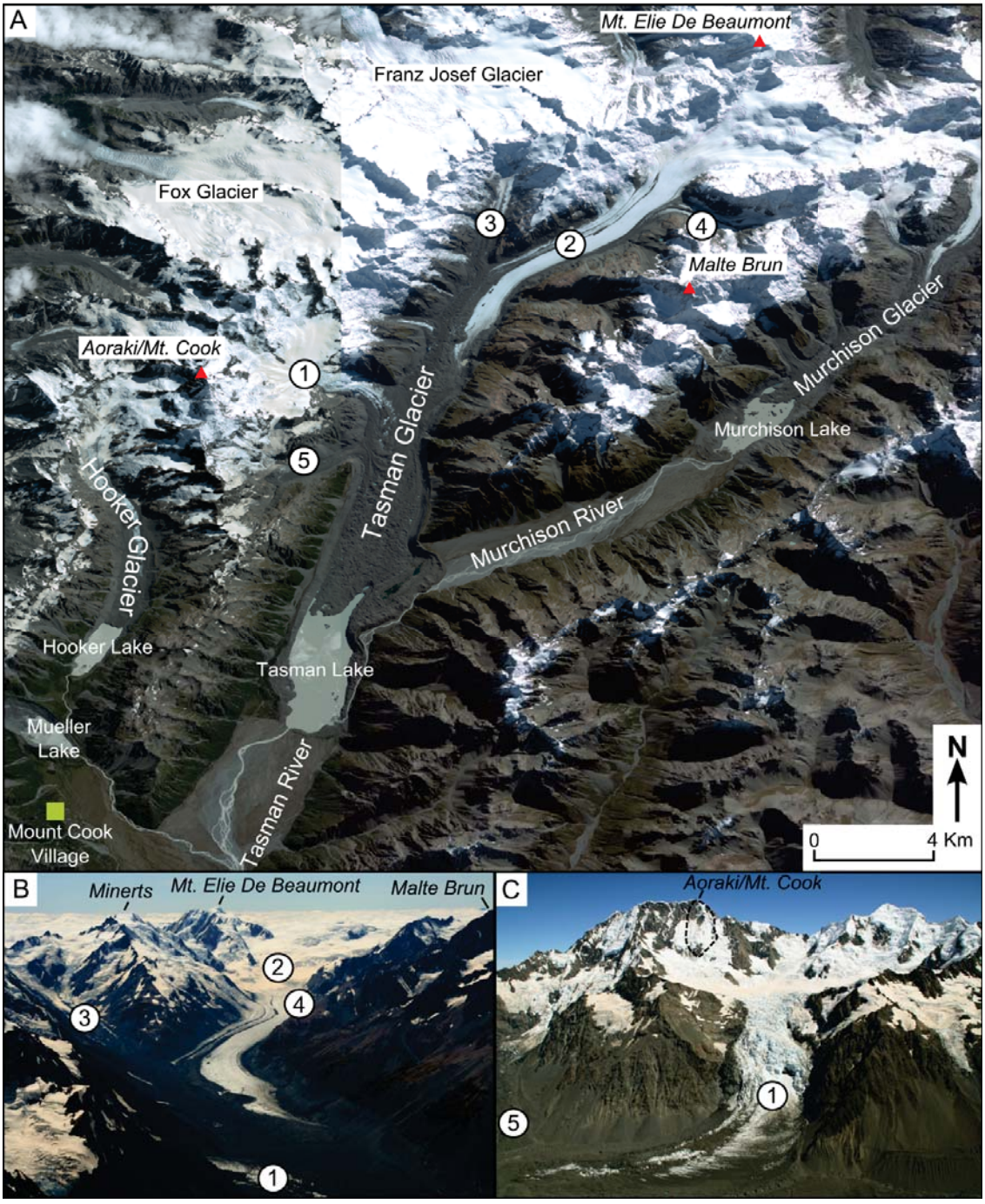

Figure 3.2: (A) Satellite mosaic (Worldview 2– 15/4/10 and 19/2/10), of Tasman Glacier and the surrounding area showing the extent of LIA glaciation. (B) and (C) are photographs looking up to the head of Tasman Glacier, and up the Hochstetter icefall respectively. Location of major flow units discussed in text also shown: (1) Hochstetter icefall, (2) upper Tasman Glacier, (3) Rudolf Glacier, (4) Darwin Glacier, and (5) Ball Glacier. Dotted line in (B) indicates the area of rock lost from *Aoraki*/Mt Cook on the 14 December 1991 (Photos: S. Winkler).

Originally surveyed by von Haast in 1862 and von Lendenfield in 1890, Tasman Glacier has been studied intermittently throughout the 20th century, giving it the longest and most detailed history of all New Zealand glaciers Studies conducted at Tasman Glacier have ranged from mapping of the glacier surface (von Lendenfeld, 1884; Kirkbride, 1989), geophysical profiling

of the glacier bed (Broadbent, 1973; Anderton, 1975; Claridge, 1983; Watson, 1995), measurement of ablation rates for clean ice and debris–cover (Kirkbride, 1989, 1995b; Purdie and Fitzharris, 1999; Röhl, 2005), mapping of flow fields from satellite imagery (Quincey and Glasser, 2009; Redpath, 2011), mapping of Tasman Lake formation (Kirkbride, 1989; Hochstein et al., 1995; Strong, 2008; Dykes et al., 2011), bathymetric mapping of Tasman Lake (Hochstein et al., 1995; Watson, 1995; Röhl, 2005) and analysis of calving processes (Purdie and Fitzharris, 1999; Röhl, 2005, 2006).

3.4.1 Mass balance

The mass balance of Tasman Glacier has been calculated by the measurements of the glacier and fluctuations of the end of summer snowline (EOSS). Direct measurements of mass balance are difficult across such a large glacier with only limited studies looking at point mass balance having been completed (e.g., Skinner, 1964; Anderton, 1975). Such studies have shown that at the time of measurement, Tasman Glacier had an annual gain in mass balance of *c.* 5 m w.e. yr^{-1} in the region of Tasman Saddle Hut (Figure 3.1), with a losses of *c.* 6 and 12 m w.e. yr^{-1} at Malte Brun and Ball Hut (Figure 3.1) respectively (Anderton, 1975).

Given the limited temporal and spatial applicability of such studies (Fitzharris et al., 1999) other proxy methods have been established to generate long–term estimates of mass balance. Based on the assumption that the ELA of a glacier is closely connected to local climate and often represents the lower–most elevation at which snow no longer remains at the end of the summer melt season, surveys of EOSS have been used to represent the annual ELA of a glacier (Chinn, 1995, 1999). This, in turn, can be used to estimate the prevailing mass balance of the glacier and its local climate (Chinn, 1995). In general, aerial photography has been used to estimate EOSS (Willsman et al., 2012), although recent advances have been made using satellite imagery (Mathieu et al., 2009).

For Tasman Glacier the EOSS has been recorded since 1977 (Willsman et al., 2012). Significant fluctuations in elevation throughout the period of study have highlighted the variability in mass balance throughout the late 20^{th} and early 21^{st} century (Figure 3.3). The mean ELA_0 for Tasman Glacier since 1977 is 1810 m, with positive deviations of the EOSS away from this indicating a higher elevation of the ELA (i.e. negative mass balance compared to long–term average), while negative deviations of EOSS indicate a lowering of the ELA (i.e. positive mass balance compared to long–term average). Periods of both positive and negative departures from the ELA_0 have been recorded since 1977, with the largest observed departures representing an increase in elevation of snow lines of 290 and 285 m, recorded in 1990 and 2011 respectively.

In contrast, negative departures away from ELA_0 (i.e. lower EOSS) appear to be weaker, although more common (Figure 3.3). Mass balance since 2000 has been characterised by both positive and negative years. However, a period of sustained strongly negative EOSS, and therefore negative mass balance, has been recorded post–2006.

Fluctuations in the EOSS indicate that there has been significant variability in the supply of mass into Tasman Glacier in recent years, controlled primarily by local synoptic climate conditions (e.g., Purdie et al., 2011b; Chinn et al., 2012). The long response time (hundreds of years) of Tasman Glacier (due its length), and the presence of supraglacial debris–cover (e.g., Kirkbride, 1995b) and the proglacial Tasman Lake (e.g., Kirkbride, 1993; Hochstein et al., 1995; Kirkbride and Warren, 1999; Dykes et al., 2011), meant that fluctuations in terminus position are unrelated to short–term variations in mass balance. However, the contemporary measurements of mass balance at Tasman Glacier do highlight that although the terminus is currently responding to longer term climatic warming (Salinger and Mullen, 1999; Mullen et al., 2010) since the LIA (Kirkbride, 1993; Chinn et al., 2012), short–term fluctuations do have an effect on glacier dynamics in the upper–reaches of the glacier.

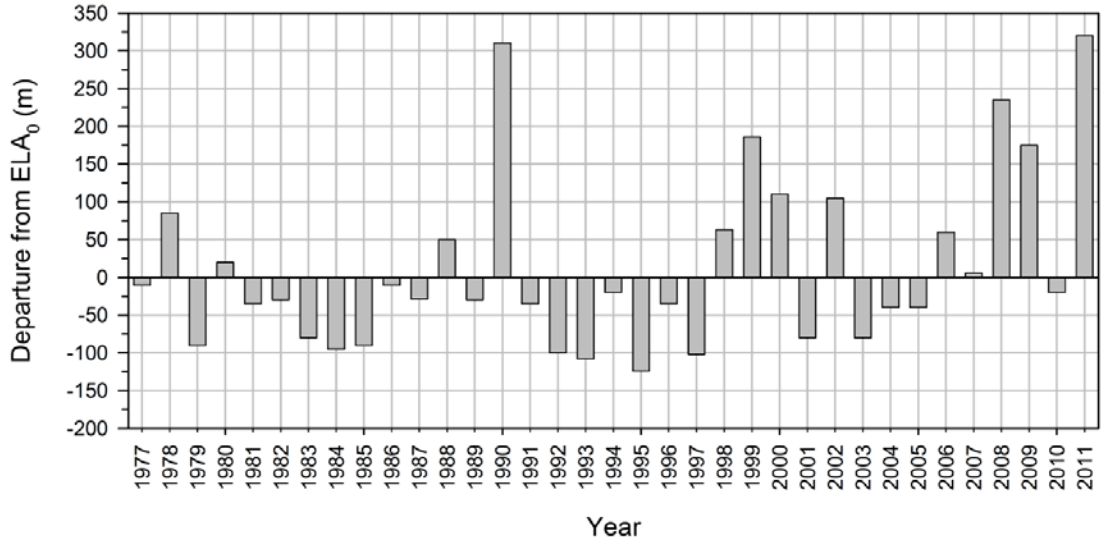

Figure 3.3: Graph showing the deviation of the EOSS away from the mean ELA (ELA_0) of Tasman Glacier between 1977 and 2011. ELA_0 for Tasman Glacier is 1810 m (Willsman et al., 2012).

3.4.2 Debris–cover

Down–valley of the Tasman–Rudolf glacier confluence (Figure 3.2A), a large supraglacial debris–cover has formed from both low–magnitude/high–frequency rock falls and rock avalanches (Kirkbride and Warren, 1999). The debris–cover consists of very poorly sorted, predominantly clast–supported angular boulders of sandstone and argillite sourced from the

surrounding slopes (Kirkbride and Warren, 1999). Lateral spreading after the inflow of the Hochstetter Glacier produces a continuous debris–cover across the glacier that extends along the lower *c.* 10 km of the glacier (Figure 3.2). This thick (*c.* 1 to 2 m) debris–cover has significantly reduced surface melt rates on the lower glacier (Purdie and Fitzharris, 1999) due to a concentration of debris near the glacier terminus (Kirkbride, 1989). Narrow tongues of clean ice have been observed (e.g., Kirkbride, 1993; Kirkbride and Warren, 1999) extending down–glacier (Figure 3.5). However, there has been an increase in the extent of debris–cover since the late 19th century as a result of increased surface ablation (promoting supraglacial melt out) and the slower evacuation of debris from the glacier system due to slower ice velocities (Kirkbride and Warren, 1999). Rock avalanches (Kirkbride and Sugden, 1992; Reznichenko et al., 2011) and the collapse of moraine walls (Blair, 1994) in the late 20th century have also contributed to the more or less continuous debris–cover. The exception to this continuous debris–cover is where gravitational reworking has exposed sections of clean ice (Figure 3.4), promoting localised increased surface melt.

Figure 3.4: Photograph showing exposed sections of clean ice and the debris thickness on the lower terminus of Tasman Glacier. Arrowed boulder is approximately 1 m in diameter.

The presence of this debris–cover over the lower portion of the glacier has meant that retreat from its LIA maximum has not taken place (Kirkbride, 1993) in a similar mode to the clean ice temperate glaciers situated west of the Main Divide (Chinn et al., 2012), such as Fox and Franz Josef glaciers (e.g., Purdie et al., 2008). Constrained by large moraines and outwash gravels deposited during neoglacial stability, Tasman Glacier has downwasted substantially from its LIA position at the end of the 19th century. This is primarily due to greater ablation occurring up–glacier on clean–ice, plus a decrease in the accumulation area of the Tasman névé (Kirkbride and Warren, 1999). Accumulation of snow only occurs above 1600 m (section

3.4.1), exposing up to 70% of the glacier length to predominantly ablation conditions (Anderton, 1975; Hochstein et al., 1995; Chinn et al., 2012). This further reaffirms the disconnection of the terminus of Tasman Glacier from short–term fluctuations in mass balance.

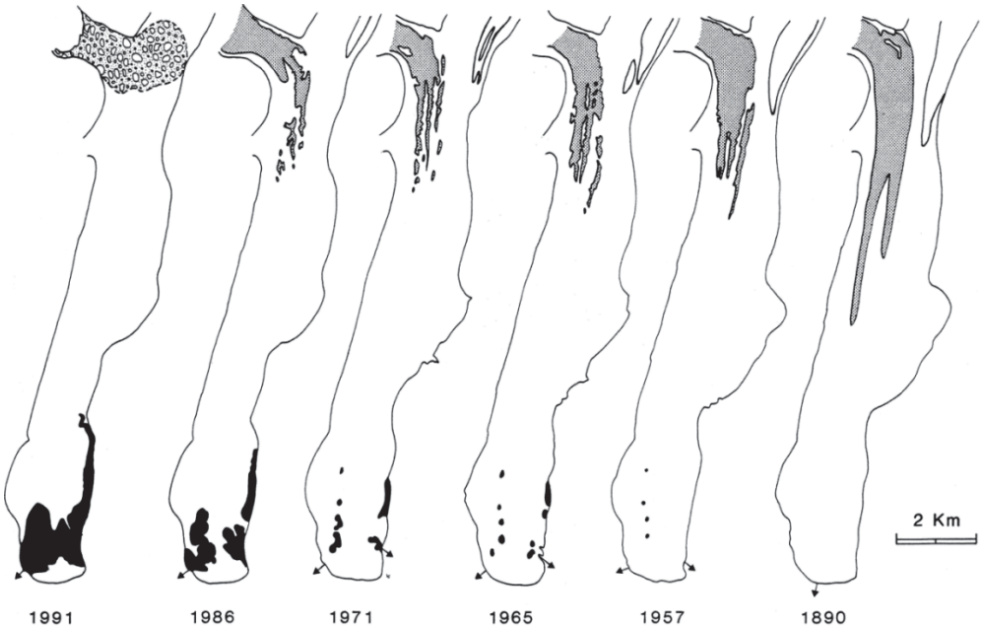

Figure 3.5: The terminus of Tasman Glacier showing the up–glacier extension of the debris–covered area since 1890. The bare–ice area is shaded, lakes are shown in black. The rest of the glacier surface is debris–covered. The 1991 map shows the area of a large rock avalanche deposit which fell on the glacier on 14 December, 1991. Arrows indicate locations of contemporary outwash streams (Kirkbride, 1993).

3.4.3 Ice velocity

The measurement of surface ice velocity at Tasman Glacier has been carried out intermittently since the survey of Broderick (1891) in 1890. Surface ice velocity measurements are difficult to compare directly (Kirkbride, 1995a) as measurements have been carried out at varying spatial and temporal scales (ranging from 3 weeks to multiple years). Kirkbride (1995a) synthesised velocity measurements for the period of 1890 to 1986, documenting a marked decrease in ice velocity since 1890, although variations in surface ice velocity between some of the surveys may represent changes in mass balance within the glacier (Chinn, 1995; Kirkbride and Warren, 1999). This general decrease in ice velocity represents a decrease in ice supply associated with changes in mass accumulation in the upper reaches of Tasman Glacier (Kirkbride and Warren, 1999).

Surface velocity measurements described by Röhl (2005) are consistent with this theory, indicating that surface ice velocity at both Ball Hut and the terminus had increased since the last measurements in the mid–1990s (Ruddell, 1995). In recent years (2000–onwards), velocities on

the lower glacier have continued to vary, with studies reporting velocities that range from 2 to 8 m a^{-1} near the terminus in 2002 (Röhl, 2006), to 20 to 50 m a^{-1} in the vicinity of the terminus calculated from satellite image feature–tracking between 2000 and 2012 (Quincey and Glasser, 2009; Redpath, 2011). Maximum ice velocities in excess of 250 m a^{-1} (Redpath et al., 2013) are commonly recorded throughout the Hochstetter Icefall (flow unit 1 in Figure 3.2) and in the upper Tasman Glacier (flow unit 2 in Figure 3.2), with recorded ice velocity varying throughout the entire glacier from year to year (Redpath, 2011).

The complex interactions between the tributaries of Tasman Glacier (flow units in Figure 3.2) complicate ice velocity measurements. This is evident in the apparent change in ice supply to the Tasman Glacier terminus, indicated by recent studies utilising feature–tracking algorithms (Kääb, 2002; Quincey and Glasser, 2009; Redpath et al., 2013). This data highlights a significant decrease in surface velocities above the Hochstetter Icefall, followed by an increase in velocity below the Hochstetter (Kääb, 2002; Quincey and Glasser, 2009; Redpath et al., 2013). This indicates that a primary source of ice to the terminus of Tasman Glacier is from the Grand Plateau (Figure 3.2) that feeds the Hochstetter icefall (flow unit 1 in Figure 3.2). However, given that ice flowing into the main trunk of Tasman Glacier from the Hochstetter Icefall is deflected down–glacier (south) and is not diverging up–glacier (north) there is still considered to be significant ice supplied from the upper catchment (Redpath et al., 2013). This suggests that although ice flow in the region above the Hochstetter–Tasman confluence is moving considerably slower than adjacent ice it is not stagnant, implying that the upper and lower Tasman are decoupled at this point, as proposed by Quincey and Glasser (2009). As a result, ice at the terminus is likely to still be sourced from the nèvè of Tasman Glacier (flow unit 2 in Figure 3.2), Rudolf Glacier (flow unit 3 in Figure 3.2) and Darwin Glacier (flow unit 3 in Figure 3.2), although not to the same extent as from the Grand Plateau.

3.4.4 Downwasting and lake formation

Downwasting due to melt under debris–cover and decreased ice supply resulted in the surface of Tasman Glacier lowering throughout the early 20th century, rather than terminus retreat due to climate warming (Salinger and Mullen, 1999; Mullen et al., 2010). Between 1890 and 1982 downwasting of the glacier surface occurred at a rate of between 0.85 and 1.2 m a^{-1} (Hochstein et al., 1995). However, Hochstein et al. (1995) argue that this rate might hide an increase in ice flux during the period of 1885–1895 when other New Zealand glaciers advanced. The downwasting rate between 1964 and 1982 is thought to be of the order of 0.85 m a^{-1} and 1.9 m a^{-1} (Hochstein et al., 1995; Chinn et al., 2012). This rate of surface lowering has continued until the present day, with mass loss due to downwasting in the order of 1.1 w.e. km^3 at a rate of *c.*

2.1 m a^{-1} along the lower 10 km of the centre flow line between 1986 and 2007 (Chinn et al., 2012).

During downwasting of the glacier surface small sink–holes developed (Figure 3.6), providing the catalyst for proglacial lake development. Such sink–holes are evident along glacier flowlines on maps of the area produced between 1883 and 1954 (Kirkbride, 1993), expanding over time. Thermokarst processes, including surface collapse and exhumation of englacial conduits, meant that by 1982 the supraglacial lakes were thought to be hydraulically connected at an elevation of 729 m (the same elevation as the Tasman River). The supraglacial lakes increased in diameter through backwasting of intermittently debris–covered walls and thermokarst erosion until 1989, when four large lakes coalesced to form a single shallow lake of irregular shape (Figure 3.5) (Kirkbride, 1993).

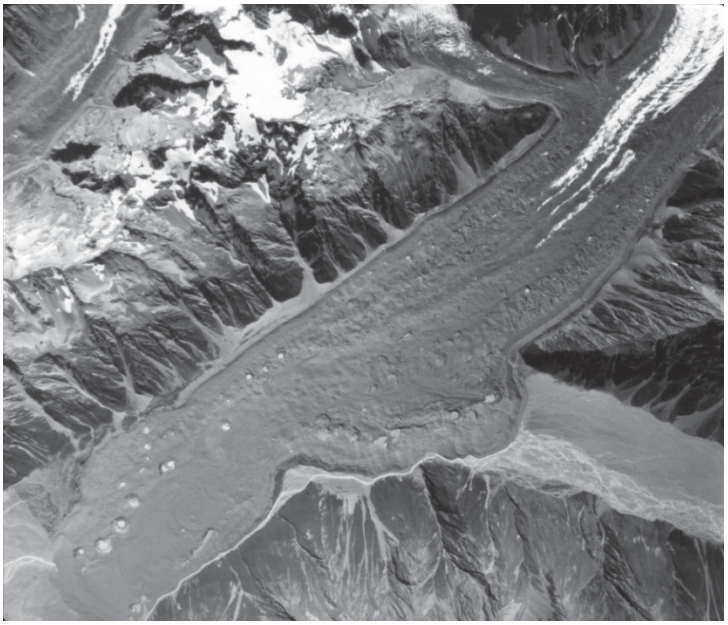

Figure 3.6: Aerial photograph of the Tasman Glacier, 25 February 1964. A number of small supraglacial sink–holes are evident on the lower and true left of the glacier. Also noticeable is a tongue of clean ice sourced from the Hochstetter Glacier on the upper section of the glacier (New Zealand Department of Lands and Survey photo 3724/24).

Retreat of Tasman Glacier up–valley has occurred via a complex combination of iceberg calving and melt of the terminus since the formation of Tasman Lake (Kirkbride and Warren, 1999; Purdie and Fitzharris, 1999; Röhl, 2006), continuing through until the present day (Strong, 2008; Dykes et al., 2011; Redpath, 2011). This retreat has been rapid, although significant temporal and spatial variations have been identified (Kirkbride and Warren, 1999; Dykes et al., 2011). For example, studies of retreat rates of the ice cliff of Tasman Glacier have indicated an increase throughout the 1990s and 2000s from *c.* 30 m a^{-1} (Purdie and Fitzharris,

1999) to 35 to 75 m a^{-1} (Röhl, 2005). This has primarily been the result of waterline melt and notch–driven calving of the subaerial ice cliff (Purdie and Fitzharris, 1999; Röhl, 2006), interspersed with sporadic larger buoyancy–driven calving events (Watson, 1995; Dykes et al., 2011). The frequency and significance of large buoyancy–driven calving events has increased in recent years (post 2006), as the glacier terminus has retreated into deeper water (Dykes et al., 2011).

3.5 Tasman Lake

Downwasting of the Tasman Glacier terminus coupled with the development of an ice–contact adverse slope (outwash head) at the glacier's LIA maximum terminal moraine have provided an effective and persistent dam for meltwater to pool behind (Figure 3.2) (Kirkbride, 1993). Tasman Lake has formed behind this dam, extending further up–valley as a result of glacier retreat. Primarily sourced from subglacial, englacial and supraglacial meltwater, the lake is also affected by precipitation and runoff from the surrounding slopes, iceberg melting, and the inflow of the Murchison River.

Tasman Lake has increased in size as Tasman Glacier continues to retreat up–valley. Conditioned primarily by iceberg calving, its formation has resulted in a rapid increase in surface area and volume since lake inception (Hochstein et al., 1995; Dykes et al., 2011). Bathymetric surveys (Figure 3.7) of the lake have been completed during its formation and development (e.g., Hochstein et al., 1995; Watson, 1995; Röhl, 2005; Dykes et al., 2011). No change in lake bathymetry was detected between the studies of Hochstein et al. (1995) in 1993, and Watson (1995) in 1995. Röhl (2005) suggested that the lake floor within 500 m of the terminal face was largely ice–cored due to its relatively irregular topography (Figure 3.7). The decrease in water–depth within the southern end of Tasman Lake between surveys is caused by increased sedimentation from two sources: (1) the Tasman Glacier and (2) the inflow of the Murchison River (Röhl, 2005; Dykes et al., 2011).

Studies of lake bathymetry at Tasman Lake have often been coupled with studies of its physical properties (limnology) such as temperature and sediment concentration. Such studies, as with lake bathymetry, have often been one–off 'spot' measurements. A range of temperature–depth profiles have been reported by studies conducted on Tasman Lake. Hochstein et al. (1995) reported that in 1993 the lake was almost isothermal with temperatures ranging between 0.3 and 0.5 °C at depths down to 120 m. A repeat study conducted in 1997 by Hochstein et al. (1998) indicated similar results. Watson (1995) identified a different temperature profile for a selection of locations throughout Tasman Lake. Temperatures at the base of his measurements (40 m)

indicated that near the ice cliff, hypolimnion temperature was around −1 °C, increasing to 0.8 °C at the surface. These temperatures were different to those found further from the ice cliff (0.4 °C increasing to 0.8 °C, respectively), and were interpreted as representing the presence of meltwater from subglacial and englacial conduits.

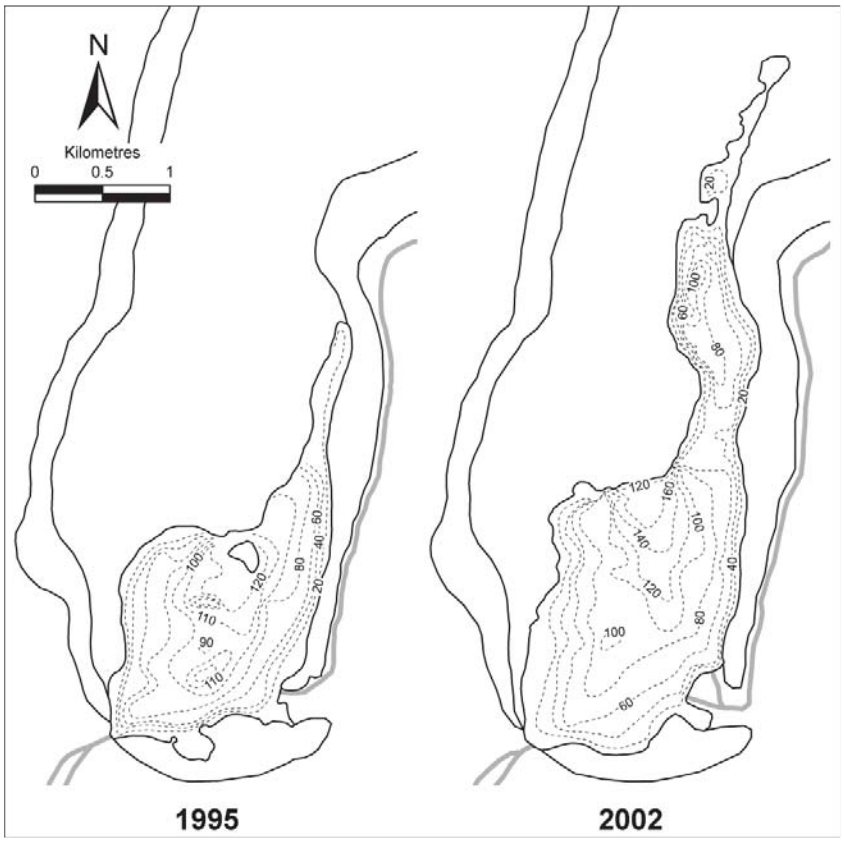

Figure 3.7: Tasman Lake bathymetric change between 1995 (Watson, 1995) and 2002 (Röhl, 2005).

Such temperature variations were not repeated in the study of Röhl (1999), where variations in temperature throughout the water column ranged from 1–3 °C. At the ice cliff, Röhl (1999) found that temperatures were isothermal at 2 °C. A second, year–long study reported by Röhl (2005) from 2000–2001 indicated that large seasonal variations occurred throughout the year. The highest temperatures were recorded during the summer months from November to March where temperatures can reach up to 11 ºC within the first few tens of centimetres, dropping to below 4 ºC within a thermocline of *c.* 0.20 m (Röhl, 2005). An annual mean temperature of 1.49 °C was recorded for the entire lake.

Sediment concentrations have also been measured at Tasman Lake. Watson (1995) identified that suspended sediment concentrations near the ice cliff were about 0.2 g l^{-1} throughout the water column. At locations further from the ice cliff, sediment concentrations increased at the surface (1.5 g l^{-1}) and bottom (2 g l^{-1}), with the intervening area having concentrations as low as

0.2 g l^{-1}. Subsequent work completed by Röhl (1999) found that sediment concentrations were relatively uniform throughout Tasman Lake, with an increase in sediment concentration at depth. At the surface values ranged from 0.13 g l^{-1} to 0.28 g l^{-1}, increasing to between 0.97 g l^{-1} and 1.0 g l^{-1} at a depth of 100 m. Contrasting figures reported by some authors (Watson, 1995; Röhl, 1999) demonstrates the great temporal variability in sedimentation processes acting at Tasman Lake.

3.6 Glaciers of the *Aoraki*/Mount Cook Region

Apart from Tasman Glacier, there are a number of other glaciers within the *Aoraki*/Mount Cook National Park that terminate into proglacial water–bodies. The Hooker, Mueller, Grey, Maud, Godley, Classen and Murchison glaciers represent the most notable examples (Figure 3.1). All proglacial lakes of the *Aoraki*/Mount Cook National Park have formed through a similar process to Tasman Glacier (Röhl, 2005; Robertson, 2012). The Hooker Glacier has received the bulk of research conducted away from Tasman Glacier, with the Mueller, Murchison, Grey, Maud, Godley and Classen Glaciers having received less attention (e.g., Kirkbride, 1993; Watson, 1995; Warren and Kirkbride, 1998; Röhl, 2005; Robertson, 2012; Robertson et al., 2012).

3.6.1 Hooker Glacier

The Hooker Glacier has responded in a similar pattern to the Tasman Glacier with downwasting under debris–covered ice taking place since the late 19th century (Hochstein et al., 1998; Robertson et al., 2013). Hochstein et al. (1998) reported that between 1915 and 1964 downwasting at the terminus occurred at a rate of 0.7 m a^{-1}, increasing to 1.0 m a^{-1} between 1964 and 1986. Downwasting eventually led to proglacial lake formation in the late 1980s, with initial retreat occurring at a rate of 70 m a^{-1} (Warren and Kirkbride, 1998). Subsequently, retreat has slowed, with a mean retreat rate of 43 m a^{-1} recorded between 2000 and 2011 (Robertson et al., 2013). Hooker Lake has increased in size since 1990 (Röhl, 2005) to 1.22 km^2 in 2011 (Robertson et al., 2013), due to the up–valley retreat of Hooker Glacier. Recent bathymetric mapping of Hooker Lake conducted by Robertson et al. (2013) indicated a maximum depth of 130 m, with a more or less uniform U–shaped cross–section (Röhl, 2005). At the terminus, a subaqueous ice 'foot' has been found to be projecting into the lake (Robertson et al., 2012).

3.6.2 Mueller Glacier

Mueller Glacier has also followed a progression of downwasting, pond growth and lake formation similar to that of other glaciers of the *Aoraki*/Mount Cook National Park. It has a low gradient (*c.* 3.7º) and has downwasted at a rate of *c.* 0.5 m a^{-1} since the early 20th century

(Watson, 1995; Röhl, 2005). The low surface gradient, coupled with downwasting, led to the formation and coalescence of supraglacial ponds throughout the 1980s, with the resulting lake having an area of *c.* 0.35 km^2 by 1994 (Watson, 1995). Lake area increased to 0.97 km^2 by 2011, with up–glacier retreat increasing from *c.* 15 to 38 m a^{-1} between 1986 and 2008 to 157 m a^{-1} between 2009 and 2010 (Robertson, 2012). Throughout this period (1986 to 2011), Mueller Lake had a more irregular lake shoreline and bathymetry than either the Tasman Lake or the Hooker Lake (Röhl, 2005; Robertson et al., 2013). The maximum depth of 31 m identified by Röhl (2005) indicated that the Mueller Lake is ice–cored, as the Mueller Glacier is *c.* 120–180 m thick (Watson, 1995). This is confirmed by the recent study of lake bathymetry and subaqueous morphology by Robertson et al. (2012) which suggested an extensive area of the lake was underlain by ice (Robertson, 2012). Furthermore, subaqueous calving events are not uncommon within Mueller Glacier's proglacial Lake (Röhl, 2005; Robertson, 2012). By 2011, the maximum depth within Mueller Lake was *c.* 83 m (Robertson et al., 2012).

3.6.3 Murchison Glacier

Murchison Glacier (Figure 3.1), like Mueller Glacier, has only recently developed a proglacial lake at its terminus. Downwasting of the glacier surface between 1900 and 1982 has taken place at a rate of between *c.* 0.7 to 1.7 m a^{-1}, with this accelerating to 2.5 m a^{-1} between 1986 to 2007 (Gellatly, 1985; Chinn et al., 2012). Supraglacial ponds that had formed through the late 20^{th} century expanded to form several large lakes that coalesced in 2001 (Röhl, 2005). After the formation of a single large lake, retreat of the glacier doubled to *c.* 46 m a^{-1}, resulting in lake growth to 1.85 km^2 by 2010 (Robertson, 2012). Within the lower glacier, ice flow is dominated by tributaries entering the main ice body, with divergent ice flow up– and down–glacier at confluences indicating stagnation within the main trunk of the Murchison (Redpath, 2011; Redpath et al., 2012). A number of smaller ponds are also present further up–glacier (Röhl, 2005). Murchison Lake also has an irregular planform, suggesting that large sections of it may be ice cored, similar to Mueller Lake.

3.6.4 Godley Valley glaciers

The Grey, Maud, Godley and Classen Glaciers all reside at the head of the Godley Valley (Figure 3.1) and represent the second main area of proglacial lake formation in the *Aoraki*/Mount Cook National Park. Lying immediately east of the Main Divide, adjacent to Murchison Valley, research conducted on the glaciers of the Godley Valley has not been as extensive as that of Tasman Glacier. No recent studies of lake bathymetry or physical properties have been conducted since the mid–1990s for the Godley Valley glaciers (Warren and

Kirkbride, 1998), with only remote sensing of the lake area having being undertaken (e.g., Röhl, 2005; Robertson, 2012).

Up until 1917 the Grey, Maud and Godley glaciers were confluent, but since the 1960s retreat of the Godley Glacier has resulted in the separation of the Godley Glacier from the Grey and Maud Glaciers. Proglacial lakes have formed at the terminus of each of the Godley–Ruth, Classen, and Grey–Maud Glaciers (Figure 3.1). Significant fluctuations in the termini of these glaciers have been identified (Warren and Kirkbride, 2003), with periods of rapid retreat and slow advances indicated by the use of remotely sensed data (Röhl, 2005; Robertson, 2012). Currently, it appears that retreat of the glaciers at the head of the Godley Valley has slowed in recent years (Warren and Kirkbride, 2003; Robertson, 2012), with the terminus of the Classen Glacier remaining stable throughout the past decade (Röhl, 2005; Robertson, 2012).

3.7 Summary and conclusions

In summary, this chapter has discussed historical and contemporary work conducted at Tasman Glacier and the surrounding glaciers of the *Aoraki*/Mount Cook National Park throughout the last century. The *Aoraki*/Mount Cook National Park's geographic and geological setting, glacier terminus characteristics and Tasman Lake evolution have also been discussed. Key findings to emerge from this analysis are:

- The Tasman Glacier is New Zealand's largest glacier, and as such has received the largest proportion of research of all New Zealand glaciers.
- Intermittent surveys have been carried out on the Tasman Glacier terminus since von Haast (1862) and von Lendenfeld (1890), showing that the glacier has significantly down–wasted over the past century.
- In general, ice velocity decreases markedly down–glacier along the centre–line, with significant decreases in ice velocity taking place since 1890.
- Contemporary ice supply to the terminus of the Tasman Glacier is sourced primarily from the Hochstetter Glacier.
- Debris–cover situated on the lower Tasman Glacier has significantly affected ablation of the lower terminus, resulting in downwasting of the lower glacier tongue instead of retreat prior to the development of Tasman Lake.
- Thermokarst development on the surface of the glacier has resulted in the formation of the Tasman Lake as supraglacial lakes have become hydraulically connected, coalescing to form one large lake.
- Since the formation of Tasman Lake, Tasman Glacier has rapidly retreated up–glacier due to a complex interaction between melt and calving.

- Tasman Lake has rapidly increased in size as a result of the calving retreat of Tasman Glacier.
- Studies of lake bathymetry and lake physical properties have produced variable results.
- The Tasman Glacier is one of a number of glaciers terminating into proglacial lakes within the *Aoraki*/Mount Cook National Park, with all lakes appearing to represent separate points along a continuum of lake evolution.

Given the rapid retreat that Tasman Glacier is currently undergoing, further research is necessary in order to document the continued response to calving as this represent a key control on glacier mass balance. Specifically, research should attempt to identify the controls of iceberg calving at varying temporal scales (e.g., decadal, seasonal, diurnal) so that the effect of calving on other freshwater–terminating glaciers can be fully understood. To address this the following chapters are structured to examine the impact and processes of calving at Tasman Glacier at multi–annular (chapter 4), sub–annual (chapters 5 and 6), and intra–calving event (chapters 7 and 8) scales.

Chapter 4: The calving retreat of Tasman Glacier

4.1 Introduction

Chapter 2 introduced and reviewed key concepts relating to the controls of mass balance for debris–covered and water–terminating glaciers alike, with specific emphasis centred on the development of a proglacial water–body through downwasting of debris–covered glacier surface and the controls of iceberg calving and the key processes involved. As has been described in chapter 3, downwasting and iceberg calving have played particularly important roles in the evolution and retreat of Tasman Glacier throughout the 20th and 21st century. Following on from chapters 2 and 3, this chapter seeks to quantify the extent of the retreat of Tasman Glacier between the inception of Tasman Lake and 2013. Particular focus will be given to the extent that iceberg calving has conditioned the historical (prior to 2000) and contemporary (2000 to 2013) ice loss and retreat.

The current retreat of Tasman Glacier, and expansion of Tasman Lake, provides an excellent opportunity to observe the spatial and temporal variability of calving over a decade of study to advance understanding of freshwater (lacustrine) calving. The objective of this chapter is to quantitatively describe the retreat of Tasman Glacier and the impact that buoyancy–driven–calving events have had on retreat between 2000 and 2013, using spatial analyses of multispectral satellite images, combined with direct observational data sets (such as oblique photographs of the terminus). This will be compared with the historical evolution of the terminus of Tasman Glacier since the formation of Tasman Lake to highlight the contrasting processes that have dominated calving and retreat. Together, these data sets will show that the retreat of Tasman Glacier between 2000 and 2013 has been significant compared to historical records and largely nonlinear, with both high–magnitude (relative to the size of the glacier) and low frequency calving influencing long term retreat.

4.2 Methods

4.2.1 Terminus and lake mapping

Terminus position, surface area, and geometry for Tasman Glacier and surface area of Tasman Lake for the years 2000–2013 were determined by digitisation, via ArcGIS®, of georeferenced multispectral ASTER (Advanced Spaceborne Thermal Emission and Reflection) satellite imagery, in combination with several oblique photographs of the terminus region. The photographs were taken from atop the western lateral moraine that flanks Tasman Glacier (Figure 4.4). ASTER imagery were orthorectified and displayed as false–colour images of the Near InfraRed (NIR) bands to facilitate spectral differences between the debris–covered terminus of Tasman Glacier and Tasman Lake in their distinction. Annual temporal spacing of ASTER images was used to highlight the long term trends in the changes in terminus and lake geometry and remove any seasonal signals. NIR multispectral bands of ASTER imagery have a pixel resolution of 15 m, allowed for the digitisation of the terminus region to within an accuracy of ± 1 pixel. As such, estimates of the maximum and minimum areas of digitised features comprise a buffer of ± 15 m. This method does not provide traditional confidence intervals, but provides an upper and lower bound estimate of the risk that feature outlines have been misidentified by ± 1 pixel (Strong, 2008).

Over the study period, retreat of the glacier did not occur in a linear fashion. To quantify the kinematic and geometric characteristics of this process, a number of area and length scales describing the glacier–lake system were investigated: Data of time–variant changes in glacier area, A_G (t), and lake surface area, A_L (t), were calculated along with changes in terminus length (or perimeter), T_L (t), in contact with Tasman Lake. Lake areas and volume prior to the period 2000–2013 were retrieved from previous studies (Kirkbride, 1989; Hochstein et al., 1995; Watson, 1995; Strong, 2008). Terminus retreat was determined by measuring the perpendicular distance between termini positions, L_n (t), evenly spaced across the lake at n–intervals, 50 m apart. Positive values were taken as terminus retreat, with negative values representing terminus advance. The velocity (or rate) of retreat $u_n = \Delta L_n/\Delta t$ was determined for every pair of ASTER images with difference in image acquisition time Δt. The locus of maximum retreat $u_{max} = \Delta L_{max}/\Delta t$ as well as its lateral shift over time can then be quantified and compared with the width–averaged retreat rate $u_{ave} = \Delta L_{ave}/\Delta t$, where L_{ave} is the arithmetic mean of L_n. Surface area data allows depiction of general trends of the large–scale retreat changes while time–series data of the linear length changes and retreat can be used to quantify the detailed spatial variability.

4.2.2 Bathymetry

Water depths for Tasman Lake were measured in April 2008 using a Humminbird 323 DualBeam Plus dual frequency echo–sounder coupled with a hand–held GPS unit. Accuracy of water–depth (z) measurements are typically ± 6 m, and point position (x, y) accuracy for the GPS unit is known to be ± 5 m. Because of congestion of icebergs at the southern end of the lake, shore–to–shore transects were not always possible, with spot measurements taken in all open–water areas. A digital elevation model and isobaths for the lake floor were then computed using triangulated irregular network (TIN) modeling in ArcGIS®.

4.3 Results

4.3.1 Spatio–temporal changes of Tasman Glacier: 2000–2013

Between 2000 and 2013 Tasman Glacier retreated *c.* 2.5 km and lost 3.51 km^2 of surface area from the lower terminus (Table 4.1 and Figure 4.1). The distribution of ice loss across the lower glacier throughout the entire study period is shown in Figure 4.1, highlighting the complex nature of retreat. Although spatially extensive, ice loss is centralised predominantly on the lower section of the terminus, both in terms of retreat and the expansion of supraglacial ponds. In comparison, minimal ice loss occurs from the northern–most section of the ice cliff within the embayment formed on the glacier's eastern margin. The net retreat over the study period is dominated by a large–scale disintegration of the lower terminus that occurred between January 2006 and April 2007. This resulted in the loss of 1.47 km^2 and in the retreat of up to (L_{max}) 1.8 km within a single year. Significant differences in retreat and surface area changes are evident prior to, and post, this disintegration of the terminus (Figure 4.1).

Between 2000 and 2006, annual area changes of the terminus of Tasman Glacier are remarkably constant with ice loss ranging from 0.10 to 0.35 km^2 a^{-1}. Similarly, until 2005 longitudinal retreat rates (u_{ave}) vary little, around an average of 46 m a^{-1}. However, the maximum retreat of the entire terminus in this period of 103 m a^{-1} was recorded between September 2005 and January 2006. This was also accompanied by a minor increase in the loss of surface area of the terminus. Notably, this increase relates not only to ice loss, but also to the capturing of several supraglacial ponds near the southern–most margin of the terminus (Figure 4.1). Excluding this period yields a maximum mean retreat of 60 m a^{-1} between April 2000 and 2001.

The disintegration of the lower terminus between January 2006 and April 2007 evident in Figure 4.1D had a significant effect on retreat. It contributes the single largest loss of ice and retreat recorded throughout the study period (Figure 4.1 and Table 4.1). Evidence will be presented in section 4.3.3 suggesting that this event may also constitute the fastest lateral ice

loss in more than 50 years at Tasman Glacier. Prior to this event, the growth of supraglacial ponds from 2000 to 2006 resulted in an increase in pond size from 0.13 km^2 to 0.46 km^2 (Figure 4.1A–C). The significant pond growth on the lower terminus appears to have altered glacier dynamics by driving the system towards disequilibrium. The disintegration of the lower terminus appears to demarcate a change in the retreat of Tasman Glacier, with a stark decrease in glacier area (Figure 4.1 and Table 4.1) by 1.47 km^2 and a dramatic shortening of the terminus length by approximately a third (2.51 km; Table 4.1).

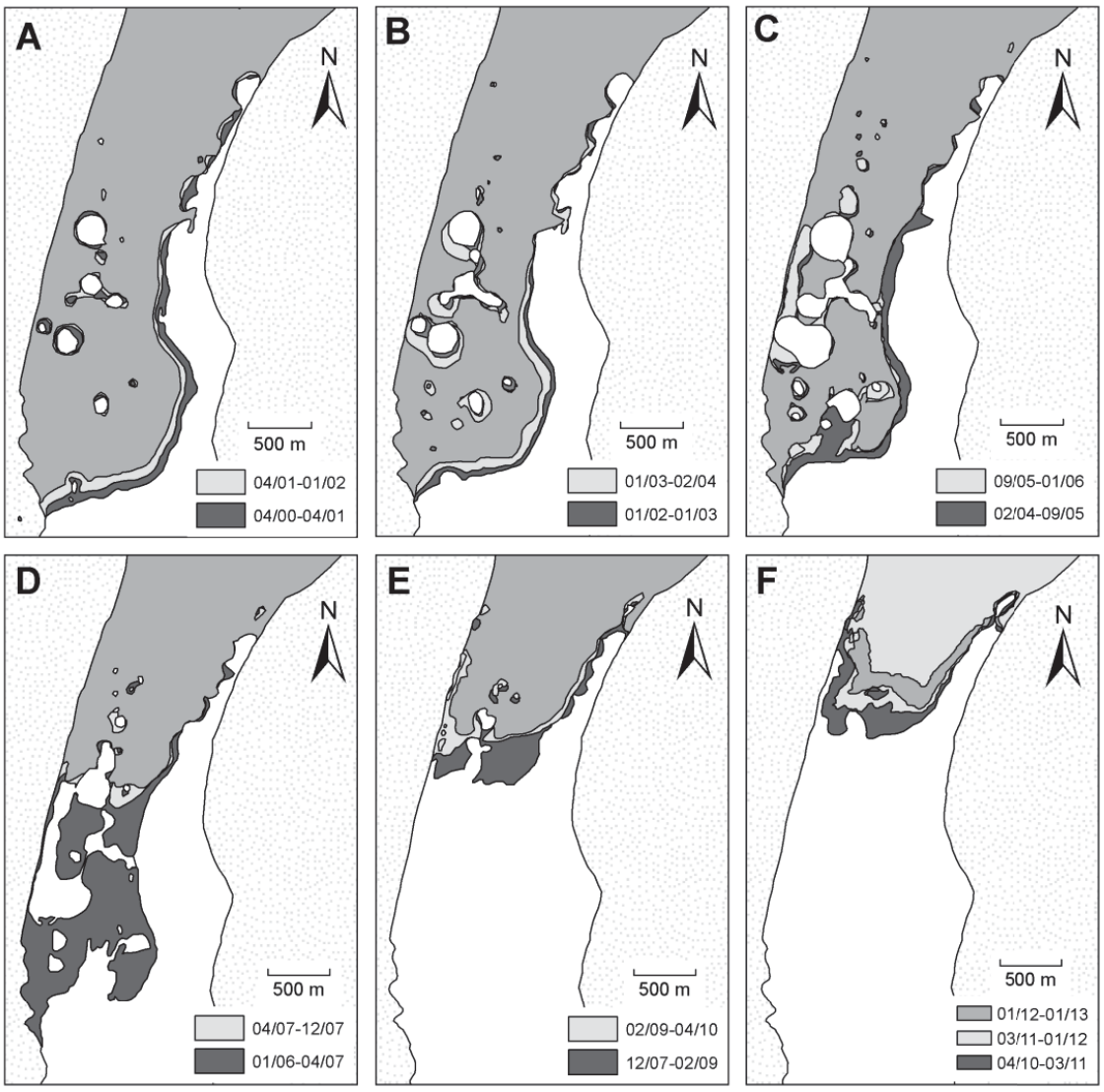

Figure 4.1: Spatial changes of Tasman Glacier between 2000 and the end of 2012 digitised from ASTER imagery. Each panel describes the plan form change of the glacier between three image dates with the final image reproduced as the base image in the following sequence. White indicates Tasman Lake and supraglacial ponds when evident on the surface of the glacier at the start of each image period. Dates reported as month/year. See Table 4.1 for date and area information.

Table 4.1: Summary of changes in glacier area, terminus retreat, terminus length and supraglacial pond area for Tasman Glacier between 2000 and 2013 based off ASTER satellite imagery. Glacier area includes supraglacial ponds that were present at the time of image capture.

Date	t	A_G	ΔA_G	$\Delta A_G/t$	T_L	L_{max}	L_{ave}	u_{ave}	u_{max}	A_S
	d	km^2	km^2	km^2 a^{-1}	km	m	m	m a^{-1}	m a^{-1}	km^2
30/04/00	-	0.00	-	-	4.97	-	-	-	-	0.13 ± 0.07
08/04/01	343	-0.21 ± 0.29	-0.21	-0.22	5.10	205	56 ± 27	60	218	0.15 ± 0.10
30/01/02	297	-0.37 ± 0.30	-0.16	-0.20	5.29	85	40 ± 27	49	105	0.21 ± 0.09
01/01/03	336	-0.46 ± 0.32	-0.09	-0.10	5.30	66	21 ± 26	23	72	0.24 ± 0.12
05/02/04	400	-0.64 ± 0.31	-0.18	-0.16	4.71	102	50 ± 25	46	93	0.39 ± 0.11
10/09/05	583	-0.90 ± 0.39	-0.26	-0.17	6.48	535	80 ± 96	50	335	0.51 ± 0.25
25/01/06	137	-1.03 ± 0.38	-0.13	-0.35	6.66	109	39 ± 34	103	290	0.46 ± 0.20
09/04/07	439	-2.51 ± 0.20	-1.47	-1.22	4.11	1847	478 ± 633	398	1536	0.03 ±0.04
07/12/07	242	-2.56 ± 0.18	-0.06	-0.09	3.49	185	37 ± 60	56	280	0.03 ±0.03
18/02/09	439	-2.83 ± 0.19	-0.26	-0.22	2.91	377	140 ± 122	116	314	0.04 ±0.07
10/04/10	416	-2.98 ± 0.17	-0.15	-0.13	3.24	319	65 ± 72	57	280	0.02 ± 0.03
03/02/11	327	-3.18 ± 0.16	-0.20	-0.22	3.88	287	94 ± 68	105	320	0.05 ±0.07
01/01/12	304	-3.31 ± 0.15	-0.14	-0.16	3.54	165	62 ± 47	75	199	0.02 ± 0.03
01/01/13	366	-3.51 ± 0.14	-0.20	-0.20	3.29	189	81 ± 32	81	188	0.01 ± 0.01
2000-2006	2096	-	-1.36	0.20	-	-	287	50	-	-
2006-2013	2533	-	-2.01	0.36	-	-	957	138	-	-
Total	4629	-	-3.51	0.28	-	-	1244	98	-	-

Note: t is the number of days between the current and previous imagery date; A_G, is the net area change referenced to the first image; ΔA_G is change in area between the current and previous imagery date; ΔA_G a^{-1}, is annual change in glacier area between image date; T_L, is length of terminus in contact with Tasman lake; L_{ave} and L_{max}, is mean and maximum retreat of the terminus between image dates; u_{ave} and u_{max}, are annual averaged and annual maximum retreat rates, respectively; and A_S, is the area of supraglacial ponds on the lower terminus.

Following this period of strongly time–variant terminus changes, glacier surface area between 2007 and 2013 continued to return to similarly constant rates of ice loss found prior to 2006. This quasi–uniform period of retreat masks increased spatial variability and up–glacier retreat between 2007 and 2013, shown in Figure 4.1 and Figure 4.2. Ice loss over this period (2007–2013) is localised over a shorter ice cliff than retreat prior to 2006, giving rise to increased rates of linear retreat (L_{ave}). The increase in retreat velocity (u_{ave}) between 2007 and 2012 highlights an important spatial aspect of retreat changes: while bulk area change rates are comparable to pre–2006 retreat, these rate changes occur over a much smaller proportion of the glacier front. In other words, retreat changes become focussed in certain areas while the remainder of the terminus remains relatively stable. For example, between January and December 2002 the surface area of Tasman Glacier decreased by 0.16 km^2 a^{-1} localised along the irregular 5.29 km ice cliff (Figure 4.1). Similar loss of surface area (0.15 km^2 a^{-1}) occurred between 2009 and 2010. However, this took place along a perimeter of ice cliff of 2.91 km. The result of this was a u_{ave} of 23 m a^{-1} and u_{max} of 72 m a^{-1} compared to a u_{ave} of 65 m a^{-1} and u_{max} of 280 m a^{-1} respectively over the two study periods. This illustrates that the rate of retreat has increased as these changes are distributed over a smaller area, but the amount of surface area lost between 2007 and 2012 is not significantly higher than during previous periods (pre–2006). This highlights the importance of describing not only changes in surface area of the glacier, but also local retreat to gauge the linear and spatial extent of ice loss at an irregular terminus.

Furthermore, the retreat of Tasman Glacier and the development of several supraglacial ponds on the western margin of the glacier has led to a change in the terminus geometry between 2007 and 2012 (Figure 4.1E–F). As a result of this pooling of water on the western margin, a second embayment has developed, similar to the eastern embayment present throughout the entire study period. The effect of these embayments has been the formation of an ice cliff at Tasman with three distinct orientations: east, west and south. During the latest period of retreat post–2007, variations in the position of the terminus within embayments on the margins of Tasman Glacier have differed considerably from the south–facing ice cliff. Indeed, the terminus within the eastern embayment remained relatively stable over the study period, apart from noticeable retreat between 2010 and 2011 (Figure 4.1F). The western embayment, formed during late 2009, has somewhat mirrored the eastern embayment formation. However, the calving of peninsulas developed along the southern section of the terminus is significantly greater than that found along the eastern and western margins.

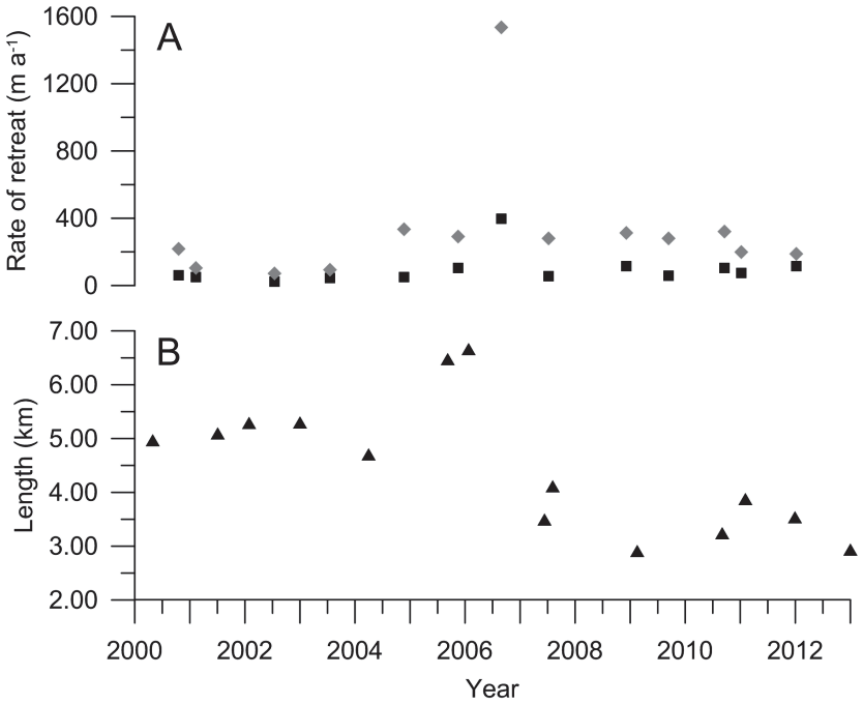

Figure 4.2: (A) Retreat rates (black squares are u_{ave} and gray diamonds are u_{max}) and (B) changes in terminus length (T_L) of Tasman Glacier between 2000 and 2013. Retreat rates highlight the variability of glacier retreat over the study period and the sharp increase in retreat between 2006 and 2007. The dramatic the shortening of the terminus in contact with Tasman Lake in 2007 indicates that retreat of the glacier is being centred over a smaller area. See Table 4.1 for values.

A secondary effect of the development of the western embayment has been the effective isolation of the central section of the terminus. This may have contributed to changes in the dynamics of the terminus in conjunction with the development of supraglacial ponds along the centre of the terminus between 2007 and 2010. The net result of this process has been the irregular and largely unsteady retreat of the terminus compared to the relatively perpendicular retreat of the terminus found between 2000 and 2004 (Figure 4.1A–B). Post–2010 no supraglacial ponds were evident in the terminus region, indicating that the entire lower *c.* 800 m of the terminus becomes one large peninsula. Calving and retreat of the ice cliffs within the western and eastern embayments (Figure 4.1) effectively isolated the entire terminus and drove it into disequilibrium. This is in contrast to the calving of relatively smaller sections and peninsulas that took place between 2007 and 2011.

4.3.2 Lake area

Between 2000 and 2012 lake area increased from 3.14 km^2 to 6.62 km^2 at an annual rate of 0.29 km^2 a^{-1} (Table 4.1). The rapid increase in lake surface area during the current study period (2000 to 2013) occurred predominantly in parallel with the retreat of Tasman Glacier (Figure 4.1). The only exception is the expansion of the lake into the area of ice that detached from the main glacier flow on the western margin of Tasman Lake in 2008 (Figure 4.4). This expansion into

areas of stagnant 'dead' ice (Quincey and Glasser, 2009) and the minor collapse of bounding moraine walls continued to have a minor effect on lake area throughout the study period. However, this expansion is at least an order of magnitude smaller than lake growth associated with the retreat of Tasman Glacier (Figure 4.1). This also means that the long–term dynamics of retreat can be inferred from the extensive record of lake area data at Tasman (1957–2013), although precise glacier area data only exist from 2000–onwards (Figure 4.3).

Table 4.2: Changes in the surface area and volume of Tasman Lake since its inception. Area and volume information between 2000 and 2013 are from this study, with data prior to 2000 retrieved from previous studies.

Date	t	A_L	ΔA_L	$\Delta A_L/t$	V	*Source*
	d	km^2	km^2	$km^2\ a^{-1}$	km^3	
01/01/1957		0.01	-	-	-	Kirkbride (1989)
02/25/1964	2611	0.06	0.05	0.01	-	Kirkbride (1989)
09/01/1975	4206	0.08	0.02	0.00	-	Hochstein et al. (1995)
01/01/1982	2314	0.56	0.48	0.08	0.11	Hochstein et al. (1995)
02/01/1986	1492	1.07	0.51	0.12	-	Kirkbride (1989)
30/12/1990	1793	1.68	0.61	0.12	-	Strong (2008)
04/30/1993	852	1.95	0.27	0.12	0.125	Hochstein et al. (1995)
02/01/1995	642	2.35	0.40	0.23	0.133	Watson (1995)
30/04/2000	1914	3.14 ± 0.20	0.79	0.15	-	*this study*
08/04/2001	343	3.35 ± 0.21	0.21	0.22	-	*this study*
30/01/2002	297	3.52 ± 0.21	0.17	0.21	-	*this study*
01/01/2003	336	3.62 ± 0.21	0.11	0.12	-	*this study*
05/02/2004	400	3.82 ± 0.20	0.20	0.18	-	*this study*
10/09/2005	583	4.12 ± 0.23	0.31	0.19	-	*this study*
25/01/2006	137	4.27 ± 0.33	0.14	0.38	-	*this study*
09/04/2007	439	5.58 ± 0.23	1.31	1.09	-	*this study*
07/12/2007	242	5.62 ± 0.22	0.04	0.06	-	*this study*
13/05/2008	-	-	-	-	0.510	*this study*
18/02/2009	439	5.99 ± 0.22	0.37	0.31	-	*this study*
10/04/2010	416	6.15 ± 0.24	0.16	0.14	-	*this study*
03/03/2011	327	6.52 ± 0.16	0.37	0.41	-	*this study*
01/01/2012	304	6.56 ± 0.25	0.04	0.05	-	*this study*
01/01/2013	366	6.62 ± 0.14	0.05	0.12		*this study*
1957-1990	10623	-	1.67	0.05	-	-
1990-2006	7287	-	2.59	0.17	-	-
2006-2013	2533	-	2.53	0.36		-
Total 1957-2012	20453	-	6.79	0.12	-	-

Note: t is the number of days between the current and previous imagery date; A, is lake area; ΔA is change in area between the current and previous date; $\Delta A\ a^{-1}$ is annual change in glacier area between image date. V is lake volume.

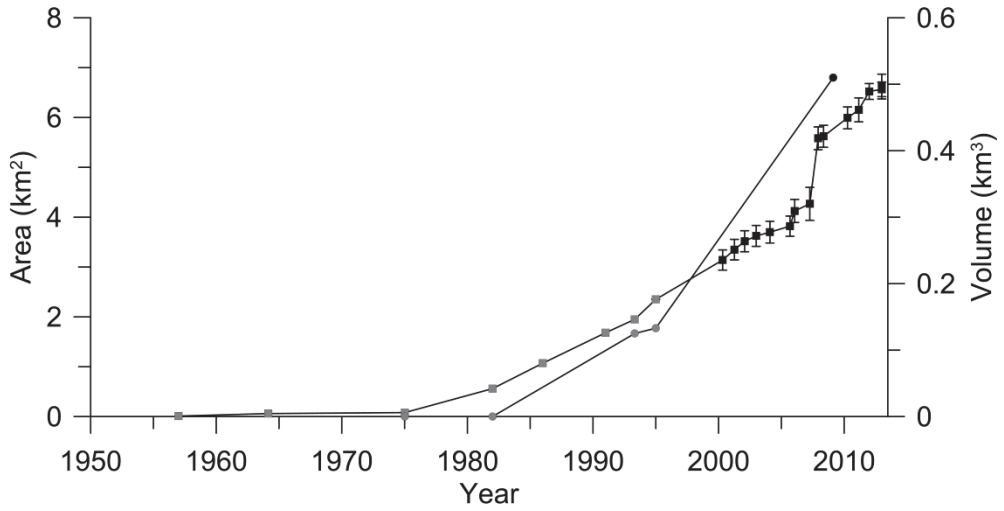

Figure 4.3: Lake area (squares) and volume (circles) for Tasman Lake since its initial formation in the late 1950s. Grey squares and circles are area and volume information from previous studies. See Table 4.2 for explanation of sources.

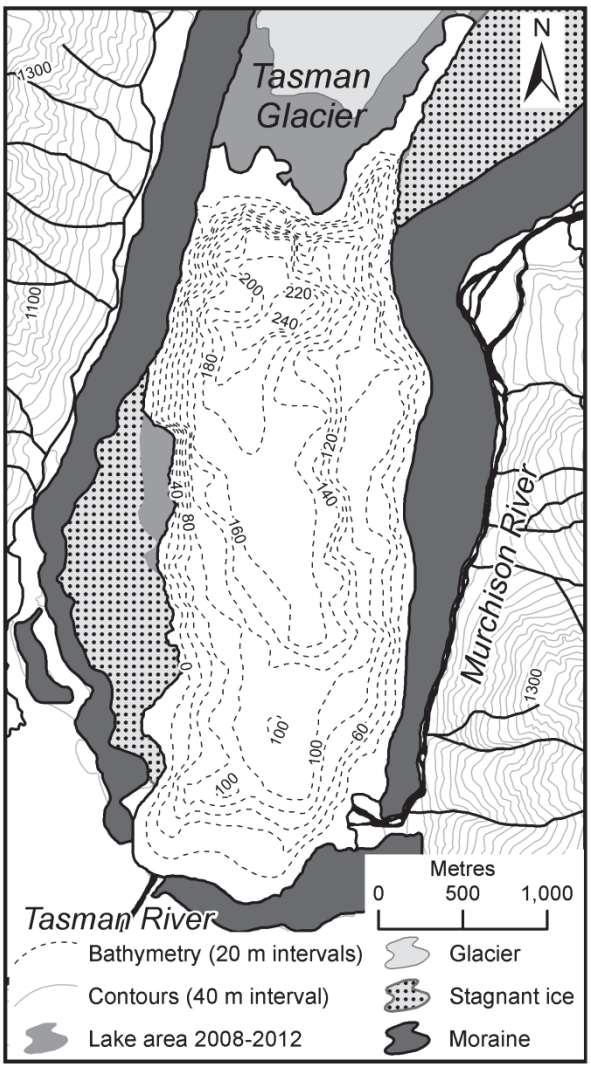

Figure 4.4: Bathymetry of Tasman Lake in 2008. The change in surface area of Tasman Lake between 2008 and 2013 is also shown.

4.3.3 Tasman Glacier: 1957–2012

To better understand the spatio–temporal changes in glacier retreat rates during the 2000–2013 study period, it is worthwhile to view them in the broader context of glacier retreat since the formation of Tasman Lake in the mid–20th century. The net change in surface area of Tasman Lake for the last 5–6 decades (1957–2012) is depicted in Figure 4.3 and Figure 4.5, and summarized in Table 4.2, with annual and net changes between 2000 and 2013 shown in Table 4.1 and Figure 4.1. There are three main phases of strongly contrasting behavior: (1) during the first 18 years after pond formation and lake inception glacier retreat (or lake area increase) advanced less than 0.01 km^2 at area change rates one or two orders of magnitude smaller than at any other time (Table 4.2 and Figure 4.5). (2) A strong and accelerating increase in glacier retreat rate occurred over the next 31 years from 1975 to 2006. The current phase (3) between 2007 through to the present comprises the largest maximum retreat. This exceeded 1 km^2 a^{-1} during the beginning of this period, and is characterized by strongly time–variant rate changes thereafter (Figure 4.5).

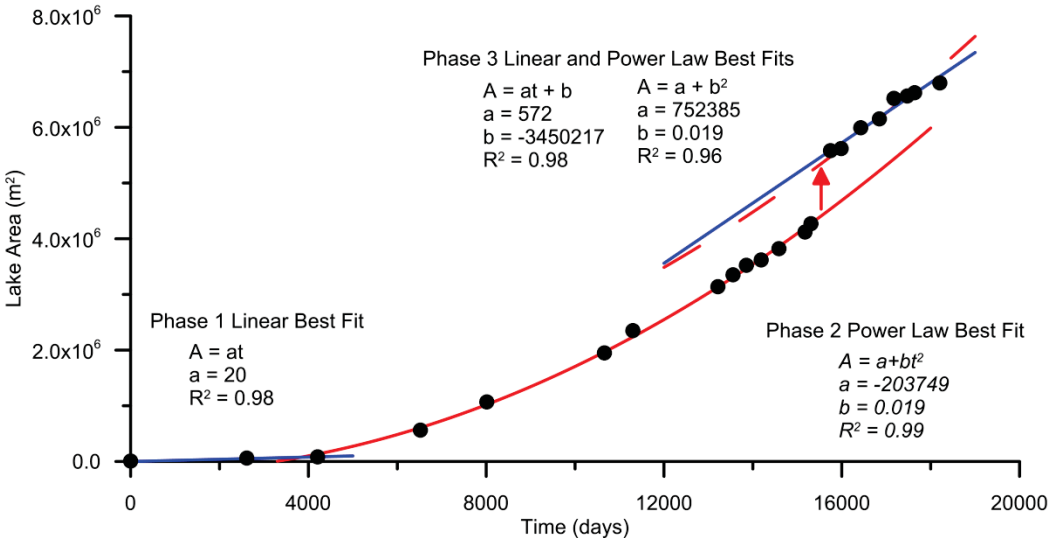

Figure 4.5: Graph of the increase in surface area of Tasman Lake between 1957 (time zero on x–axis) and 2012, showing the three phases of retreat. Also shown are the best fit linear and power–law functions for the three phases discussed in the text. The red arrow indicates the large shift in lake area that occurred between 2006 and 2007.

To understand glacier retreat in freshwater–terminating settings, phases (2) and (3) as well as the relatively sudden transition (relative to the long–term evolution of Tasman Lake) between them in 2006–2007, become very important. Intriguingly, data of area vs. time for the 31 year long phase (2) can be almost perfectly fitted by power–law regression functions of the form:

$$A(t) = a + bt^n \tag{4.1}$$

where a and b are regression coefficients and exponents n with values of 1.2 to 2.1 yield very good regressions ($R^2 > 0.97$). Indeed, power–law regressions with an exponent n = 2 yield regression coefficients $R^2 > 0.99$, indicating that retreat during phase (2) is well described by a constant acceleration of 38 000 m^2 a^{-2}. The same power–law also closely describes glacier retreat post–2007, as well as the large–scale terminus disintegration of 2006–2007. Annular variations are slightly more scattered around this function of constant acceleration than they are prior to 2006, as indicated in the increased unsteadiness inferred from retreat velocity data. However, the data set is still slightly too short to infer whether the 2006–2007 event will continue to have an effect on glacier margin equilibrium.

The ability to describe accelerating lake growth (or glacier retreat) for almost four decades by a single functional form of the area against time has important implications. It suggests that the large–scale disturbance of terminus disintegration between 2006 and 2007 was the first, and thus far only, event of this kind and magnitude. Identifying the forcing behind this disturbance is of great importance as it will help the understanding and forecasting of glacier retreat of freshwater terminating calving margins. Further clues towards this can be derived from the bathymetry of Tasman Lake.

4.3.4 Tasman Lake bathymetry and water depth at the terminus

The bathymetry of Tasman Lake from the 2008 survey is shown in Figure 4.4. In general, Tasman Lake basin morphology shows a well–defined trough running north–south along the centre–west of the lake with steep–sided slopes. Water depth increases away from the moraine dam dropping to 100 m depth within 500 m of the southern end of the lake, before gradually decreasing to 150 m between 1000 and 3000 m (Figure 4.6 and Figure 4.7). Another sudden drop in water depth to 240 m is present in the region closest to the terminus position at the time of survey (2008). The rapid shoaling towards the 2008 terminus position (Figure 4.4) indicates the presence of a subaqueous ice ramp extending from the terminal cliff (Dykes et al., 2011; Robertson et al., 2012). A comparison between bathymetric maps produced in 1993 (Watson, 1995), 2002 (Röhl, 2005), and 2008 (*this study*) indicates a decrease in water–depth within the southern end of the lake, while retreat of Tasman Glacier has significantly increased water depth from *c.* 140 to 240 m between 1995 and 2008. Differences in water depth at the location of the Tasman Glacier terminus at the times of previous surveys indicates the presence of an ice–cored section of the lake, or a subaqueous ice ramp similar to that identified in the 2008 survey (Dykes et al., 2011).

The changes in the bathymetry of Tasman Lake have resulted in a significant increase in lake volume in conjunction with the increase in lake surface area. They also indicate that Tasman

Glacier has retreated through a glacially–excavated trough (Figure 4.6). This has had the effect of dramatically increasing maximum water–depth at the terminus, as can be seen in Figure 4.7, from *c.* 150 m to *c.* 240 between 2006 and 2008, altering terminus dynamics by increasing buoyant forces applied to the glacier front. The effect that these buoyant forces have had on Tasman Glacier can be expressed by the closeness of the terminus to the point of flotation. Flotation thickness, h_f (Figure 2.11), of a terminus is defined as Equation (2.3).

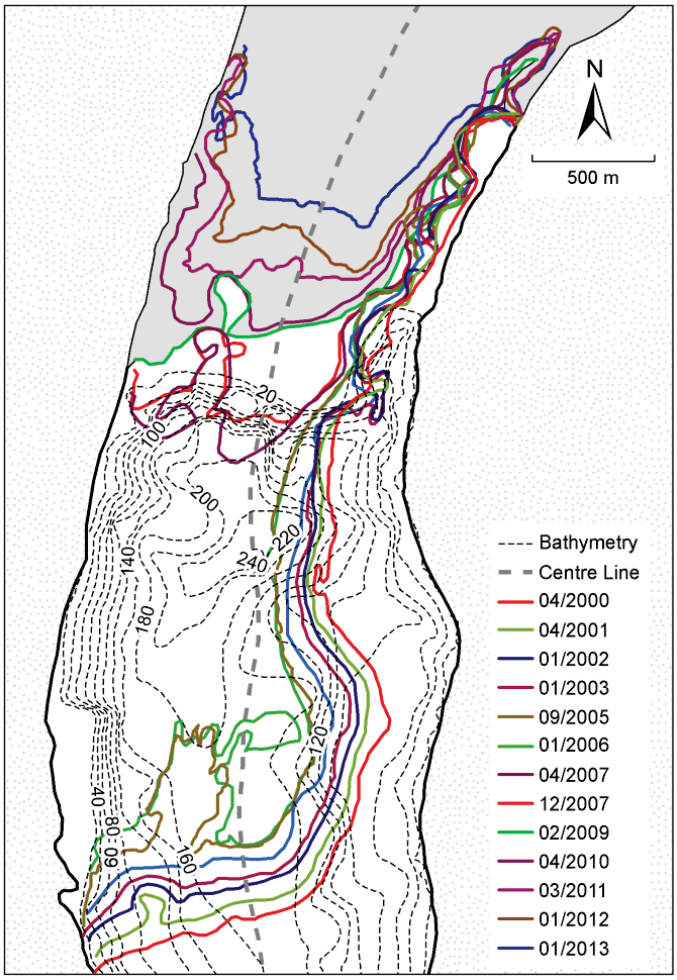

Figure 4.6: Terminus positions of Tasman Glacier between 2000 and 2013 overlaid on Tasman Lake bathymetry (20 m contour interval) from 2008. Also shown is the centre line of Tasman Glacier along which the long profile in Figure 4.7 is derived. Supraglacial ponds on the lower glacier are not shown.

Mean water depth at the terminus in 2008 was 157 m, giving an h_f of 171 m. As a result, the ice thickness ('freeboard') above the waterline (i.e. subaerial ice cliff height, h_s) to induce flotation would have been <14 m. The subaerial ice cliff of Tasman Glacier varied between 5 and 35 m in 2008, indicating that some sections of the terminus were at the point of flotation. However, when maximum water depth (240 m) is substituted into Equation (2.3) h_f becomes 262 m, resulting in flotation of the terminus when $h_s < c.$ 22 m. This indicates that at the time of survey

in 2008, the entire central section of Tasman Glacier would have been subjected to significant buoyant forces.

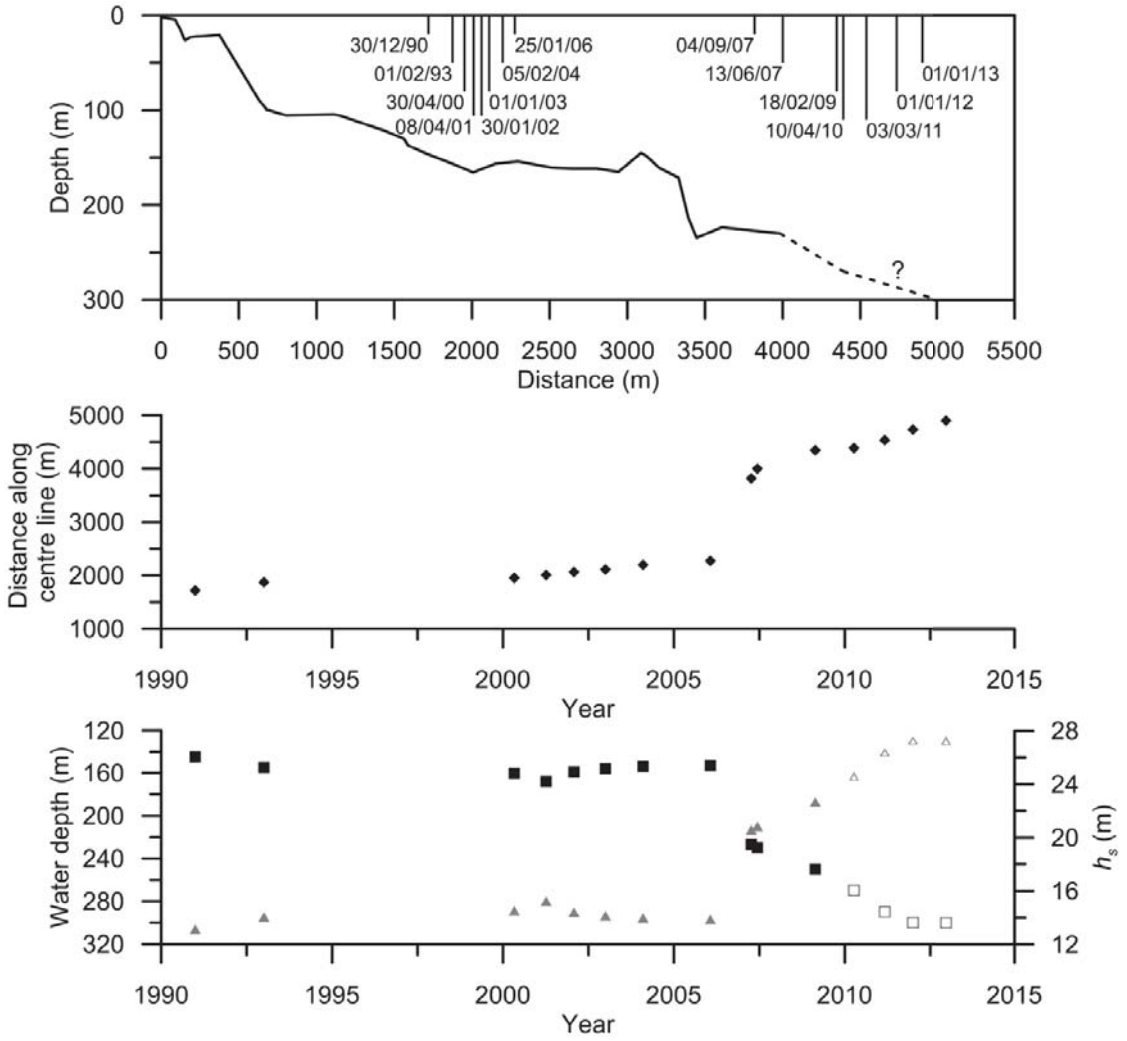

Figure 4.7: (A) Long profile of Tasman Lake along the former centre line of Tasman Glacier from the southern margin moraine dam, with terminus positions derived from satellite imagery. Rapid shoaling towards the terminus in 2008 evident in Figure 4.6 is not shown as terminus position has retreated past this point. Dotted line indicates the inferred water–depth calculated by terminus uplift. (B) Distance along centre line in Figure 4.6 and (C) water depth (squares) at those locations. Also shown in (C) is the subaerial freeboard height (h_s) below which flotation of the glacier is initiated. Hollow points indicate estimated water depths and freeboard height.

Using the centre–line water–depths shown in Figure 4.7C, h_s was calculated for the retreat of Tasman Glacier between 1990 and 2013 to highlight the importance of water depth and flotation on retreat (Figure 4.7C). Centre–line positions were used as it represented the position of greatest depth along the terminus throughout. h_s remained relatively stable at *c.* 14 m between 1990 and 2006, increasing strongly to *c.* 21 m in 2007. Water–depths post–2008 can be inferred based on the assumption that the upward displacement of the terminus during calving indicates that Tasman Glacier was in hydrostatic equilibrium, allowing for the calculation of water depth

(h_w) at the terminus (Warren et al., 2001). The tilting and exposure of thermo–erosional notches above the waterline prior to a large calving event on 22 August 2010 provides evidence for uplift and flotation of the terminus. The 45° angle of the notches shown in Figure 4.8B and the sloping nature of notches away from highest notch point provide clear evidence for uplift due to buoyant forces, rather than being exposed by a *c.* 25 m decrease in lake level. Furthermore, visual observations during July and August 2010 (G. Pearson, *pers. comm.*, 2010) describe the progressive uplift and tilting of the terminus, independent of lake level fluctuations. The minimum water depth (h_{wf}) at the terminus required to induce flotation is $h_{wf} = 9h_s$. Prior to the displacement of the terminus in August 2010, h_0 = 30 m – giving a water depth of 270 m. Water depths between 2011 and 2013 were estimated based on a lead line survey of the ice proximal zone in 2012 that indicated depths greater than 300 m (B. Ward, *pers. comm.*, 2012), increasing h_s to *c.* 27 m. Subaerial ice cliff height was not observed to change significantly between 2008 and 2013, continuing to range between 5 and 35 m. As a result, buoyant forces applied to the terminus in 2008 would have increased significantly through to 2013.

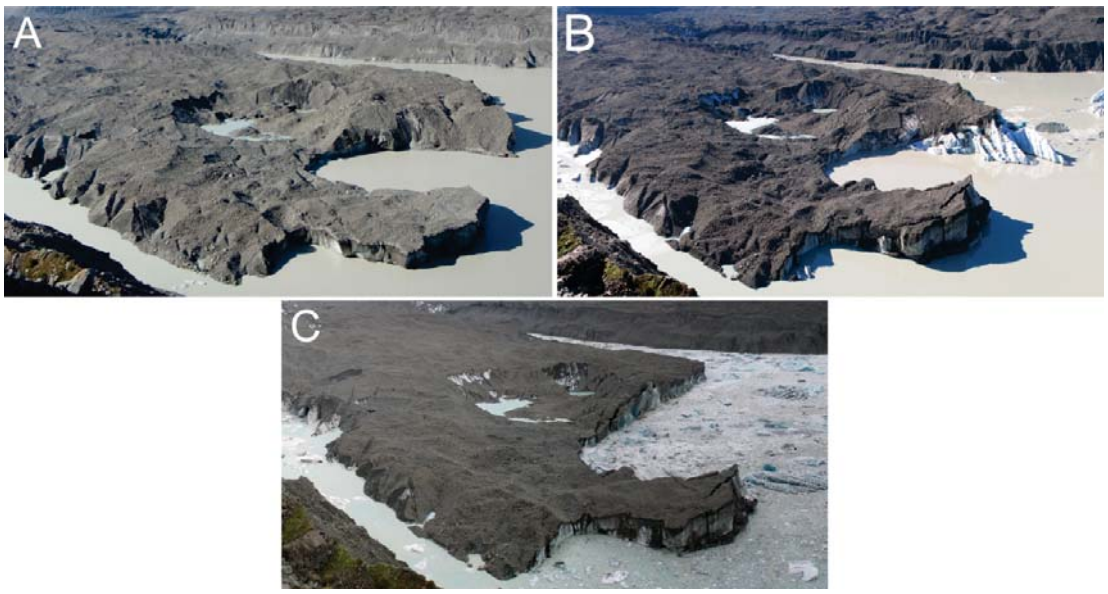

Figure 4.8: Photographs of large calving event in August 2010 initiated by flotation and buoyancy of the terminus. The sequence of photographs shows the terminus prior to (A) and mid (B) uplift. (C) Shows the post calving geometry. Uplift and flotation occurred over a 30 day period (Photos: G. Pearson).

4.4 Discussion

The thinning of Tasman Glacier and the development of Tasman Lake has played an important role in the evolution of the glacier over the past century. Given the spatial and temporal variability of retreat identified above and the indication of recent acceleration in retreat over the study period (2000 to 2013), particularly the disintegration of the lower terminus in 2007, understanding the historical context of retreat is vital. The following sections provide a

synthesis of the formation of Tasman Lake and retreat of Tasman Glacier so that key processes and thresholds can be identified. Key to this is the importance of water depth and flotation of the terminus on conditioning the recent period (2007–2013) of accelerated retreat.

4.4.1 Synthesis of Tasman Glacier calving retreat

4.4.1.1 Lake formation and growth: 1950s–1990

The development of Tasman Lake and the retreat of Tasman Glacier have been summarised by many authors (e.g. Kirkbride, 1993; Hochstein et al., 1995), with the key controls driving lake formation identified as the presence of a supraglacial debris–cover, a low surface slope angle and decreased mass input into the lower glacier due to sustained negative mass balance since the LIA. Downwasting of the terminus of Tasman Glacier was initiated in the early 20th century by an extended period of significant warming (Salinger et al., 1993; Hochstein et al., 1995), resulting in the lowering of the lower glacier's surface at a rate between 0.3 and 1.2 m a^{-1} since 1890 (Hochstein et al., 1995). Over the same time period, ice velocities also decreased significantly across the lower glacier. Indeed, decrease in surface ice velocity near the confluence of Ball Glacier varied from as high as 167 m a^{-1} during the austral summer of 1890/1891 to a minimum of 98 m a^{-1} as mapped by Kirkbride (1995a) in 1957, 1971 and 1986, from boulder displacement in sequential aerial photos. At the terminus, ice velocity also decreased from an average maximum of 13 m a^{-1} between 1957 and 1971 to 8 m a^{-1} between 1971 and 1986 (Kirkbride, 1995a).

The result of this downwasting and deceleration on the low gradient (<1.5^{o}) debris–covered terminus was the collapse and exposure of englacial conduits (Kirkbride and Spedding, 1996) and the pooling of meltwater. This led to the development of sink–holes and supraglacial ponds across the surface of the lower glacier (Kirkbride, 1993; Benn et al., 2001). As negative mass balance and decreased ice velocities continued throughout the mid–20th century, such ponds were able to persist for extended periods of time (i.e. decades), perforating the debris–cover evident along the lower Tasman Glacier (Kirkbride, 1993). Such small supraglacial ponds are evident along glacier flow lines on maps of the area produced since 1883 (Kirkbride, 1993) and had expanded significantly by the mid–1950s. The small supraglacial ponds increased in diameter through melt of the intermittently debris–covered walls and calving at pond margins (Benn et al., 2001; Röhl, 2008). These ponds were hydraulically connected by 1982, accelerating expansion until four large ponds coalesced to form a single shallow lake of irregular shape by 1990 (Kirkbride, 1993). This increase in pond expansion can be seen in Figure 4.3 and Figure 4.5 and represents the onset of rapid acceleration in the growth of Tasman Lake and the retreat of Tasman Glacier.

4.4.1.2 Calving retreat: 1990–2006

Since its formation, Tasman Lake expanded primarily via the retreat of Tasman Glacier due to iceberg calving and subaqueous melt (Kirkbride, 1993; Hochstein et al., 1995; Purdie and Fitzharris, 1999; Röhl, 2006; Dykes et al., 2011). After an initial period of disintegration as ice–cored sections of the lake bottom calved as a result of the coalescence of supraglacial ponds (Kirkbride, 1993), a semi–transverse ice cliff formed across the terminus of the glacier, extending up into the eastern embayment (Figure 4.1). Although calving occurred along the entire ice cliff through until 2006 (Purdie and Fitzharris, 1999; Röhl, 2006; Dykes et al., 2011), ice loss was primarily centred along the southern section of the ice cliff (Figure 4.1) (Dykes et al., 2011). Retreat of the glacier via calving was driven by low–magnitude/high–frequency events (Purdie and Fitzharris, 1999; Röhl, 2006) initiated principally by thermo–erosional notching due to waterline melt (Kirkbride, 1993; Purdie and Fitzharris, 1999; Röhl, 2006). However, this is not to discount other forms of calving as contributing to ice loss, with calving unrelated to thermal undercutting (such as flake or subaqueous) also observed through this period (Röhl, 2005).

Terminus retreat had increased to over 30 m a^{-1} by 1995 due to calving and ice loss via subaqueous and subaerial melt (Purdie and Fitzharris, 1999). This continued at a similar rate through until the early 2000s (Röhl, 2006), albeit with greater variability (30 to 75 m a^{-1}). Retreat rates calculated in the present study (Table 4.1) indicate a similar increase in variability since 2000 extending through until 2006. The variability in retreat rates between 2000 and 2006 (reported in Table 4.1) indicates that there were significant temporal variations of retreat at the sub–decadal level, often influenced by the spatial variability of calving and ice loss (e.g., incorporation of ponds into Tasman Lake).

This variability may also be the result of fluctuations in ice velocities (Kirkbride and Warren, 1999; Röhl, 2006; Quincey and Glasser, 2009; Redpath, 2011). Direct measurements of ice velocity by Kirkbride and Warren (1999) indicate that ice velocity had increased to between 11 and 24 m a^{-1} in 1995, indicating an acceleration in glacier flow since the formation of Tasman Lake. However, Röhl (2005, 2006) later measured ice velocities in the order of 2 to 8.5 m a^{-1} between 2001 and 2002. This decrease may indicate variability in the survey methods and lengths, or variability in the ice supply. Nevertheless, ice velocities between 1990 and 2006 were not great enough to match ice loss by melt and calving. However, extensional flow towards the terminus observed by Kirkbride and Warren (1999) may account in part for the variability of retreat by inducing greater crevasse development, therefore providing discontinuities in the glacier along which calving is initiated (Benn et al., 2007b).

In contrast to annual retreat rates, surface area growth of Tasman Lake (and therefore Tasman Glacier retreat) showed a marked acceleration over the period 1990 to 2006 since Tasman Lake was formed, as discussed in section 4.3.3. The cause of this non–linear expansion of the lake is unclear and may be related to a positive feedback between calving and glacier acceleration (Kirkbride and Warren, 1999; Benn et al., 2007b), increased water depth (Brown et al., 1982; Kirkbride and Warren, 1999), increased melt associated with a larger proglacial water–body (Warren and Kirkbride, 2003), or a sustained decrease in mass flux into the terminus. It is likely that a complex combination of all these factors that has led to the acceleration of retreat with no one process acting in isolation.

4.4.1.3 Terminus disintegration: 2006–2007

During the expansion of Tasman Lake and retreat of Tasman Glacier between 1990 and 2006, downwasting of the lower terminus continued and resulted in the extensive formation of supraglacial ponds evident in Figure 4.1A–C. Pond development and growth appears to have been centralised in the area of greatest depth as evident in the 2008 bathymetry of Tasman Lake (Figure 4.9). As surface topography of a glacier typically mirrors bed topography (Benn and Evans 2010), the development of supraglacial ponds in this area is likely to be related to the surface expression of this depression in the glacier bed providing a loci for the pooling of meltwater and the collapse of englacial conduits (Benn et al., 2001; Röhl, 2006, 2008). This coupled with the decrease in ice velocities between 1995 and 2002 (Röhl, 2005) and the low gradient (< 1.5°) nature of the lower glacier tongue between 1990 and 2006, provided all the necessary conditions for pond development (Sakai et al., 2000; Benn et al., 2001; Röhl, 2008).

Once hydraulically–connected to the main drainage network (either englacially or to the main lake), the rate of pond growth accelerated between 2003 and 2006 as a result of enhanced subaerial and subaqueous melt and calving (Sakai et al., 2000; Benn et al., 2001; Röhl, 2008). Decreased ice velocity of the lower glacier between 2004 and 2006, evident in Redpath (2011, p. 115), also appears to correspond to the expansion of supraglacial ponds over this period of time. By 2006 supraglacial ponds on the lower glacier had expanded to 0.46 km^2, including ponds partially connected in planform to Tasman Lake. Once connected to the lake, increased water temperature and circulation within the ponds dramatically increased the rate of ice loss from the terminus of Tasman Glacier, significant altering terminus dynamics (Röhl, 2008).

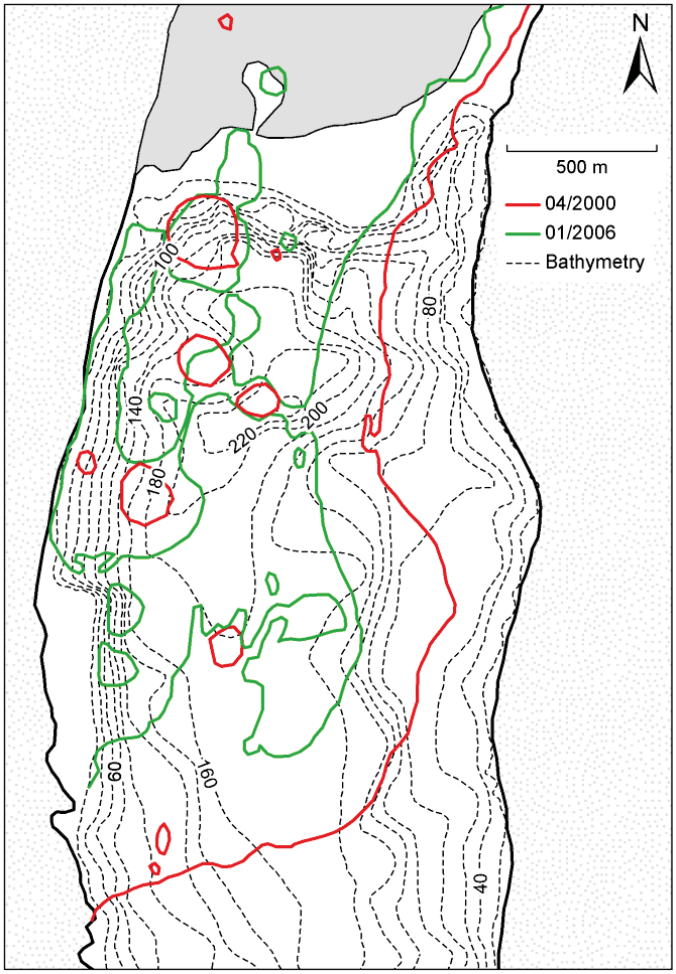

Figure 4.9: Bathymetric map of Tasman Lake with the position of the Tasman Glacier terminus and the extent of supraglacial ponds in April 2000 and January 2006. In general, pond growth is in the region of greatest water depth of Tasman Lake in 2008.

It was this rapid expansion of supraglacial ponds and retreat of the glacier down a reverse slope into deeper waters (Figure 4.7) that led to the disintegration of a large section of the lower terminus between 2006 and 2007 and the loss of 1.47 km^2 of ice (Table 4.1). Figure 4.10 and Figure 4.11 show the terminus of Tasman Glacier before and after this event. They indicate that a large planform area of formerly debris–covered ice in the January 2006 satellite image (Figure 4.1D) had been lost by pond and lake expansion and calving by March 2007 (Figure 4.10A). As pond growth primarily occurs in a horizontal direction (Röhl, 2008), the planform area lost is assumed to have remained ice cored as large sections of the glacier visible in Figure 4.10A remained *in situ* up until the entire section disintegrated (Figure 4.11). The loss of ice via the expansion of ponds on the lower glacier would have significant increased buoyant forces acting at the terminus zone as the substitution of water for ice within depressions decreases the ice overburden pressure in the order of 10 tonnes m^{-2} (Röhl, 2008). Pond expansion also had the effect of decreasing ice thickness of a large area of the terminus to below lake level. Retreat of the glacier into progressively deeper waters occurred between 2000 and 2006 (Figure 4.7), with

the greatest water depths recorded in the bathymetric survey in 2008. Hence, in the area of ice loss in 2007 (Figure 4.1), increased torque arising from buoyant forces (Dykes et al., 2011) across this section of the terminus would have been significant. This is important because as grounded fresh–water glacier termini become buoyant and attain flotation, the rate of ice loss increases substantially as a result of changes in glacier dynamics and stress regimes (Warren et al., 2001; van der Veen, 2002; Röhl, 2008). It was the increase in stresses from applied buoyant forces that led to the disintegration of large section of the terminus during the start of April 2007 (Figure 4.11). This event produced numerous large icebergs (Figure 4.10B) that calved coherently from the terminus.

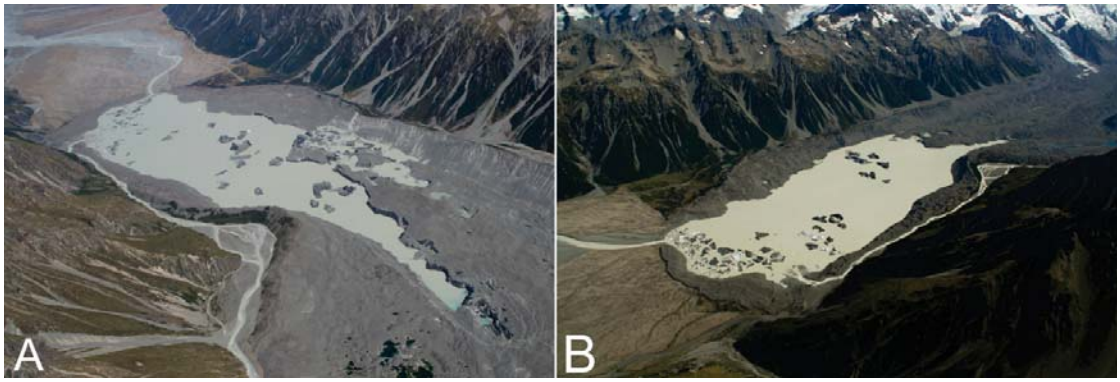

Figure 4.10: Oblique aerial photography of the terminus of Tasman Glacier in (A) March 2007 showing the state of the terminus immediately prior to breakup (Photo: S. Winkler) and (B) February 2008 after breakup. Note that several large and coherent icebergs have already calved from the terminus in (A) and that a large number of icebergs were preserved over the following year.

Previous work (e.g., Dykes et al., 2011) has indicated that terminus disintegration in April 2007 was potentially initiated by significant rainfall falling within the region in the months prior to calving. Rain falling within the Tasman Glacier catchment can cause up to 5 m increase in lake level over short (*c.* 48 hours) time periods (see chapter 5). Such fluctuations at an unstable terminus have the potential to instigate calving by exceeding the threshold of flotation (Boyce et al., 2007). The direct link between lake level fluctuations and buoyancy–driven calving at Tasman Glacier remains unclear as not all events of this type are associated with increased lake–level (chapter 8). However, at a terminus approaching the critical threshold for flotation, lake–level fluctuations may increase stress into the terminus region, further destabilising the terminus and increasing the likelihood of high–magnitude calving events. This is discussed further in the following sections.

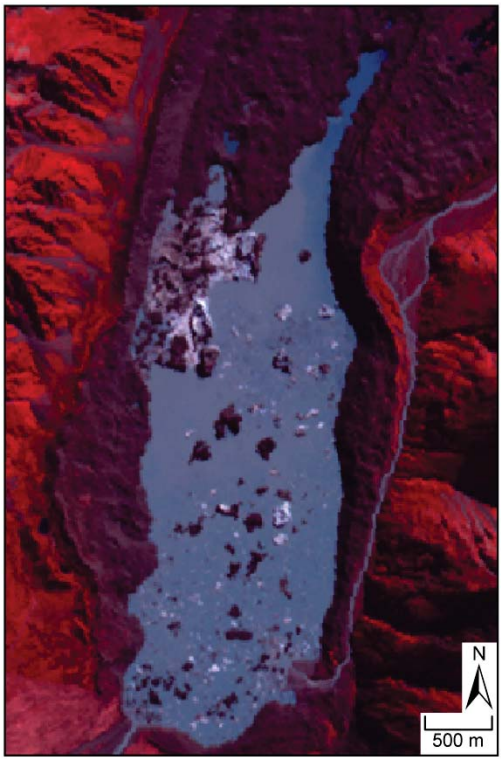

Figure 4.11: False colour ASTER image of Tasman Lake at the start of April 2007 showing the disintegration of the lower section of the Tasman Glacier terminus pictured in Figure 4.10A. The presence of white icebergs within the region of the former terminus indicates that calving has taken place in the days prior to image acquisition.

4.4.1.4 Calving retreat: 2007–2013

Following the disintegration of the lower terminus in 2007, water–depth at the glacier front increased significantly as Tasman Glacier receded into the glacially–excavated trough (Figure 4.7), driving the glacier further from equilibrium. As a result, the glacier has entered a period of increased retreat distinct from the retreat seen prior to 2006, although not to the same extent as found between 2006 and 2007 (Figure 4.2). This is not inherently evident in changes in surface area (Figure 4.2), as the rate of growth has remained at similar levels to that prior to 2006 (Figure 4.5). However, given the dramatic shortening of the terminus in contact with Tasman Lake (*L*), and consistently increased retreat rate recorded between image acquisition dates (Table 4.1), it is clear that retreat has increased. This increase in retreat is suggested to have been driven by a transition in the style and impact of calving at Tasman Glacier. A period of high–magnitude, low frequency, buoyancy–driven calving events has commenced that is being superimposed on top of the high–frequency, low–magnitude, calving events that have continued to occur. This has been triggered by the increase in water–depth at the terminus due to disintegration of the terminus in early 2007 increasing the potential for flotation of the terminus (Figure 4.7C), changes in basin morphology and the continued presence of supraglacial ponds in the terminus region.

Ice loss and retreat between 2007 and 2011, shown in Figure 4.1D–F, appears to follow a cyclical sequence characterised by the calving of large ice peninsulas which developed as a result of formation of supraglacial ponds along the centre–line of the lower terminus. Formation of such peninsulas effectively isolates large sections of the central terminus removing support from surrounding ice and valley sides and increasing sensitivity to buoyant forces (van der Veen, 2002; Boyce et al., 2007). Calving retreat to the up–valley edge of supraglacial ponds takes place via a series of large calving events, with this cycle of retreat then repeated. Two examples of this progression are shown in Figure 4.8 and Figure 4.12. Figure 4.12 shows a series of icebergs that calved from a peninsula that developed during late 2008 giving rise to 378 m of retreat of the eastern peninsular between 2007 and 2009 (Figure 4.1). This process was again repeated during August 2010, when a section of the terminus approached flotation and became uplifted due to isolation from surrounding lateral support (Figure 4.9). This peninsula calved on the 22 August in a single calving event, leading to the rapid up–glacier retreat of the terminus by *c.* 260 m. This sequence is also evident for several other calving events that took place between 2007 and 2012 (see chapter 8) and highlights the continued importance of supraglacial ponds in ice loss from the terminus of Tasman Glacier.

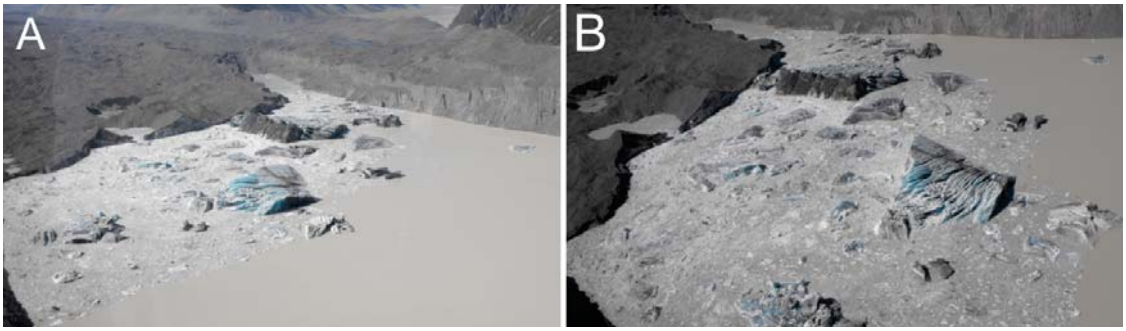

Figure 4.12: Photographs of large calving events at Tasman Glacier that was initiated by flotation and buoyancy of the terminus in February 2009. Note that the icebergs have rotated as they calved from the terminus.

A secondary effect of this increase in ice loss from the terminus has been an apparent increase in ice velocity at the terminus (Redpath, 2011). For example, feature–tracking applied to ASTER images between 2000 and 2010 by Redpath (2011) suggests that there is an increase in surface ice velocity (to between 30 and 50 m a^{-1}) within the terminus region, compared with lower velocities further up–glacier of the terminus. Several authors (Kirkbride, 1993; Kirkbride and Warren, 1999; Redpath, 2011) have attributed this glacier speed–up with extensional flow towards the terminus due to the presence of Tasman Lake. This extensive flow is evident in Figure 4.13, indicated by the development of transverse crevasses in the terminus zone, and has been identified during previous periods of retreat (Figure 6 in Kirkbride and Warren (1999)). The effect of this extensive flow is the potential thinning of the lower glacier, further increasing

its susceptibility to buoyancy–driven calving (Benn et al., 2007b). However, the extent to which this has affected calving and Tasman Glacier's retreat between 2007 and 2011 is currently still unclear due to the large changes in terminus geometry and a lack of complete records of glacier thinning and detailed velocity measurements at the terminus.

Figure 4.13: Photograph showing the terminus of Tasman Glacier in May 2012. Note that no supraglacial ponds are present on the lower glacier tongue as well as the increase in glacier slope present from *c.* 700 m (white dotted line) up glacier from the terminus. It was along this line that the calving occurred in February 2013. Also note the depression present running along the centre of the glacier (black dotted line) and the presence of transverse crevasses at the terminus (arrowed).

Analysis of the January 2012 and January 2013 ASTER images indicates that there are no supraglacial ponds within the terminus region, in contrast to 2007 and 2011 (e.g., Figure 4.12). This is further corroborated by Figure 4.13, which shows that not only are there no supraglacial ponds, but that the slope of the glacier increases *c.* 700 m up–glacier from the terminus. In general, the surface slope of the glacier past this point increases from ~2° to between 3° and 4°. This increase in surface slope has the effect of limiting the ability of water to pool and for supraglacial ponds to form (Sakai et al., 2000). As a result, the development and isolation of peninsulas that have initiated large buoyancy–driven calving events identified between 2007 and 2011 may become even less frequent. Given that Tasman Glacier still terminates into deep water (>300 m), the terminus is still being subjected to increased torque from buoyant forces (see the following section for description), albeit potentially over a larger area. For example, the development of the western embayment since 2009 has had the effect of isolating the entire glacier front from the lateral margins. The result of this was the calving of the entire lower section of the glacier in February 2013 (see section 8.4.5 for description).

4.4.2 Terminus flotation and retreat

Evidence for the uplift and flotation of the Tasman Glacier terminus between 2006 and 2013 has been presented in section 4.3.4. Terminus uplift occurs as a glacier approaches flotation due to

thinning associated with longitudinal stretching and subaerial melt decreasing ice overburden pressure (van der Veen, 1996; Warren et al., 2001). Continued downwasting and retreat into deeper waters led to a reduction in ice cliff 'freeboard' height of Tasman Glacier, causing the terminus to reach a point where flotation, and calving, became inevitable. From the calculated flotation thickness (Figure 4.7) and observed uplift (Figure 4.8), it is clear that uplift and flotation exerted significant bending forces on the terminus post–2007, with external variables other than waterline melt influencing calving and the retreat of the glacier. Previous studies (e.g., Warren et al., 2001; Boyce et al., 2007) at freshwater–terminating calving margins have also highlighted the potential of terminus flotation and its effect on calving processes and glacier retreat. Observations from Norway (Theakstone and Knudsen, 1986), Iceland (Howarth and Price, 1969), Switzerland (Tsutaki et al., 2013), Arctic Canada (Holdsworth, 1973), Alaska (Lingle et al., 1993; Boyce et al., 2007; Trüssel et al., 2013), Patagonia (Warren et al., 2001) and this study indicate that localised sections of freshwater margins can attain flotation for extended periods of time (months to years). This is in contrast to temperate tidewater glaciers, where floating margins are unstable features that typically calve within days or weeks of attaining flotation (O'Neel et al., 2003; Walter et al., 2010).

Several hypotheses have been proposed to account for the differences in the stability and duration of flotation between tidewater and freshwater glaciers as it may account for, in part, up to an order of magnitude difference in calving rates (Trüssel et al., 2013). Boyce et al. (2007) has suggested that terminus uplift and flotation is possible at freshwater margins if uplift occurs over an extended period of time (months to years), allowing for viscoelastic deformation rather than brittle fracture. This is possible because freshwater termini, unlike tidewater calving margins (which are subjected to daily perturbations such as tidal flexure), experience fewer fluctuations in their proglacial water body (Boyce et al., 2007). Boyce et al. (2007) illustrated this process in their study of Mendenhall Glacier, Alaska, where flotation (initiated by long–term mass wastage) of a section of the glacier was sustained over a 2 year period by ice creep and lateral support of grounded ice near bedrock margins. Calving of this uplifted section of the terminus occurred in a series of discrete events predominantly associated with 0.3 m increases in lake level.

Contrasting subaqueous melt rates between tidewater and freshwater calving margins have also been suggested as a potential driver for increased instability of sections of calving termini approaching flotation. Trüssel et al. (2013) propose that once a glacier becomes ungrounded due to thinning and flotation, a cavity at the base of the glacier may form. In a tidewater environment this cavity would be subjected to high basal melt rates (in excess of 1 m d^{-1} (Motyka et al., 2003a; Motyka et al., 2011; Xu et al., 2013)) due to increased water circulation

of warm ocean water at the base, driven by the upwelling of subglacial freshwater. Thinning of the glacier due to subaqueous melt within the cavity increases buoyant forces acting on the ungrounded section, leading to rapid destabilisation and calving back to the grounding line. In freshwater settings, temperature and density differences between incoming subglacial water and the proglacial water body are small (Motyka et al., 2003a). This limits water circulation and heat exchange to the glacier front, leading to decreased subaqueous melt rates when compared to tidewater settings. As a result, subglacial thinning occurs at a slower rate, meaning that under the same climatic conditions an ungrounded tidewater terminus will thin more rapidly. The result of this is that buoyant forces are more rapidly applied to tidewater margins compared to freshwater settings. When this is combined with the frequency of proglacial water body perturbation, it appears to account for floating sections of tidewater glaciers calving more rapidly than freshwater glaciers.

As a result, the lag–time (at tidewater and freshwater margins alike) between flotation being attained and calving of the buoyant section appears to be a function of basin morphology and terminus geometry, subaqueous melt, and the size and frequency of perturbations in proglacial water level. At Tasman Glacier the time between flotation and calving was typically in the order of months rather than years (section 4.4.1.4 and Chapter 8), as reported at similar freshwater–terminating glaciers such as Mendenhall Glacier (Boyce et al., 2007). This accelerated rate of destabilisation between similar freshwater margins is attributed primarily to the limited lateral support of uplifted sections of Tasman Glacier (due to basin morphology and supraglacial pond development) and the size and frequency of lake level changes during flotation. Increased subaqueous melt of a cavity formed beneath Tasman Glacier may also play a factor in the shorter lag–time between flotation and calving. However, as previous studies have indicated that water temperatures within Tasman Lake (Röhl, 2005) appear to be of the same order of magnitude as other freshwater glaciers (Boyce et al., 2007; Trüssel et al., 2013) it is not considered here to be a major factor. However, this assumption may be proven unture if future studies are able to overcome current difficulties (e.g., the inherently hazardous environment of a calving terminus) in quantifying the effect of subaqueous melt rates on glacier dynamics and buoyancy–driven calving.

Basin morphology and terminus geometry on the other hand, coupled with lake level fluctuations, play a more significant role in the lag–time between flotation and calving. Support from the lateral margins at Mendenhall led to the ice being able to deform via ice creep. In comparison, uplift and calving at Tasman was concentrated on sections of the terminus that had become isolated from the surrounding glacier and moraine walls (Figure 4.1). The isolated sections were thus able to oscillate freely, increasing the likelihood of brittle fracture at the pivot

point. Oscillations of the isolated sections of the terminus were applied by fluctuation in lake level due to rain falling within the Tasman Glacier catchment. Although Mendenhall Glacier was subjected to seasonal fluctuations in lake level, it does not appear to have the same range or frequency of significant rises in lake level as Tasman Glacier (chapter 5). As mentioned previously, an increase in lake level of 0.3 m is associated with the breakup of an uplifted section of Mendenhall Glacier (Boyce et al., 2007). In comparison, lake level within Tasman Lake fluctuates regularly up to *c.* 5 m within 48 hour periods (chapter 5), typically during the spring/summer period. Such fluctuations in lake level of Tasman Lake commonly occur two to three times a month, compared to the one to two times a season at Mendenhall Glacier. Consequently, the number of times that the point of calving failure is subjected to increased tensile stresses due to flexure between the oscillating and stable sections of the terminus would have been greater at Tasman. However, the importance of lake level fluctuations as the trigger of calving, as was the case at Mendenhall Glacier, is unclear for the retreat of Tasman Glacier between 2007 and 2013; some calving events were associated with increased lake level while others were not (discussed more in chapter 8). This may indicate that lake level cannot only play a part in initiating buoyancy–driven calving events, but can also play a role in the long term evolution of floating sections of the terminus.

4.4.3 Thresholds of retreat at Tasman Glacier

From the analysis presented in section 4.3.3 and the description of processes acting at the terminus of Tasman Glacier throughout lake formation and calving retreat (section 4.3.3), three distinct periods can be identified. They relate to: (1) the initial formation and expansion of supraglacial ponds and the development of Tasman Lake between 1950s and 1990; (2) the accelerated expansion of Tasman Lake and the retreat of Tasman Glacier via calving processes and the incorporation of supraglacial ponds; and (3), a sharp increase in lake growth and retreat between 2006 and 2007 followed by continued rapid retreat conditioned by flotation and buoyancy–driven calving.

The initial formation of Tasman Lake during the 20th century has been described by several authors (e.g., Kirkbride, 1993; Hochstein et al., 1995), with three phases punctuated by two key thresholds of lake formation and retreat identified by Kirkbride (1993). The development of supraglacial ponds that form via the pooling of meltwater and collapse of englacial conduits on the lower reaches of debris–covered glaciers with very low surface slopes (< 1.5^{o}), represent the first threshold. This threshold marks a transition in the dominant ablation regime from slow melt under debris–cover (phase 1) to rapid melting of exposed ice walls and at pond edges (phase 2). Once formed, ponds expand and coalesce due to the efficient loss of ice due to melt and calving at pond margins (Benn et al., 2001; Röhl, 2008), eventually forming a single lake. Threshold 2

occurs when the formed lake eventually develops a transverse ice cliff and retreats into deep water due to the melting and/or disintegration of the ice floor of the lake. At this point the calving of icebergs dominates retreat and the glacier enters a third phase of rapid retreat. Kirkbride (1993) observed that Tasman Glacier had progressed through the initial two phases, with the third phase of rapid retreat imminent by 1990. This is corroborated by this study in that the thresholds identified by Kirkbride (1993) could be seen to mark the transition points between periods of retreat at Tasman Glacier, with the first threshold marking the transition into the initial period of lake growth (1950s–1990) and the second threshold the transition into accelerated retreat (periods 2 and 3: 1990 onwards).

However, other researchers (e.g., Strong, 2008) have argued that the continued importance of pond growth between 1990 and 2000 indicates that the second threshold was not met until 2000. This appears to be a slightly arbitrary point given the ongoing significance of supraglacial ponds on conditioning, at least in part, the loss of mass from the lower glacier and retreat through until 2007 when the lower section of the glacier disintegrated (section 4.4.1.3). It was only at this point that buoyant forces applied to the terminus became significant enough to affect calving and the retreat of Tasman Glacier on a consistent basis, a consideration in the second threshold in Kirkbride's model (Kirkbride, 1993). It could therefore be argued that the second threshold was only met in 2007. However, given that retreat of Tasman Glacier via the expansion of Tasman Lake has accelerated since 1990 (Figure 4.5), the timing of the second threshold being met is argued here to have occurred during the early 1990s and not 2007. This is because calving from the terminus has contributed significantly to ice loss post–1990; Tasman Lake had penetrated to the base of the glacier across a large area at this point (Hochstein et al., 1995; Purdie and Fitzharris, 1999), and, acceleration of ice velocities and the development of extensional flow within the terminus region post–1990, highlighted by Kirkbride and Warren (1999) has also taken place.

A third threshold has also been suggested for Tasman Glacier (Kirkbride and Warren, 1999; Röhl, 2005; Dykes and Brook, 2010) where stability in the terminus position will occur due to a combination of mass flux and bed topography. The exact timing and position at which stability of the terminus will be attained is not known precisely due to limited knowledge of the current and predicted mass balance of Tasman Glacier, and the poor resolution of known bed topography.

4.4.4 Glaciers of the Aoraki/Mount Cook National Park and a model for proglacial lake evolution

The development and expansion of proglacial lakes within the *Aoraki*/Mount Cook National Park between 1955 and 2013 is shown in Figure 4.14. All proglacial lakes significantly increased in surface area due to glacier retreat between 1955 and 2013, with Tasman Glacier experiencing the largest increase (Figure 4.14A). Converting surface areas into a percentage of their last reported area (Figure 4.14B), two significant trends become apparent. The first is that the Grey/Maud and Clessen lakes had already developed and expanded by the time of their first measurement in 1965 (Robertson, 2012). Secondly, there is similar exponential growth of Godley, Hooker, Murchison, Mueller and Tasman lakes. Only the timing of the transition into accelerated expansion differs, with all proglacial lakes having formed a single lake by the late 1980s. Once a single lake had formed at the terminus of each glacier, a phase of rapid lake expansion due to glacier retreat took place (Kirkbride and Warren, 1997; Warren and Kirkbride, 2003; Röhl, 2005; Robertson, 2012). This phase of rapid retreat has continued through to the end of the reporting period at all glaciers, although temporal variations exist. For example, deceleration in lake growth is occurring at a number of glaciers (e.g., Grey/Maud and Godley), suggesting they may transition out of their current phase of rapid retreat.

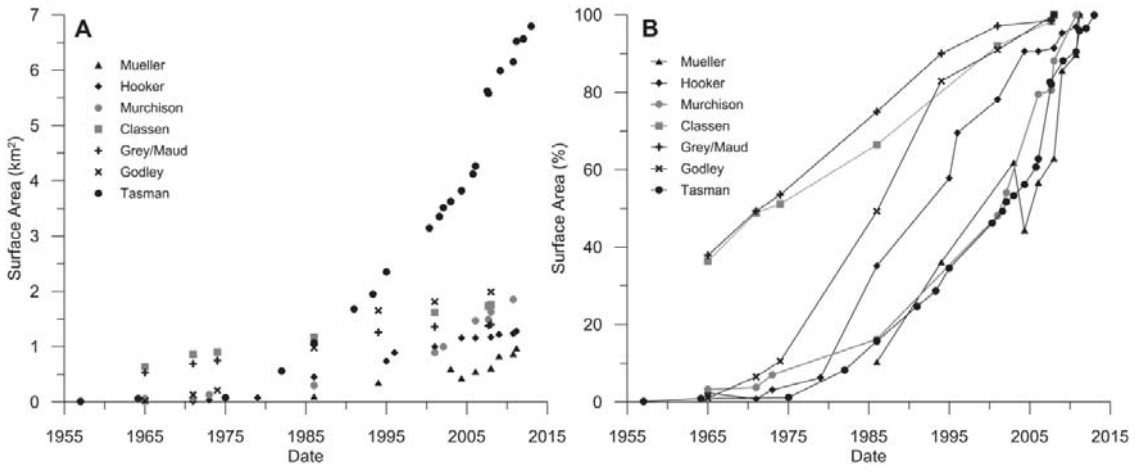

Figure 4.14: (A) Surface area of glacial lakes in the Mount Cook National Park between 1955 and 2013. Data for Tasman Lake is shown in Table 4.1, with the data for the all other glacier lakes from a combination of data sources compiled by Robertson (2012): Mueller (Watson, 1995; Röhl, 2005; Robertson, 2012), Hooker (Warren and Kirkbride, 1998; Robertson, 2012), Murchison (Robertson, 2012), Classen (Robertson, 2012), Grey/Maud (Warren and Kirkbride, 1998; Robertson, 2012), and Godley (Warren and Kirkbride, 1998; Robertson, 2012). (B) The percentage of lake growth with respect to time the six proglacial lakes between 1955 and 2013 is shown so a comparison between lakes is possible. 100 % refers to the last surface area of the proglacial lake reported.

The similarity in the progression of proglacial lakes in Figure 4.14 indicates that similar processes must be acting on termini, albeit to different temporal and spatial extents. As noted

above for Tasman Glacier (section 4.4.1), the acceleration of lake growth and glacier retreat between 1990 and 2013 was related to a combination of increased water depth at the terminus and positive feedback between calving and glacier acceleration, with melt associated with a larger proglacial water–body also having a potential influence. Similar changes have been observed throughout the other glaciers reported in Figure 4.14 (Watson, 1995; Hochstein et al., 1998; Röhl, 2005; Robertson, 2012) and highlight the importance of water depth and calving on conditioning glacier retreat, with the timing and extent of lake expansion conditioned by basin morphology and glacier dynamics of specific glacial systems.

As the formation and evolution of proglacial lakes within the *Aoraki*/Mount Cook National Park appears to follow similar patterns of lake evolution and glacier retreat (Kirkbride, 1993; Röhl, 2005; Robertson, 2012), the extent of individual lakes at any one time has been considered to represent a glacier's position within a sequential series of stages of broader lake evolution and glacier retreat (Kirkbride, 1993; Robertson, 2012). Robertson (2012) has proposed a four–stage model to account for the transition of a debris–covered downwasting termini through to the development of a stable proglacial lake (Figure 4.15). The first three stages of lake growth are similar to Kirkbride's model (Kirkbride, 1993), identifying the transition from ablation being dominated by sub–debris melt, through to the development, expansion, and coalescing of supraglacial ponds (stages 1 and 2). Expansion of the single lake due to calving (stage 3) subsequently takes place via a series of sub–stages of steady (3a), rapid or accelerating (3b), and decelerating (3c) lake growth (Figure 4.15) that disconnects the glacier from responding to variations in climate (Kirkbride, 1993; Kirkbride and Warren, 1999; Benn et al., 2007b). Lake growth within stage three may switch between sub–stages due to changes in basin topography (e.g., accelerated glacial retreat through a depression or deceleration over a bedrock rise) or changes in mass flux at the terminus. Eventually lake growth, and therefore glacier retreat, stabilises (stage 4) as the glacier reaches equilibrium due to a combination of basin morphology and glacier dynamics. This stabilisation is assumed to take place as the glacier retreats to a point where bedrock topography begins to intercept lake level, or mass flux at the terminus equilibrates. This model of proglacial lake evolution (Figure 4.15) suitably describes the retreat of Tasman Glacier and surrounding glaciers in the *Aoraki*/Mount Cook National Park to a degree where processes between the different stages are able to be identified, such as those described in sections 4.4.1 and 4.4.3.

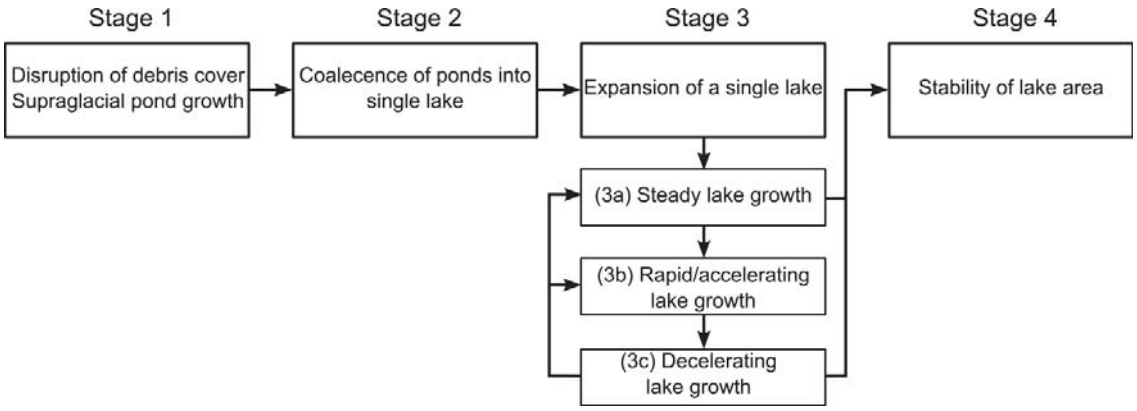

Figure 4.15: Stages of lake growth proposed by Robertson (2012) for lakes within the *Aoraki*/Mount Cook National Park. Once ponds have formed (stage 1) and coalesced (stage 2) on a downwasting debris–covered terminus, expansion of the proglacial lake (stage 3) takes place through a series of steady (3a), rapid/accelerating (3b) and decelerating (3c) sub–stages. Finally stability is attained due to basin morphology and glacier dynamics (stage 4).

4.5 Conclusions

The continued rapid expansion of Tasman Lake and the accelerated retreat of Tasman Glacier documented by previous studies have continued through the 13 year period of terminus evolution studied here. In general, Tasman Glacier lost a total of 3.51 km^2 of surface area resulting in the mean up–glacier retreat of the terminus by 1.2 km between 2000 and 2013. Significant spatial and temporal trends in ice loss throughout this period existed, punctuated by the disintegration of the lower terminus in early 2007 and the loss of 1.47 km^2 of glacier area. Prior to this (2000–2006), mean retreat along the entire length of the terminus was 50 m a^{-1}, with glacier surface area decreasing by 1.36 km^2 only. Post–2007 the rate of glacier area change returned to similar levels to those prior to 2006, whilst glacier retreat rates increased to between 57 and 117 m a^{-1}. This increase in retreat is the result of the shortening of the ice cliff, meaning that the same surface area changes were being applied across a smaller area of the terminus. Spatial and temporal variability in ice loss between 2000 and 2013 is associated with changes in external and internal parameters. The result of thinning and retreat of Tasman Glacier into deeper waters of Tasman Lake has been to significantly alter terminus dynamics, leaving the glacier susceptible to buoyant forces. This has led to the instability of Tasman Glacier's terminus, which appears to have resulted in a significant shift in dominant calving style from waterline melt and thermo–erosional notch–driven calving (Röhl, 2006) to high–magnitude, low frequency, buoyancy–driven calving. These large calving events highlight the importance of buoyancy–driven calving on the retreat of Tasman Glacier post–2007 and the importance of glacier dynamics and proglacial water–body characteristics on priming such events. While Tasman Glacier continues to thin and terminate in deep water (>300 m), buoyancy–driven calving will continue to dominate retreat, until such point in time where the glacier retreats into shallower water or ice supply increases.

The retreat of Tasman Glacier between 2000 and 2013 has represented the continuation of the rapid expansion of Tasman Lake throughout the late 20th century. Based on changes in the surface area of Tasman Lake, its expansion (and therefore glacier retreat) since formation can be categorised into three documented phases, incorporating: (1) the development and expansion of supraglacial ponds between the 1950s and 1990; (2) accelerated expansion of Tasman Lake at a rate of 38 000 m^2 a^{-2} due to increased calving and melt between 1990 and 2006; and (3) a sharp increase in lake growth and retreat between 2006 and 2007 followed by continued rapid retreat conditioned by flotation and buoyancy–driven calving. The intervals between these phases of retreat mark key thresholds in the evolution of Tasman Lake. Namely, the transition from melt below supraglacial debris to the expansion of supraglacial ponds, through to the coalescence of ponds and the rapid retreat of Tasman Glacier via calving retreat. These thresholds can also be represented in a four stage model of proglacial lake evolution that has been proposed for glacier of the *Aoraki*/Mount Cook National Park (Robertson, 2012) and provides a mechanism by which the processes acting at each stage can be assessed. Importantly, this four–stage model (and others like it) indicate that after responding to initial climate forcing that leads to downwasting of the glacier surface, lake expansion and retreat occurs independent of climate until basin morphology allows for mass flux at the terminus to equilibrate.

Understanding the processes and mechanisms operating throughout the calving retreat of Tasman Glacier therefore provides insights into the response of debris–covered freshwater–terminating glaciers to changes in glacier dynamics, geometry and proglacial water body characteristics. The results presented in this chapter are consistent with previous observations of buoyancy–driven calving at similar freshwater calving glaciers (Kirkbride, 1993; e.g. Warren et al., 2001; Boyce et al., 2007; Robertson, 2012). Indeed, the importance of terminus thinning (due to downwasting and decreased ice supply and retreat into deeper waters), basin morphology and short–term perturbations in proglacial water–level (associated with increased rainfall) appear to be key parameters that condition buoyancy–induced calving. Future research focussing on the controls on calving at Tasman Glacier at shorter time–scales (e.g., sub–annual and individual event) are needed to identify how processes and rates of calving are affecting the long–term trends in glacier retreat and lake expansion in response to the parameters causing buoyancy–driven and other calving events. Some of these key factors and concepts are explained in the following chapters.

Chapter 5: Analysis of sub–annual retreat and iceberg calving at Tasman Glacier, 2011–2012

5.1 Introduction

A gap in the current literature exists that allows linking short–term variations in calving and calving processes to the longer–term retreat of water–terminating glaciers such as Tasman Glacier. The goal of this chapter is to develop the first comprehensive dataset of calving over a sub–annual time–frame as a base to answer the following research questions:

1. What is the temporal distribution of calving at Tasman Glacier over a year of study?
2. Are there any spatial or temporal patterns?
3. Are there any differences between types or magnitudes of calving events?
4. Are there any key factors controlling observed patterns?

A time–lapse camera overlooking Tasman Glacier to monitor calving events between October 2011 and November 2012 serves as the key instrument in these quests. Time–lapse imagery allows for the identification of patterns in calving (such as temporal distribution and number of events) at seasonal/monthly/daily time–scales. The high sampling rate also provided an excellent opportunity to describe how iceberg calving varied spatially, the mechanisms controlling calving, and how significant each event (i.e. calving magnitude) was to terminus evolution and glacier retreat. This data can be compared with other observational datasets, such as climate and proglacial lake characteristics, to better understand the relationships between calving and external forces acting on the glacier and its calving margin.

5.2 Background

To better understand calving processes, calving events need to be observed in more detail so that the controls and triggers of individual calving events can be identified (Chapuis et al., 2010). The inherent dangers and difficulties of obtaining data directly from calving margins have limited the ability of researchers to study calving events directly (Benn et al., 2007b). Recently, focus has shifted from describing the results of calving at water–terminating glaciers

(i.e. the calving rate), to identifying the distribution of individual calving events at temporal scales greater than those achieved through the use of satellite imagery and aerial photography. For example, several researchers have utilised time–lapse imagery (e.g., Chapuis et al., 2010; Rivera et al., 2012), direct visual observation of termini (e.g., O'Neel et al., 2003; Chapuis and Tetzlaff, in press), and seismic detection of iceberg calving (e.g., O'Neel et al., 2007; Amundson et al., 2008) to describe calving at high temporal and spatial resolution. In these studies, the distribution of individual calving events could be determined at hourly, daily, monthly and seasonal time scales. It has been shown that at tidewater calving margins the temporal distribution of calving is highly dynamic and episodic in nature, with significant differences in the distribution of calving in relation to the magnitude (i.e. size) of the calved sections (e.g., O'Neel et al., 2007; Amundson et al., 2008; Chapuis et al., 2010).

At freshwater–terminating glaciers research to characterise the temporal and spatial distribution of calving at shorter then annual scales has been somewhat limited. The majority of studies have focused on annual calving rates (e.g., Brown et al., 1982; Sikonia, 1982; Funk and Rothlisberger, 1989; Warren et al., 1995b; Naruse and Skvarca, 2000; Warren and Kirkbride, 2003; Röhl, 2006) as the calving rate at freshwater margins is thought to be at least an order of magnitude lower than at tidewater glaciers (Warren et al., 1995b; Warren and Aniya, 1999; Skvarca et al., 2002; Warren and Kirkbride, 2003; Haresign, 2004; Benn et al., 2007b).

At Tasman Glacier, iceberg calving occurs across a wide range of temporal and spatial scales. The lateral size of individual calving events varies by almost 5 orders of magnitude, ranging from very small (sub–metre) to very large events (encompassing the entire width of the terminus *c.* 1 km across). However, temporal variations in calving freshwater–terminating glaciers remain poorly characterised, with only annually derived calving rates available based on repeated satellite imagery (e.g., Strong, 2008; Quincey and Glasser, 2009; Dykes et al., 2011) and short–term process based studies (e.g., Purdie and Fitzharris, 1999; Röhl, 2006). The only estimate of calving frequency at Tasman Glacier comes from Röhl (2005, 2006), who estimated that between 2000 and 2003 calving events that encompassed the entire vertical height of the subaerial ice cliff at a single location occurred every 4–6 weeks.

5.3 Methods

During the study period of October 2011 to November 2012, several techniques have been utilised to identify and characterise the temporally– and spatially–variable calving events at Tasman Glacier. As first–hand observations for the 12–month study period were deemed to be unrealistic, a time–lapse camera was deployed overlooking the terminus. This was coupled with

the use of satellite imagery to determine changes in the planar geometry and area of the glacier during the study period. Time–series data from a water–level and temperature logger, and two automatic weather stations located within the region of Tasman Glacier were also used.

5.3.1 Terminus and lake mapping

The terminus position and geometry of Tasman Glacier for the year October 2011 to November 2012 was digitised from georeferenced multispectral ASTER (Advanced Spaceborne Thermal Emission and Reflection) satellite imagery in ESRI ArcGIS. ASTER imagery was orthorectified and displayed as false–colour images of the Near InfraRed (NIR) bands to allow for the easy distinction between the debris–covered terminus of Tasman Glacier, and Tasman Lake. NIR multispectral bands of ASTER imagery have a pixel resolution of 15 m, allowing for the digitisation of the terminus region to within an accuracy of ± 1 pixel. Changes of terminus position less than 15 m can be assumed to be true if they are matched to retreat identified by a secondary source (e.g., time–lapse photography). Seven images were used to quantify the terminus position and geometry: 03/03/2011, 01/01/2012, 22/03/2012, 22/04/2012, 24/05/2012, 11/06/2012, and 01/01/2012. The timing of ASTER image acquisition and image quality meant that the temporal coverage throughout the study period (October 2011 to November 2012) did not match exactly with time–lapse imagery. Where several images were available over short periods of time during the study period a monthly spacing of satellite images was maintained where possible.

The perpendicular distance (L) between terminus positions in successive images was measured at a spacing of 50 m along the initial terminus position to calculate the change in the terminus position at each location (Figure 5.1). Retreat of the glacier was defined as positive values and glacier advance as negative values of the partial differences $\Delta L/\Delta t$, where t is image acquisition time. Spatially averaged values of L for the three aspect regions (the western embayment, eastern embayment and southern ice cliff, see section 5.3.4.2 for more detail) were also investigated to describe a mean perpendicular change in terminus position (L_{mean}) for these regions. Time–averaging at daily to annual scales allowed the mean rate of change ($u_r = \Delta L_{mean}/\Delta t$) for each image interval to be computed for the three aspect regions.

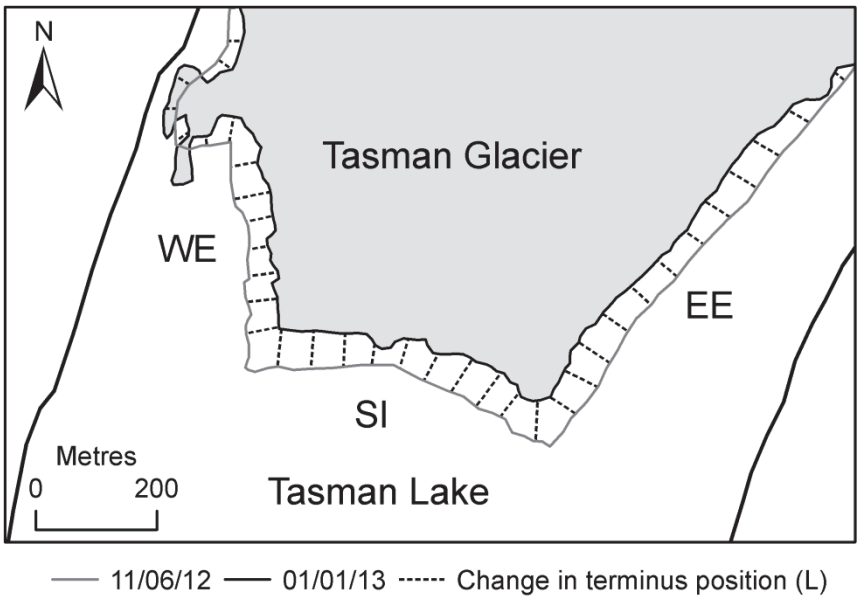

Figure 5.1: Map showing an example of how retreat of the terminus of Tasman Glacier was calculated by measuring the perpendicular distance between image dates (*L*) at a spacing of 50 m along the initial terminus position. Also shown are the three regions that are used to analyse spatial variations in retreat; WE is western embayment, EE is eastern embayment and SI is southern ice cliff (see section 5.3.4.2 for more detail).

5.3.2 Water–level and temperature

Changes in lake level were recorded to describe the response of Tasman Lake to water inputs (e.g., meltwater and rainfall) and the effect of changes in lake level to calving at Tasman Glacier. Fluctuations in water–level and temperature of Tasman Lake were recorded using an HOBO® U20 water–level logger, deployed at the southern end of Tasman Lake (Figure 5.2). The logger operated during the entire study period, from October 2011 and November 2012. Logging intervals ranged from 2 to 30 minutes depending on the time between surveys. Lake temperature data was recorded by the logger throughout the study period, and was calibrated to an accuracy of ± 0.37 °C over the range of -20 °C to 50 °C (Onset Computer Corporation, 2006). Previous research of lake temperature for Tasman Lake has shown great spatial and temporal variability (e.g., Hochstein et al., 1995; Röhl, 2005). At the logger location, Röhl (2005) noted that the greatest temperature decreases were between 5 to 20 m below the lake surface, indicating that lake temperatures recorded by the logger (located approximately 4 m below the waterline) in this study describe the general changes in temperature for the upper part of the water column.

Data was retrieved during five survey checks (see Table 5.1 for times). After data retrieval it was not possible to reset the water level logger to the same depth, and as a result relative lake level changes are reported here. Normalisation of lake level data was accepted by assuming that the last water–level pre–retrieval and first water–level recorded post redeployment were the

same, as redeployment occurred within a 20 minute time–frame. This provides a continuous record of relative lake level changes throughout the study period.

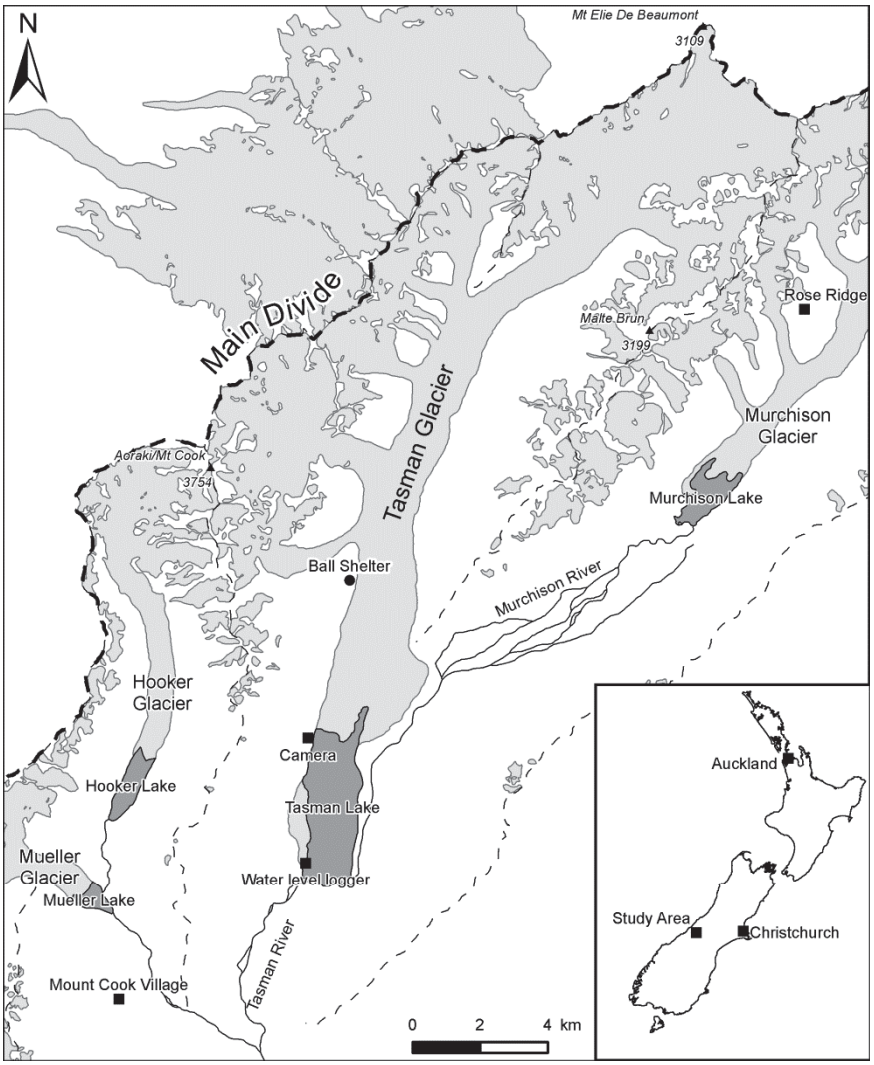

Figure 5.2: Location of Tasman Glacier and Tasman Lake showing the surrounding glaciated region (light grey) and the position of the time–lapse camera, water level logger and automatic weather stations at Mount Cook Village and Rose Ridge. Major ridgelines are highlighted by dotted lines. Proglacial lakes are shown in dark grey.

5.3.3 Climate

Climate data used in this study was obtained from NIWA (National Institute of Water and Atmospheric Research) and Meridian Energy Ltd., who operate automatic weather stations (AWS) at Mount Cook Village (MCV) and Rose Ridge (RR) respectively (Figure 5.2). The MCV AWS is located at 765 m a.s.l, approximately 7 km southwest of the Tasman Glacier terminus. The data obtained included maximum and minimum air temperature and precipitation, recorded on an hourly and daily basis. Data was retrieved for the entire study period from the CliFlo climate database (http://cliflo.niwa.co.nz). The RR AWS is located in the Murchison

Valley, east of the Tasman Glacier at an elevation of 1940 m a.s.l (Figure 5.2). RR data was used to identify climate variations in the upper Tasman Glacier as well as the Murchison Valley. Climate data obtained from RR included daily precipitation and mean air temperature. The data obtained from RR is considered by Meridian Energy Ltd. to be of commercially sensitive nature, and as a result permission was only given to report monthly averages here.

5.3.4 Direct record of individual calving events

To directly record calving events a Mobotix™ M24M–Sec 3 M pixel colour digital camera, with an expandable memory of up to 32 GB, was mounted on a tripod and placed on top of the western lateral moraine (Figure 5.3). During the study period the camera was powered by an external power supply. Initial plans to upload imagery data remotely and in real–time were abandoned because of poor 3G mobile phone reception at the observation site during the study period. Instead, images were retrieved sequentially during each of five survey/equipment–check visits. The camera had the largest possible view of the terminus that provided suitable spatial resolution to identify and classify calving events. All care was taken in locating and stabilising the time–lapse camera over the entire study period. However, difficulties were encountered from wildlife adjusting the pointing angle of the camera, snow, dust, battery failure, and the need to relocate the camera approximately 3 metres at the start of the third survey period due to the collapse of a section of the moraine wall into Tasman Lake. Degradation in image quality over some periods was also encountered due to kea (*Nestor notabilis*) scratching the lens cover of the camera, requiring it to be changed three times throughout the study period during camera inspections. The camera operated during daylight hours for 390 days, recording images at 1 hour, 30 minute, or 5 minute sampling intervals (Table 5.1). The increase in sampling interval over the study period was used to better constrain the timing of calving events.

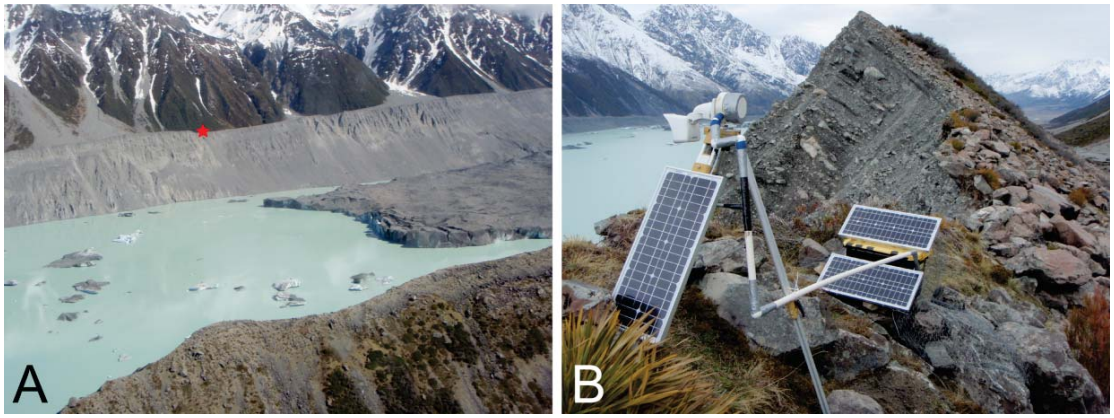

Figure 5.3: (A) Photograph showing the position of the time–lapse camera set atop the unstable western lateral moraine (star). The camera was later moved from this position as the section under the power supply box collapsed into Tasman Lake. (B) Photograph of the time–lapse camera setup on the western lateral moraine.

Table 5.1: Overview of the time–lapse image record for Tasman Glacier, showing the start and end date between survey periods, number of days of operation, and sampling interval.

Survey period	Start date	End date	Number of Days	Sampling interval (min)
1	27/10/11	08/12/11	42	60
2	08/12/11	03/02/12	57	30
3	03/02/12	03/26/12	52	5
4	03/26/12	03/05/12	38	5
5	03/05/12	20/11/12	201	5
Total	27/10/11	03/05/12	390	-

The minimum detection size of a calving event was determined by the camera resolution, the distance between the camera and the calving location, and quality of the image (e.g., cloud coverage, lens scratches). Given optimal conditions (i.e. no scratches on the lens cover, image taken in the middle of a clear day, and the calving event occurring at the closest point to the camera) the smallest detectable event was estimated to be *c.* 5 m^3. However, across the entire study period a conservative lower bound estimate of the smallest detectable calving size was in the order of *c.* 20 m^3. Small calving events occurring in the close western embayment (see section 5.3.4.2) could be detected to a higher degree of resolution than events in the distant southern ice cliff and eastern embayment.

From the image record individual calving events were manually identified based on several features visible pre and post calving. Firstly, the visible loss of ice from a section of the terminus (Figure 5.4) was used to identify and constrain the size of the calving event. Post–calving geometry was often indicated by the presence of new 'blue' ice in the section of the ice cliff that calved (Figure 5.5). Secondly, the presence of waves emanating from the epicentre of calving (Figure 5.4) served to identify calving events that had occurred close to the time that an image was taken. Finally, the presence of new icebergs in Tasman Lake in the region immediately in front of the ice cliff confirmed calving. Icebergs ranged from sub–metre to hundreds of metres in size and often varied in colour based on their origin. For example, icebergs calved from the subaerial ice cliff are white in colour due to the presence of air bubbles (Figure 5.5), whereas basal ice is bubble–free and has a dark blue appearance (Figure 5.6). Intermediary colours represent ice from a position between the subaerial ice cliff and the basal zone, or when present on the subaerial ice cliff represent a recent calving event.

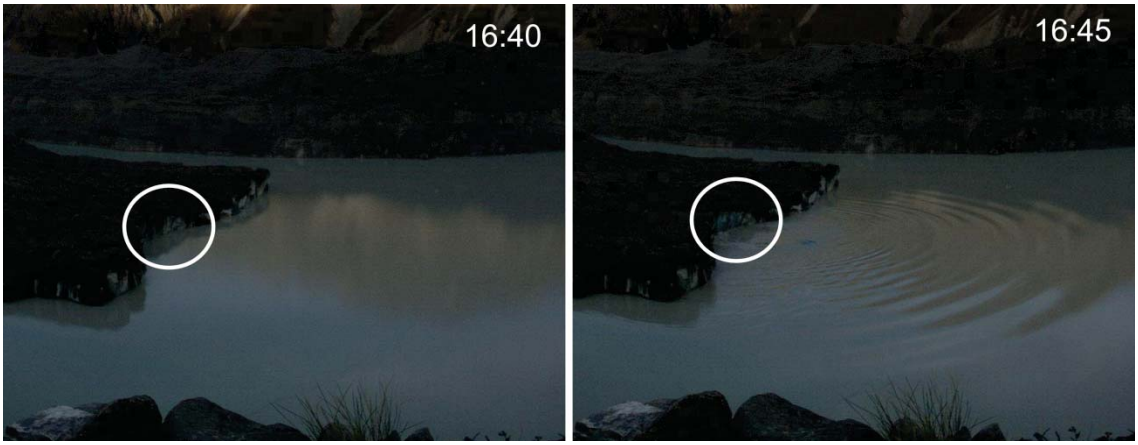

Figure 5.4: Sequential images from the time–lapse camera showing the visible loss of ice (circled) from the southern ice cliff on 24/04/12. The waves emanating from the epicentre of calving suggest that calving has recently taken place and aid in locating the calving event.

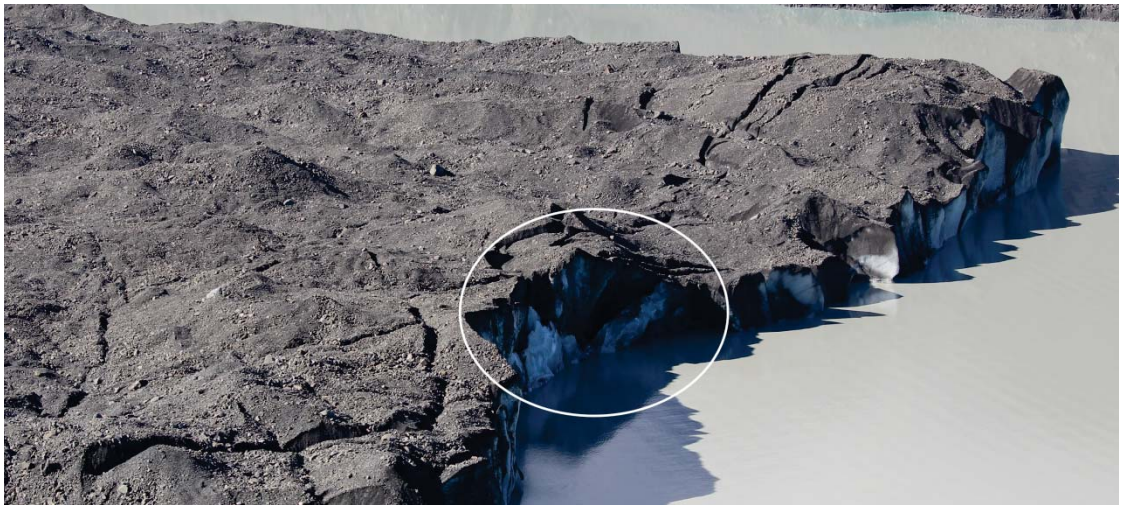

Figure 5.5: Photograph taken by the author of the terminus of Tasman Glacier on 28/04/12 after a series of calving events over multiple days (including the event shown in Figure 5.4). Note the newly exposed blue ice indicating recent calving in the centre of the ice cliff (circled) compared to the un–calved white ice along the rest of the ice cliff.

Figure 5.6: Deep blue basal ice present immediately after a large subaqueous calving event on 02/04/2012.

To characterise the temporal and spatial variations in calving each event was classified according to several physical parameters to provide a basis for further interpretation and quantification of calving at Tasman Glacier over the study period. The physical parameters used in this study were: the timing of calving, the region where calving took place (see section 5.3.4.2), the vertical extent of the calving event (see section 5.3.4.3), and whether a thermo–erosional notch (Röhl, 2006) had formed at the base of the subaerial ice cliff prior to calving. Pre–and post–calving geometry and terminus morphology was also noted to aid in further classification of calving events, but were not defined by specific categories. The mechanism leading to calving and relative size (magnitude) of an individual calving event was then inferred (section 5.3.4.5) to create a subjective measure of the controls and relative importance of calving on terminus evolution and retreat.

5.3.4.1 Timing of calving

The camera image frequency is at least an order of magnitude greater than the previously estimated rate of calving events at Tasman Glacier (e.g., Röhl, 2005; 2006). Thus, patterns in the temporal variability of calving can be understood at daily, monthly and seasonal time–scales. The timing of an individual calving event was assigned to the mean time duration between the images bracketing it. This provides an error estimate for the timing of an individual calving event. For example, a calving event observed during a period with a sampling interval of 60 minutes will have an error of ± 30 minutes for correctly identifying event time, whereas an event observed with a sampling interval of 5 minutes will have an error of ± 2.5 minutes.

Two special cases were used when assigning the timing of calving: (1) when a calving event obviously occurred at or immediately prior to an image being taken (Figure 5.7); or, (2) where calving took place while the camera was not operational (either at night or due to power failure). In the first case the timing of the calving event was approximated visually, with an error of one quarter the sampling frequency used. For example, an event occurring simultaneously with image capture with a sampling interval of 5 minutes will have an error of ± 1.25 minutes. The timing of calving events while the camera was non–operational was also assigned to the mean time between the images bracketing the calving. These events therefore have a significantly higher error (e.g., up to ± 240 minutes for night time events) associated with them.

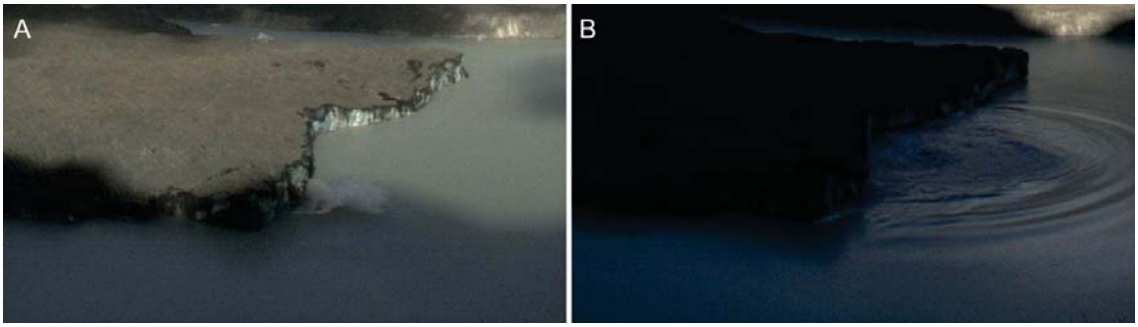

Figure 5.7: Cropped time–lapse images showing calving events occurring (A) simultaneous to the photograph, and (B) immediately before the image was taken. The spray of water and particles emanating from the point of calving can clearly be seen in (A), indicating image capture and calving occurring simultaneously. Waves emanating from the epicentre of calving shown in (B) suggest calving has taken place in the minute prior to image capture.

5.3.4.2 Calving regions

External variables (such as water–depth) vary significantly across the terminus, potentially affecting the distribution of calving throughout the study period. Division of the terminus into three regions, based on natural breaks in terminus geometry, was used to analyse whether any spatial variation in calving is present at Tasman Glacier. Surface morphology of the terminus in the three regions also differs (expressed primarily by the distribution of surface crevasses), potentially affecting the conditions required for a particular style of calving to dominate. The three regions of the terminus were (Figure 5.8): (1) the eastern embayment, (2) the western embayment, and (3) the southern ice cliff. Each region incorporated the subaerial ice cliff and ice distal subaqueous area.

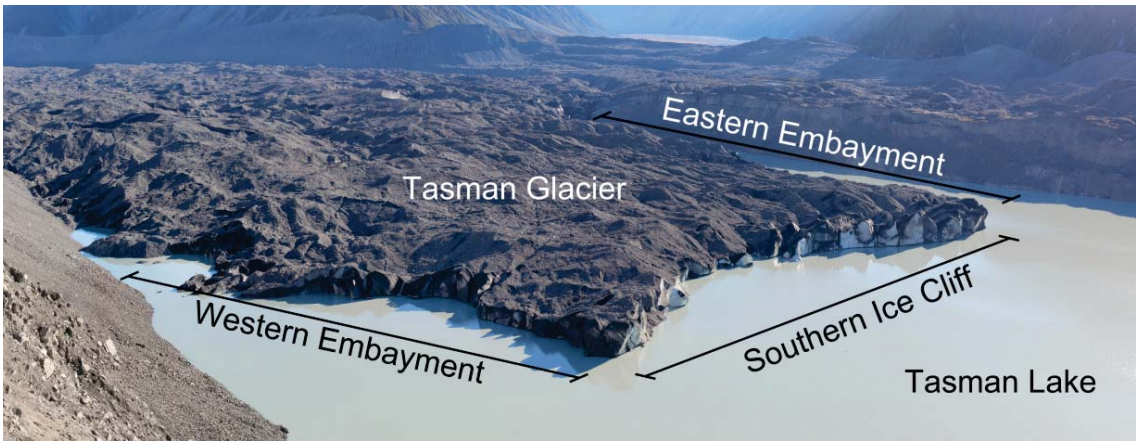

Figure 5.8: Photo of the terminus of Tasman Glacier on 13/12/12 showing each of the three spatial regions set using obvious natural breaks in aspect.

5.3.4.3 Vertical extent of calving

The vertical extent of a calving event provides an important parameter that is easily determined from time–lapse imagery to aid in further interpretation of calving events. The absolute height

of calving will naturally vary across all calving events and is typically associated with the height of the subaerial ice cliff (Röhl, 2005). To standardise a vertical height scale across the entire terminus a five point scale was used to assign the vertical extent of calving. This scale describes the section of the ice cliff that has calved, rather than measuring the absolute height of the calved section. These five categories are illustrated in Figure 5.9.

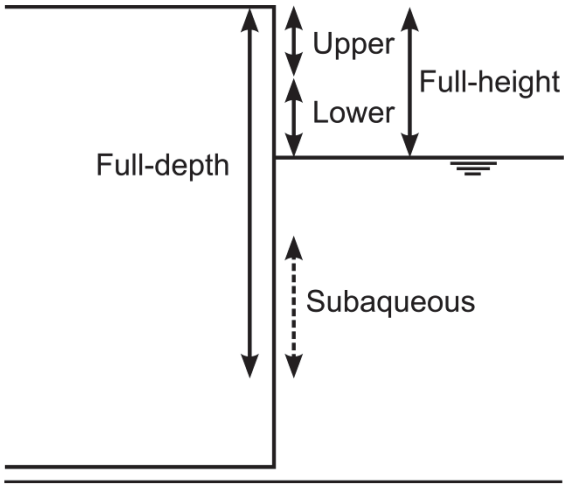

Figure 5.9: Diagram showing the five categories of vertical extent used in this study. Upper and lower refer to the upper and lower half of the subaerial ice cliff, respectively. Full–height is the entire subaerial ice cliff, whereas full–depth calving events comprise the loss of a height greater than the subaerial ice cliff height. Subaqueous refers to calving from the subaqueous section of the ice cliff or "ice foot".

The vertical extent of calving was primarily determined based on a comparison between pre– and post–calving images, with the colour of the resulting icebergs also used to identify the source location. Full–depth calving was distinguished by the large–scale nature of such events and incorporation of the subaerial ice cliff during calving (Figure 5.10).

Figure 5.10: Image showing icebergs ranging in colour from deep blue (basal ice) through to primarily white/dirty icebergs after a full–depth calving event at 13:05 29/04/12.

5.3.4.4 Mechanisms of calving

Calving of an individual iceberg may occur in many different ways. The way an individual iceberg–calving event occurs is an important indication of the underlying processes driving calving, whether directly controlled by glacier mechanism or other external variables. To understand how calving dynamics at Tasman Glacier vary over a range of temporal and spatial scales the mechanism of calving was inferred based on available data (time–lapse images and visual observation), previous studies at Tasman Glacier (Purdie and Fitzharris, 1999; Röhl, 2005, 2006) and observation from similar calving margins (e.g., Kirkbride and Warren, 1997; van der Veen, 2002; Benn et al., 2007b). From time–lapse images the mechanism leading to calving was interpreted using pre– and post–calving terminus geometry (e.g., vertical/concave/convex ice cliff), terminus morphology (e.g., crevasses was present prior to calving), vertical extent, and the presence of a thermo–erosional notch at the base of the ice cliff. From this information, four categories of calving mechanisms were used to describe all calving events. They were: (1) over–steepening of the subaerial ice cliff (e.g., Reeh, 1968; Hanson and Hooke, 2000; Benn et al., 2007b); (2) thermo–erosional notching undercutting the ice cliff at or below the waterline (e.g., Röhl, 2006); (3) buoyancy–induced calving (e.g., Lingle et al., 1993; Warren et al., 2001; Benn and Warren, 2002; Boyce et al., 2007); and (4) subaqueous calving (e.g., Motyka, 1997).

The conditions for classifying an event into one mechanism category were based primarily on the pre–calving geometry of the ice cliff. Over–steepening of the subaerial ice cliff prior to calving (characterised by a forward bending or concave subaerial ice cliff (Figure 2.12A)) led to such a classification (Figure 5.11A), irrespective of whether or not a thermo–erosional notch was present at the base of the ice cliff. Where a thermo–erosional notch was present (Figure 2.12B) and the pre–calving geometry indicated a vertical or convex ice cliff (Figure 5.11B), the calving style was assigned to thermo–erosional–notch–induced. Buoyancy–induced calving (Figure 2.12C) incorporated all events where flotation of the calved section prior to calving was noted (Figure 5.11C–E). Subaqueous calving incorporated calving events originating below the waterline (Figure 2.12D), identified by the presence of new dark blue icebergs present in Tasman Lake with the absence of any originating subaerial fracture (Figure 5.11F–G).

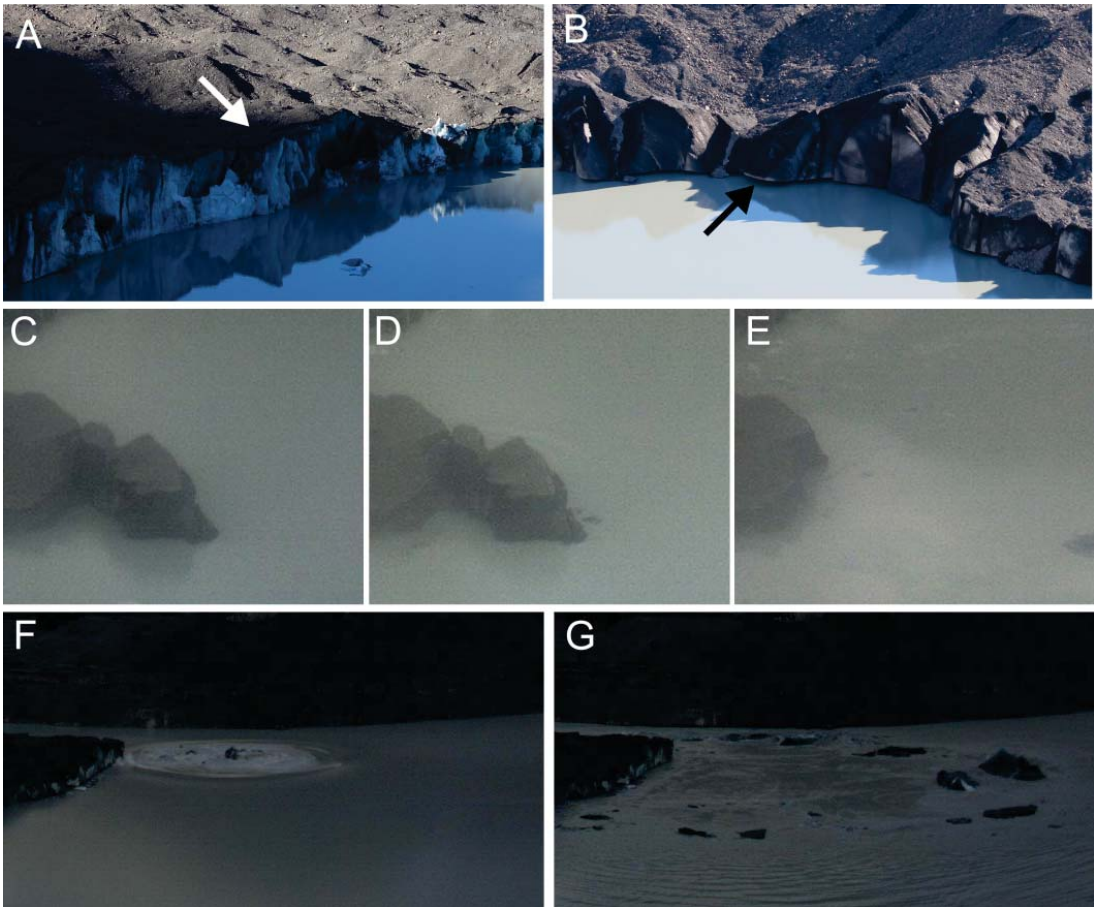

Figure 5.11: Examples of pre–calving terminus geometry and morphology for (A) Over–steepening of the subaerial ice cliff, (B) thermo–erosional notching undercutting the ice cliff at or below the waterline, (C–E) buoyancy induced calving, (F–G) subaqueous calving.

5.3.4.5 Calving magnitude and volume

The qualitative size of icebergs (representing calving *magnitude*) calved from Tasman Glacier was inferred to create an estimated volume of ice that is lost during calving events and is an integer with a minimum value of 1. The magnitude scale is intended to be approximately logarithmic (O'Neel et al., 2007; Bartholomaus et al., 2012) so that a differentiation can be made between smaller and larger events. Calving events of similar volumes were grouped so that magnitude 1 events were less than 10^3 m^3, up to the largest magnitude (18) events greater than 10^6 m^3. An open ended measurement scale was used so that natural variations in calving size could be identified (O'Neel et al., 2003; Chapuis and Tetzlaff, in press), with the error (variability) of the magnitude size estimated to be ± 1. Such qualitative assessments of event size have been used effectively by several researchers (e.g., Warren et al., 1995a; O'Neel et al., 2003; O'Neel et al., 2007; Bartholomaus et al., 2012; Chapuis and Tetzlaff, in press) to differentiate iceberg size and shed light onto the controls and importance of calving on terminus evolution and retreat.

From this open–ended magnitude scale, the average volume of each integer value was estimated based on the approximate iceberg dimensions (length, width, depth) of ten example events from each integer increment identified in time–lapse images. Where ten events were not identified for a given integer size all identified events of that magnitude were used. Dimensions were estimated to the nearest 5 m, potentially resulting in an overestimation of low magnitude and underestimation of high magnitude events. As a result, a conservative error was calculated as ± 10 m for each dimension (length, width, and depth) estimate for magnitudes 1–9 and ± 50 m for magnitudes 10–18. However, as estimated volumes cover 4 orders of magnitude (Table 5.2 and Figure 5.12) the impact of such overestimations on the overall significance of volume loss during the study period is not high. The geometric mean volume for each increment in the magnitude scale was then assigned to all events of that magnitude integer value, other than the estimated events, so that the distribution of volume loss could be assessed over the entire study period.

Table 5.2: Estimated iceberg volumes and errors for the perceived size of individual calving events. Several classes of magnitude were not observed throughout the study period and therefore do not have an estimate of volume.

Magnitude	Number of events	Mean volume (m^3)
1	10	283
2	10	1190
3	10	2718
4	10	7289
5	10	13537
6	10	17192
7	3	27901
8	5	73305
9	4	116960
10	-	-
11	-	-
12	1	1000000
13	-	-
14	1	1408000
15	-	-
16	-	-
17	-	-
18	1	6000000

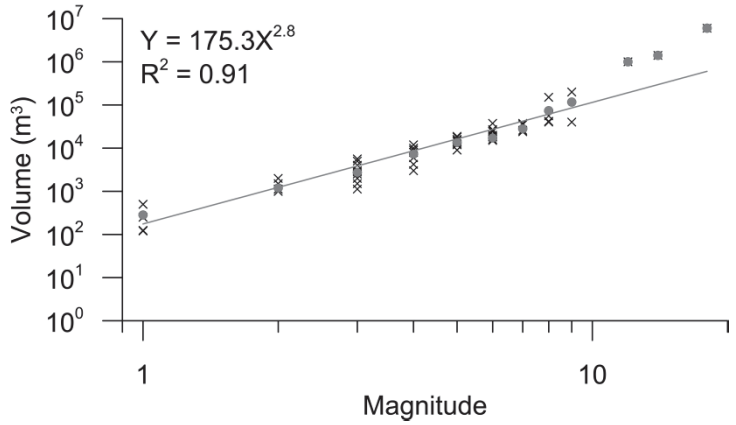

Figure 5.12: Distribution of volume measurements for the example events (crosses) in each magnitude increment (log–log scale). The mean for each event is also shown (grey circles) Volume up to magnitude 6 are based on ten example events for each magnitude. The limited number of data points for magnitude 1 and 2 events is an artefact of the resolution to which event dimensions could be determined (*c.* 5 m). Power–law fit and regression equation is also shown.

5.4 Results

5.4.1 Terminus geometry change

The terminus geometry of Tasman Glacier changed during the study period (October 2011 to November 2012), primarily as the result of iceberg calving. Changes in terminus position, determined from ASTER satellite images, are shown in Figure 5.13 and Table 5.3. Due to the intermittent nature of ASTER imagery acquisition, derived terminus positions did not match exactly with the study period and as a result changes in terminus position between March 2011 and January 2013 are shown to highlight the overall variability of retreat. From Figure 5.13 it is clear that over the entire study period the retreat of Tasman Glacier has been centred predominantly along the southern and western ice cliffs. Minor retreat along the eastern embayment ice cliff is also centred towards the southern end of the ice cliff, highlighting the fact that most major changes in terminus geometry have resulted in the up–glacier retreat of Tasman Glacier. The result of this has been the retreat of the glacier *c.* 223 m along the southern ice cliff (Table 5.3) at a rate of 0.57 m d^{-1} (206 m a^{-1}).

The greatest change in terminus position occurred between March 2011 and March 2012 (Table 5.3). Figure 5.14 shows time–lapse images that correspond to the March 2011 and March 2012 ASTER images. From the images it is clear that prior to October 2011 a large section of the terminus had already been lost. This was primarily centred along the southern ice cliff, with retreat of the terminus to the up–glacier side of a supraglacial pond that had developed on the lower glacier (Figure 5.13). Between October 2011 and January 2012 ice loss from Tasman Glacier appears to involve relatively minor retreat along the southern ice cliff and the southern

section of the western ice cliff (Figure 5.14). Retreat subsequently accelerated between January 2012 and June 2012 as the peninsula (that had developed on the western side of the southern ice cliff) was lost.

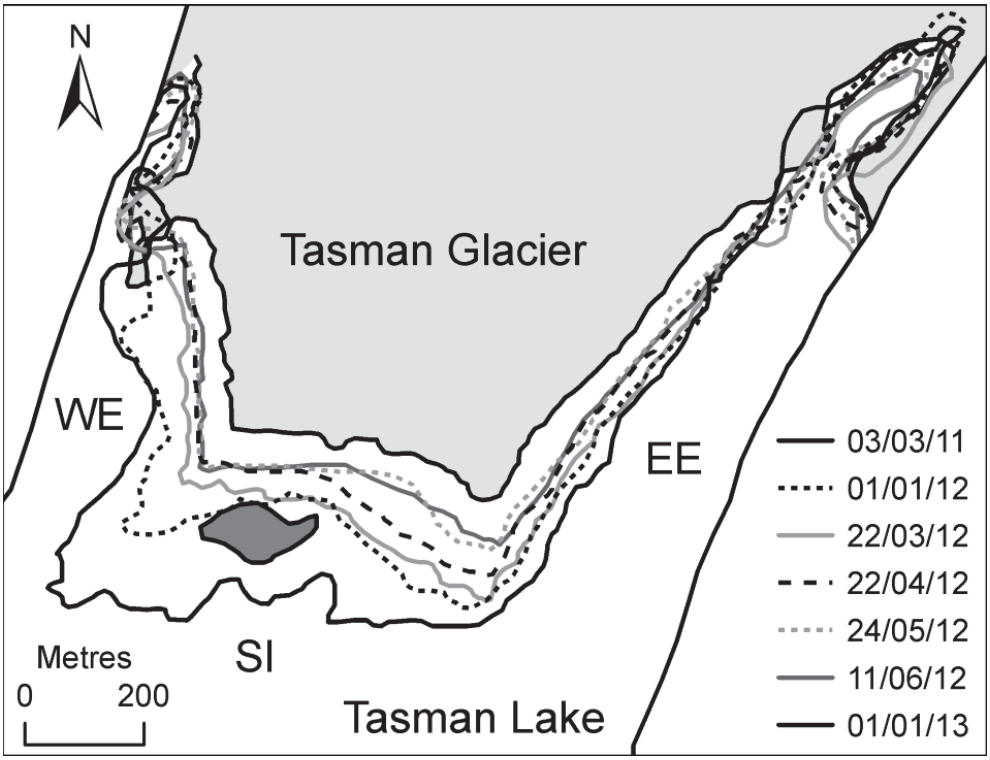

Figure 5.13: Changes in the terminus of Tasman Glacier between March 2011 and June 2012 from ASTER satellite imagery. Dark grey area on the lower terminus in March 2011 is a supraglacial pond. WE, is western embayment. SI, is southern ice cliff. EE, is eastern embayment.

Table 5.3: Retreat data of Tasman Glacier from ASTER satellite imagery for the three ice cliff regions used in this study, indicating the regional variability of retreat between March 2011 and January 2013. Positive values represent up–valley retreat, whereas negative values indicate the down–valley movement of the terminus (i.e. advance of the glacier).

Date	t	WE			SI			EE			Entire
		L_{mean}	L_{max}	u_r	L_{mean}	L_{max}	u_r	L_{mean}	L_{max}	u_r	T_L
	d	m	m	$m\ d^{-1}$	m	m	$m\ d^{-1}$	m	m	$m\ d^{-1}$	km
03/02/11											3.88
01/01/12	305	35 ± 27	81	0.11	110 ± 40	165	0.33	24 ± 9	37	0.07	3.54
23/03/12	82	33 ± 48	113	0.40	36 ± 30	133	0.43	2 ± 19	17	0.03	3.16
22/04/12	30	26 ± 7	36	0.88	37 ± 8	50	1.24	20 ± 6	30	0.66	3.05
24/05/12	32	11 ± 8	30	0.36	34 ± 24	74	1.07	11 ± 9	23	0.36	2.97
11/06/12	18	-4 ± 17	20	-0.21	6 ± 14	27	0.31	1 ± 14	22	0.04	2.94
01/01/13	209	34 ± 15	62	0.16	57 ± 10	70	0.27	44 ± 14	68	0.21	3.29
Total	467	137	347	0.28	280	494	0.57	102	197	0.21	

Note: t, is the interval between image dates; L_{mean}, is the mean retreat of the glacier between current and previous image dates; L_{max}, is the maximum retreat between image dates; u_r, is rate of retreat (L_{mean} divided by t to determine daily rate); T_L, is the perimeter length of the terminus in contact with Tasman Lake.

Retreat between March and June 2012 occurred almost entirely along the southern ice cliff, with comparably smaller losses centred along the southern margins of both the western and eastern ice cliffs (Table 5.3). Retreat (37 ± 8 m) along the length of the southern ice cliff was relatively uniform between March and April 2012 occurring at a rate of 1.24 m d^{-1}, with the only major retreat taking place between April and May 2012. This retreat was centralised on the eastern section of the southern ice cliff (Figure 5.13), and was significantly affected by a large calving event in this region on 29 April that lead to 74 m of retreat (Table 5.3).

The terminus of Tasman Glacier was stable between May and June 2012 (Table 5.3), with glacial advance evident along the central and western sections of the southern ice cliff (Figure 5.13). This is not considered to be an artefact of the short time period between images and the error associated with image digitisation, as when compared to images taken on those respective days (Figure 5.14), little change in the terminus is visible. Tasman Glacier may, therefore, be able to temporarily sustain glacial advance during periods of decreased calving.

Between June 2012 and the end of the study period u_r for the western embayment (0.16 m d^{-1}), southern ice cliff (0.27 m d^{-1}) and eastern embayment (0.21 m d^{-1}) were similar, as shown in Figure 5.13. A secondary effect of this retreat was the shortening of all three ice cliffs either through up–glacier retreat of the terminus shortening the western and eastern embayments, or due to the narrowing of the southern ice cliff. This may indicate that towards the end of the study period the southern sections of the western and eastern embayments and the southern ice cliff were subjected to a similar set of conditions. In comparison to the retreat of the southern section of the terminus, the northern sections of both embayments indicate a more complex pattern of advance and retreat likely linked to limited variability in the external variables (i.e. uplift of sections of the glacier, and higher ice velocities).

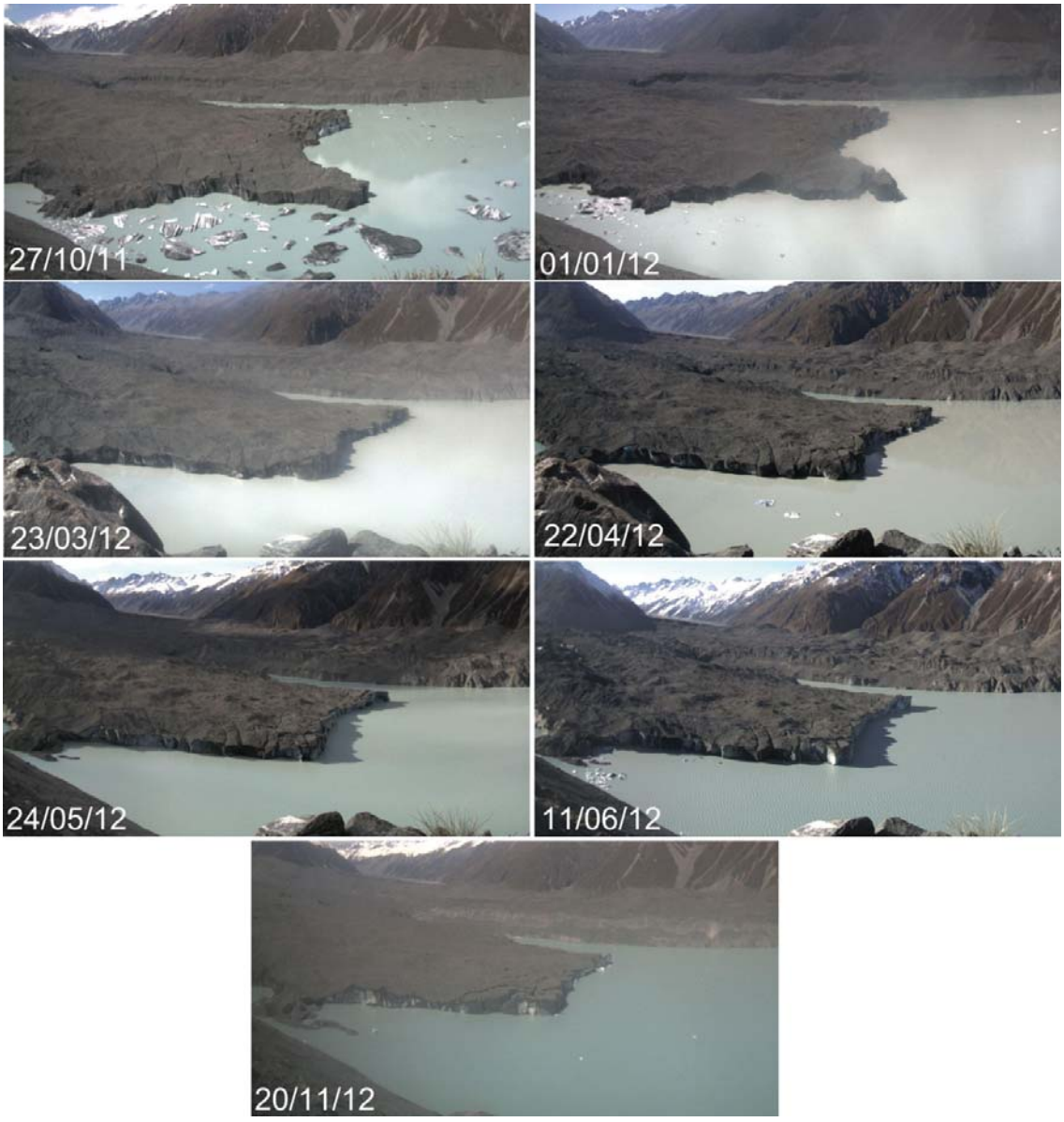

Figure 5.14: Time–lapse images taken at the beginning and end of the study, as well as at approximately the same time as satellite imagery used in Figure 5.13. Note that the pointing angle and location of the camera was changed between some images.

5.4.2 Temporal distribution of calving

Calving at Tasman Glacier occurred throughout the 390 days that the time–lapse camera was operational between 27 October 2011 and 20 November 2012. A total of 365 calving events were identified, at a rate of 0.94 events d^{-1}. However, the temporal distribution of calving events across the study period is not uniform, with calving events highly variable and broadly distributed. For example, calving events only took place on 196 days, with two or more events on 99 days of the 390 day study period. January and February 2012 had the highest number of calving events (72 and 48 respectively), with six occurring on 03/01/12 – the maximum number of events recorded in a day. Five calving events also took place on both 10/02/2012 and

29/04/2012. Figure 5.15 and Table 5.4 show the monthly distribution of calving events across the study period. They indicate that in general, the number of events increased moderately through November and December 2011, reaching a maximum in January 2012. Calving continued at an elevated rate throughout February 2012, although not to the same level as in January, and subsequently tailed off between March and June 2012. The number of calving events only increased again in October and November 2012.

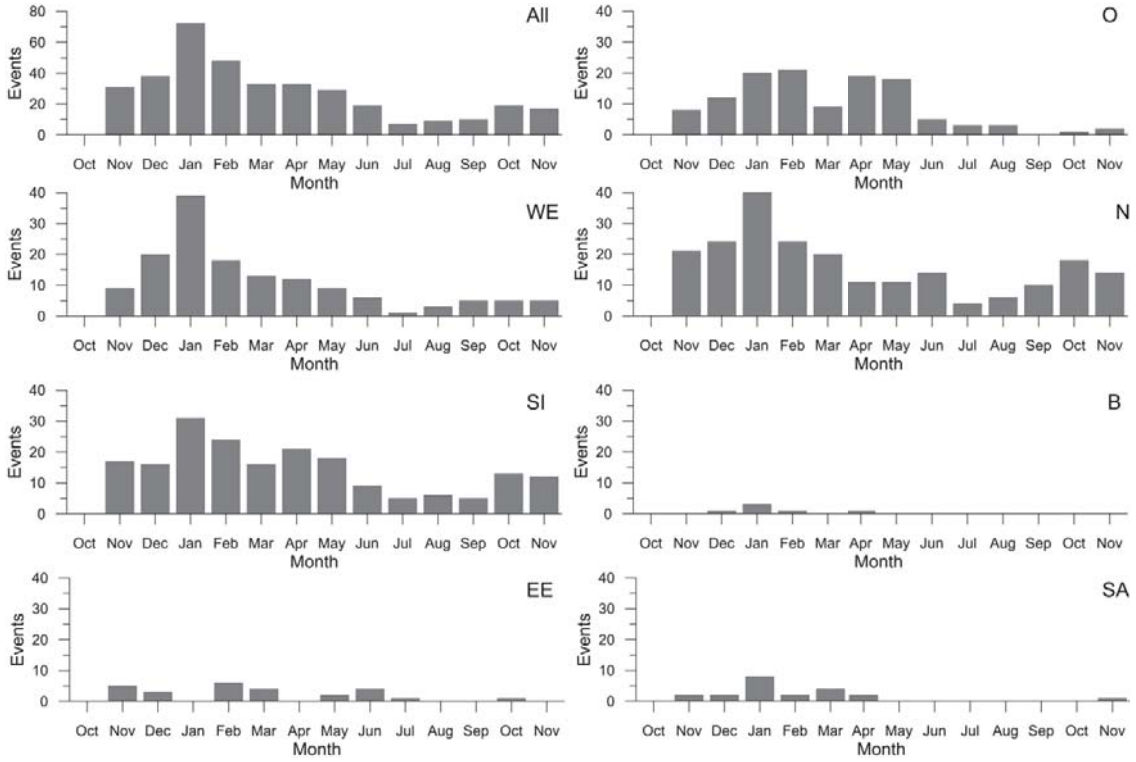

Figure 5.15: Calving events grouped by month showing the distribution of events for the entire data, regions and mechanism of calving. 'All' refers to the entire dataset, 'EE' is eastern embayment, 'SI' is southern ice cliff and 'WE' is western embayment. 'B' is buoyancy–driven calving, 'N' is thermo–erosional notch calving, 'O' is over–steepening calving, and 'SA' is subaqueous calving.

Table 5.4: Summary of calving events by month, showing the total number of events as well as a breakdown of calving events by the region they took place, and the mechanism of calving.

Month	EE					SI					WE					Total				
	O	N	B	SA	Total	O	N	B	SA	Total	O	N	B	SA	Total	O	N	B	SA	Total
Oct–11	-	-	-	-	-	-	-	-	-	-	-	-	-	-	-	-	-	-	-	-
Nov–11	-	5	-	-	5	7	8	-	2	17	1	8	-	-	9	8	21	-	2	31
Dec–11	-	1	-	2	3	10	6	-	-	16	2	17	-	-	19	12	24	-	2	38
Jan–12	-	1	-	-	1	15	13	2	1	31	5	26	2	7	40	20	40	4	8	72
Feb–12	-	6	-	-	6	18	6	-	-	24	3	12	1	2	18	21	24	1	2	48
Mar–12	-	3	-	1	4	8	7	-	1	16	1	10	-	2	13	9	20	-	4	33
Apr–12	-	-	-	-	-	16	3	1	1	21	3	8	-	1	12	19	11	1	2	33
May–12	1	1	-	-	2	13	5	-	0	18	4	5	-	-	9	18	11	-	-	29
Jun–12	1	3	-	-	4	4	5	-	-	9	-	6	-	-	6	5	14	-	-	19
Jul–12	-	1	-	-	1	3	2	-	-	5	-	1	-	-	1	3	4	-	-	7
Aug–12	-	-	-	-	-	3	3	-	-	6	-	3	-	-	3	3	6	-	-	9
Sep–12	-	-	-	-	-	-	5	-	-	5	-	5	-	-	5	-	10	-	-	10
Oct–12	-	1	-	-	1	1	12	-	-	13	-	5	-	-	5	1	18	-	-	19
Nov–12	-	-	-	-	-	2	9	-	1	12	-	5	-	-	5	2	14	-	1	17
Total	2	22	-	3	27	100	84	3	6	193	19	111	3	12	145	121	217	6	21	365

Note: EE is eastern embayment, SI is southern ice cliff and WE is western embayment, B is buoyancy–driven calving, N is thermo–erosional notch calving, O is over–steepening calving, and SA is subaqueous calving.

The monthly statistics highlight the seasonal variability of calving events at Tasman Glacier, with the vast bulk of events occurring from mid–summer into autumn. However, seasonal and inter–seasonal variability becomes more pronounced when the daily distribution of calving events are analysed. Figure 5.16 shows the number of calving events per day, with 5 and 30–day running means overlaid. The daily distribution of calving events during the study varied significantly, with periods of elevated activity superimposed over the seasonal variability. The 5–day running mean for all events in Figure 5.16 indicates that calving events tend to be grouped, with several calving events occurring within a short period (3–4 days), interspersed with periods of little or no calving. This pattern of calving event grouping is characteristic for the entire study period, but it is most distinct during December 2011 and April/May 2012.

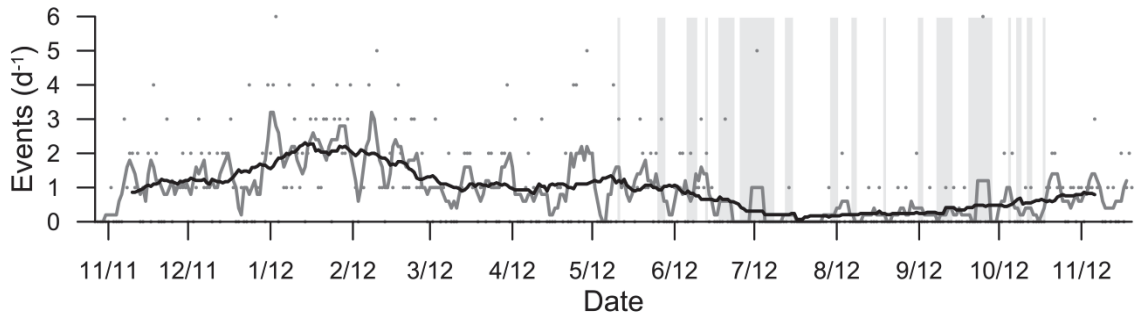

Figure 5.16: Plot showing the daily totals (dots) of calving events at Tasman Glacier. Also shown are the 5–day (grey line) and 30–day (black line) running mean across the entire study period. Grey bars represent days that the camera was not operational. The 5–day running mean shows the variability in calving over the study period, while the 30–day running mean indicates the general increase in the number of calving events during January and the start of February 2012.

In general, the rate of calving events increased dramatically in January 2012, with the mean number of events increasing from 1.0 to 2.3 events d^{-1}. Figure 5.16 illustrates that not only did calving events take place on almost every day throughout January 2012, but that events appear to be more grouped, with three or more calving events taking place on 15 separate days. Increased calving continued into February 2012, although the number of events did decrease towards the end of the month, as shown by the 30–day running mean in Figure 5.16. The number of calving events continued at a relatively steady rate of *c.* 1 event d^{-1} between March and May 2012. However, when the daily distribution of events across each month is considered, an increase in variability is evident. March daily calving data indicates that events were distributed throughout the entire month, typically dominated by one or two events on the days that calving occurred. In contrast, calving during April and May 2012 consists of periods of quiescence and increased activity, with an increase in the number of events associated with a single large calving event which destabilised a section of the terminus. The number of events diminishes throughout the winter months between June and September 2012. Several periods of

multiple calving events in a single day between June and October 2012 are an artefact of events occurring during periods where the time–lapse camera was non–operational. However, when the 30 day running mean is considered, these events do not have a significant impact on the rate at which calving events occurred, particularly in relation to periods of elevated activity.

5.4.3 Mechanisms of calving

Iceberg calving events were grouped into four categories of calving mechanisms to understand their diversity and potential links to underlying processes. The total number of calving events is shown in Figure 5.17, with the temporal distribution of calving events by mechanism of calving shown in Figure 5.18. Thermo–erosional notch–driven calving events totalled 217 events (Table 5.4), dominating calving over the study period with 60 percent of all calving events. Over–steepening calving events followed with a total of 121 events (33 percent), whilst subaqueous and buoyancy–driven calving totalled only 21 events (5 percent) and 6 events (2 percent) respectively.

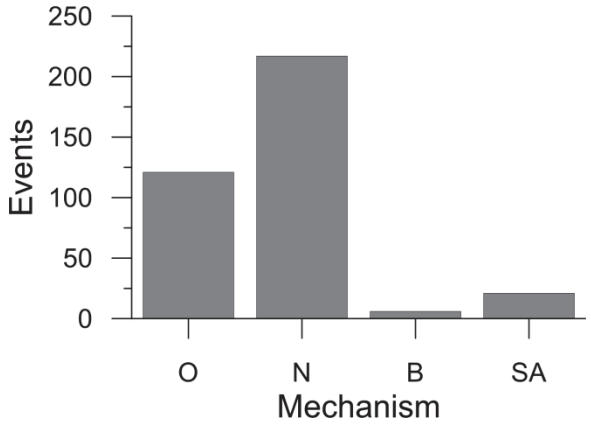

Figure 5.17: Graph showing the total number of calving events for each of the four mechanisms identified in this study. O is over–steepening calving, N is thermo–erosional notch calving, B is buoyancy–driven calving, and SA is subaqueous calving.

The temporal variability of the four different calving mechanisms can be clearly seen in Figure 5.18. Thermo–erosional notching and over–steepening calving events accounted for almost all events (93 percent) recorded throughout the study period (Figure 5.17). However, over–steepening calving events showed more temporal variability than thermo–erosional notching events. Over–steepening events increased steadily between November 2011 and February 2012, dropping sharply in March 2012, before returning to similar levels as January and February 2012 in April and May 2012. Between June and November 2012 over–steepening events became sporadic with a total of only 14 events taking place over the six month period.

In contrast, thermo–erosional notching events mirror the temporal distribution of calving events for the entire dataset (Figure 5.16). A maximum number of 40 thermo–erosional notching calving events were recorded in January 2012, after a gradual increase from 21 and 24 events in November and December 2011. Notch–induced calving subsequently declined in March 2012 (20 events) and again in April 2012 to just 11 events (Table 5.4). After a marginal increase to 14 events in June 2012 (Table 5.4) thermo–erosional notch induced events decreased to almost zero throughout the winter months, before increasing again during October–November 2012 (Figure 5.18).

Buoyancy–induced and subaqueous calving events were more sporadic throughout the study period, with the number of calving events considerably lower than over–steepening and thermo–erosional notching events (Figure 5.18). However, both buoyancy and subaqueous events are typically associated with larger calving events (section 5.4.7), and therefore have as much, if not more, impact on the stability of the terminus than smaller events.

Given the temporal distribution of calving mechanisms throughout the study period it is clear that the increase in calving events during January and February 2012 (Figure 5.16) is primarily the result of an increase in thermo–erosional notching events. Indeed, notch–driven calving events dominate all months apart from April 2012, where over–steepening events dominated.

From the daily counts of calving mechanisms (Figure 5.18), several periods of elevated activity occurred at a sub–monthly scale. For example, during periods of increased calving during January–February 2012, thermo–erosional notching events took place on successive days. This increased the total number of calving events during January–February 2012, even though these elevated periods of calving were interspersed with minimal activity (Figure 5.18). This pattern of “grouped” events is also evident in the distribution of over–steepening calving events. However, this grouping of events is not as distinct with only two periods of elevated activity in February and April and May 2012. These periods of elevated activity occurred at different times to the thermo–erosional events, indicating distinct controlling factors affecting the increase in each type of calving mechanism.

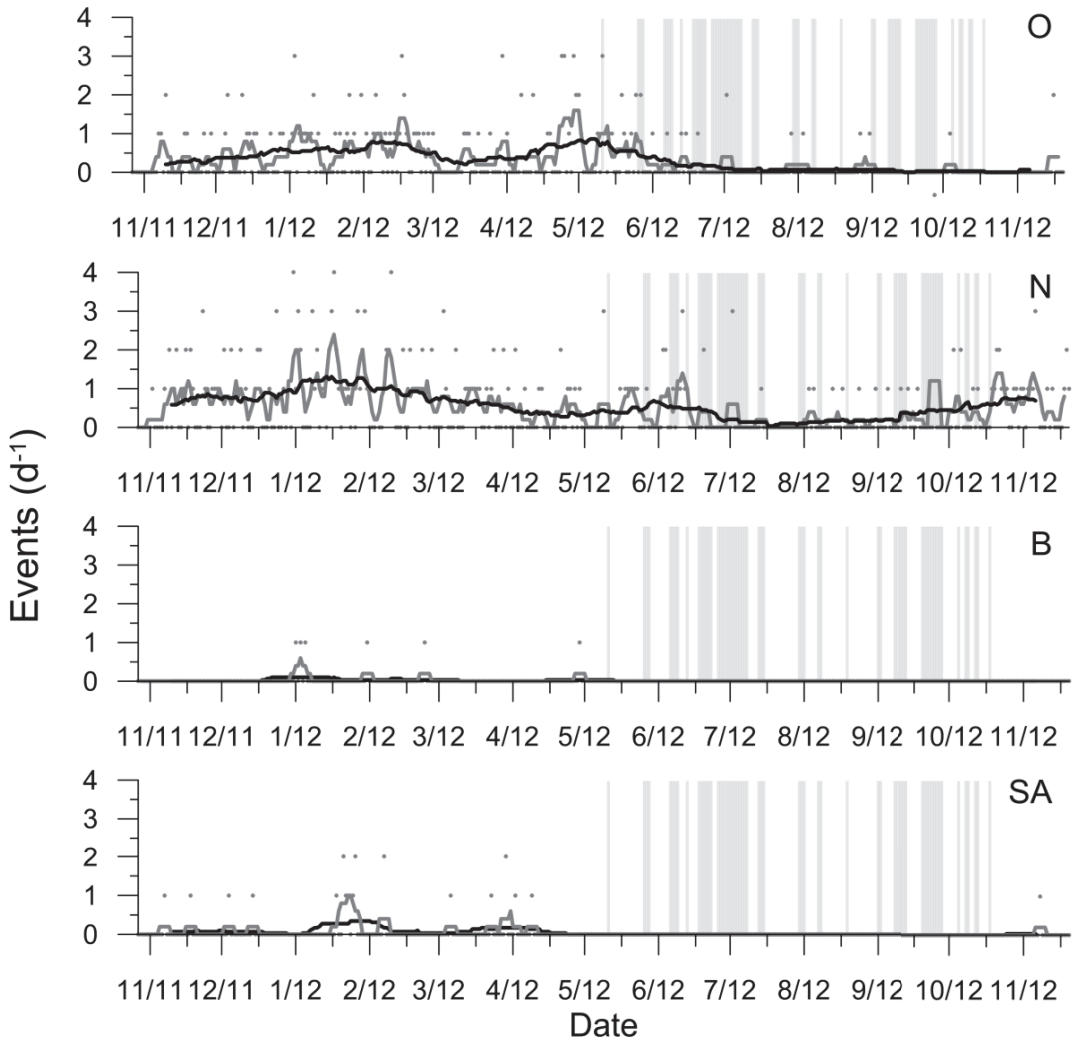

Figure 5.18: The number of calving events per day graphed by the mechanism of calving. Also shown are the 5–day (grey line) and 30–day (black line) running mean across the entire study period. Grey bars represent days that the camera was not operational due to factors such as interruption of the power supply. Note the periods of elevated activity able to be identified in over–steepening (O) and thermo–erosional notch (N) driven calving event graphs highlighting the grouping of events with respect to time. In contrast, buoyancy (B) and subaqueous (SA) events were less common.

5.4.4 Vertical extent of calving

Calving at the terminus of Tasman Glacier took place predominantly along the full–height and lower section of the subaerial ice cliff (Figure 5.19). This is unsurprising as notch–driven calving events were the dominant process. By definition, notching can only initiate calving of the lower section and full–height of the subaerial ice cliff, as a notch at the base cannot initiate calving in the upper section of the ice cliff. This is evident in Figure 5.20 where only calving of the lower section and full–height of the subaerial ice cliff were recorded between October 2011 and November 2012. This also accounts for the dominance of lower and full–height calving events across all vertical sections of the ice cliff (Figure 5.19). In contrast, over–steepening events covered both the upper and lower sections of the subaerial ice cliff as well as full–height

calving (Figure 5.9). Over–steepening events also appear to be inherently related to the high–magnitude buoyancy–driven calving events, particularly the buoyancy event on 29/04/12 where full–height over–steepening events increased significantly. Full–depth and subaqueous calving were intermittently distributed throughout the study period.

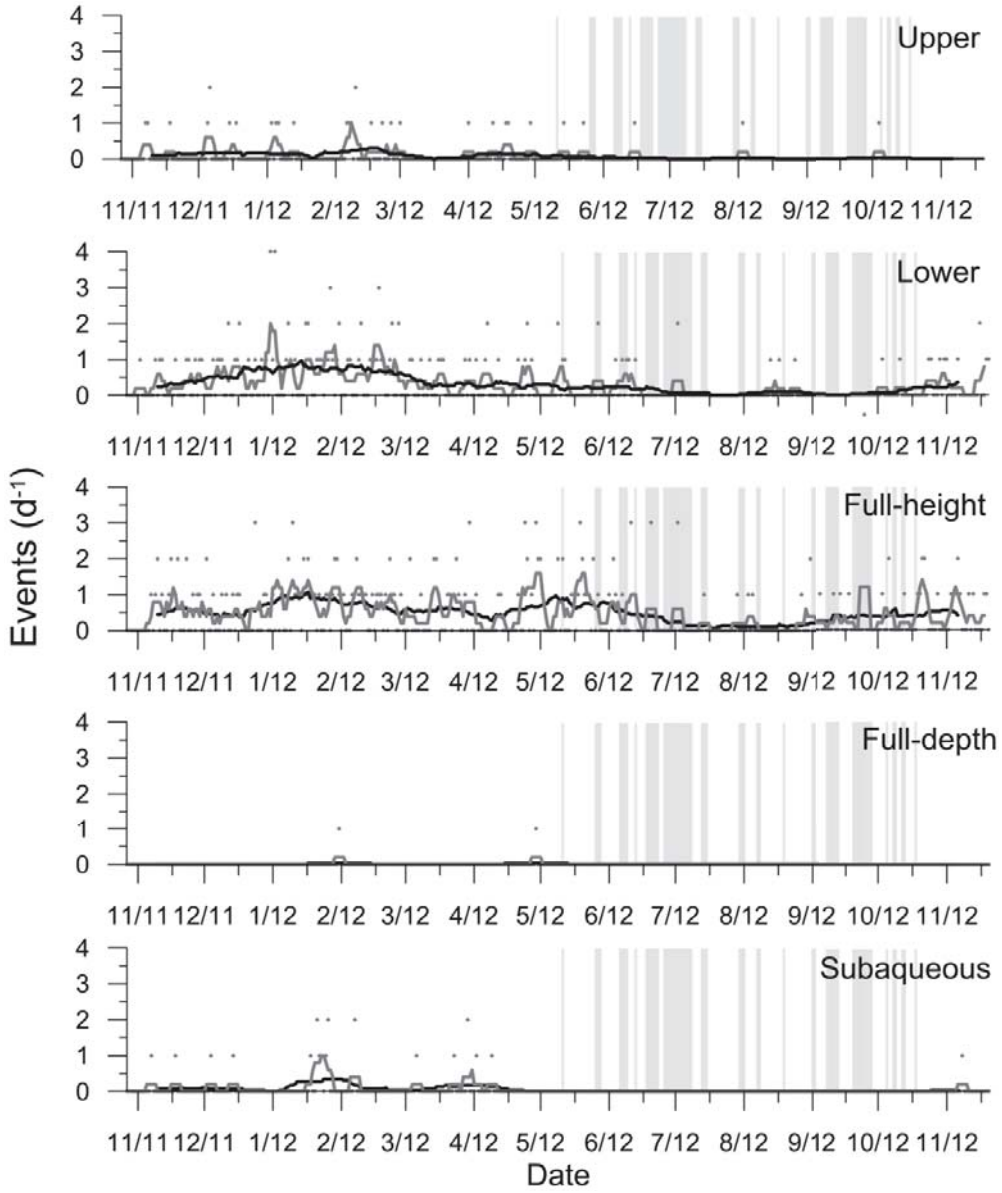

Figure 5.19: Daily distribution of the vertical extent of the calved sections of the ice cliff. Also shown are the 5–day (grey line) and 30–day (black line) running mean across the entire study period. Grey bars represent days that the camera was not operational. See section 5.3.4.3 for explanation of extents.

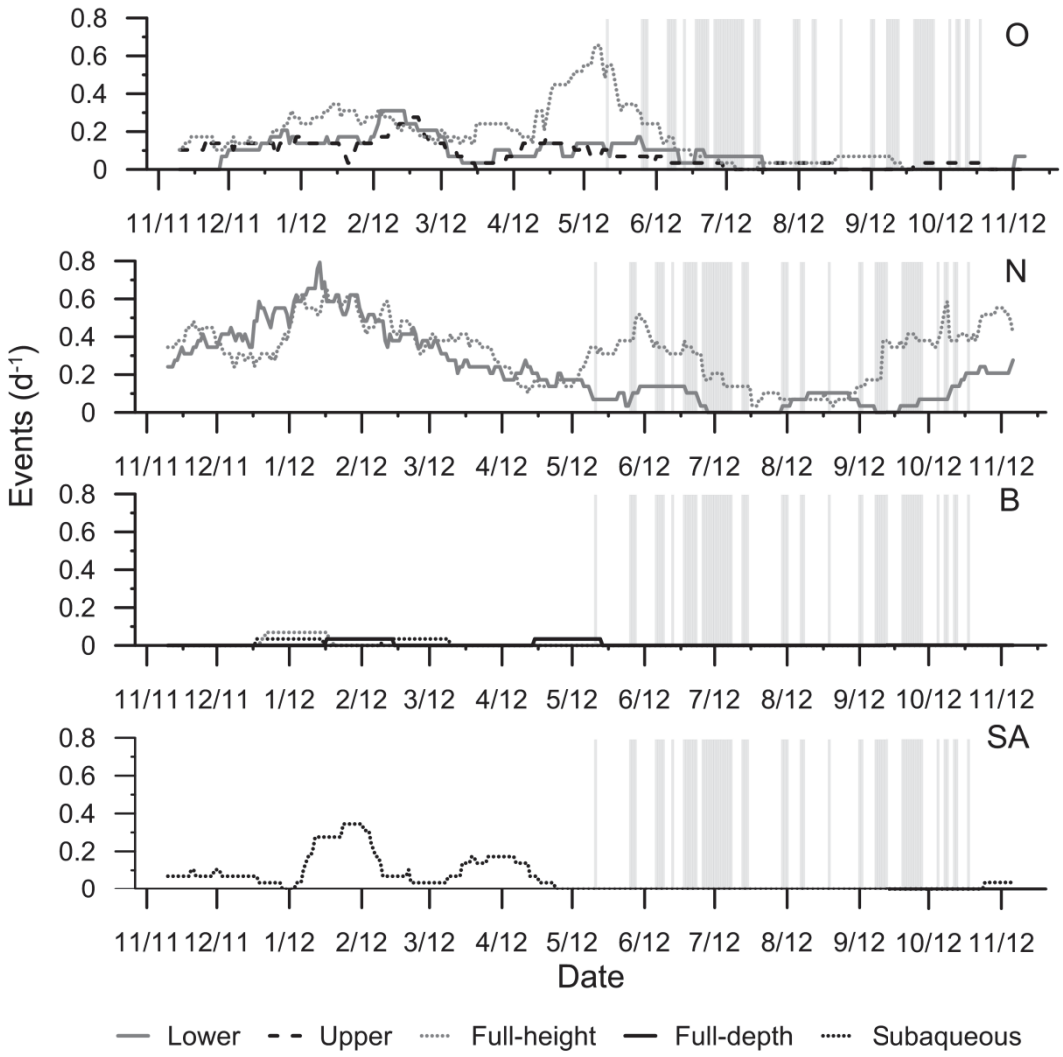

Figure 5.20: The distribution of 30–day running means for the different vertical sections of the ice cliff by the mechanism of calving. Grey bars indicate periods where the camera was not operational. Due to the parameters selected, notching events could only occur at the lower section and full–height of the ice cliff, while over–steepening events (O) could occur throughout the subaerial section of the ice cliff. N is notching events, B is buoyancy events, and SA is subaqueous events (see section 5.3.4.4).

5.4.5 Regional distribution of calving

Regional patterns of calving were evident during the study period, with the number of calving events within any one region appearing to fluctuate independently. The spatial distribution of calving within the western embayment and the southern ice cliff (Figure 5.21) in general mirrored the overall variability of calving shown in Figure 5.16, with both peaking in January 2012. However, throughout the entire study period the actual spatial distribution of calving events across the three regions showed inherent differences.

Calving within the western embayment increased rapidly throughout November and December 2011, peaking in January 2012 with 40 calving events. The number of calving events then

decreased to a relatively lower rate of between 6 to 12 events per month between April and June 2012, before decreasing to sporadic individual events throughout the majority of the rest of the study period.

The exception to this was a slight increase in events towards the end of the study in November 2012. In contrast, calving along the southern ice cliff fluctuated to a greater extent. Calving was steady throughout November and December 2011 prior to a sharp increase in calving events in January and February 2012. Calving marginally decreased in March 2012 before increasing again in April and May 2012. Again, a significant drop in calving occurred over the winter months before increasing again in October and November 2012.

The eastern embayment showed a sporadic distribution of calving events throughout the entire study period. However, this is likely to be an artefact of the limited view of the eastern embayment by the time–lapse camera, with the actual distribution of calving events more likely to follow a similar pattern to the western embayment.

The daily distribution of calving further informs the peaks in calving each region of Tasman Glacier (Figure 5.21). Within the western embayment, the peak calving in January 2012 resulted not only from an increase in the number of days that had calving events, but also an increase in the number events per day, with two or more events occurring on 16 separate days. Calving tailed off dramatically through March to April 2012, with little or no calving taking place for extended (up to 7 days) periods of time.

Along the southern ice cliff there was a greater distribution of daily calving events than occurred in the western embayment. Several periods of little or no activity were interspersed with single days where multiple calving events took place. Multiple–event days tended to be more isolated when compared to the western embayment and were distributed across all spring/summer months. One exception to this was an increase in the number of calving events per day at the end of April and start of May 2012.

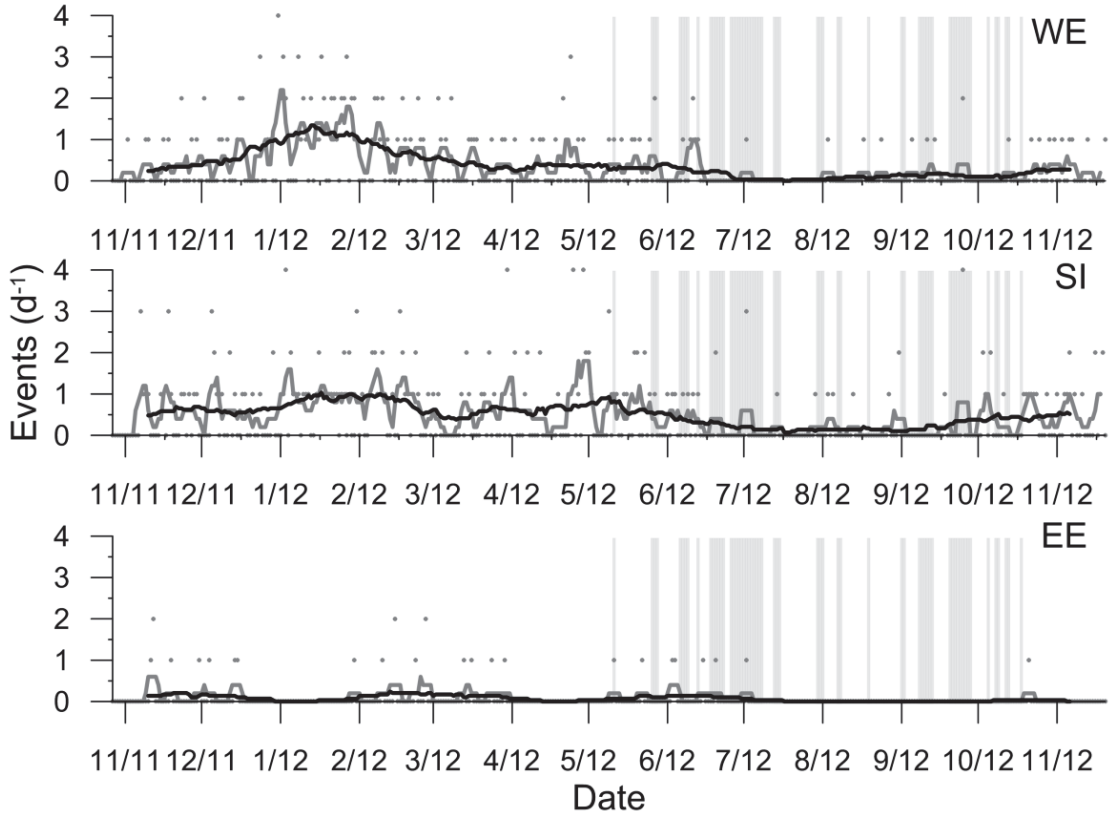

Figure 5.21: The number of calving events per day within each of the three regions. Also shown are the 5–day (grey line) and 30–day (black line) running mean across the entire study period. Grey bars represent days that the camera was not operational. The number of calving events increases during January and February 2012 in both the western embayment (WE) and southern ice cliff (SI). However, increases are more pronounced in the western embayment. Limited calving was observed along the eastern embayment (EE) due to the limited view of the time–lapse camera.

Within each sub–region calving was dominated primarily by a single mechanism (Figure 5.22 and Table 5.4), indicating a potential link to the factors controlling calving within each region. Thermo–erosional notching dominated calving in the western embayment, accounting for 81 of the 111 calving events (77 percent). Over–steeping and subaqueous calving events also took place in the western embayment, but the number of these events was insignificant when compared to notching events. Calving was more varied along the southern ice cliff with over–steepening the primary form of calving (100 events, 52 percent), followed by thermo–erosional notching (84 events, 44 percent). Calving within the eastern embayment was primarily associated with thermo–erosional notching (81 percent).

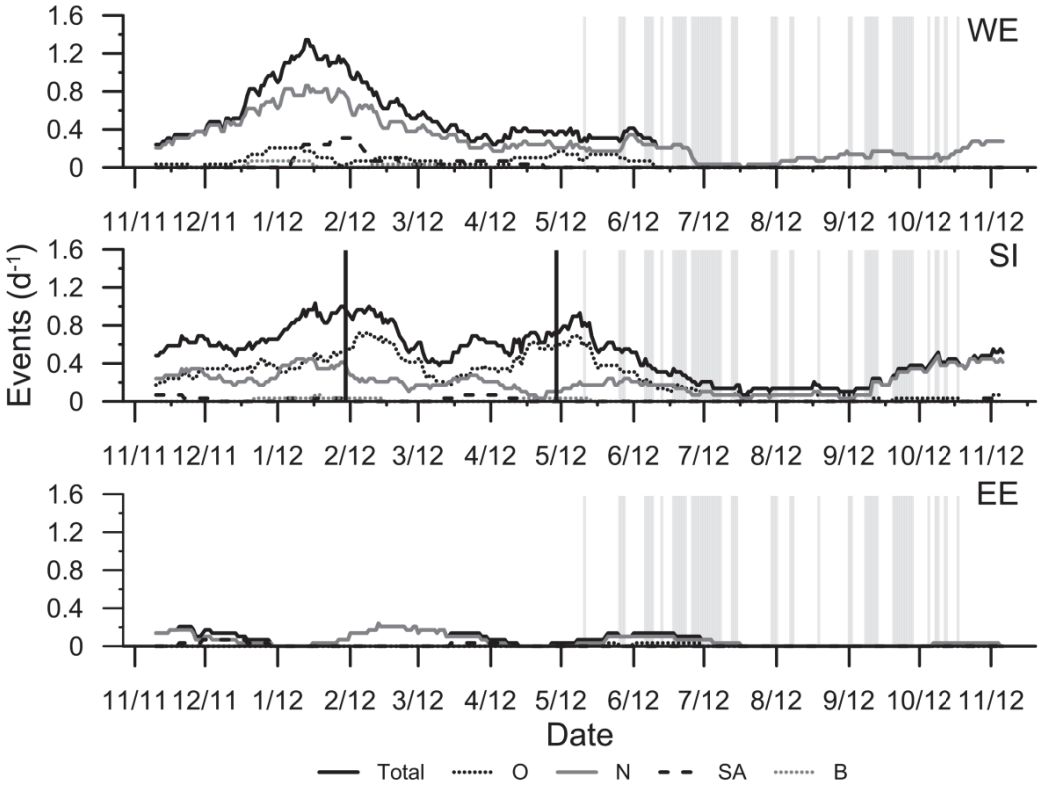

Figure 5.22: The distribution of the 30–day running mean calving frequencies by the four mechanisms used in this study along the western embayment ice cliff (WE), the southern ice cliff (SI), and the eastern embayment (EE). Grey bars indicate periods where the camera was not operational. Note that in the western embayment total calving frequency and notch driven calving mirror each other. Vertical black lines indicate the two largest volume calving events to occur.

The spatial distribution of the calving mechanisms throughout the study period highlights the variability of calving mechanisms with respect to time as well as the spatial setting. Thermo–erosional notching follows the same temporal distribution across the study period in both the western embayment and southern ice cliff, although notch driven calving was higher in the western embayment over the study period (Figure 5.22). In contrast, over–steepening calving events are almost entirely centred along the southern ice cliff, with only 15 events recorded within the western embayment (Table 5.4 and Figure 5.22). Over–steepening events along the southern ice cliff peaked in February 2012 (Figure 5.22), with a similar number of events also recorded in January and April 2012 (Table 5.4).

5.4.6 Diurnal distribution of calving

To assess the distribution of calving events diurnally, all events were grouped by the hour of the day in which they occurred. Calving during night time hours was included as a separate subset (Table 5.5) between the last image taken (2100 hours) and first image taken (0500 hours). Figure 5.23 shows the hourly counts of calving events. From this it is clear that calving events

were distributed throughout the day. However, the distribution is uneven, with significant differences between the morning, middle, and end of the day apparent. Calving events were predominantly grouped between the hours of 0900 and 1800, increasing gradually throughout the day, with peaks at 1200 and again at 1600 hours. Hourly counts of calving events tail off towards the end of daylight hours to levels similar to those found at the start of daylight hours. This skewed distribution suggests that some external force is acting on the terminus region affecting the distribution of calving.

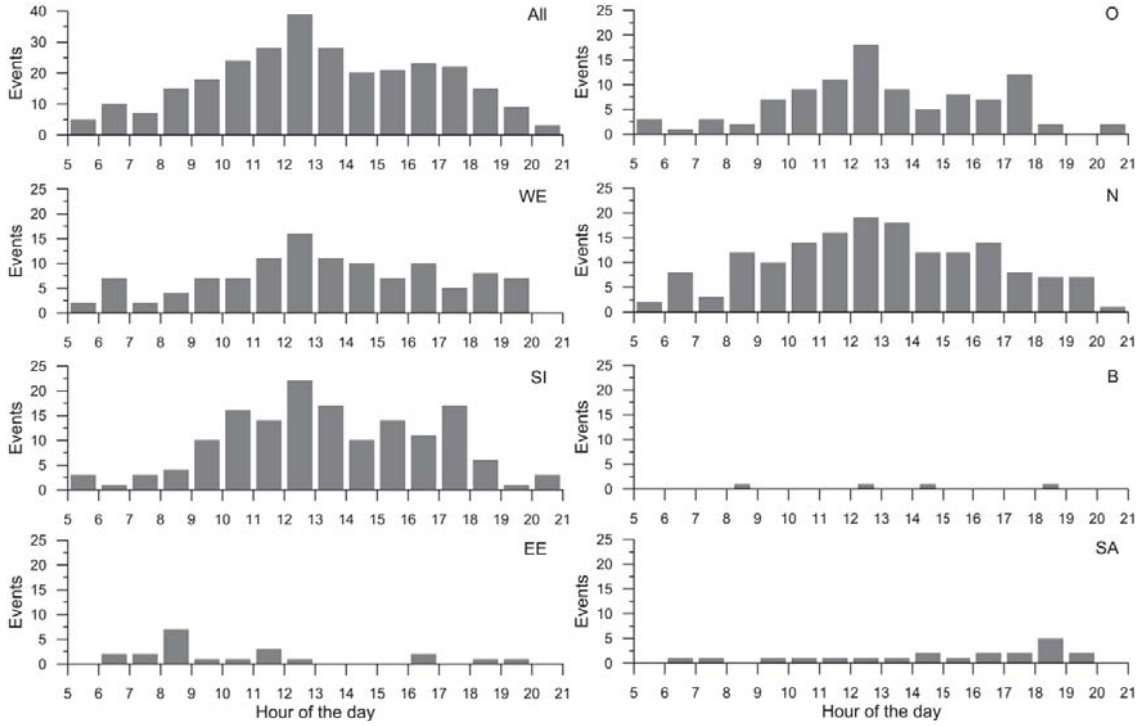

Figure 5.23: The distribution of calving events by the time of day that they occurred, showing the distribution of events for the entire data (All), regions (western embayment (WE), southern ice cliff (SI), and eastern embayment (EE)) and mechanism (over–steepening (O), notch (N), buoyancy (B), and subaqueous (SA) calving) of calving. The 78 calving events recorded during night time hours are not shown.

A total of 78 calving events were identified as taking place during night time hours the camera was not operational. Assuming an even distribution of events throughout the night, an average of 5.5 events per hour across the unobserved period would have occurred. This highlights the dominance of calving during daylight hours. Although there is potential for underestimating the number of calving events over the unobserved night time period, any underestimation is not likely to significantly affect the observed distribution of calving events identified in this study. Furthermore, several events classified as occurring during night hours may have taken place during daylight times when the camera was not operational, due to camera power failure (several days between June and October 2012).

Table 5.5: Table showing the breakdown of calving events by region and mechanism by the hour within which a calving event took place.

	Region			Mechanism				Total
Time	EE	SI	WE	B	N	O	SA	
06:00	0	3	2	0	2	3	0	5
07:00	2	1	7	0	8	1	1	10
08:00	2	3	2	0	3	3	1	7
09:00	7	4	4	1	12	2	0	15
10:00	1	10	7	0	10	7	1	18
11:00	1	16	7	0	14	9	1	24
12:00	3	14	11	0	16	11	1	28
13:00	1	22	16	1	19	18	1	39
14:00	0	17	11	0	18	9	1	28
15:00	0	10	10	1	12	5	2	20
16:00	0	14	7	0	12	8	1	21
17:00	2	11	10	0	14	7	2	23
18:00	0	17	5	0	8	12	2	22
19:00	1	6	8	1	7	2	5	15
20:00	1	1	7	0	7	0	2	9
21:00	0	3	0	0	1	2	0	3
22:00 – 05:00	6	41	31	2	54	22	0	78
Total	27	193	145	6	217	121	21	365

Note: EE is eastern embayment, SI is southern ice cliff, WE is western embayment, B is buoyancy driven calving, N is thermo–erosional notch calving, O is over–steepening calving, and SA is subaqueous calving.

The overall trend in the temporal distribution of calving events is mirrored within the southern ice cliff and the western embayment (Figure 5.23), with a somewhat more pronounced second peak evident for the southern ice cliff. The sporadic distribution of calving events in the eastern embayment is down to the limited number of observed events. Similarly, the general distribution for all calving events is also evident in the mechanism dataset, with thermo–erosional notch–driven calving echoing the overall distribution. Over–steepening events have a more pronounced bimodal distribution, with the main mode at 1200 and second mode at 1700 hours. This result provides further indication that external forces control the timing of calving at Tasman Glacier on a diurnal time scale.

5.4.7 Event magnitude and volumes

The temporal distribution of perceived magnitudes for all identified calving events is shown in Figure 5.24. Predominantly all events were below a magnitude of 9, except for three large events of 12, 14, and 18 on 02/04/12, 29/04/12 and 30/01/12 respectively. Events of a magnitude below 9 were associated with estimated volumes between 10^3 to 10^5 m^3 (Figure 5.12), in comparison to the three large calving events that had estimated volume in excess of > 10^6 m^3. Large, high magnitude calving events (magnitudes 12–18) were associated with

buoyancy and subaqueous calving (Figure 5.25) that encompassed a large section of the subaqueous or a full–depth section of the ice cliff (section 5.3.4.3). In comparison, lower magnitude events (magnitudes 1–7) were typically composed of calving from the subaerial ice cliff (upper, lower and full–height). Magnitude 8 and 9 events represented an intermediary step between low and high magnitude calving events, as they were typically initiated by buoyant forces though only along isolated sections of the terminus. This upper bound limit of low magnitude calving events (*c.* 7) appears to relate to the largest calving potential event size from the subaerial ice cliff associated with over–steepening and notch driven calving events that encompassed volume losses of up to 28×10^4 m^3 per event.

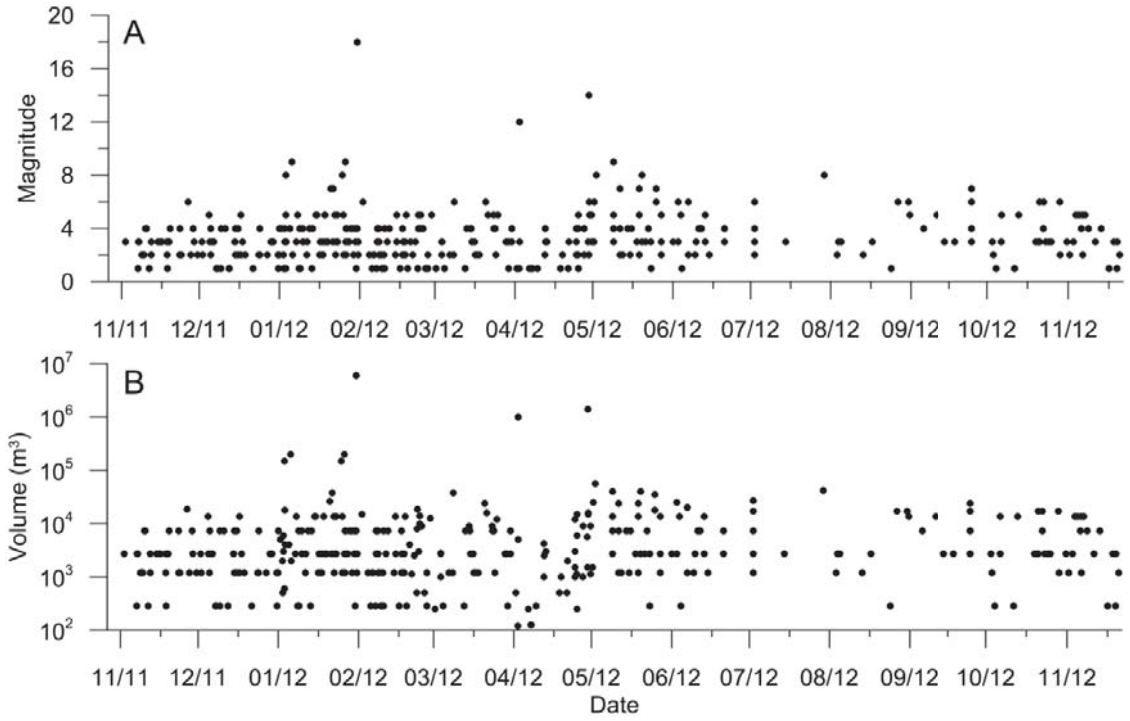

Figure 5.24: The distribution of magnitudes (A) and inferred volumes (B) for the identified calving events between October 2011 and November 2012.

Using the approximate volume of each individual calving event (based on its magnitude) the temporal distribution (Figure 5.24) and impact on the total loss of volume associated with calving (Figure 5.26) was assessed. The total volume loss from observed calving events between October 2011 and November 2012 was estimated as 1.12×10^7 m^3. It is clear from Figure 5.26 that the three large calving events on 30/01/12, 02/04/12 and 29/04/12 had the greatest impact on ice loss via calving. In comparison, although lower magnitude events dominated the distribution of calving events, net cumulative loss is lower than that of high magnitude events.

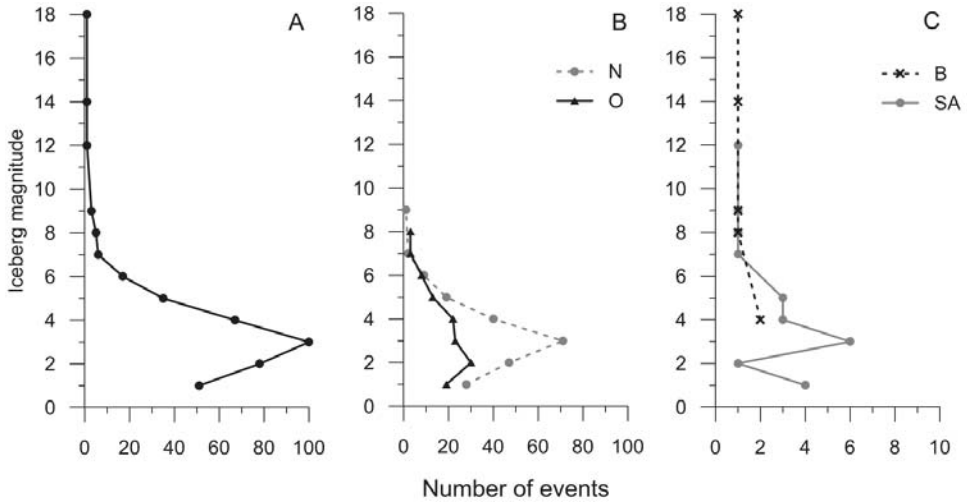

Figure 5.25: The distribution of calving events within each magnitude class for (A) all calving events, (B) notch (N) and over–steepening (O) calving events, and (C) buoyancy–driven (B) and subaqueous (SA) calving events. See Table 5.2 for estimated volumes of each magnitude increment.

Buoyancy–driven calving accounted for 68 percent of total ice loss, the greatest volume loss of all four main styles of calving. Subaqueous calving accounted for 12 percent of calving ice loss, notch–driven 11 percent, and over–steepening 9 percent. This further highlights the importance of low–frequency, high magnitude events on the total ice loss from calving, as buoyancy–driven and subaqueous calving were the least frequent of all calving events. However, high–frequency, low–magnitude events still played an important part in the loss of ice via calving from the terminus of Tasman Glacier (20 percent of total volume loss).

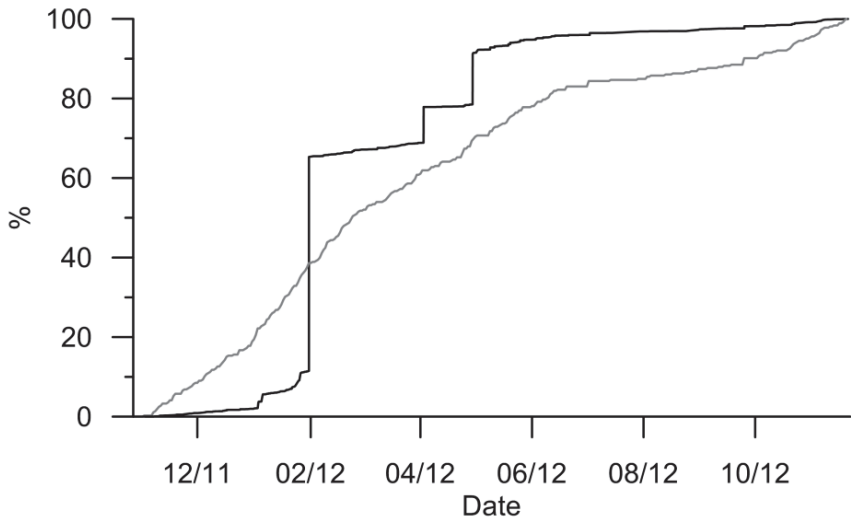

Figure 5.26: Cumulative percentage plot of volume (black line) and the number of events (grey line) throughout the study period. Large steeps in the percentage of volume lost over the study period are associated with high magnitude buoyancy and subaqueous calving events.

5.4.8 Climate and lake characteristics

Climate data recorded at Mount Cook Village (MCV) and Rose Ridge (RR) AWS as well as lake level and temperature records for Tasman Lake show broad variability in climate and lake environment between October 2011 and November 2012. Daily data is also used to further inform and highlight the significance of short term variations in climate on Tasman Glacier and Tasman Lake.

5.4.8.1 Rainfall

Rainfall fluctuated throughout the study period, showing differences not only temporally, but also spatially, between the two AWS (i.e. along the length of Tasman Glacier). At RR and MCV AWS (Table 5.6 and Figure 5.27) monthly rainfall across all complete months varied markedly throughout the study period, with 638 mm recorded at MCV in October 2012. After elevated levels of rainfall throughout November 2011, rainfall at MCV was relatively lower between January and April 2012, before increasing marginally over the winter months between May and July 2012. During the austral spring rainfall increased significantly resulting in a total of 1271 mm falling in September and October 2012. In contrast, rainfall at RR fluctuated markedly, outlining the spatial variability of rainfall along the length of Tasman Glacier. For example, in December 2011, the month with the highest level (408 mm) of rainfall at RR, the lowest recorded monthly rainfall for a complete month was registered at MCV. A decrease in rainfall over the winter period between June and September 2012 is associated with snowfall at RR.

Table 5.6: Monthly climate data for AWS located in Mount Cook Village and Rose Ridge.

Month	Mount Cook Village		Rose Ridge	
	Rainfall (mm)	Mean temperature (°C)	Rainfall (mm)	Mean temperature (°C)
Oct 2011	8	10.6	26.5	2.9
Nov 2011	379	10.4	336.5	3.1
Dec 2011	111	14.5	408	7.1
Jan 2012	217	14.0	167.5	7.1
Feb 2012	179	13.6	293.5	6.9
Mar 2012	199	11.2	274	4.9
Apr 2012	202	10.5	240	5.7
May 2012	346	5.8	204.5	1.2
Jun 2012	299	2.7	88.5	-2.4
Jul 2012	256	2.8	207.5	0.4
Aug 2012	170	4.4	88	-1.0
Sep 2012	633	6.2	208.5	-0.5
Oct 2012	638	7.0	257	-0.4
Nov2012	98	9.6	103.5	2.2

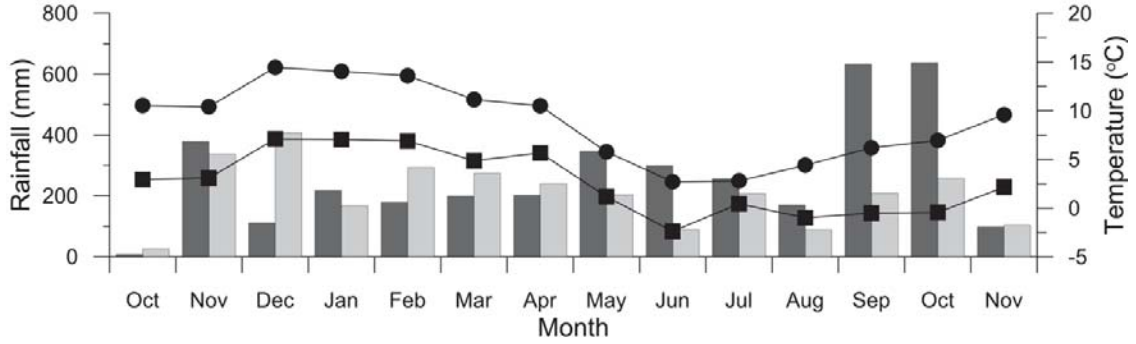

Figure 5.27: Monthly rainfall (bars) and mean air temperature (lines) at MCV (dark grey bars and circles) and RR (light grey bars and squares) AWS. October 2011 and November 2012 are incomplete months, with only 3 and 20 days (respectively) of data included.

Daily rainfall at RR (not shown) and MCV (Figure 5.28A) AWS indicates that the timing of rainfall at both stations is similar, but the amount of rainfall recorded can vary significantly. For example, the maximum daily rainfall recorded between October 2011 and May 2012 occurred on 14/12/11 with over 240 mm falling at RR, compared to only 49 mm at MCV. Maximum daily rainfall of 127 mm at MCV was recorded on 20/11/11, compared to only *c.* 50 mm falling at RR. This not only highlights the spatial variability of rainfall across the length of Tasman Glacier, but also that total monthly rainfall totals can be heavily influenced by single events. For instance, a single day's rainfall has the potential to account for up to 60 % of all rainfall in a month.

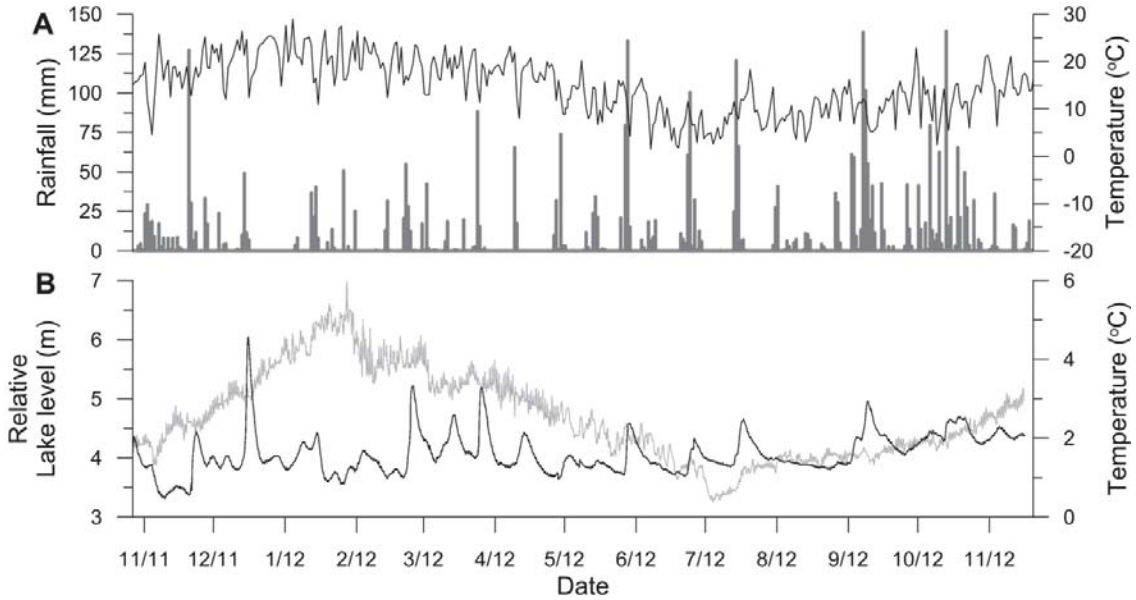

Figure 5.28: Daily rainfall (grey bars) and maximum air temperature (solid black line) at Mount Cook Village (A) for the period 27 October 2011 to 3 May 2012. (B) Lake level (black line) and lake temperature (grey line) for Tasman Lake over the concurrent period of time as A and B is also shown to highlight the dynamic link between rainfall, air temperature, lake level and lake temperature.

Figure 5.28A indicates that rainfall was relatively sporadic throughout, with large periods of little or no rain. This is particularly evident for the period from the end of December 2011 through to February 2012. During this time maximum rainfall at both AWS exceeded 30 mm only twice, reaching a maximum of 50 mm. Sporadic rainfall patterns continued throughout most of the study period, with periods of elevated rainfall that continued for more than three consecutive days only evident in September and October 2012. This sustained rainfall resulted in the highest monthly rainfall, recorded in September and October 2012.

5.4.8.2 Air temperature

Air temperature at MCV and RR showed similar trends (Figure 5.27) throughout the study period. Recorded temperatures were different due to differing locations and elevations (Figure 5.27 and Table 5.6), but show the gradual increase in air temperature between October and November 2011 at both AWS, prior to peaking in December 2011. Mean daily temperatures at MCV were recorded between October 2011 and February 2012, with a maximum of 21.2 °C. At RR mean daily temperature mirrored the same peak in air temperature recorded at MCV, reaching a maximum of 7.1 °C (Table 5.6). Temperature declined at both stations through March to July 2012, increasing again through to the end of the study period in November 2012. Daily air temperature (Figure 5.28A) reveals the inter–month variability of air temperature. However, extended periods (10 days or more) of constant air temperature are evident over the study period. One such period exists between 19/12/11 and 29/12/11 where temperature consistently averaged > 20 ^{o}C at MCV. This period of relative stability continued through to the middle of January 2012, after which variability increased. At MCV a strong diurnal signal in temperature variation was present throughout the study period Figure 5.29.

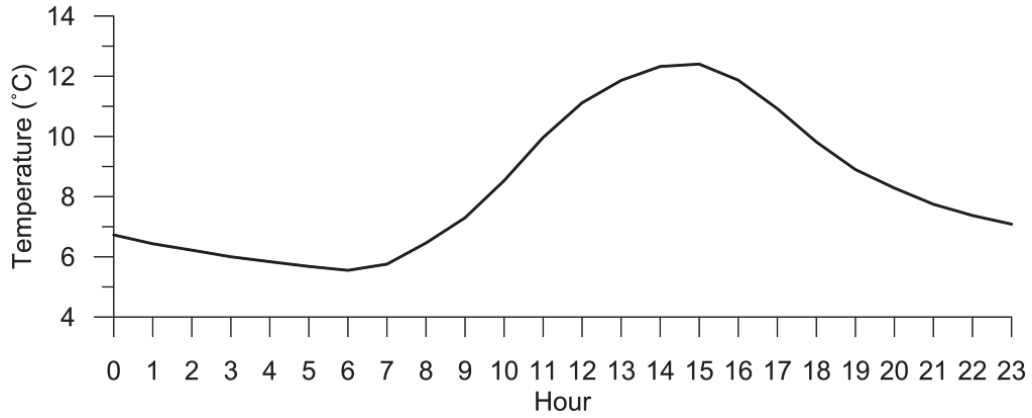

Figure 5.29: Diurnal distribution of mean hourly air temperature at MCV between 27 October 2011 and 20 November 2012.

5.4.8.3 Lake level

Tasman Lake underwent significant fluctuations in water level throughout the study period (Figure 5.28B). Although no significant trends are evident between October 2011 and November 2012, several periods of short term fluctuations ranging from 0.05 m to 2.1 m did take place. These fluctuations varied in timing and duration, but appear to reflect rainfall, temperature, and diurnal melt cycles. Rainfall events had the greatest impact on lake level, with rapid increases generally coincident with rainfall recorded at one or both AWS used in this study. For example, the greatest increase in lake level of 2.1 m was coincident with 246.5 mm of rainfall recorded at Rose Ridge on 14/12/11. This is repeated throughout the study period with the height and duration of lake level fluctuations closely related to the amount and duration of rainfall events.

Lake level also fluctuated with respect to air temperature and glacial melt. During periods of little or no rainfall, lake level increased during successive days of high temperatures. This is particularly evident between 22/12/11 and 29/12/11 when lake level increased by 0.11 m at the same time that consistent elevated temperatures were recorded at both AWS. On a shorter timescale the same effect can be seen a lake level increases daily towards the later part of daylight hours (Figure 5.30), typically peaking between 1400 and 1600 hours. This diurnal fluctuation in lake level is consistent throughout the study period, with a maximum lake level increase of 0.05 m recorded. Diurnal fluctuations are best observed during periods of relative lake stability, with lake level increases resulting from rainfall tending to overprint the relatively small scale changes at a daily level.

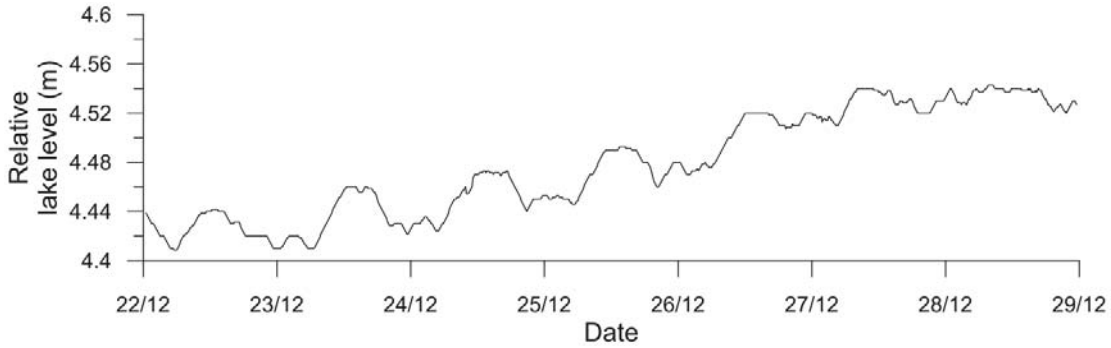

Figure 5.30: Diurnal fluctuations in relative lake level of Tasman Glacier over a seven day period in December 2011.

5.4.8.4 Lake temperature

Temperature of the upper water column of Tasman Lake shows a general trend of warming from 2 °C in October 2011 to 6.6 °C January 2012 (Figure 5.28C). This gradual increase in lake temperature was interspersed with periods of stability and short decline, which coincided with

rainfall in the catchment. Lake temperature sharply declined at the end of January 2012 before levelling off though February 2012 at 3.5 °C. This sharp decline did not coincide with any large rainfall events or air temperature, but does occur after a significant calving event which lead to clogging of the outlet of Tasman Lake with icebergs, proximal to the area where the logger was located. Another sharp drop at the start of March 2012 led to lake temperature decreasing to 2.5 °C, prior to a steady future decline in temperature to 0.2 °C between April and July 2012. Tasman Lake was partially frozen throughout July 2012 (D. Callesen, *pers comm.*, 2012), coinciding with the lowest lake temperatures recorded. Temperatures increased gradually between July and November 2012, returning to a similar level as recorded at the start of the study period.

5.5 Discussion

From the analysis of time–lapse imagery and the identification of the temporal and spatial variability of calving with respect to the timing and location of calving events, it is clear that several trends in calving are evident between October 2011 and November 2012. Both the retreat of Tasman Glacier and distribution of calving events show distinct temporal (e.g., seasonal, inter–month, diurnal) and spatial (e.g. regional and inter–regional) variations. From these datasets the underlying processes controlling calving and retreat at the different temporal and spatial scales will be discussed in relation to terminus geometry, glacier dynamics, climate (rainfall and temperature) and lake characteristics (lake level and temperature). The interaction between calving mechanisms and external variables is also described here to illustrate what the main driving forces for the different types of calving are and how they were distributed throughout the study period.

5.5.1 Comparison between the retreat of Tasman Glacier and identified calving events

Calving events have had a significant impact on the retreat of Tasman Glacier over the period October 2011 to November 2012. Not only were there large temporal variations in the frequency of calving events, but also in the spatial distribution of calving events across the terminus. Over the study period, this spatial variability was evident in not only the frequency of calving events (Figure 5.20), but also changes in terminus position and the retreat of Tasman Glacier (Figure 5.13).

Between March 2011 and November 2012, the retreat of Tasman Glacier was not uniform across the entire length of the terminus. Increased retreat between March 2011 and January 2012 was related to the length of time this observation period covers, and the development of the peninsulas due to the presence of a supraglacial pond at the centre of the southern ice cliff in

March 2011 (Figure 5.13). Hence, the retreat rate at the beginning of the observation period (October 2011) was above the mean value. At this time, the eastern and western embayment were characterised by an irregular ice cliff that included two prominent peninsulas, that developed at the margins of the southern ice cliff. Calving was centred along the two peninsulas and the western ice cliff throughout the first part of the study period, particularly along the western peninsula. In comparison, there was limited retreat along the eastern ice cliff over this period of time (Figure 5.13).

After this initial retreat, a distinct seasonal cycle of retreat becomes evident, with variations in retreat rate during spring/summer/autumn (October to May) and winter (June to September) clearly observable (Figure 5.13 and Table 5.3). In general, a steady increase in retreat rate is evident between January and March 2012, followed by a rapid increase between March and April 2012. When calving frequencies are considered, there is a slight contrast. Although the pronounced seasonal signal is also apparent throughout the study period, the frequency of calving events increased again through spring 2011, reaching a peak in January and February 2012 with a maximum of *c.* 2 events d^{-1}. The minimum frequency was recorded during the winter months (June to September) with 0.1 event d^{-1}. Interspersed between these two end periods is a slightly elevated frequency of events over the autumn period (April and May). The differing peaks in retreat rate (April/May) and calving frequency (January/February) is likely to be an artefact of the time interval between images and the potential impact of an increase in smaller calving events within the image periods affecting calving frequencies.

5.5.2 Temporal patterns in calving events

The temporal variations in calving throughout the study period are related to the interaction between the four different calving processes, glacier dynamics, and external variables such as lake level and temperature. The clear seasonal increase in the frequency of calving events throughout the study period is related primarily to the fluctuations in thermo–erosional notching and over–steepening calving events (Figure 5.31). This is unsurprising as notching and over–steepening events together accounted for 93 percent of all events, with notching events the more dominant (60 percent). However, these types of events are inherently limited in size to the subaerial ice cliff. In comparison, buoyancy and subaqueous events were typically higher in magnitude, but occurred intermittently. Each of the four processes is discussed here in greater detail to identify the potential underlying controls of each and their significance on the retreat of Tasman Glacier.

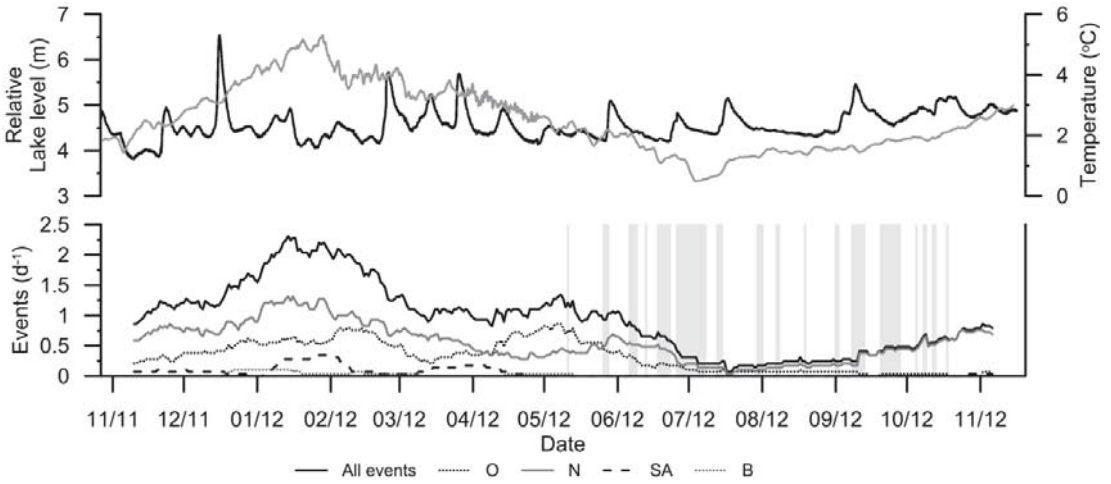

Figure 5.31: Comparison plots between (top) lake level (black line) and temperature (grey line) and the (bottom) 30–day running means for each of the four calving mechanism between October 2011 and November 2012. Grey bars signify days the camera was not operational.

5.5.2.1 Thermo–erosional notch calving

Röhl (2006) and Benn et al. (2001) identified that conditions within the forming notch are fundamentally affected by the interplay between cliff geometry, water temperatures and currents both within and distal to the notch, the presence/absence of debris at the waterline, and the stability of lake level. However, the distribution of calving over seasonal or annual time–scales shows clearly that longer term conditions that enhance or limit notch formation are the primary rate–controlling factors, while site specific variations represent only a minor control. Specifically, between 2011 and 2012 lake level stability and temperature, coupled with cliff geometry, have the greatest influence on the distribution of notch–driven calving events. The rate of notch formation is inherently linked to lake level stability and lake temperature, whereas cliff geometry controls the distribution and absolute timing of calving events.

The increase in notching events between December 2011 and February 2012 coincided with both the highest recorded lake temperatures and an extended period of relatively stable lake levels (Figure 5.31). Lake level fluctuated no more than *c.* 0.5 m, except for a short–term increase in lake level associated with high rainfall at the end of December 2011. This provided the pre–conditions for frequency of notch–induced calving, as waterline melt was focussed within a narrow vertical range (Röhl, 2006). The combination of these two variables also appears to be a contributing factor to an increase in calving frequency in June 2012. Again, lake level remained relatively constant over the period of increased calving frequency. This highlights that even though lake temperature was declining, the stability of lake level allowed for the waterline melt to be focussed over a narrower vertical band. Similarities in the frequency of notching events and lake temperature indicate that there is likely to be some interplay at a

seasonal timescale, with shorter term variations linked to lake stability. This would explain why during winter months (July to September), when lake temperature was at its lowest, notch–driven calving decreased to almost zero even though lake level remained stable for an extended period of time (Figure 5.31).

The point at which notch formation will typically induce calving is when ice cliff height and notch depth have a ratio between 1.5 and 2.0 (Röhl, 2006). As a result, cliff height and geometry play an important role in controlling the timing of individual calving events by affecting when the section of ice will become unstable. Using average notch formation rates (0.1 to 0.3 m d^{-1}) reported by Röhl (2006) for the observed period of lake level stability observed between December 2011 and the middle of February 2012 (77 days), the potential length of undercutting could have ranged from *c.* 8 m (0.1 m d^{-1}) to *c.* 23 m (0.3 m d^{-1}). Although significant uncertainties are associated with these rates, due in part to fluctuations in lake level of *c.* 0.5 m, they provide an indication of the magnitude of undercutting that may have occurred across the Tasman Glacier terminus and the importance of lake stability on notch formation.

However, the point at which calving is initiated is more commonly associated with the presence of pre–existing lines of weakness (Röhl, 2006; Benn et al., 2007b). Example notching events are shown in Figure 5.32. These example events indicate that calved sections tend to break off after becoming isolated from the surrounding ice, either via subaerial melt, crevasse formation, or other calving events. A fracture perpendicular to ice cliff orientation is initiated as the ice is unable to be supported any longer, either developing along another pre–existing line of weakness or a newly formed fracture.

As this type of calving is controlled by notch development and its ability to destabilise the subaerial ice cliff, the vertical movement of lake level away from the notch or ice cliff retreat to the back of the notch effectively resets the notch system. The loss of the entire section due to a large calving event along which a notch is developing also resets the system. The result of this is that calving due to notch development can be limited by the increase in calving due to other calving processes (such as buoyancy driven calving).

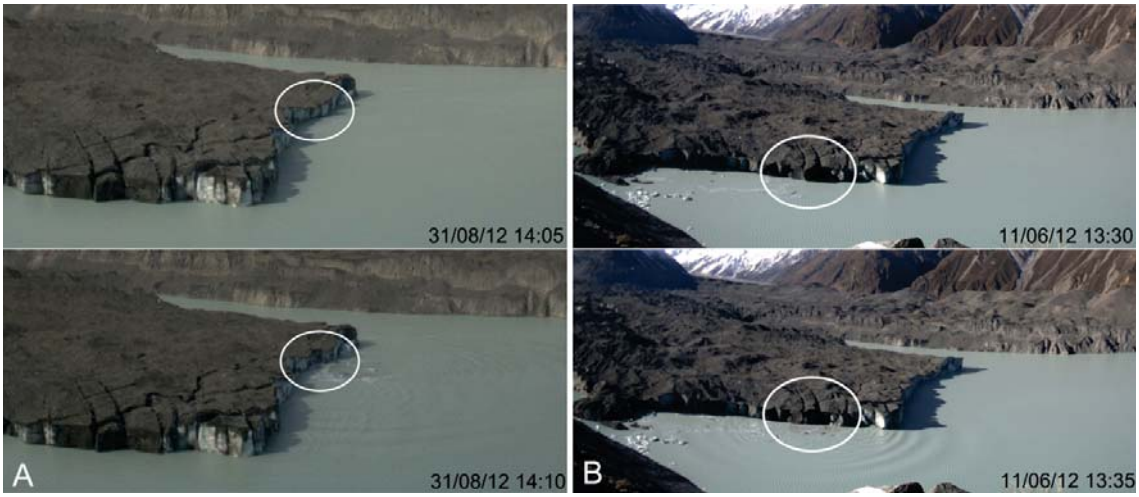

Figure 5.32: Calving due to formation of a thermo–erosional notch at the waterline. (A) Example of a thermo–erosional notch event from the southern ice cliff. Note the undercut nature of the ice cliff prior to calving. (B) The undercut calved section has become isolated and undercut due to calving from the surrounding area and formation of chevron crevasses near the terminus.

5.5.2.2 Over–steepening calving

Over–steepening calving events are characterised by the development of an over–hanging or concave ice cliff that calves due to development and penetration of a crevasse immediately up–glacier. This over–hanging section develops as a result of either force imbalances vertically along the subaerial ice cliff (e.g., Hughes, 2002; Hanson and Hooke, 2003), or smaller calving events at the waterline (e.g., Kirkbride and Warren, 1997) removing the underlying ice support (typically via small notching events). In both cases the net result is the forward rotation of the top of the ice cliff. Calving of these sections takes place as the crevasse penetrates to the point ice cannot resist the tensile stress induced by the unsupported section of the cliff, typically in the vicinity of waterline. Figure 5.33 shows two examples of the pre– and post–calving geometry of a section of the ice cliff that had become over–steepened due to a prior calving event in front of it in the hours prior.

Similar to the increases in notch–driven calving, over–steepening events also increased between December 2011 and February 2012, and again during May 2012 (Figure 5.31). However, the cause of these increases is not as clear as for notching events. As over–steepening events are inherently linked to the stability of the subaerial ice cliff, any force imbalances that result in the forward bending of the ice cliff will typically cause calving. For example, variations in ice velocity between the top and base of the subaerial ice cliff (due to hydrostatic and cryostatic forces), loss of support from the base of the glacier due to smaller waterline calving events (Kirkbride and Warren, 1997), and extensive flow of the terminus after high magnitude calving events can all induce force imbalances and over–steepening. It is unclear whether the gradual

increase in events over the spring/summer is related to increased extensional flow towards the terminus, an increase in the vertical velocity gradient and force imbalances, meltwater entering crevasses at the terminus increasing penetration, increased waterline calving due to notching decreasing the support of the overlying ice, or a combination of these factors. Previous work at Tasman Glacier has indicated that the development of shear bands associated with forward bending of the terminus are not likely as subaerial melt is too high and calving occurs too frequently for it to develop and be sustained (Kirkbride and Warren, 1997; Röhl, 2005).

Figure 5.33: Over–steepening calving event in (A) the western embayment and (B) the southern ice cliff. The section of the terminus that calved in (A) was over–steepened after a large calving event removed the section in front in the hours prior to this calving event.

However, the increase in events recorded during February and May 2012 appears to be directly related to two high magnitude calving events at the end of January and April 2012. The calving of these large sections of the glacier had the effect of removing substantial backpressure acting on the section up glacier. As the terminus readjusted to the new force regime, increased tensile stresses at the surface of the glacier would have resulted in increased crevassing, providing the necessary lines of weakness for calving to be initiated once they penetrated to a depth necessary to initiate calving (typically the same level as the waterline). The effect of the high magnitude events was to increase the rate of calving events as a result of this induced instability. This process was also observed in relation to smaller calving events (e.g., Figure 5.33) that still removed the full–height of the subaerial ice cliff, similar to the processes described by Kirkbride and Warren (1997).

5.5.2.3 Buoyancy–driven calving

Buoyancy–driven calving events are caused by the fracture of ice due to the upward buoyant forces applied to the terminus as a result of the density differences between ice and water.

Buoyancy–driven calving events were the least common of all events, with only six identified throughout the entire study period. However, buoyancy–driven calving accounted for the largest and most energetic events, including the largest recorded event during the study period on 30/01/12 (Figure 5.34). Uplift of the terminus was evident in the days and weeks prior to calving on 30/01/12 (Glacier Explorers, *pers. comm.*, 2012). Given their nature, high–magnitude buoyancy–driven events had a significant impact on the retreat of the glacier. For example, the large buoyancy driven calving events on 30 January and 29 April 2012 (Figure 5.34) resulted in a maximum retreat of 120 m and 60 m, respectively. This accounted for almost all of the retreat of the southern ice cliff over the two periods shown in Figure 5.13.

The size and extent of the calved section associated with buoyancy–driven calving, makes it unclear whether these calving events occurred as a single coherent section or as a series of events. Given that several large icebergs were present in the time after calving on 30/01/2012 (Figure 5.34), and that the geometry of the terminus prior to calving was in the form of two peninsulas, it is unlikely that the ice all calved as a single section. Rather, the calving of one section of the terminus likely triggered calving along the entire length of the terminus.

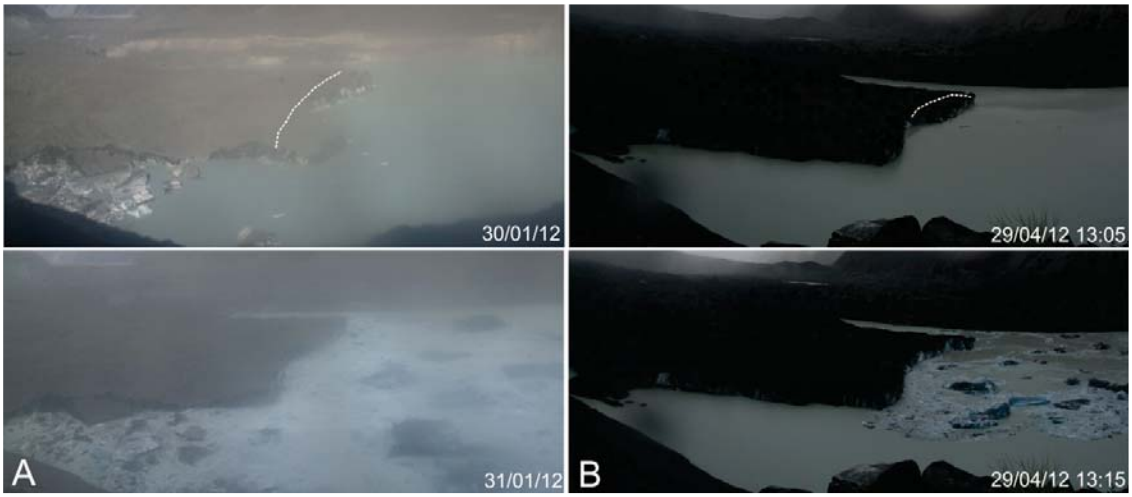

Figure 5.34: The high magnitude buoyancy–driven calving events observed throughout the study period occurring along (A) the entire width of the terminus overnight of 30/04/12 and (B) from the eastern section of the southern ice cliff on 29/04/12. The resulting icebergs have a mixture of white ice through to deep blue icebergs indicating that calving has occurred throughout the majority of the ice column. The dotted line indicates the calved section in the upper image. Image quality is degraded for the 30/01/12 event due to scratches on the lens.

As noted above, high magnitude buoyancy driven calving events have the effect of increasing the potential for over–steepening events to occur, but also limit notching events by resetting any notches that had formed prior to the event. Over short time–scales (months) calving variability can be strongly influenced by the occurrence of larger buoyancy–driven calving events. The

result of this can be an increase in smaller over–steepening events and the limiting of notching events in the short–term.

Interestingly, both of the large magnitude buoyancy–driven calving events appear to be preceded by subaqueous events. The January event was preceded by subaqueous calving in the boundary region between the southern ice cliff and the western embayment, with the April event preceded by a large subaqueous event on 02/04/12. In the time between the subaqueous calving event and subsequent failure of the large section of the ice cliff, extensive crevasses developed in the region of the line of failure (Figure 5.35). These crevasses were clearly obvious by the 13–14 April, had become more prominent by the 21 April, and were quite large by 25 April. The formation of crevasses in this manner appears to be linked with the subaqueous event, which could have decreased the support at the base of the subaqueous ice cliff. The result of this would have been the development of surface crevasses due to increased tensile stress at the surface of the glacier. Consequently, support at the base of the ice column was lost. Increased basal crevassing (van der Veen, 1998a) may also have resulted if the isolated section was subject to increased torque due to lake–level changes, as it was no longer supported and would be able to oscillate in isolation of the remaining ice cliff. It is unclear to what extent subaqueous events prime the large calving events, but given their potential and the observations presented here, they may play a significant role.

Also, the two high–magnitude buoyancy–driven events were not directly associated with increased lake level as has been found in other studies (e.g., Boyce et al., 2007), but occurred after periods of relatively stable lake level. However, significant fluctuations in lake level were recorded prior to the period of lake level stability, which would have increased stress at the juncture with grounded ice, increasing fracture propagation as the floating sections of the glacier oscillated. When this is coupled with increased surface lowering and calving due to melt and subaerial calving, the bending moment applied to the isolated sections of the glacier may have been great enough to initiate failure. This indicates that thinning of the glacier and the presence of deep water drives the terminus to the point of flotation (Warren et al., 2001; Boyce et al., 2007), but that short–term processes (lake level fluctuations, subaerial melt and calving) play a critical role in inducing fracture propagation and calving failure.

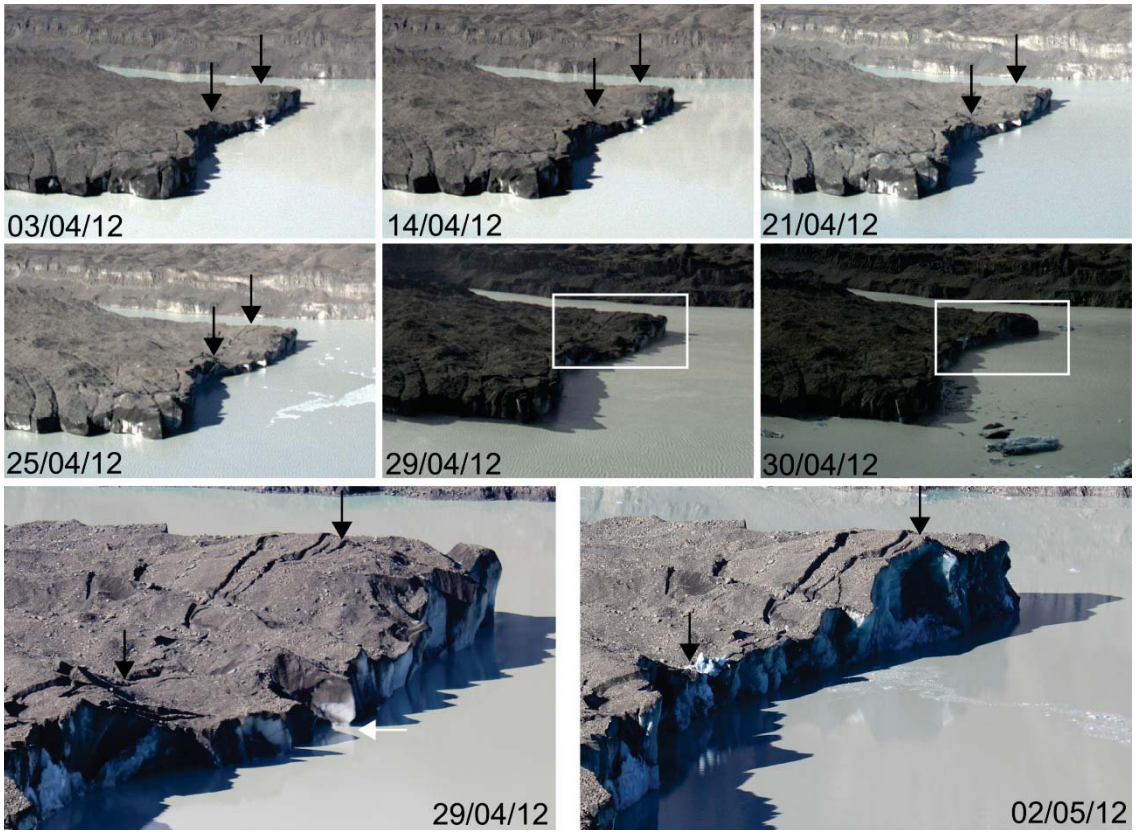

Figure 5.35: The development of surface crevasses immediately up glacier prior to the calving event on 29/04/12 (shown in Figure 5.34). Black arrows indicate the region in which crevasses formed throughout the month of April after a subaqueous calving event. White box indicates the area shown in the close up images on 29/04/12 and 02/05/12. White arrow indicates an exposed thermo–erosional notch present prior to the calving event. Note the highly irregular surface present in the 02/05/12 image highlighting the potential for large events to increase smaller over–steepening calving.

Although buoyancy–driven calving events were dominated by the two high–magnitude events described above, relatively smaller events were also identified where small sections of the glacier became isolated and subjected to buoyant forces. Figure 5.36 shows two examples from within the western embayment and the peninsula that developed between the southern ice cliff and western embayment. These calving events indicate that although buoyancy–driven calving is typically associated with high–magnitude events, it can initiate calving across a wide range of spatial scales.

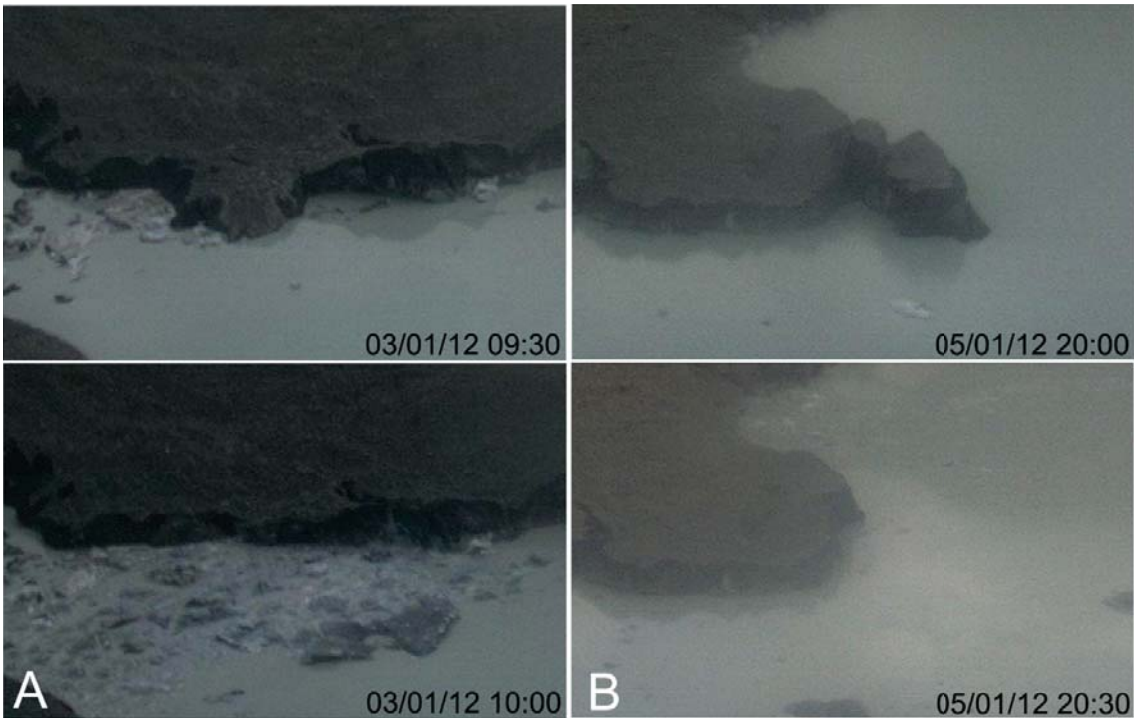

Figure 5.36: Lower magnitude buoyancy–induced calving events on the (A) 03/01/12 and (B) 05/01/12, indicating that buoyant forces affect calving at a range of spatial scales.

5.5.2.4 Subaqueous calving

Subaqueous calving takes place as buoyant forces subjected to the ice cliff below the waterline initiate fractures and lead to the detachment of a section of ice (Motyka, 1997; Benn et al., 2007b). Due to the infrequent occurrence of subaqueous calving events it is unclear whether seasonal trends are significant. However, all subaqueous calving events recorded at the terminus of Tasman Glacier took place between November and April which potentially indicates a seasonal signal. This is not surprising as subaqueous calving is dynamically linked to all other calving events, either through the development of a subaqueous ice 'foot' (e.g., Kirkbride and Warren, 1997; Robertson et al., 2012) or due to loss of lateral support from surrounding ice or bedrock and moraine margins, increasing buoyant forces (Warren et al., 1995a; Motyka, 1997; Warren et al., 2001). The result of this is that when calving frequency increases the potential for subaqueous calving increases too. A secondary impact may be that due to an increase in subaqueous melt or debris redistribution lines of weakness that subaqueous calving may be initiated on can be exposed or developed. This is likely to increase the potential for subaqueous calving to occur (Motyka, 1997; Robertson et al., 2012).

When large sections of the glacier are lost via high magnitude calving events (typically associated with buoyancy–driven calving) the longer term (> 1 day) potential for subaqueous calving to occur may be limited. This is because the subaqueous geometry is effectively reset as all potentially unstable subaqueous sections of ice cliff would have been lost during the larger

calving event. This scenario was likely the cause for the two high magnitude calving events shown in Figure 5.34, as no subaqueous calving events were identified during the months following these events (Figure 5.31).

Figure 5.37: Image sequence showing a subaqueous calving event in the area in front of the southern ice cliff. Note the deep blue nature of the calved icebergs.

5.5.3 Regional patterns of calving and retreat

There are clear spatial and temporal differences in the retreat of the three sections of the Tasman Glacier terminus (the western embayment, southern ice cliff, and eastern embayment (Figure 5.13)). This spatial variability is explored here to identify whether there is a link between calving and retreat within each region and external variables such as terminus geometry, glacier dynamics, and the lake characteristics adjacent to each ice cliff.

5.5.3.1 Western embayment

Within the western embayment, retreat of the ice cliff occurred in a west to east direction and was irregularly distributed along the ice cliff during the initial stages of the study period (March 2011 to January 2012). A relatively straight ice cliff developed from March 2012 onwards (Figure 5.13), except at the northern end of the embayment where a section of the terminus was being uplifted. The retreat of the ice cliff showed a strong seasonal signal with the temporal distribution of calving events mirroring this (Figure 5.22). The seasonal variability was almost entirely controlled by the thermo–erosional notch–driven calving events, accounting for 77 percent of all events. However, other forms of calving also contributed to ice loss, via larger calving events and shortening of the ice cliff length. The dominance of notch–driven calving is related to a combination of the terminus geometry and glacier dynamics, coupled with the limited variability of lake characteristics, and indicates that the glacial and proglacial regime is inherently different to the southern ice cliff.

Given the distribution of surface crevasses and previous estimates of surface ice velocity (e.g., Redpath, 2011) across the current lower terminus it can be assumed that generally ice flows towards the southern ice cliff, with lower velocities likely along the western ice cliff. Very few crevasses were formed parallel to the western embayment ice cliff throughout the entire study. As a result, the lines of weakness that calving events typically require for initiation were not present, with parallel crevasses only developing behind isolated sections due to force imbalances associated with notching. However, transverse and chevron crevasses associated with extensive flow perpendicular to the southern ice cliff did have an effect of isolating blocks, increasing the potential for calving by removing lateral support (Figure 5.32B).

The western embayment ice cliff was also typically more convex then the southern ice cliff. This may be due to the orientation (west facing) of the ice cliff, making it more susceptible to subaerial melt compared to the south facing southern ice cliff. Melt of bare ice zones on debris–covered glaciers can lead to significantly higher rates of ablation compared to debris–covered ice (Benn et al., 2001). The result of melt along the exposed ice cliff is that supraglacial debris at the top of the ice cliff is lost as it is no longer supported. This has the effect of further exposing the upper section of the ice cliff to solar radiation as it is exposed for a greater amount of time, increasing the melt of the upper cliff.

The combination of lower ice velocities and higher rates of ice melt at the terminus provided the necessary cliff geometry (Röhl, 2006) for notch–induced calving to dominate over other processes. This coupled with the increased lake temperatures over the spring/summer period and

the stability of lake level (Figure 5.28), accounts for the pronounced seasonal signal in the number of calving events.

A large number of subaqueous events also occurred within the western embayment potentially indicating that it is ice–cored to some extent. An indication for this can be seen in Figure 5.38 where two large icebergs were driven towards the terminus due to adiabatic winds. The close presence of the large iceberg (iceberg 1 in Figure 5.38) near the southern ice cliff indicates that no substantial ice foot protruding from it to at least a depth of ~180 m (given a subaerial iceberg height of 20 m), with the distance away from the ice cliff due primarily to the geometry of the iceberg. In contrast, the iceberg on the western side of Tasman Lake (iceberg 2) appears to be grounded distal to the entrance of the western embayment. This does not appear to be due to the geometry of the iceberg itself as an image from the following day shows the same iceberg (iceberg 2) in close proximity to the southern ice cliff.

Figure 5.38: The numbered icebergs indicate the potential presence of a subaqueous ice ‘foot’ within the western embayment and the absence of one along the southern ice cliff. The inability of either of the icebergs to enter the eastern and western embayment indicates that those sections are ice cored, whereas the close proximity of the icebergs to the southern ice cliff indicate a near vertical ice cliff. The height of each iceberg is ~ 20 m.

The ice–cored nature of the western embayment is unsurprising as the process of ice ‘foot’ development (Robertson et al., 2012) documented by previous studies (e.g., Kirkbride and Warren, 1997; 1999; Warren, 1999; Benn et al., 2001; Haresign and Warren, 2005) follows the same pattern as has been described for the western embayment. Calving (here dominated by

thermo–erosional notching events) leads to the retreat of the subaerial ice cliff. If the retreat is greater than the loss of mass per unit area of the corresponding subaqueous margin this will lead to the development of a subaqueous ice ramp (Robertson et al., 2012). In the case of the western embayment the subaqueous ice ramp has survived due to a combination of lateral support provided by the western lateral moraine and the supply of debris–cover to the subaqueous margin via the slumping of the lateral moraine into the lake at this location (D. Callesen, *pers comm.*, 2012).

5.5.3.2 Southern ice cliff

Calving along the southern ice cliff varied significantly in terms of both seasonal fluctuations and calving mechanisms. All calving processes were represented throughout the study period (Figure 5.22), with over–steepening events having the highest frequency, followed by notching events. These smaller magnitude calving events were interspersed with large–magnitude buoyancy driven calving events that overprinted small magnitude calving events, resulting in considerable up–valley retreat of Tasman Glacier. The presence of these high–magnitude events indicates that the southern ice cliff is unstable in nature, with an increased potential for uplift and buoyancy driven calving. The cause of this is a complex interaction between glacier dynamics and the presence of the deep water found along the terminus (>300 m).

The principal flow of Tasman Glacier at the terminus is perpendicular to the southern ice cliff (Redpath et al., 2013). This is supported by the observation that transverse crevasses developed behind the ice cliff throughout the study (Figure 5.39) as principal tensile stress is normal to glacier flow. Not only does this indicate the principal flow regime at the terminus, but also that there is clear evidence of extensive flow indicative of an increase in velocity within the 100 m immediately up–glacier of the southern ice cliff. The resulting transverse crevassing within this zone leads to the over–steepening of the subaerial ice cliff and provides a greater number of lines of weakness along which calving can be initiated.

Figure 5.39: View of the southern ice cliff showing transverse crevasses (dotted white line) developed at the terminus of Tasman Glacier indicating flow direction and the presence of extensive flow towards the southern ice cliff.

The southern ice cliff does not receive a large amount of direct sunlight due to the southwards orientation, with the ice cliff predominantly in shadow all day. This has the effect of decreasing the amount of solar radiation that acts on the ice cliff, potentially decreasing subaerial melt compared to the western and eastern embayments, which as discussed, characteristically have more convex subaerial ice cliffs. Together with the potential of higher velocities, this may leave the southern ice cliff more susceptible to over–steepening calving events by preserving the ice cliff during periods of stability.

However, as discussed in section 5.5.2.2, increased over–steepening throughout February and May 2012 was associated with high–magnitude buoyancy–driven calving events that left behind an unstable ice cliff post–calving. The consequent increase in force imbalances along the southern ice cliff led to the forward bending of the subaerial cliff. This process controlled the overall distribution of calving events throughout the study period.

The buoyancy–driven calving events that triggered increased rates of over–steepening events are inherently linked to glacier dynamics, water–depth and fluctuations in lake level of Tasman Lake. Primarily the susceptibility of a water–terminating glacier to buoyant forces is related to the thinning of the glacier, increase in water–depth at the terminus and loss of support from surrounding ice or margins. Water–depth along the southern ice cliff is the greatest, reaching depths in excess of 300 m (B. Ward, *pers. comm.*, 2012), and appears to indicate that the glacier is currently retreating down a reverse slope. Consequently buoyancy forces increase as the glacier thins and retreats, increasing the potential for a bending moment to be induced by the

increased supply of meltwater into the glacier system or perturbation in lake level (Warren et al., 2001; Boyce et al., 2007).

For the two large–magnitude buoyancy events that took place along the southern ice cliff a combination of these factors drove the entire length (30/01/12 event), or sections (19/04/12 event) of it, to disequilibrium causing an increase in torque associated with buoyant forces. The irregular shape of the ice cliff prior to the 30/01/12 event had the effect of focussing buoyant forces on the two protruding peninsulas that had developed in part due to the supraglacial pond present prior to the beginning of the study. Subaerial and subaqueous calving and melt would have increased buoyancy of the southern ice cliff through the removal of support. The result was the calving of each of the peninsulas as separate events, with one event initiating the other. A similar set of circumstances also occurred during the 29/04/12 event; this event has been discussed in more detail in section 5.5.2.3.

5.5.3.3 Eastern embayment

Limited observations of calving from the eastern embayment hinder the identification of a controlling mechanism of calving and the evolution of the ice cliff. However, given the similarity with the western embayment it is assumed that thermo–erosional notching played an important part in the retreat of the ice cliff over the study period. The retreat that was identified was only minor (Figure 5.13) in comparison with the western embayment and southern ice cliff, indicating that processes operating in this region may not be as effective as along the southern ice cliff and in the western embayment, or that they are acting on a different time scale.

The main surface outflow from Tasman Glacier has historically originated from the northern point of the eastern embayment (Röhl, 2005). This continued throughout the study period (Glacier Explorers, *pers. comm.*, 2012), resulting in the input of relatively colder meltwater into the eastern embayment. Decreased efficiency of melt at or below the waterline due to this inflow may limit the formation and penetration of waterline notches in the eastern embayment. A decrease in the frequency of calving events would result as notches will take a longer period of time to destabilise the subaerial ice cliff.

As was evident within the western embayment, several subaqueous calving events were observed in the southern end of the eastern embayment. This again suggests that the area within the eastern embayment is ice cored, with subaerial melt and calving exceeding that of subaqueous mass loss. Robertson et al. (2012) also concluded that this region was ice cored from sub–bottom surveys within a section of the eastern embayment.

5.5.4 Diurnal variations in calving

The distribution of calving events throughout the day indicates that significant diurnal variations are present, with calving tending to increase towards the afternoon (Figure 5.23). As over–steepening and notching events dominated the total number of calving events, the diurnal fluctuation in calving must be associated with an external variable that affects both of these events equally. The most likely of these is the diurnal temperature cycle present at Tasman Glacier. Figure 5.30 shows a clear diurnal signal in the fluctuations of the level Tasman Lake, associated with the increased input of meltwater associated with the diurnal temperature cycle (Rothlisberger and Lang, 1987; Jansson et al., 2003; Nienow et al., 2005). This diurnal melt is also evident from the plume of meltwater that regularly develops throughout the day in the western embayment due to the overflow of the less dense meltwater (Figure 5.40). The apparent relationship between the diurnal increase in calving, temperature cycle and meltwater production provides a potential link between temperature, meltwater and calving.

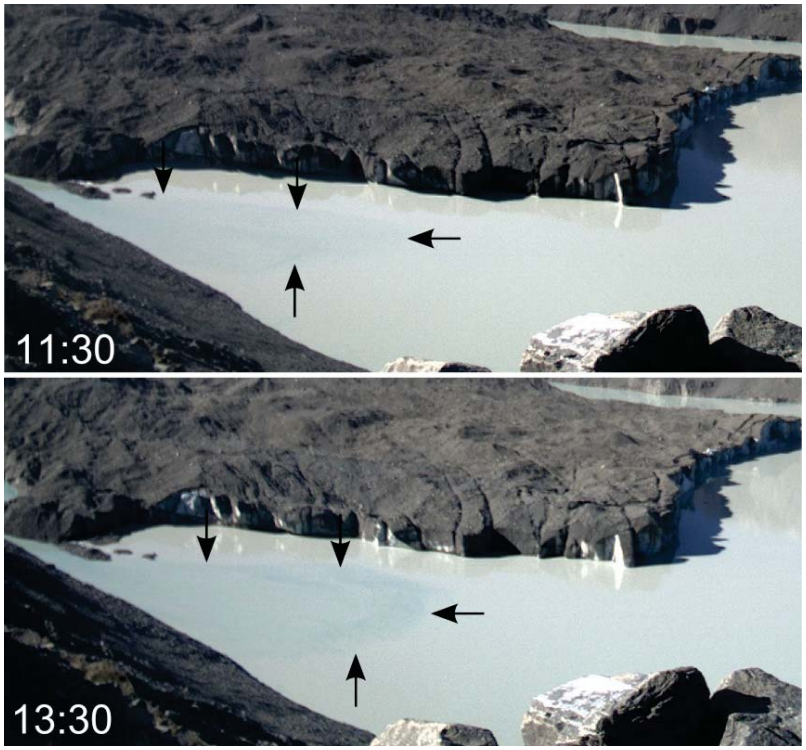

Figure 5.40: Overflow (arrowed) of meltwater into Tasman Lake that regularly develops throughout the day from the diurnal melt cycle within the western embayment of Tasman Glacier.

As both over–steepening and notching events are inherently linked with the stability of the ice cliff and the development of a crevasse to provide a line of failure, the inclusion of meltwater into the system may potentially accelerate the penetration of the crevasses over a short time

period. The inclusion of water within a crevasse increases its potential to penetrate deeper than dry crevasses (Benn et al., 2007a; 2007b) as hydrostatic pressure at the tip of the fracture overcomes the compressive stress of the ice at depth. At a section of the glacier that has already been driven to disequilibrium, the inclusion of meltwater may provide the catalyst for calving to be initiated. Furthermore, the yield stress of ice decreases as temperature increases (Benn et al., 2007b), potentially increasing the likelihood of calving as temperature generally increases throughout the day (Figure 5.29). The combination of these two factors (decreased yield stress and meltwater) could explain why calving tended to increase in concert with increases in meltwater production (e.g., van der Veen, 1997).

5.5.5 Factors contributing to calving

The temporal and spatial variability in calving events has highlighted several key factors that contribute to the overall distribution of calving events at Tasman Glacier, a mid–latitude freshwater–terminating glacier. These factors include: the effect of climate at seasonal and diurnal scales, waterline melt and thermo–erosional notching, terminus geometry and structure, and basin morphology. Each factor affects calving at Tasman Glacier at different spatial and temporal scales. Seasonal variation in low–magnitude, high–frequency, notch and over–steepening events are primarily controlled by climate variations. The timing and style of individual calving events are affected by site specific factors such as waterline melt and notch development, and how preconditioned the ice cliff is to calving through the presence of crevasses. Longer–term variations in calving via high–magnitude, low–frequency events are controlled by basin morphology, which in turn affects water–depth at the terminus and whether the glacier is retreating down a reverse–slope. These key factors are elaborated on in the following sections.

5.5.5.1 Climate and meltwater

Due to the mid–latitude location of Tasman Glacier and the resulting large variations in climate throughout the year (Figure 5.28), temperature and rainfall have affected the distribution of calving events at a variety of time–scales, from seasonal to diurnal. Increased temperatures over spring and summer months would have increased subaerial melt and also temperature within the upper section of the water column (Röhl, 2005). Subaerial melt affects not only the geometry of the subaerial ice cliff (Purdie and Fitzharris, 1999; Benn et al., 2001), but also the production of meltwater into the glacier system. This has already been shown to have an effect on whether a vertical or convex ice cliff is present at the terminus (section 5.5.3), but also on the diurnal distribution of calving at Tasman Glacier (section 5.5.4). However, the warming of the upper layers of the water column appears to have a greater affect on the seasonal distribution of

calving than subaerial melting, by enhancing waterline melt and notching (Figure 5.31). In contrast, rainfall within the Tasman Glacier catchment has the effect of limiting notch formation and calving rates on sub–seasonal time–scales by vertically moving the water level of Tasman Lake. Such increases in lake level associated with rainfall also affect the terminus by inducing greater upward buoyant forces (Boyce et al., 2007).

5.5.5.2 Waterline melt and notching

Waterline melt and thermo–erosional notch formation played an important role in the driving subaerial calving at Tasman Glacier, appearing to contribute to the strong seasonal signal evident (Figure 5.31). As has been discussed in section 5.5.2.1, the development of a notch at the waterline significantly affects the stress regime of the ice cliff, introducing instability in to the system and causing calving to be initiated (Iken, 1977). This process has been well documented at calving margins globally (Warren, 1999; Benn et al., 2001; Haresign and Warren, 2005), as well at Tasman Glacier (Kirkbride and Warren, 1997; Purdie and Fitzharris, 1999; Warren and Kirkbride, 2003; Röhl, 2006). Water–terminating margins that display the cyclical process of notch formation and calving (e.g., Vieli et al., 2002; Warren and Kirkbride, 2003) all appear to show a strong seasonal variability, linked primarily to temperatures in the proglacial water body. This would explain the apparent correlation between calving rate and water temperature found by Warren and Kirkbride (2003). However, as noted both above and by Röhl (2006), a complex interaction between lake temperature, lake level, debris supply, and ice cliff and notch geometry controls the local distribution of notches at the ice cliff. Increased lake temperature may therefore provide the necessary conditions to enhance notch formation and calving, but the rate of formation at any one location is controlled by site specific variables.

5.5.5.3 Terminus structure and geometry

Glacier flow and velocity variations provide a principal control on terminus geometry and structures through the development of crevasses as they induce tensile stress at the glacier front, providing the necessary preferential lines of weakness along which calving is initiated (Powell, 1983; Benn et al., 2007b). At Tasman Glacier the complex arrangement of crevasses (Figure 5.41) is caused by the variations in ice flow and the fact that a large section of the terminus (the southern ice cliff) is effectively unsupported as it terminates in >300 m of water. The effect of this has been a contribution to the spatial and temporal variability of calving. For example, the dominant flow regime effectively perpendicular to the current orientation of the western embayment ice cliff and the development of fractures parallel to the ice cliff is not favourable as crevasses will inherently develop normal to the principal stress regime. This can be seen in Figure 5.41A–B, in the form of chevron crevasses. The opposite is true for the southern ice cliff

where the development of transverse crevasses (Figure 5.39 and Figure 5.41) has played an important role in calving. Transverse crevasses develop normal to this principal stress (i.e. parallel to flow), which in this case is parallel to the southern ice cliff due to force imbalances at the unsupported ice cliff or acceleration in basal motion as a result of decreased drag at the base of the glacier as flotation is approached (Vieli et al., 2000; O'Neel et al., 2005).

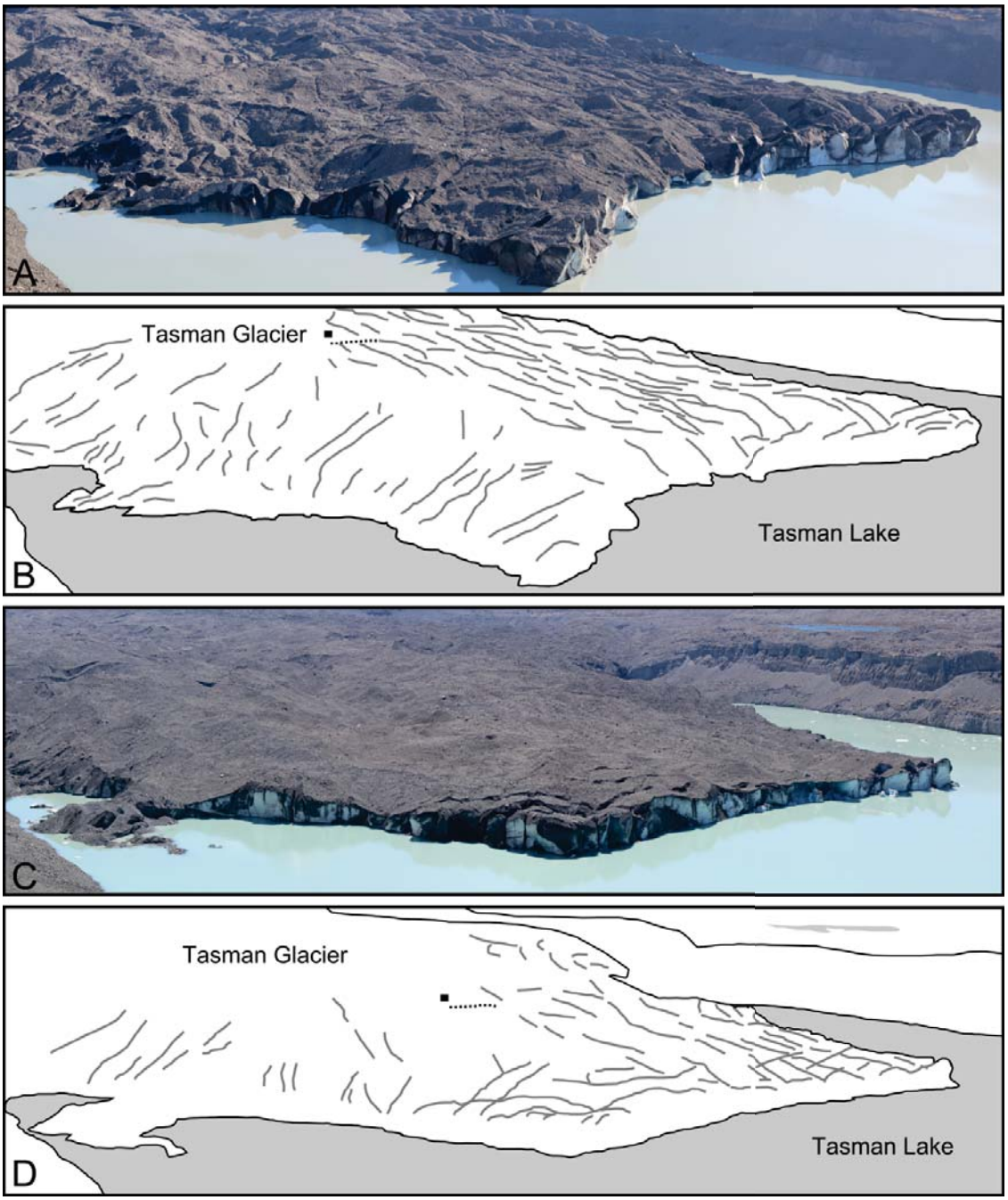

Figure 5.41: Images of the Tasman Glacier terminus in December 2011 (A) and November 2012 (C), with interpretation of identifiable crevasses, (B) and (D) respectively. Note the highly complex arrangement of structures that appear to cut across each other, indicating that not only flow velocity, but also terminus geometry plays an important control on the development of crevasses. Square and dotted line on the glacier surface indicates the approximate position of a bolder and ridge in the two images.

The extensive presence of longitudinal crevasses on the eastern surface of the glacier (Figure 5.41) indicates that lateral expansion is occurring. This is due to the unloading of pressure along the unsupported eastern embayment ice cliff as it is no longer confined by surrounding ice or valley walls. The effect of longitudinal crevasse development is to provide lines of weakness for calving events to take place within the eastern embayment, as they are aligned parallel to the ice cliff. A secondary effect is to isolate blocks of ice along the eastern section of the southern ice cliff as transverse crevasses cross–cut longitudinal fractures, removing lateral support from ice blocks and leading to the initiation of calving.

5.5.5.4 Basin morphology

Basin morphology at Tasman Glacier controls not only the geometry of the terminus, but also the depth of water that the glacier terminates into. It is the water–depth at the terminus that appears to provide a key control on longer–term retreat of Tasman Glacier, conditioning the high–magnitude, low–frequency calving events observed between October 2011 and November 2012. Where a glacier thins or retreats into deep water the terminus is subjected to bending forces as hydrostatic equilibrium is no longer maintained (Warren et al., 2001; Boyce et al., 2007). Given the significant water depths at the terminus of Tasman Glacier throughout the study period as well as that the glacier appears to be retreating down a reverse slope (Figure 4.4) significant bending forces were being applied to the terminus throughout the study period. This, coupled with the continued downwasting of the terminus and calving, led to the high–magnitude buoyancy–driven calving observed in January and April 2012 (Figure 5.34).

5.5.6 Comparison with previous research

5.5.6.1 Previous research at Tasman Glacier

Studies that have looked at processes of calving at Tasman Glacier have identified the importance of waterline melt on the development of thermo–erosional notches as the rate–controlling element for calving and retreat (Purdie and Fitzharris, 1999; Röhl, 2006), with buoyancy–driven calving only recently recognised as a contributing mechanism (Dykes et al., 2011). Due to the increase in water–depth at the terminus, as Tasman Glacier has retreated into an over–deepened trough, notch–driven calving did not control ice loss from the terminus to the same extent as during previous phases of retreat (chapter 4). As increased upward–bending forces have been applied to the terminus due to sections of the terminus becoming buoyant, the bulk of ice loss from Tasman Glacier was caused by high–magnitude, low–frequency, buoyancy–driven calving events between October 2011 and November 2012. However, notch–driven calving has continued to be important throughout the period from October 2011 to

November 2012, accounting for the majority of all calving events recorded. As a result, the processes (such as lake level and temperature) that were identified by Purdie and Fitzharris (1999) and Röhl (2006), have continued to have an effect on the terminus dynamics and calving rates, just not to the same extent on glacier retreat.

5.5.6.2 Frequency of calving events

Both notching and buoyancy–driven calving act over extended periods of time (days to weeks), resulting in the relatively low (*c.* 0.1–2 events d^{-1}) temporal frequency of calving events observed at Tasman Glacier compared to other calving margins. In contrast, the frequency of calving events at tidewater glaciers is significantly higher, ranging from *c.* 1 event h^{-1} to *c.* 40 events h^{-1} to at some glaciers (O'Neel et al., 2003; O'Neel et al., 2007; Chapuis and Tetzlaff, in press). This difference between contrasting calving margins represents calving events of a rate at least an order of magnitude higher at tidewater glaciers. The cause of this is still unclear, although it is likely due to the density difference between fresh and saline water inducing greater subaqueous melt rates (Motyka et al., 2011; Trüssel et al., 2013), greater ice velocities and longitudinal stretching creating a more perversely fractured and crevassed terminus (Meier and Post, 1987; Vieli et al., 2000; O'Neel et al., 2001), and the daily flexure of the terminus due to tidal forcing (Boyce et al., 2007; Trüssel et al., 2013).

However, the significantly lower rates of calving events at Tasman are likely to be associated with the low abundance of crevasses in comparison to tidewater glaciers. Relatively lower velocity gradients at the termini of freshwater glaciers cause low longitudinal strain rates, leading to the lesser crevassed surface when compared to tidewater calving margins (Meier and Post, 1987; Vieli et al., 2000; O'Neel et al., 2001). As crevasses provide lines of weakness along which calving is typically initiated, the less extensive the crevassing within the terminus area, then lower the potential for calving events to occur. In comparison to tidewater glaciers, the terminus of Tasman Glacier is not heavily crevassed. This potentially limits the frequency of low–magnitude high frequency calving as decreased crevasse density restricts the number of fractures along which calving occur. As a result, the rate of calving events is controlled by notching at the waterline, which initiates calving over longer time frames (4–8 weeks).

5.5.6.3 Seasonal distribution of calving events

Seasonal trends in calving event frequencies at Tasman Glacier are common at both freshwater and tidewater calving margins, caused by factors that contribute to enhancing low–magnitude events. At Tasman Glacier this was found to be related to changes in lake temperature affecting waterline melt rates and the development of thermo–erosional notches. Over summer months

the duration and intensity of solar radiation acting on the proglacial water–body is greater than over winter months, increasing the ability for water to melt ice via conduction and increasing convection rates at the terminus (e.g., Röhl, 2005).

At tidewater glaciers, increased summer calving is also linked to an increase in water temperature due to warmer ocean currents, which increases subaqueous melting. At Hansbreen Glacier this is associated with an increase in waterline notching (Vieli et al., 2002) which destabilises sections of the subaerial ice cliff, similar to that occurring at Tasman Glacier (section 5.5.2.1) and other freshwater terminating glaciers (e.g., Kirkbride and Warren, 1997; Warren and Kirkbride, 2003). However, the more general increase in calving at tidewater margins is associated with an increase in subaqueous melt (O'Neel, 2000; Vieli et al., 2001; Motyka et al., 2003a), due to changes in fjord temperatures and circulation (Motyka et al., 2003a), and the speed up of the glacier potentially associated with increased meltwater supply (Meier and Post, 1987; Krimmel, 1997). This increases the rate of calving by increasing crevasse development and penetration, thinning the terminus, and increasing force imbalances.

During winter months, where calving is limited, the advance of tidewater glaciers is possible as ice flux into the terminus is greater than the loss of mass via calving and melt (Vieli et al., 2002; Motyka et al., 2003a). However, even though calving at Tasman Glacier decreases to almost zero over winter months no obvious advance of the glacier is evident, indicating that at present calving and melt of the terminus over this winter period must match ice flux into the terminus. This is unsurprising as annual ice velocities in the terminus region are low (< 50 m a^{-1}), representing a low ice flux. Furthermore, subaerial and subaqueous melt occurs year–round, albeit at variable levels (e.g., Röhl, 2005). The period of limited calving at Tasman also only encompasses three months (July, August and September). Compared to the six to eight months at similar tidewater margins (Vieli et al., 2002; Motyka et al., 2003a), the period of low calving rates over winter months is short–lived suggesting that Tasman Glacier does not have the required time to advance to the same degree as tidewater glaciers even if ice supply was greater than ablation at the terminus.

5.6 Conclusion

From the use of ASTER satellite imagery and time–lapse photography the distribution of retreat and calving events indicate significant temporal and spatial variations in calving at Tasman Glacier through the period October 2011 to November 2012. A dominant seasonal trend in calving was observed, with the number of calving events reaching a maximum during spring and summer months (December to April). This seasonal signal was primarily related to an

increase in thermo–erosional notch–driven calving, although over–steepening events also contributed, albeit to a lesser extent. Regional patterns in calving between the three sections of the ice cliff were also controlled by notch–driven and over–steepening events. In contrast, buoyancy–driven and subaqueous calving events were intermittently distributed throughout, with no significant seasonal trends observable. Buoyancy and subaqueous events were also the largest of all events and occurred independently of all other events.

The complex arrangement of processes acting on the terminus of Tasman Glacier indicates that no single variable controls the rate and distribution of calving events. Instead, multiple processes act on the terminus to control the spatial and temporal (daily, sub–seasonal, seasonal and annual) distribution of calving. Temporal and spatial distributions of notch–driven calving appear to be linked to increases in lake level stability and temperature. The latter provided the conditions to enhance notching during the year, with the former controlling notch formation at sub–seasonal timescales. Overprinted on the seasonal distribution of calving across the entire terminus is the impact of high–magnitude, low–frequency, buoyancy–driven calving events, although intermittent buoyancy events had the greatest contribution to the overall retreat of Tasman Glacier.

Four key factors have been identified that have contributed to observed temporal and spatial trends in calving. They are: climate variations at seasonal and diurnal scales; waterline melt and notching; geometry and structure of the terminus; and basin morphology. Calving at Tasman Glacier is highly sensitive to changes in all these variables, with diurnal variations overprinted on seasonal patterns. For example, long–term trends in calving events, and particularly the generation of high–magnitude, low–frequency buoyancy–driven calving events, appear to be controlled specifically by variations in glacier flow and the geometry of the glacier and proglacial water body (i.e. water depth). Low–magnitude, high–frequency, calving events such as notch–driven and over–steepening calving are controlled by ice cliff geometry, subaerial and subaqueous melt, and lake characteristics affecting the seasonal and sub–seasonal variability. Similar results have been found at both freshwater and tidewater glaciers globally (e.g., Benn et al., 2007b), indicating that the controls of calving at these margins are similar. Further analysis of the dataset is needed to assess the significance with which the observed variability in calving rates can be attributed to external variables. Nevertheless, results presented here have shown that the frequency of calving events is at least an order of magnitude different, indicating that although calving is governed by similar controls there must be a contrast of conditions present (e.g., density differences of fresh and saline water, velocity gradients, or perturbations in proglacial water level) to generate this difference.

Chapter 6: Statistical analysis of sub–annual iceberg calving at Tasman Glacier, 2011–2012

6.1 Introduction

The temporal and spatial distribution of calving events at Tasman Glacier between October 2011 and November 2012 discussed in chapter 5 has shown that calving throughout the study period was highly variable. However, certain patterns and trends are evident within the dataset. For example, a seasonal trend occurs in association with over–steepening and the development of notches at the base of the subaerial ice cliff. In order to further quantify how external variables and conditions of individual calving events control calving pattern and the retreat of Tasman Glacier at various time–scales, a statistical analysis was applied to the dataset. In particular, this chapter investigates the following key questions:

1. Are calving events randomly distributed with respect to time or do they tend to group or cluster?
2. Can high–frequency and small–volume calving events trigger high–magnitude ice break–offs, or vice versa?
3. Is ice cliff pre–conditioning through calving indicative of the occurrence and calving style of follow–up events?
4. Are external variables (or certain combinations of several variables) acting on the glacier–lake interface decisive factors that would allow forecasting the likelihood of calving?

To determine whether external variables have had an effect on the calving distribution, the observed distribution of calving volumes was modelled to quantify dependencies on lake temperature, fluctuations in water depth, and the volume of calved icebergs. A secondary component of the analysis aims at modelling the identified pattern in calving styles. In particular, this analysis investigates whether a given style of calving increases the probability that the same style or another style will occur next, and whether there is any time–dependence to this problem. From this analysis a greater understanding of the processes and factors affecting

calving at Tasman Glacier can be gained. The aim of this chapter is, therefore, threefold: (1) characterise and model the distribution of calving event volumes, (2) model the observed calving rate and compare this to external variables, and (3) analyse the inter–event dependency of calving event styles and their variability over a full annual cycle of calving at Tasman Glacier.

6.2 Calving volumes

6.2.1 Distribution of volumes

To determine the variability of event volumes over the study period, data of the cumulative calving–size frequency against calving event volumes was fitted with a variety of one and two parameter distributions (Figure 6.1). Parameters used in fits were estimated by maximum likelihood or method of moments. Of all distributions applied to the logarithm of volume, the gamma distribution gives the best (and indeed only satisfactory) fit. Using the gamma distribution fit, probability density functions (PDF) were converted to volume and are shown in Figure 6.2. Interestingly, the distribution has a positive mode at *c.* 2500 m^3, and an extremely long tail. This is in close agreement with the observed distribution of calving event magnitudes shown in Figure 5.25. The long tail is associated with low–frequency, high–magnitude calving events, which were observed to dominate the total volume lost due to calving during the study period Figure 5.26.

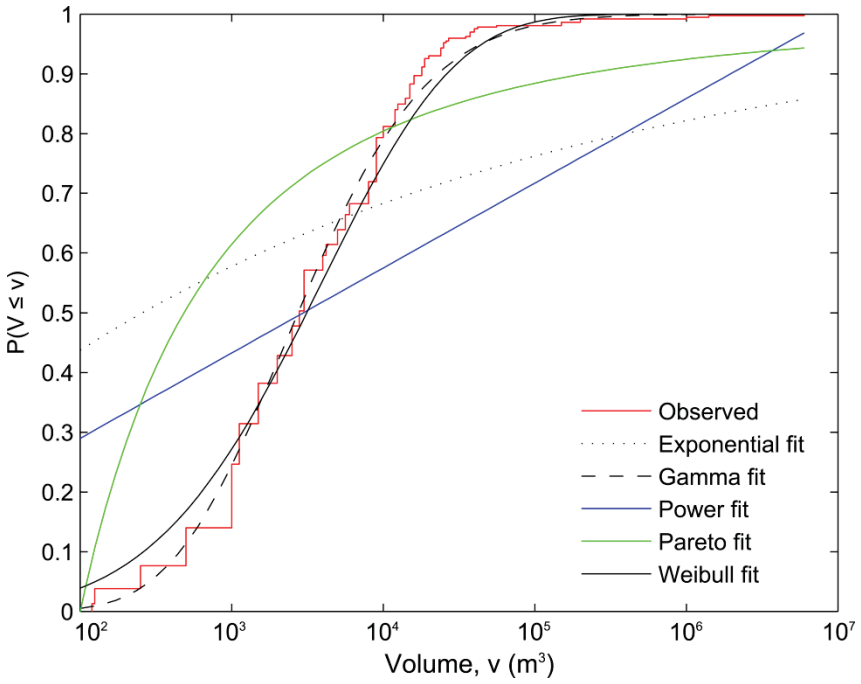

Figure 6.1: Cumulative calving frequency (normalised to 1) against logarithm of volume fitted with a variety of distributions. Only a gamma distribution gives a satisfactory fit to the observed volume distribution.

6.2.2 Volume as a function of time

The variability of calving event volumes over time can be expressed by fitting the logarithm of volume as a local linear regression (Hastie et al., 2001, section 6.1.1) against time (Figure 6.3). Based on this regression the optimal bandwidth λ as determined by cross–validation is approximately 15 days. However, the result for 30 days is also shown to aid comprehension of the long–term trends. From the local linear regression there is a slight tendency for the mean of log volume to increase in winter (days 214 to 310), although the largest calving event volumes took place in summer. Large calving event volumes observed between days 35 to 190 (summer and autumn months) in Figure 6.3 appears to be an artefact of the long tail (i.e. large distribution of calving event volumes) mentioned above and shown in Figure 6.2. For example the largest calving events throughout the entire study period (1.4×10^6 m^3) took place in January 2012 (day 95), which affected the volume distribution (Figure 6.2). Although physical conditions at the terminus ultimately control the size of calving events, the fact that several larger calving events occurred in summer may also be related to the higher frequency of calving (Figure 6.3), increasing the likelihood for larger calving events to occur.

However, the overall mean volume of calving events in summer (dominated by high–frequency, low–magnitude events ($< 1\times10^3$ m^3)) was comparably lower than during the winter observational period (approximately between days 214 and 310). In comparison, there are far fewer low volume calving events recorded over winter months, resulting in an increase in mean log volume. Although this potentially indicates a shift in the response of the ice cliff to external variables, an observational artefact cannot be ruled out whereby smaller winter month events may have been overlooked. Hence, there is no clear time dependency for calving event volumes throughout the study period, suggesting that an event of any size is able to occur at any time at Tasman Glacier. The same phenomena were also observed for notch–driven and over–steepening events when examined separately.

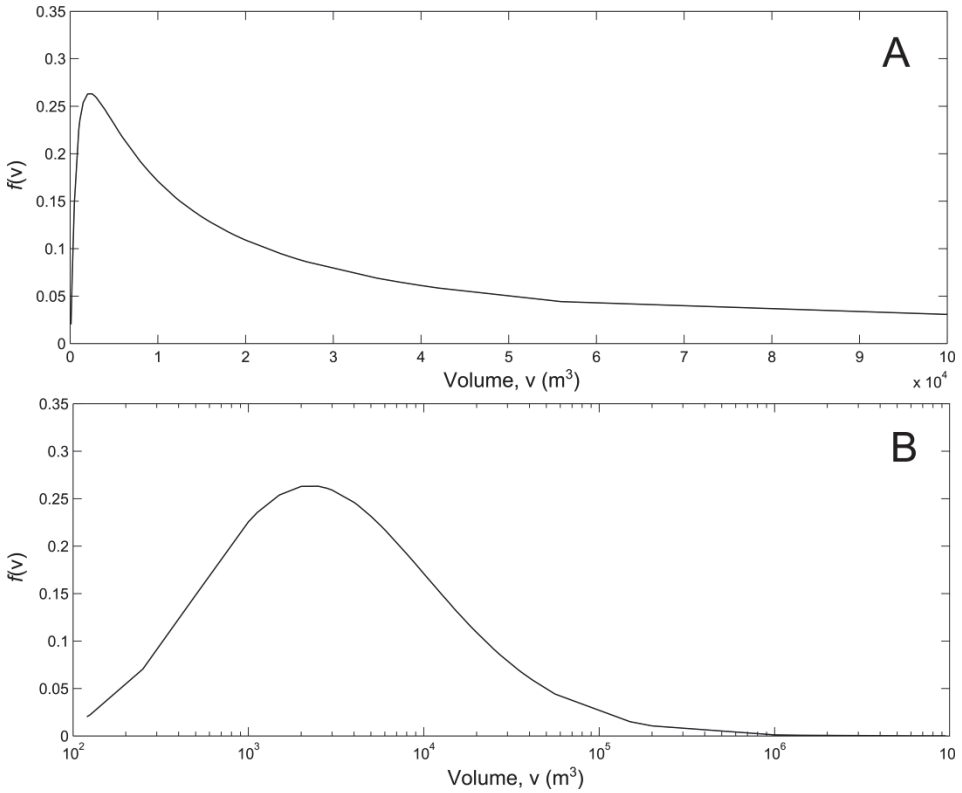

Figure 6.2: PDF converted to calving volume using the gamma distribution shown in Figure 6.1. Botch linear (A) and log (B) volumes scales are shown to highlight the overall distribution of calving event volumes. Note that the long tail (very large volumes) is not shown in A.

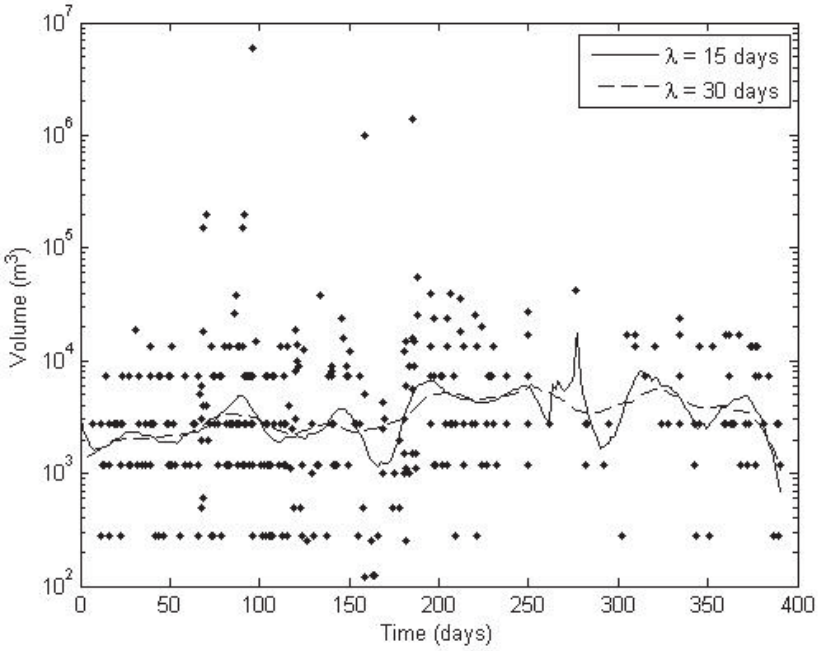

Figure 6.3: Local linear regression of log(volume) against time in days since the start of the observation period. Time zero refers to the first day of the study period, 27 October 2011. Note the overall increase in mean event volumes during winter months (approximately 214 to 310 days) when compared to the rest of the dataset.

6.3 Time dependent model for calving rate

A time dependent model for calving rate at Tasman Glacier was developed to assess the effect of external variables and the influence of previous calving events on the likelihood of calving rate. A proportional hazards Weibull renewal model (Green et al., 2013), a class of statistical survival models, was fitted to the observed calving events, with the form:

$$\lambda(r) = ar^b \tag{6.1}$$

where, λ is calving occurrences, *a(t)* is the proportional hazard term as a function of time, *r* is the time in days between events, and *b* is a constant. Using this model the volume of the previous event, lake temperature and lake level are compared to the model results to determine the ability of each variable to act as a predictor of calving. Lake temperature and lake level are represented by the average and standard deviation over the 5 days (of readings at 15 minute intervals) preceding the event. Five days was found to be the optimal length of time by examining the log–likelihood of the model on the full data set. The logarithm of the temperature (in ºC) was found to provide the best result for model inputs as well as the correct boundary condition at freezing.

By definition, the proportional hazard model assumes that the conditions for calving are set up by what happens prior to the interval preceding the calving event. This is necessary if the model is to be used for forecasting, as the quantities required in the forecast must be available at the time the forecast is made (i.e. at the time of the previous event). As the average time between events was found to be in the order of *c.* 1 event d^{-1} (section 5.4.2) using the five day average of model inputs (lake temperature and lake level) does not seem to be a critical assumption for forecasting the calving rate at a daily time–scale. A diurnal analysis was not attempted because of the larger errors in event timings during darkness.

To assess whether the model input had a significant effect on the daily calving rate was determined by examining the Akaike information criterion (AIC; Akaike, 1977), which balances degree of fit against number of excess parameters. From this analysis the optimal model for the calving occurrences (λ) could be derived as:

$$\lambda(r\,|V,T,D)=1.991e^{(0.968T-0.392D)}r^{-2.06} \tag{6.2}$$

where *r* is the time (in days) since the preceding event, *V* is the log volume of the previous event, and *T*, *D* are, respectively, the five day average lake level and log–temperature preceding

the previous event. Log volume was not found to be a significant function of calving occurrences (i.e. calving rate). Diagnostics for the model (see Bebbington, 2013) were satisfactory (a serial correlation of 0.017 (P–value = 0.74, not significant)), and there was no significant deviation from stationary and exponential intervals in the transformed process (Figure 6.4), indicating that the model result adequately accounted for the distribution of calving events at Tasman Glacier.

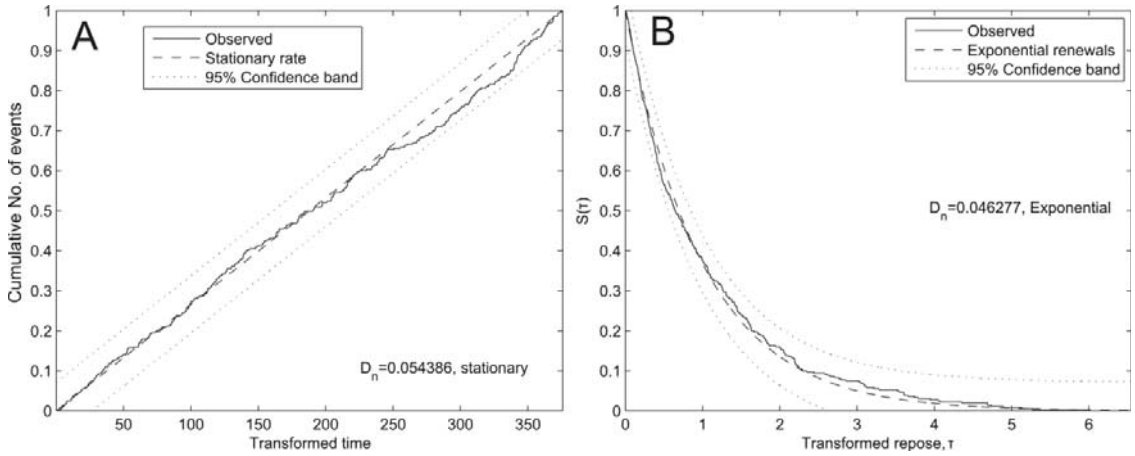

Figure 6.4: Comparison plots of the observed calving rate with the stationary rate (A) and exponential intervals (B) from the fitted model of calving occurrences at Tasman Glacier. The compensator used is Poisson.

The fitted model itself is depicted in Figure 6.5C, with the actual time–series data of lake temperature and lake level shown in Figure 6.5A and Figure 6.5B, respectively. When compared with the fitted model, lake temperature encourages calving throughout the year, and is present at an approximately seasonal cycle throughout the study period. In comparison, increased lake level discourages calving, and hence, rainfall events (which increase lake level) result in a decrease in calving rate and fewer calving events. This becomes clearly visible in Figure 6.5 around the 50, 120, and 150 day marks where rapid increases in lake level decreased the calving rate over a short period of time (*c.* 4–5 days). The impact of increased lake level appears to decrease over winter months as the calving rate is already suppressed due to lower lake temperature. This effect is shown in Figure 6.6, where the impact of lake level and temperature vary together.

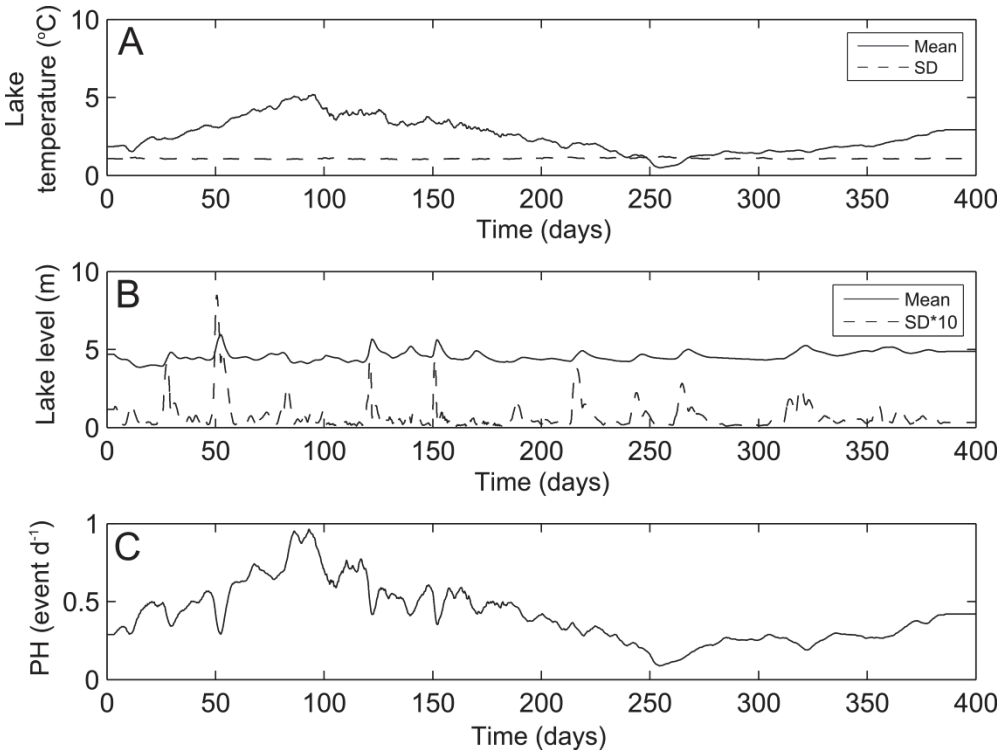

Figure 6.5: Variations in (A) lake temperature and (B) lake level (depth) between 27 October 2011 and 22 November 2012. The fitted proportional hazard model for all styles of calving events is shown in C.

In contrast to lake temperature and lake level, the volume of calved icebergs does not appear to be a significant factor in the derived model of calving rate, as indicated by its absence from Equation (6.2). The absence of volume as a significant factor was also confirmed by fitting the volume history model (Bebbington, 2008), which agrees with the previous interpretation (section 6.2) that no time–dependence in event volume size exists.

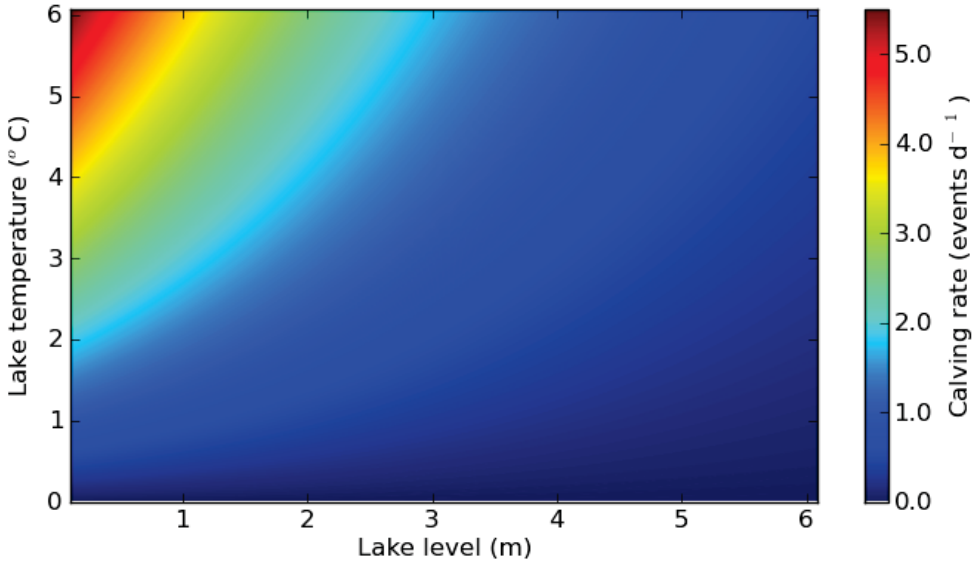

Figure 6.6: Plot showing the influence of lake temperature and lake depth on calving rate.

An interesting implication from Equation (6.2) is that its exponential functional form describes a tapering off in the probability of calving. To test whether this is indeed the case the survival probability (Prob(R > *r*)), or the probability that the time interval between events is > *r*, was calculated. Assuming that Equation (6.2) is true, the survival probability of calving occurrences is:

$$S(r) = e^{(-ar/(b+1))} \tag{6.3}$$

In contrast, if the data were represented by a Poisson process (i.e. purely random interval between calving events) then λ would be equivalent to a constant rate and the survival probability curve would be memoryless:

$$S_{pp}(r) = e^{(-Nr/Y)} \tag{6.4}$$

where N is the number of calving events (365 events), and Y is the total number of days of study (390 days). Modelling the survival probability for a variety of lake levels and temperatures (Figure 6.7) shows there is clearly a tendency for the rate of calving events to cluster. Therefore, there is a higher probability for events to occur near other events for the majority of temperature ranges when lake level is low when compared to the reference curve (Figure 6.7A–C). The tendency for the clustering of calving events decreases for all temperatures with respect to increased lake level (Figure 6.7C–D), confirming the complex relationship between the two external variables of calving rate at Tasman Glacier shown in Figure 6.6. The physical cause of this tendency to cluster is likely to be related to the distribution of notching and over–steepening events as they account for almost all of the observed calving events.

6.4 Analysis of Calving Style

6.4.1 Correlations between successive events

To assess the effect that individual events have on a subsequent event, analysis was carried out to determine whether calving event styles were randomly distributed, or if calving events of a particular style resulted in another similar style calving event. To do this a Markov chain analysis (cf. Cronin et al., 2001) was performed for the transition from one style to another. The resulting transition matrix (probability of the next style given the previous style):

$$P = \begin{array}{c} \text{prev\next} \\ \text{B} \\ \text{N} \\ \text{O} \\ \text{SA} \end{array} \begin{array}{c} \begin{array}{cccc} \text{B} & \text{N} & \text{O} & \text{SA} \end{array} \\ \begin{bmatrix} 0 & 0.50 & 0.50 & 0 \\ 0.01 & 0.65 & 0.28 & 0.06 \\ 0.03 & 0.50 & 0.44 & 0.03 \\ 0 & 0.57 & 0.24 & 0.19 \end{bmatrix} \end{array} \tag{6.5}$$

indicates that there is a higher probability for notch–driven (N) events to follow all types of calving events, followed by over–steepening events (O). The zeros in Equation (6.5) for buoyancy (B) and subaqueous (SA) events are not indicative of a zero probability of that style following the previous style, but are the result of the small number of that type of previous event.

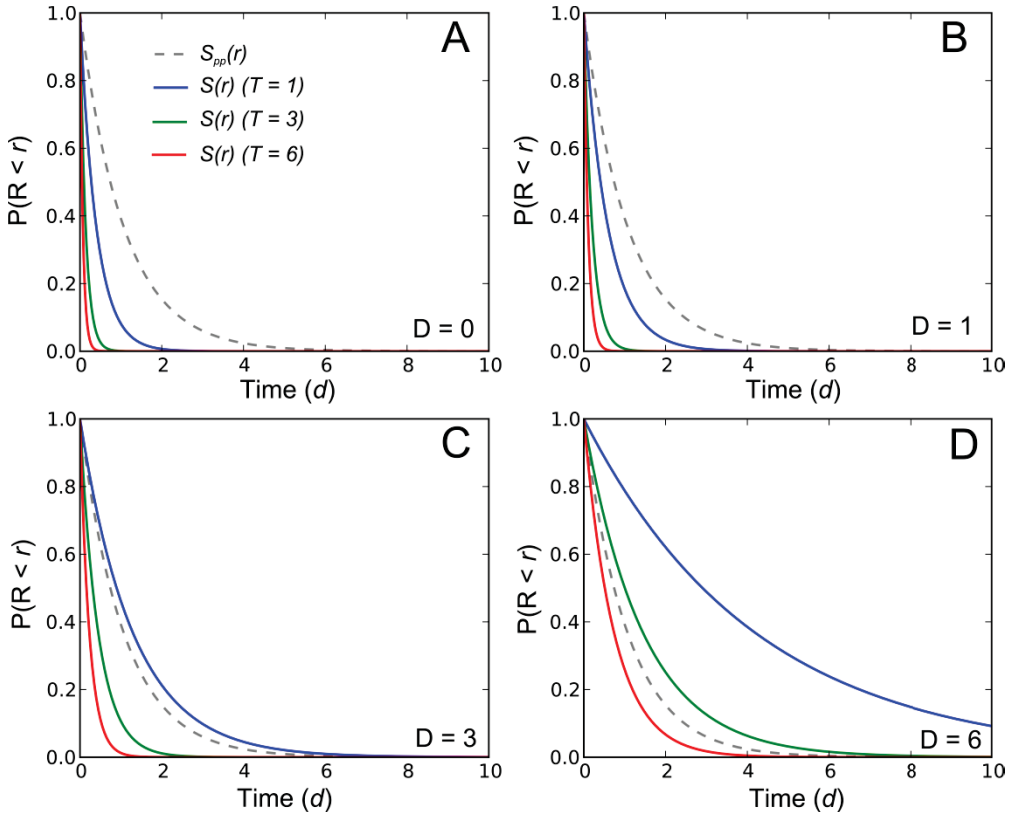

Figure 6.7: The modelled (Equation (6.3)) survival probability (Prob(R>*r*)) of calving occurrences (i.e. the probability that the time between events is > *r*) for a variety of lake temperatures (T (ºC) = 1, 3, 6) and lake levels (D (m) = 0, 1, 3, 6). The reference curve (grey dotted line) is the modelled survival probability given a Poisson process (Equation (6.4)).

To test whether the distribution of probabilities in Equation (6.5) are indicative of the observed calving events at Tasman Glacier, an analysis of independence (i.e. styles of calving events are random) was carried out using a chi–square test of event styles. However, reporting calving styles as notching, over–steepening, buoyancy, and subaqueous the contingency table is too unbalanced (Table 6.1). To better assess independence, buoyancy and subaqueous events were combined under the assumption that they have a similar effect on terminus stability, with the results of the combined analysis of independence reported in Table 6.2. From Table 6.2 it is

clear that styles of events do not occur randomly throughout the period of study. In particular, combining Equation (6.5) and Table 6.2 there is a tendency at Tasman Glacier for notching and over–steepening calving events to be followed by an event of the same type, rather than one of another type.

Table 6.1: Contingency table showing chi–square test results to determine the independence of calving styles for buoyancy (B), notch (N), over–steepening (O), and subaqueous (SA) calving events. Expected counts are reported below observed counts, with chi–square contributions printed below expected counts.

	B	N	O	SA	Total
B	0	3	3	0	6
	0.1	3.56	1.99	0.35	
	0.099	0.088	0.507	0.346	
N	2	141	60	13	216
	3.56	128.18	71.80	12.46	
	0.684	1.283	1.940	0.023	
O	4	60	53	4	121
	1.99	71.80	40.22	6.98	
	2.017	1.940	4.059	1.273	
SA	0	12	5	4	21
	0.35	12.46	6.98	1.21	
	0.346	0.017	0.562	6.148	
Total	6	216	121	21	364

Chi–Square = 21.602, DF = 9

Table 6.2: Contingency table of chi–square test results to determine the independence of calving styles grouping buoyancy and subaqueous events (B/SA. Notch (N) and over–steepening (O) calving events remain separate. Expected counts are reported below observed counts, with chi–square contributions printed below expected counts.

	N	O	B/SA	Total
N	141	60	15	216
	128.18	71.80	16.02	
	1.283	1.940	0.065	
O	60	53	8	121
	71.80	40.22	8.98	
	1.940	4.059	0.106	
B/SA	15	8	4	27
	16.02	8.98	2.00	
	0.065	0.106	1.992	
Total	216	121	27	364

Chi–Square = 11.556, DF = 4, p–value = 0.021

6.4.2 Style–time dependence

The general trends in the styles of calving events have already been presented in Figure 5.18 and discussed in section 5.5.2. To establish whether the identified trends are statistically significant, an analysis of the occurrence of each style over time was carried out using a contingency table (Table 6.3), where time is binned into days 0 to 68, 68 to 103, 103 to 156, 156 to 227 and 227 through to the end of the study (390 days). The time bins used were set so that each had approximately equal numbers of total expected events. The original contingency table (Table 6.3) is again too unbalanced, so buoyancy and subaqueous events are merged to make the chi–squared approximation valid (Table 6.4).

Table 6.3: Contingency table showing chi–square test results to determine whether there is any style–time dependence. Buoyancy (B), notch (N), over–steepening (O) and subaqueous (SA) calving events are compared approximately to time bins 0 to 68 days, 68 to 103 days, 103 to 156 days, 156 to 227 days, and 227 days onwards to have approximately equal numbers of total events in each. Expected counts are reported below observed counts, with chi–square contributions printed below expected counts.

	0 to 68	68 to 103	103 to 156	156 to 227	227 to 390	Total
B	1	3	1	1	0	6
	1.23	1.17	1.25	1.15	1.20	
	0.044	2.878	0.050	0..020	1.200	
N	49	37	43	28	60	216
	44.59	42.21	45.18	41.62	43.40	
	0.436	0.643	0.106	4.455	6.349	
O	21	23	26	39	12	121
	24.86	23.54	25.19	23.21	24.20	
	0.600	0.012	0.026	10.750	6.150	
SA	4	8	6	2	1	21
	4.32	4.08	4.37	4.03	4.20	
	0.023	3.752	0.606	1.021	2.438	
Total	75	71	76	70	73	364

Chi–Square = 41.560, DF = 12, p–value < 0.001

From Table 6.4 it can be concluded that the likelihood of each style changes with respect to time at Tasman Glacier. In particular, between days 156 and 227 (start of winter period at Tasman Glacier) the likelihood of notch–driven calving events decreases, whilst the likelihood of over–steepening events increases. This situation then reverses over the following period (days 227 to 391) as temperatures tend to increase at the start of spring.

Table 6.4 Contingency table showing chi–square test results to determine whether there is any style–time dependence, with buoyancy and subaqueous events grouped (B/SA). Notch (N) and over–steepening (O) calving events remain separate, with time bins the same as Table 6.3. Expected counts are reported below observed counts, with chi–square contributions printed below expected counts.

	0 to 68	68 to 103	103 to 156	156 to 227	227 to 390	Total
N	49	37	43	28	60	216
	44.59	42.21	45.18	41.62	43.40	
	0.436	0.643	0.106	4.455	6.349	
O	21	23	26	39	12	121
	24.86	23.54	25.19	23.21	24.20	
	0.600	0.012	0.026	10.750	6.150	
B/SA	5	11	7	3	1	27
	5.55	5.25	5.62	5.18	5.40	
	0.054	6.291	0.338	0.916	3.585	
Total	75	71	76	70	73	364

Chi–Square = 40.713, DF = 8, p–value < 0.001

6.5 Discussion

Combining the analyses presented here and in chapter 5, several important factors have been identified that control the temporal distribution of calving at annual and inter–event time–scales. These are:

1. There is no observable time–dependency in the volume of calving events;
2. External parameters (i.e. lake temperature and changes in lake level) have significant control on enhancing and suppressing calving rates; and
3. The probability of a particular calving style changes with respect to time.

The potential physical controls and applicability of modelled results and relationships are discussed in this section to elaborate on important factors affecting calving at Tasman Glacier.

6.5.1 Calving event volumes

The volume of calving events at the terminus of Tasman Glacier varied significantly (by up to four orders of magnitude) throughout the October 2011 to November 2012 study period. Calving event volume shows no time dependency during this period (Figure 6.3), with the probability of events of a given size skewed towards smaller volumes (*c.* 2500 m^3), although the distribution has a long tail (Figure 6.2). Event sizes are, therefore, essentially randomly distributed. The ability for high–magnitude calving events to occur anytime throughout the year does fit well with longer term observations of buoyancy–driven calving at Tasman Glacier taking place in both summer and winter months alike (chapter 8). However, the previous results of (A) that ice–loss due to calving is dominated by low–frequency and high–magnitude events

(chapter 4) and (B) that over longer time–scales (i.e. c. 5–10 years; and the longer than annual data set analysed statistically here) accelerated ice–loss suggests that a long–term time–dependency of very large calving events may be present. This may be due to the fact that the statistical model developed in section 6.2 is limited to the observed conditions and may not transfer to conditions more extreme than those observed (e.g., extrapolation to longer term trends).

In contrast, the skewed probability distribution (Figure 6.2) towards smaller event volumes (with a positive node at *c.* 2500 m^3) is likely to be a function of the size of icebergs able to calve from the subaerial ice cliff. As discussed in section 5.5.2, subaerial ice cliff height does not vary significantly along the terminus of Tasman Glacier, and hence provides an upper geometrical limit on the available volume of calving. This is because calving events that are typically associated with this volume range are either initiated by over–steepening of the subaerial ice cliff or the development of a notch at the waterline. Each of these processes appear to be self limiting as destabilisation of the ice cliff tends to occur as a function of ice cliff height (Röhl, 2006). This limits the available volume of ice that can calve, as larger sections that are destabilised due to (for example) the development of a thermo–erosional notch are more likely to calve as several smaller events rather than a single larger event (Röhl, 2006). Further, evidence for this occurring at Tasman Glacier also comes from Equation (6.5) and Table 6.1 that indicate that notching and over–steepening events tend to be followed by an event of the same type.

A secondary function of the random distribution of event volumes is that it has no effect on calving rates, indicated by the absence of volume from Equation (6.2). The timing and extent of calving events are inherently related to the presence of fractures in ice at the terminus, either having been advected to the calving front or forming as a result of force imbalances at the terminus due to over–steepening and notching of the base of the subaerial ice cliff. This means that the volume of a previous event will only have an effect if, post–calving, ice cliff geometry is preferential for initiating a secondary calving event. For example, a calving event of a particular volume in one location is unlikely to have an effect on subsequent calving events at any other location except at an adjacent position along the terminus. As a result, increased calving from the subaerial ice cliff may only facilitate a secondary event where the original event destabilises the ice cliff further, a process that is independent of event volumes. Furthermore, enhanced calving by this process is inherently variable and controlled by site specific factors (e.g., subaerial ice cliff geometry).

Unlike subaerial (notching and over–steepening) calving events, high–magnitude events inherently alter the dynamics of the subaerial ice cliff by leaving a highly fractured surface that is very unstable across a large area of the terminus. As mentioned in section 5.5.2.2, this can lead to an increase in over–steepening events. However, this was not observed at Tasman Glacier during the study period as high–magnitude calving events typically took place during night time hours or leading into darkened conditions, so an increase in calving associated with such events was not able to be fully quantified, if it does indeed exist. For these reasons it is unsurprising that event volume has no effect on calving rate as the proportional hazards model incorporates events across the entire length of the terminus. This result may change if the spatial extent of observations is limited to an isolated region, but due to the relatively long return time for calving events at a single location (in the order of 4 to 6 weeks (Röhl, 2006)) a longer survey period would be needed to fully quantify this.

Similar, random distributions of calving event volumes from water–terminating calving margins has been observed by several researchers (e.g., O'Neel et al., 2003; Chapuis et al., 2010; Chapuis and Tetzlaff, in press) and is in close agreement with the results presented in section 6.2. For example, Chapus and Tetzlaff (in press) found that there was no statistically significant relationship between the size of a preceding and subsequent event at Kronebreen and Sveabreen Glaciers, Svalbard. However, observations of high–magnitude calving events from tidewater and outlet glaciers often can result in elevated calving activity in the minutes and hours following the high–magnitude calving events (O'Neel et al., 2007; Amundson et al., 2008). This suggests that in general the volume of a calving event may have a near field effect on enhancing calving rates, with larger events simply affecting a larger area of the calving margin. Higher resolution observations of calving that can encompass night time hours may be able to better elucidate whether the event volumes have no effect on calving rates, or if there is a threshold of event size above which calving rate is enhanced.

6.5.2 Temporal variability in iceberg calving

Throughout the study period the style of calving varied, as seen with the rate of calving events (Figure 5.16, Figure 6.5 and Table 6.4). In general, the decrease in the likelihood of notch–driven calving and the relative increase in over–steepening events over winter months is inherently related to the effect of external variables on the Tasman Glacier terminus. The variability in calving at Tasman Glacier has been repeatedly shown to be associated with changes in lake temperature and lake level (section 5.5.2 and Figure 6.5). It is clear that over annual time–scales increased lake temperature enhances the calving rate, leading to the observed seasonal cycle of calving observed from the original dataset (Figure 5.16). Over

shorter time–scales (days) increased lake level has the opposite effect on calving by suppressing the calving rates. The extent to which calving rate (Equation (6.2)) varies with respect to changes in lake level and temperature can be seen in Figure 6.6. This shows that where lake level is relatively stable, changes in lake temperature have a significant effect on calving rates. In contrast, when lake level increases (typically over short time–scales) the effect of temperature on calving rates decreases rapidly.

The potential cause for the relationships between calving rates and increased lake level has already been discussed at length in section 5.5, but relates to an increase in notching rates that destabilise the subaerial ice cliff, these occur at a greater rate due to enhanced thermal conduction between the warmer lake and the ice cliff at the waterline (Röhl, 2006). Suppression of notching either occurs as temperatures decrease, limiting notching rates, or changes in lake level move the position of the warm upper layer of water vertically away from the developing notch (Benn et al., 2001; Röhl, 2006), effectively resetting the notching process. With notch–driven events accounting for 60 percent of all calving events it is unsurprising that the fluctuation of variables that enhance and suppress calving contribute significantly to the annual cycle of calving observed at Tasman Glacier. In comparison, subaqueous and buoyancy–driven calving are episodic in nature and are controlled by changes in longer–term factors that affect the terminus of Tasman Glacier (e.g., basin morphology and terminus downwasting) and so do not appear to be controlled by annual cycles in external parameters such as lake temperature (see chapters 4 and 8 for a wider discussion).

Similarly, due to the way calving events were categorised by their style of calving (section 5.3.4.4), over–steepening events (accounting for 33 percent of calving events) may have had a thermo–erosional notch developing at the waterline, but were classified as over–steepened as the subaerial ice cliff overall was over–steepened. As a result, antecedent conditions that enhance the development of a thermo–erosional notch and notch–driven calving can also contribute to over–steepening calving events, by introducing enough instability in the system to initiate calving. However, processes other than notch formation affect over–steepening calving events (e.g., force imbalance of the terminus). Therefore, a decrease in conditions that enhance notch–driven calving does not necessarily result in a decrease in over–steepening events. Such a situation was observed during winter months at Tasman Glacier where the likelihood of notching events decreased, while the likelihood of over–steepening events increased. The cause of the increased likelihood of over–steepening calving events is difficult to identify from the current dataset, but may be associated with the fact that a decrease in notch–driven calving may have resulted in an increased potential for over–steepening of the subaerial ice cliff to occur due to other processes acting at the terminus. Such conditions that enhance over–steepening may act

over greater time–scales then notching, meaning that they are not overprinted by increased notch–driven calving during winter months.

The modelled calving rate shown in Figure 6.5C does, however, reaffirm the observation that lake temperature significantly influences calving rates over seasonal time–scales (chapter 5), with lake level altering calving rates over shorter–terms. This agrees, in part, with previous research into the calving processes at Tasman Glacier (e.g., Purdie and Fitzharris, 1999; Röhl, 2006) and similar freshwater–terminating glaciers (e.g., Kirkbride and Warren, 1997), but puts more emphasis on lake temperature than previously acknowledged. This is unsurprising as the present study has documented the effect of notch development over an entire annual cycle, something that has been missing from previous short–term and process–based research. Although more extensive measurements of lake temperature, notching rates and calving rates are required to further quantify the interaction of lake temperature and calving, results presented here have shown that lake temperature is a more important control on calving rate than previously thought (e.g., Röhl, 2006).

However, because the likelihood of each calving event style changes with respect to time, it is not possible to simply use (cf. Cronin et al., 2001) the product of Equations (6.2) and (6.5) to model the time to the next event of a given style (e.g., the time between notching events). A suitable relationship may be able to be formulated if a larger dataset (e.g., several years) of calving event observations can be analysed to determine whether the possible trends in calving identified here are significant.

6.5.3 Clustering of events

Although event volumes do not directly influence the distribution of calving throughout the study period, a tendency for events to cluster was observed (Figure 6.7), with events of the same type more likely to follow each other than events of another type (Table 6.2). One potential reason for event clustering has been introduced in section 6.5.1 and is associated with the destabilisation of a section of the ice cliff relating to a previous calving event. This process may have an intermittent effect on event clustering, particularly for over–steepening events. However, as large proportion of calving events resulted from the development of a thermo–erosional notch a more plausible explanation is related to the conditions that originally led to the initiation of calving.

Section 6.5.2 has shown that calving events at an inter–event time scale were controlled by lake temperature and lake level. Such processes may also contribute to the increase in probability of

calving events to cluster (Figure 6.7). This is associated with the fact that the antecedent conditions which enhance calving rates and initiate notch–driven calving in the first instance are still present after calving. This means that the likelihood of another calving event occurring in a short period of time after the initial calving event remains relatively high as long as conditions that enhance calving continue. For example, increased lake temperatures and a stable lake level enhance notch–driven calving (section 5.5.2.1 and 6.5.2), resulting in an increased likelihood that a notch–driven calving event will be followed by another event of the same style. Such notch–driven calving events can occur at any point along the ice cliff while conditions remain favourable for notch development, resulting in a decrease in the time between calving events. This can be clearly seen in Figure 6.7, where the survival probability increases (i.e. the time between calving events increases) with a decrease in lake temperature and increase in lake level.

6.5.4 Wider implications and model improvements

Improved understanding of the processes and factors that have affected the distribution of calving at Tasman Glacier through the use of the proportional hazards model indicates that with improvements it may be of use in forecasting or predicting the likelihood of calving events at not only Tasman Glacier, but also calving margins globally. In particular, the importance of changes in lake temperature and lake level on the distribution of calving events at Tasman Glacier indicates that the modelled results could be used for a variety of purposes. For example, they have wider implications for: hazard warning and mitigation for tourist operators on Tasman Lake; improved understanding of the contribution of meteorological processes of calving through the combination of proportional hazard model results and climate data; the use of the model to establish and/or verify analytical/numerical physical models; and the potential for model results to be incorporated into models predicting the contribution of iceberg calving to glacier retreat and the response of glaciers to climate change.

The ability for the proportional hazard model (introduced in this chapter to account for the distribution of calving events) to be combined with climate data to aid in the development of physical based calving models, and wider models of glacier response to climate change, is of particular importance. This is because the current generation models developed to account for calving processes at retreating calving margins cannot account for a variety of calving proceses. The creation of more holistic models that take into account of not only changes in glacier dynamics as drivers of calving and retreat (e.g., Benn et al., 2007a), but also external variables (such as lake temperature), will lead to more accurate predictions of the response of glaciers to changes in climate through not only decreases in ice supply as ice melt, but also the mechanical loss of ice via calving from termini.

Such future modelling studies may be improved by further refining definitions of the extent and characteristics of individual events due to the complexity of calving events, with each additional complication multiplying the amount of data required. This may result in a broadening of calving styles when analysing the distribution of calving events at a sub–annual scale by grouping them into: (1) all events originating from the sub–aerial ice cliff, and (2) calving from the subaqueous ice cliff and large events triggered by buoyant forces. Increasing the temporal resolution of calving observations at Tasman Glacier will also allow analysis of calving variability to be extended across multiple annual cycles, to determine whether those trends described in this study are representative, and if long–term trends are also present. Similarly, increasing the area of Tasman Glaciers terminus visible, and being able to fill in data gaps present at night time and during some winter months may shed light on potential controls of calving that have only been inferred in chapter 5.

Such limitations in the present dataset can be overcome with higher resolution records by observers, the use of terrestrial photogrammetry to better constrain event volumes, ground based radar, and seismic monitoring (e.g., O'Neel et al., 2007; Chapuis et al., 2010; Bartholomaus et al., 2012; Chapuis and Tetzlaff, in press). In particular, seismic monitoring of calving events provides a promising technique to characterise event volumes and intra–event features over extended periods of time (e.g., years) that may be critical for developing more complete statistical and physical models of calving events. However, with these caveats in mind the present analysis has significantly advanced the understanding of the temporal distribution of calving events at Tasman Glacier, and has identified key relationships that require future study.

6.6 Conclusions

From the analysis of the temporal distribution of calving events presented in chapter 5, the observed variability in calving events and the impact of selected external variables of calving have been further analysed in this chapter to better understand calving at an annual and inter–event time–scale. From statistical analysis of calving event distributions and volumes it is clear that volume does not play a part in controlling the annual distribution of calving events, a result also found at similar calving glaciers globally. To analyse the effect that external parameters have on the temporal distribution of calving at Tasman Glacier, a proportional hazards Weibull renewal model was applied. It could be shown that the observed distribution of calving events is controlled by lake temperature at an annual time–scale over the entire study period (October 2011 to November 2012). At shorter time–scales (e.g., days) fluctuations in lake level suppresses calving rates, even in the presence of high lake temperatures. When these results are

combined with the fact that calving events of specific styles appear to be followed by events of the same type, and that the likelihood of event types vary over the study period, several important advances in the understanding of calving at Tasman Glacier have been made through this analysis.

In particular, the effect of lake temperature and lake level on the distribution of calving events has reaffirmed the importance of these two variables on controlling calving at Tasman Glacier. This is due to the effect that these variables have on the development of thermo–erosional notches at the waterline of the subaerial ice cliff and resulting notch–driven calving, the most frequent of all calving events. With respect to lake temperature, calving rates are increased as lake temperature increases, as the warmer upper layer of water accelerates notch–development. This accelerated notch development can be interrupted by changes in lake–level which shift the position of the waterline away from a developing notch, suppressing calving rates. The impact of lake temperature and lake level may also cause the observed tendency for calving events to cluster throughout the study period, as conditions that enhance calving rates (through enhancing notching) can lead to calving at any point along the ice cliff as long conditions do not change.

The greater depth of analysis presented in this chapter has reaffirmed conclusions discussed in chapter 5, highlighting the statistical significance of external variables on controlling calving rates at Tasman Glacier. It has also allowed establishment of a robust quantitative model to forecast the likelihood of calving at Tasman Glacier that can be tested on other freshwater terminating glaciers and tidewater glaciers worldwide. When combined with high resolution datasets (e.g., seismic analysis of calving events) the processes and controls of calving at freshwater and tidewater glaciers alike will be better constrained, aiding in the development of future models of calving and its contribution to mass balance and ice loss from water–terminating glaciers in general.

Chapter 7: Seismic detection of calving events at a lake–calving glacier, Tasman Glacier

7.1 Introduction

In this chapter individual calving events and their associated seismicity at the terminus of Tasman Glacier are analysed to gain a better understanding of intra–event seismic signals that are generated during calving and how they vary across both size and style of event. This is not intended to be an in–depth analysis of the geophysics of icequakes and calving–generated seismic signals, but utilises parameters from previous studies (e.g., Qamar, 1988; O'Neel et al., 2007; Amundson et al., 2008; Amundson et al., 2010; Walter et al., 2010; Bartholomaus et al., 2012) to identify the characteristics of seismic signals that are generated by calving at Tasman Glacier. These characteristics will be used in an attempt to relate the observed iceberg magnitude (size) to seismic parameters, and determine whether it is possible to automatically identify and catalogue events without the use of visual or photographic observations.

7.2 Background

Due to the energetic nature of calving, several studies (e.g., Qamar, 1988; O'Neel et al., 2007; Bartholomaus et al., 2012; Walter et al., 2012) have shown that iceberg calving events across the range of sizes generate measurable seismic energy. Such seismic signals generated in association with glaciers and glacial termini are broadly termed *icequakes* (Neave and Savage, 1970; Wolf and Davies, 1986; Qamar, 1988; O'Neel et al., 2007). Recently, the generation of calving–generated seismic signals has become an increasingly important field of study. It provides a technique to passively and remotely identify and describe calving events (O'Neel et al., 2007), removing the inherent dangers and difficulties historically encountered by researchers (Benn et al., 2007b). An emerging body of literature (e.g., Qamar, 1988; O'Neel et al., 2007; Amundson et al., 2008; Bartholomaus et al., 2012; Walter et al., 2012) has developed to identify the seismic signals that are emitted during iceberg calving and how these signals relate to specific characteristics of the calving process (e.g., iceberg size, style of calving, etc.). Such

studies have typically used a combination of visual and photographic observations coupled with passive seismic arrays at the termini of calving glaciers to match the timing of events to seismic signals generated. Using this methodology, authors (e.g., Qamar, 1988; O'Neel et al., 2007; Bartholomaus et al., 2012) have identified that virtually every iceberg calving event produces a low–frequency seismic event. These calving–generated icequakes have several characteristics which differentiate them from those generated by earthquakes and other glacial processes (e.g., basal motion). For example, seismograms of calving events are typically: (1) emergent, (2) long lived (2–1000 s), (3) have durations similar to calving events, (4) have an absence of *P*– and *S*–wave arrivals and (5) have high energy between 1–30 Hz, dominated by lower frequencies (*c.* 1–5 Hz).

Currently, there is no consensus as to what mechanism during the calving process is associated with the release of seismic energy (Bartholomaus et al., 2012). Because calving–induced icequakes have been identified across all magnitudes of calving events a wide range of source mechanisms have been suggested (section 2.6), including: ice fracturing (e.g., Neave and Savage, 1970; Cichowicz, 1983; Roux et al., 2008; Walter et al., 2009; West et al., 2010), fluid–driven crack propagation (e.g., Métaxian et al., 2003; O'Neel et al., 2007), hydraulic transients in subglacial conduits (e.g. St Lawrence and Qamar, 1979; Winberry et al., 2009), iceberg harmonic tremor (IHT; e.g., MacAyeal et al., 2008), rotations and scraping of icebergs on the glacier and proglacial foreland (e.g., Tsai et al., 2008; Amundson, 2010), and the interaction between icebergs and the surface of the proglacial water body (e.g., Bartholomaus et al., 2012). It is the last two mechanisms (iceberg scraping and interaction with the water surface) that currently provide the greatest potential to account for calving–generated seismograms, indicating that the style of calving appears to have a significant impact on calving–seismicity.

However, given the limited number of studies there is still no clear understanding for how calving–generated seismicity relates to specific styles of calving, the loss of mass via individual calving events, or to any underlying physical processes associated with each calving event. Hence, there is a need to identify, describe and account for calving–generated seismicity at a greater number of glaciers globally (Bartholomaus et al., 2012). Thus far the bulk of literature published on calving seismicity has focussed on the tidewater and outlet glaciers of Alaska and Greenland, with only one dataset available for freshwater–calving glaciers (Richardson et al., 2010; Richardson et al., 2012). Identifying and describing calving–generated seismicity at differing margins will provide a better understanding of whether the observed seismic energy is associated purely with the process and style of calving, or if external factors play a role. Tasman Glacier, a retreating freshwater–terminating glacier, provides an opportunity to describe calving seismicity at a type of calving margin not yet fully represented by the current body of literature.

Iceberg calving occurs across a wide range of temporal and spatial scales at Tasman Glacier, from high frequency–low magnitude subaerial calving through to low frequency–high magnitude (hundreds of metres in size) buoyancy–driven calving events. The seismicity associated with calving events can thus be identified and described across a broad spatial continuum.

7.3 Methods

To analyse the seismic energy generated by iceberg calving at Tasman Glacier, a combination of field data were used to identify and describe a range of calving events. In order to do this, seismic recording and time–lapse photography were used to characterise individual calving events over a three month period – February to April 2012. As calving at Tasman Glacier is episodic in nature, with only *c.* 1 event d^{-1}, direct visual observations were determined unrealistic, so time–lapse photography was used to isolate individual calving events as data presented here represents only a portion collected over a 12 month campaign (October 2011 to November 2012).

7.3.1 Time–lapse photography

A Mobotix™ M24M–Sec 3 M pixel colour digital camera situated atop the western lateral moraine was deployed between October 2011 and November 2012 to directly record calving events. Images were originally recorded at 1 hour intervals, with the sampling interval increased to 5 minutes during daylight hours in February 2012 to better constrain the timing of calving events. Individual calving events were manually identified from the image record based on several features visible pre– and post–calving (section 5.3.4). The mechanism or style of calving and relative magnitude of an individual calving event was inferred for each event based on the vertical extent of calving, the presence of a thermo–erosional notch (Röhl, 2006) and the pre– and post–calving geometry and terminus morphology. The combination of these features was used to create a subjective measure of each calving event, including an estimate of the magnitude (size) of individual calving events. Error in assigning event magnitudes is assumed to be ± 1 magnitude increment (section 5.3.4.5). This record of calving events provided the basis for the identification of events within the seismic record.

7.3.2 Seismic recordings

Seismometers are able to capture and record seismic signals at regional and global scales, providing high resolution datasets that give insights into the mechanisms and size of calving and other glacier–generated seismic signals (Qamar, 1988; O'Neel et al., 2007; Amundson et al., 2008; Bartholomaus et al., 2012). Seismic signals from the Tasman Glacier terminus were

recorded using a broadband seismometer (BB) deployed on the lower glacier surface (Figure 7.1). The Guralp 6–TD 3–component broadband seismometer, with a flat response between 30 s and 50 Hz (sampling at 100 Hz), was placed at the debris–ice interface under *c.* 0.6 m of debris so as to provide the best coupling to Tasman Glacier and decrease any potential path effects (O'Neel and Pfeffer, 2007). The seismometer was deployed for the period October 2011 through until November 2012. However, memory limitations and equipment malfunctions limited the period of useful data that was able to be retrieved. The most complete recording period was collected between 20 February and 30 April 2012. This period also relates to the highest resolution image was set (5 minute interval) acquired during a 12 month campaign to document calving at Tasman Glacier. The seismic data was converted to velocity from raw counts, but was not corrected for instrument response as the flat response and no gain of the seismometer within the frequency range of interest meant that response deconvolution was unnecessary (Bartholomaus et al., 2012). Dates and times are reported in coordinated universal time (UTC).

Processing of seismic data was carried out using the ObsPy toolbox for Python (Beyreuther et al., 2010). To standardise the identification of calving event onset and ending, the levels of background noise were compared with the identified event waveforms. The first deviation of a calving–induced waveform away from background noise was set as onset time, so as to incorporate the entire event waveform in analysis. To determine event ends, the amplitude value at onset was initially set as a threshold for the end of the calving–induced waveform, with the event end occurring when waveform amplitude decreased below this point. Although this worked well for a large proportion of events, it was found that using a value double the initial onset value provided better results for all events identified in the calving record. Using the start and end times, the integrated amplitude (as a proxy for energy released during each event) was calculated by integrating over the absolute values of the raw waveform data. The maximum amplitude and frequency content of calving–induced icequakes within the start and end times were also determined to describe the characteristics of waveforms.

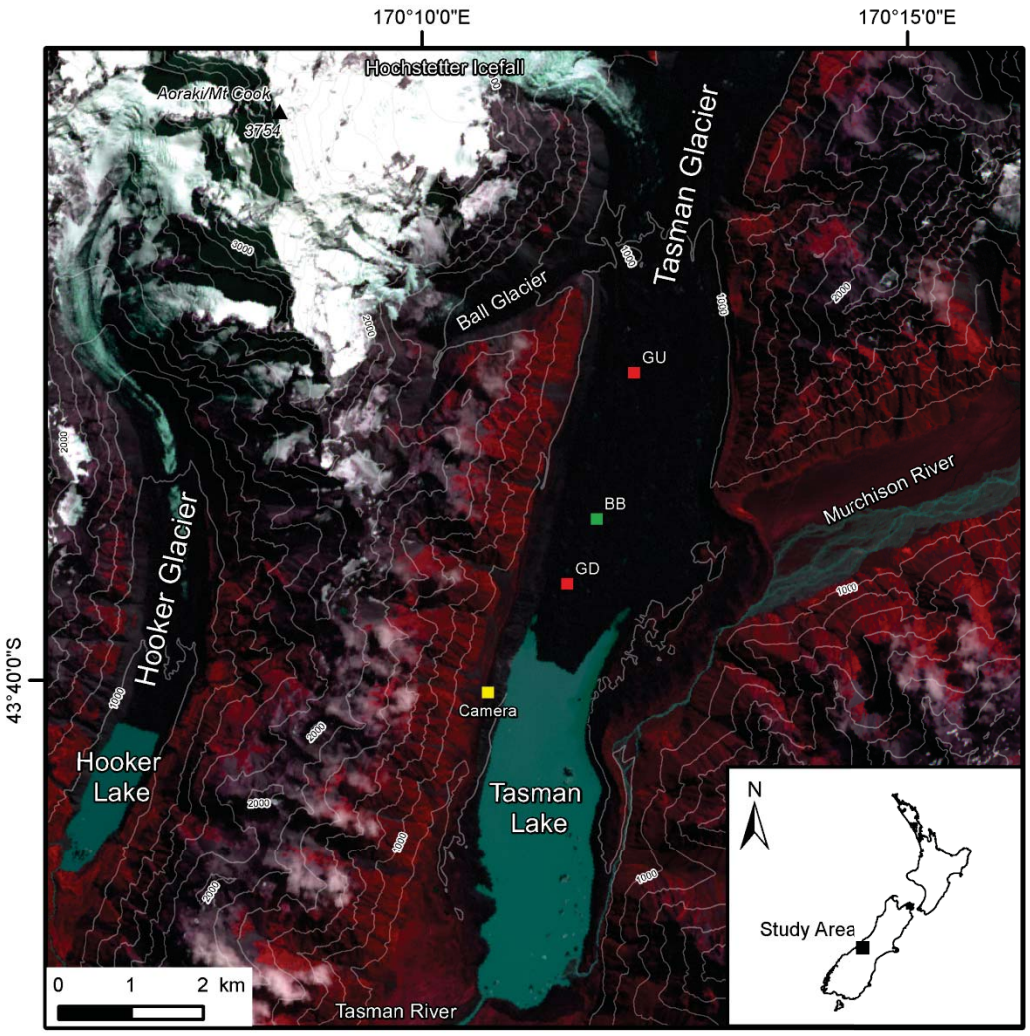

Figure 7.1: Map of the lower Tasman Glacier and Tasman Lake. The location of the broadband seismometer (BB), two geophones (GD and GU, Appendix C) and the time–lapse camera positions over the survey period. Background image is a false colour ASTER (Advanced Spaceborne Thermal Emission and Reflection) image taken on 26 February 2012. Topographic contour interval is 200 m and is from LINZ NZTopo Database (www.linz.govt.nz).

7.4 Analysis

7.4.1 Calving events

Between 22 February and 30 April 2012 a total of 79 calving events at the Tasman Glacier terminus were identified in the image record at a mean rate of 1.2 events d^{-1}. Of the 79 recorded events the estimated volume of each individual event ranged from 10^3 to 10^6 m^3 (Figure 7.2) and incorporated calving events initiated by over–steepening and notching of the subaerial ice cliff, as well as buoyancy–driven and subaqueous calving. Calving from the subaerial ice cliff (over–steepening and notch–driven calving) dominated the total number of calving events. Combined over–steepening (32 events) and notch–driven (34 events) calving accounted for 91 percent (72 events) of all events. In comparison, only four subaqueous (6 percent) and two buoyancy–driven (3 percent) calving events were observed during the study period. However, subaqueous and

buoyancy–driven events were associated with the largest volumes calved. For example, subaqueous calving on 02/04/2012 and buoyancy–driven calving on 29/04/2012 both had volumes of *c.* 1×10^6 m^3 (Figure 7.2).

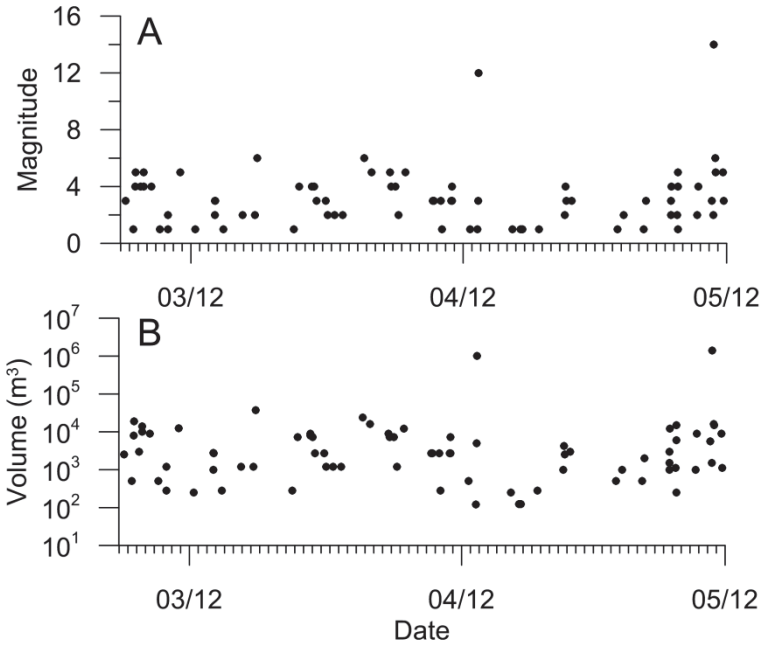

Figure 7.2: Temporal distribution of calving event magnitudes (A) and estimated volumes (B) at the Tasman Glacier terminus between 22 February and April 30 2012. See section 5.3.4.5 for information on magnitude scale and volume estimation.

Of the 79 calving events identified in the time–lapse image dataset, 64 had a clearly identifiable seismic signal recorded by the broadband seismometer. The remaining 15 events were unable to be definitively identified in the seismic record as they occurred during night time hours or at a time of elevated regional seismic activity, so were not included in the analysis. A further seven events were also identified in the seismic record, as multiple sections of the terminus calved at the same location during the bracketing time–lapse images. They are treated here as separate events as the time between events was enough for seismicity associated with calving to return to background levels prior to the second event (Figure 7.3). A total of 71 calving events with associated seismic signals were documented over the study period.

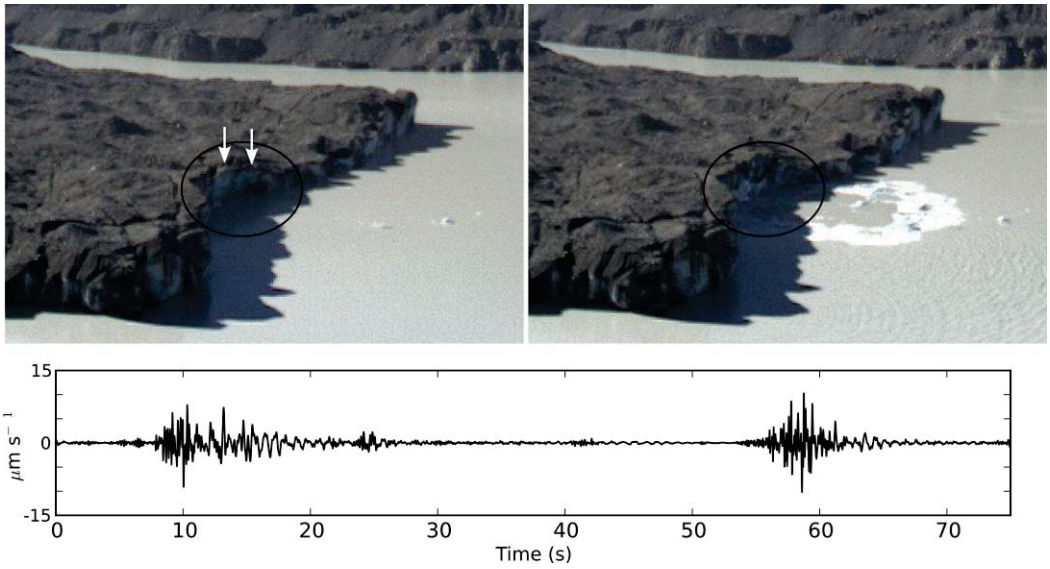

Figure 7.3: Example of an unfiltered seismic waveform recorded on the vertical channel of BB showing two separate calving–generated seismic signals generated by calving at the same location between image pairs. Arrows indicate the two separate sections that calved between images. Time zero is UTC 24/04/2012 22:42:30.

7.4.2 Examples of calving–generated seismic signals

To characterise the observations of calving–generated seismograms, several example icequakes are presented here to show how calving–generated signals can differ between events. Example events are subdivided into three categories encompassing calving from the subaerial ice cliff, subaqueous calving and buoyancy–driven calving. To discern the evolution and characteristics of these events the seismic data is presented in its raw waveform (e.g., Figure 7.4B), absolute values of waveform and associated running mean (e.g., Figure 7.4C), and spectrogram of seismic data surrounding each calving event (e.g., Figure 7.4D). Pre– and post–calving time–lapse images (e.g., Figure 7.4A) are also shown for example calving events.

7.4.2.1 Subaerial calving

Subaerial calving events have been shown to be initiated by either subaerial ice cliff over–steepening or the development of a thermo–erosional notch at the base of the subaerial ice cliff. The typical characteristics of subaerial calving events and their associated icequakes are described here in relation to six example events from the terminus of Tasman Glacier. Three examples are from over–steepening events and three from notch–induced calving events across a range of iceberg magnitudes (sizes)

7.4.2.1a Over–steepening events

The first example (Figure 7.4) relates to the calving of a small volume (*c.* 125 m^3) of ice from the lower section of the subaerial ice cliff. The seismic signal has an asymmetric form with an

emergent onset of approximately two seconds between the initial deviation away from background noise levels (Figure 7.4B–C) and reaching the maximum unfiltered amplitude of 1.9 μm s^{-1}. During this period of time low frequencies between 2 and 13 Hz are present, with a 'step' in seismic amplitude (Figure 7.4B and C) centred around 5 Hz at 3.5 seconds in Figure 7.4D. Following this emergent onset there is a rapid increase in seismic energy centred between 1–3 Hz (Figure 7.4C), which continues for *c.* 7 seconds throughout the main phase of the seismic signal. A second increase in amplitude between 4 and 12 Hz at 10 seconds in Figure 7.4D marks the end of the main signal form, with seismic amplitudes continuing between 0.5 and 3 Hz for an extended period of time. A protracted coda returns to background levels from *c.*17 seconds.

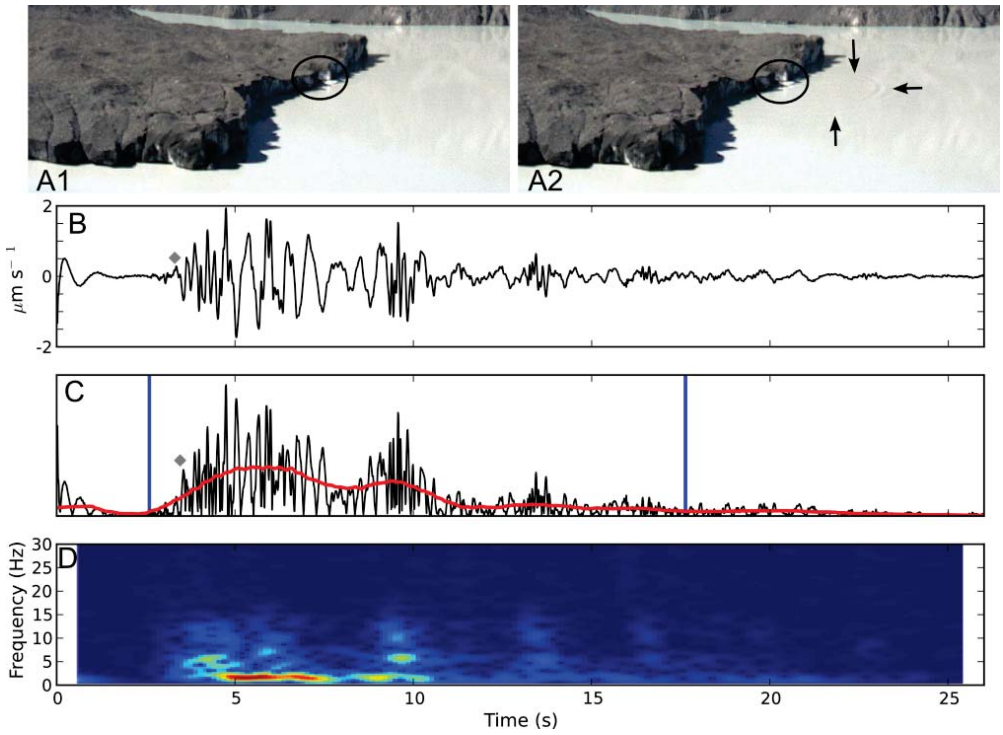

Figure 7.4: Pre and post time–lapse images (A) of a subaerial calving event at the Tasman Glacier terminus, unfiltered vertical component of the seismic waveform (B), absolute of values seismic data (C), and spectrogram of the unfiltered waveform (D). Circles in the pre– and post–calving images in (A) indicate the calved section, with arrows representing the extent of waves emanating from the location of calving. The calving event had an iceberg size (magnitude) of 1 (*c.* 125 m^3) and originated from the lower section of the subaerial ice cliff that had become over–steepened. Maximum ground velocity (B) in the vertical component was 1.9 μm s^{-1}. The onset and end timing of calving (blue vertical lines in C) was calculated based on the deviation of the signal away from the background noise using a running mean of absolute values of the seismic waveform (red line in C). Calving was considered to have ended when the running average had returned to the onset value. Absolute values of the seismic data also show the gradual onset of calving and highlights the 'step' in icequake amplitude (grey diamond) discussed in the text. The spectrogram (D) of the event was computed showing the log of spectral amplitude between 0.5 and 30 Hz, as a function of time. Warm (reddish) colours define high spectral amplitudes; cold (bluish) colours represent lower amplitudes and background. Time zero is UTC 07/04/2012 00:23:50, with calving onset at 00:23:52.6.

The second example (Figure 7.5) is of a magnitude 3 (*c.* 2700 m^3) over–steepening calving event from the upper section of the subaerial ice cliff (Figure 7.5A). Again the seismic waveform is asymmetric with a gradual onset of *c.* 1 second and a sudden increase in seismic amplitude between 4 to 5 Hz. Low frequency (1–3 Hz) seismic signals increased after onset, along with weak increase between 5 and 10 Hz. Maximum amplitude of 4. 6 μm s^{-1} was reached at the 5.5 s mark, with peaks at both 3 and 8 Hz evident in Figure 7.5D. After 5 seconds from the start of the calving event only low–frequency (*c.*1 Hz) seismicity is present through to the end of the protracted coda. The duration of the calving event was 22.8 seconds, with calving–induced seismicity returning to background levels beyond this point.

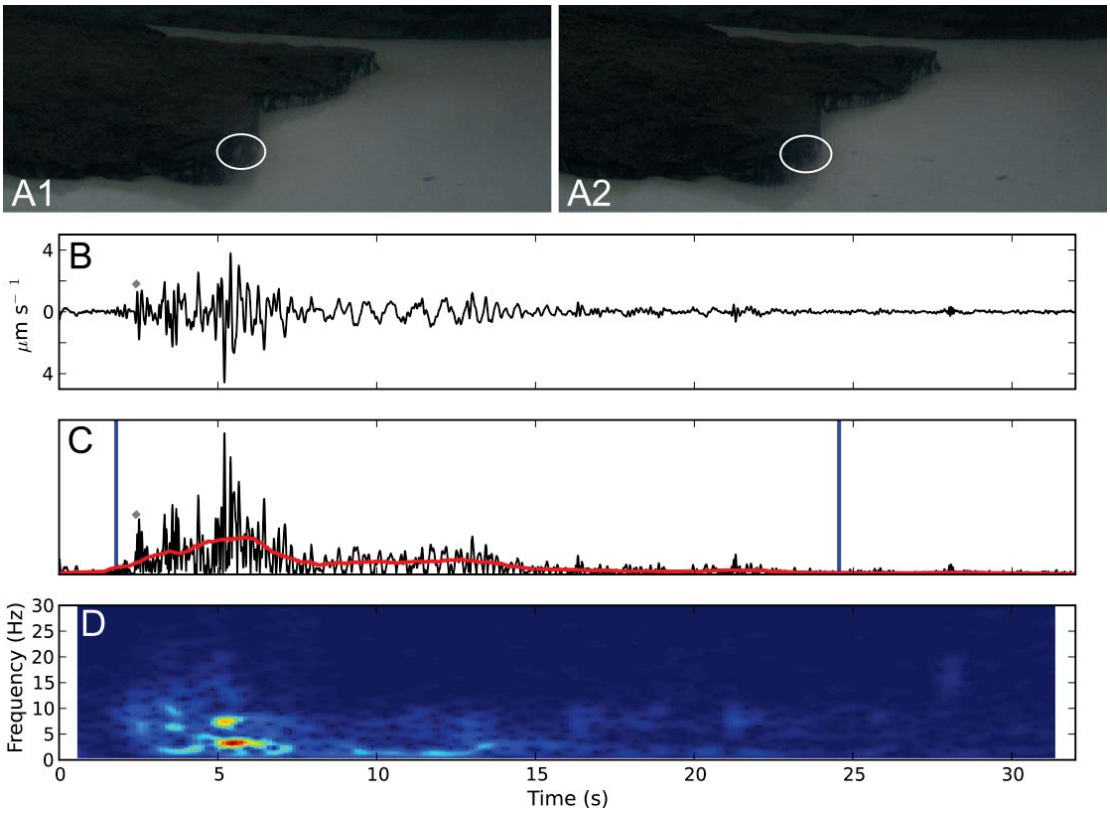

Figure 7.5: A–D sows the same data types as in Figure 7.4, except for a iceberg magnitude 3 (*c.* 2700 m^3) calving event from the upper section of the subaerial ice cliff that had become over–steepened prior to calving (circled in A). The calving event had a gradual onset up until a step in amplitude (grey diamond). Maximum vertical ground velocity was 4.6 μm s^{-1}. Time zero is UTC 22/02/2012 00:29:14, with calving onset (first blue vertical line) at 00:29:15.8.

The third example of subaerial calving (shown in Figure 7.6) is of a magnitude 4 (*c.* 7300 m^3) over–steepening driven calving event of the entire subaerial ice cliff. Onset of the signal increases gradually over a 3 second period before reaching the first of two peaks in seismic amplitude. The first of the two peaks occurs at the 7 second mark in Figure 7.6 and consists of moderate to weak power at frequencies between 3.5 and 13 Hz. The second peak coincides with

high spectral levels at 4.5 Hz, with slightly weaker responses between 1–3 Hz. The presence of low frequency 1–3 Hz seismic waves continues for 7.5 seconds, diminishing in power over time. The total time of the event through until the seismic waveform returns to background levels is 26.8 s, with the maximum amplitude of 8.4 μm s^{-1} reached during the first peak in the waveform data.

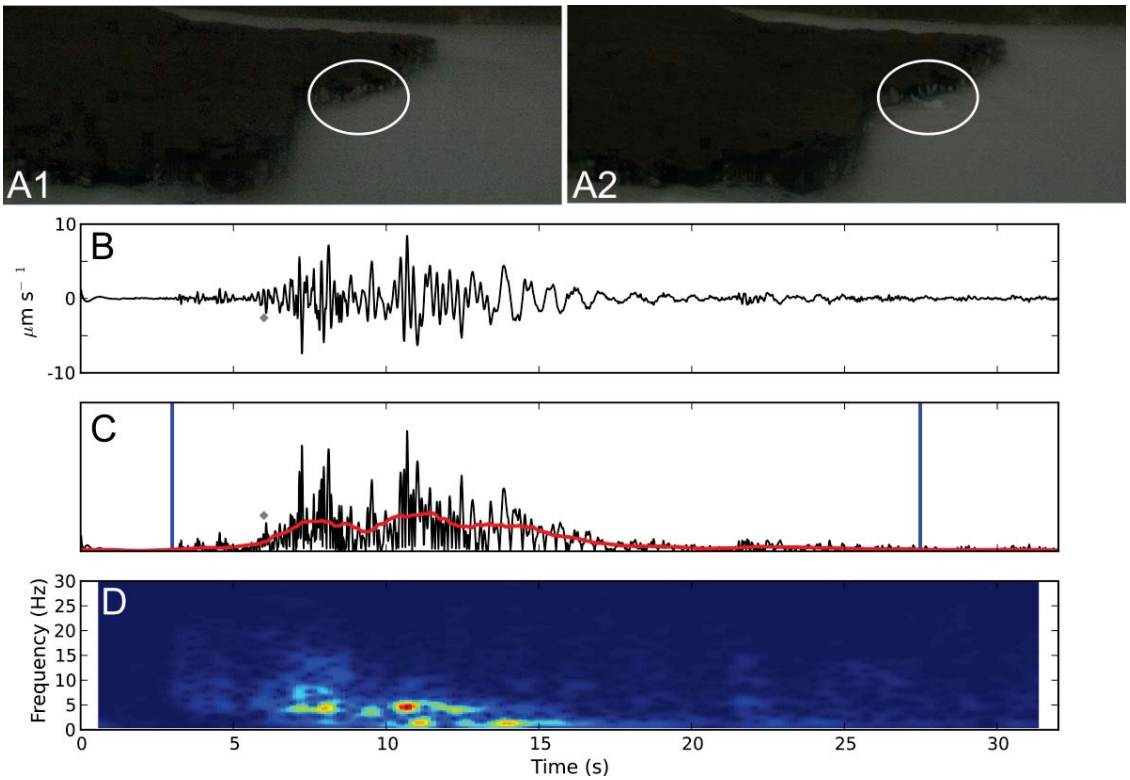

Figure 7.6: A–D show the same data types is in Figure 7.4, except for a iceberg magnitude 4 (*c.* 7300 m^3) calving event of the entire height of the subaerial ice cliff that had become over–steepened prior to calving (circled in A). The calving event had a gradual onset up until a step in amplitude (grey diamond). Maximum vertical ground velocity was 8.4 μm s^{-1}. Time zero is UTC 14/03/2012 05:54:50, with calving onset at 05:54:53.0.

7.4.2.1b Thermo–erosional notch events

The first example of a subaerial event resulting from the development of a thermo–erosional notch, which destabilised the ice cliff by removing support from the base, is a magnitude 2 (*c.* 1200 m^3) calving event from the western embayment subaerial ice cliff. Signal waveform for the calving event shows a gradual onset peaking at 4.1 μm s^{-1} (Figure 7.7B). Seismic energies in the associated spectrogram (Figure 7.7D) for the event are distributed across a range of frequencies between 4 and 16 Hz. This broad range of frequency response (between 4 and 11 Hz) continues for the main phase of the icequake between 4 and 9 seconds, shown in Figure 7.7. Also evident during this time is the presence of low frequency (1–3 Hz) seismic waves that occur through to the end of the elevated passage of seismic activity (second blue line in Figure 7.7C)

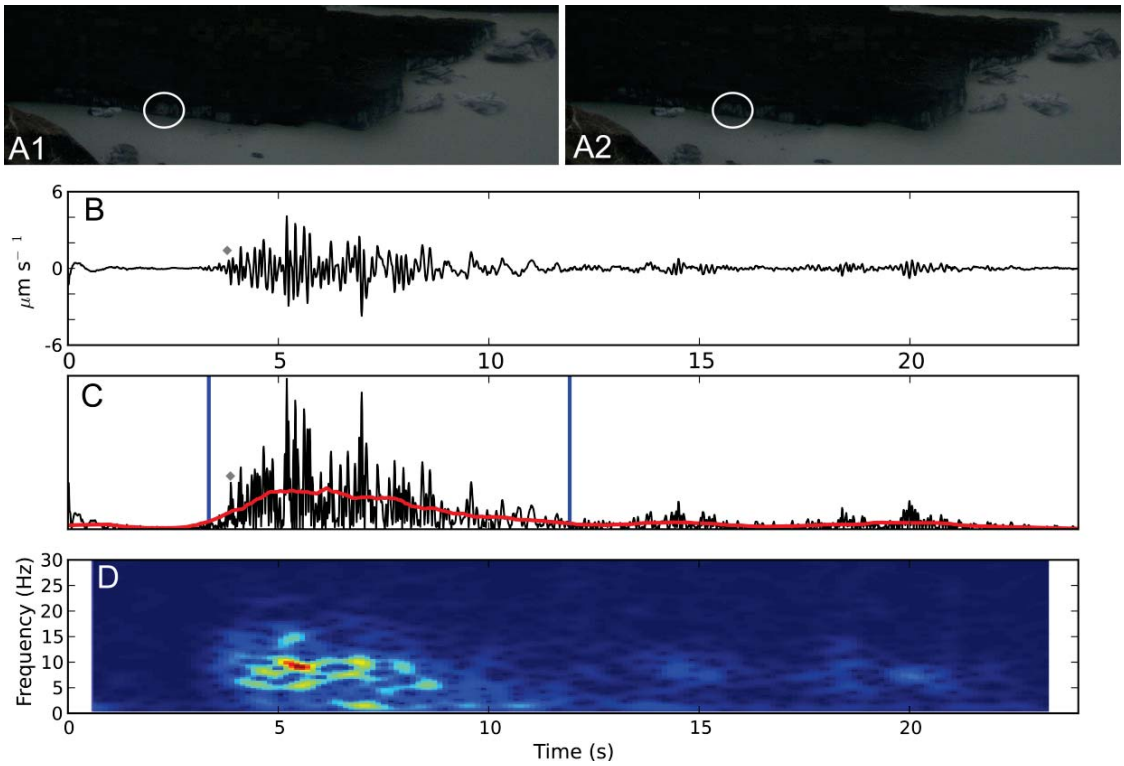

Figure 7.7: Magnitude 2 (*c.* 1200 m^3) notch–driven calving event from the subaerial ice cliff in the western embayment. A–D are the same data types shown in Figure 7.4. The circled section in A1–2 is the location of calving. Time zero is at UTC 03/03/2012 04:59:22 and the start of the calving event is at 04:59:25.0 (first blue line in C). Maximum vertical ground velocity was 4.1 $\mu m\ s^{-1}$.

The second notch–induced calving event is shown in Figure 7.8, and describes the detachment of a magnitude 3 (*c.* 2700 m^3) iceberg from the western embayment ice cliff (Figure 7.8A). The vertical seismic waveform data show two distinct phases, an initial gradual onset (Figure 7.8B) and elevated frequencies between 5 and 16 Hz (Figure 7.8C), followed by a rapid increase (Figure 7.8B) in frequencies between 2.5 and 9 Hz (Figure 7.8C). It is during this second phase that seismic waves reach their maximum amplitude of 6.2 $\mu m\ s^{-1}$. Elevated seismic signal at 3 Hz continues for *c.* 6 seconds after reaching this maximum at 8 seconds in Figure 7.8, with the entire signal decaying to background levels by the 17 second mark.

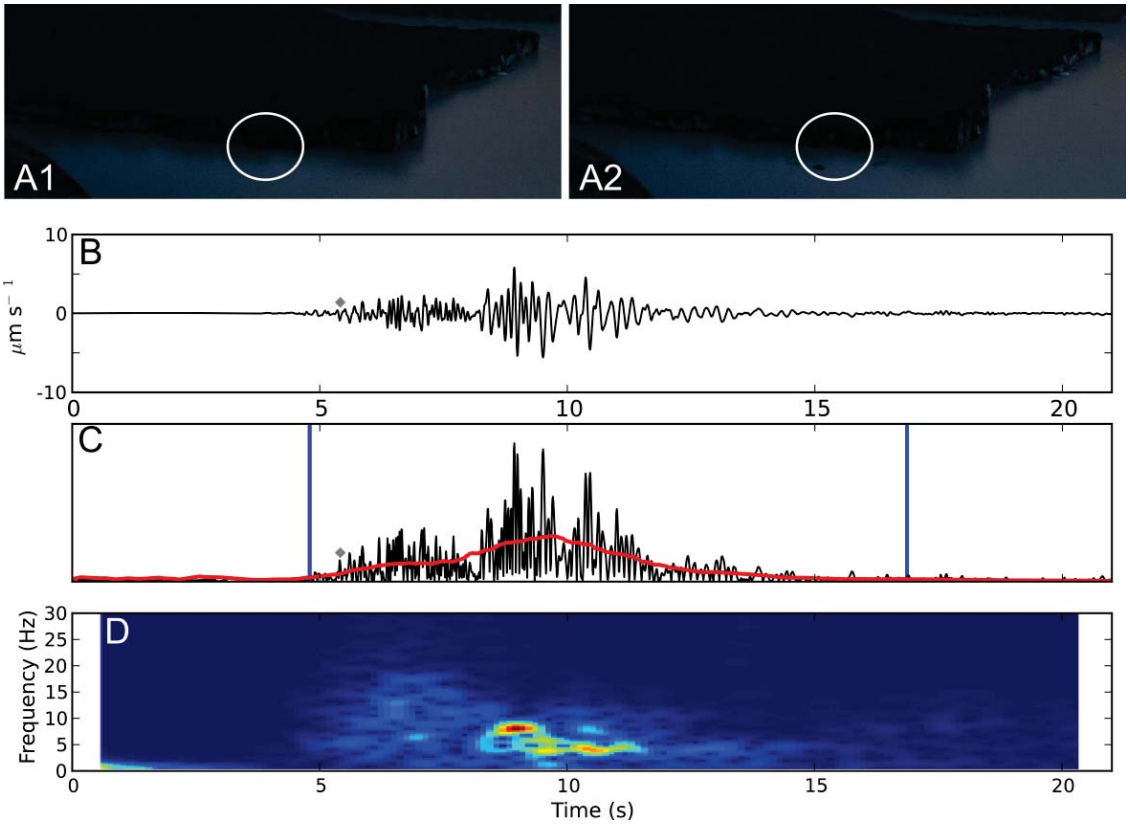

Figure 7.8: Magnitude 3 (*c.* 2700 m^3) notch–driven calving event from the subaerial ice cliff in the western embayment. A–D are the same data types shown in Figure 7.4. The circled section in A1–2 is the location of calving. Time zero is at UTC 02/04/2012 04:39:47 and the start of the calving event is at 04:39:50.8 (first blue line in C). Maximum vertical ground velocity was 6.2 μm s^{-1}.

The third example of notch–driven calving events is for a magnitude 5 (*c.* 13500 m^3) calving event from the eastern section of the southern ice cliff (Figure 7.9A). After an initial increase in seismic wave form amplitude at the start of Figure 7.9B, ranging between 3 and 15 Hz (Figure 7.9D), amplitude rapidly peaks at 6.5 seconds to 24 μm s^{-1}. This peak occurs across a range of frequencies between 1 and 10 Hz, centred around 4 Hz (Figure 7.9D). This 4 Hz peak in power diminishes within 1 second, with lower frequency 1–3 Hz signals continuing though until the end of the protracted coda at 26 seconds in Figure 7.9D.

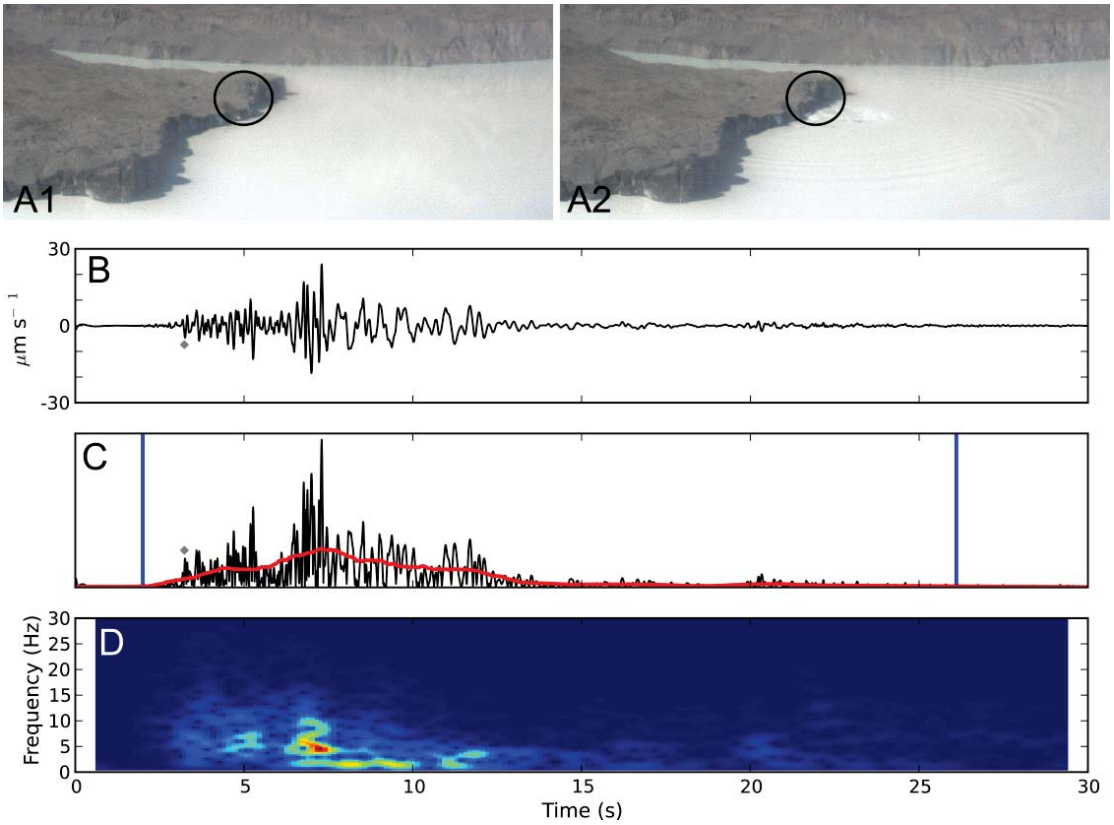

Figure 7.9: A–D are the same data types shown in Figure 7.4 for a magnitude 5 (*c.* 13500 m^3) calving event of the entire height of the subaerial ice cliff that was undercut by a thermo–erosional notch prior to calving (circled in A). The calving event again had a gradual onset up until a step in amplitude (grey diamond). Maximum vertical ground velocity was 24 μm s^{-1}. Time zero is UTC is 21/03/2012 01:24:07, with calving onset at 01:24:09.0.

7.4.2.2 Buoyancy–driven calving

The largest calving event at the terminus of Tasman Glacier during the period that the seismometer was operational was a magnitude 14 buoyancy–driven calving event which resulted in the loss of 1.4×10^6 m^3 of ice (Figure 7.10A). Associated with this event is a complicated seismic waveform that continued for approximately 180 seconds, during which five major peaks in amplitude occurred (Figure 7.10C). Onset of the calving–induced icequake was emergent, with 15 seconds between the initial deviations away from background seismic levels and the increase in amplitudes prior to the first peak. After this first peak, elevated seismic activity continued, punctuated by four subsequent peaks. Maximum vertical amplitude was 51.5 μm s^{-1}, attained during the fifth peak (Figure 7.10B). Each peak in seismic amplitude is dominated by low frequency 1–3 Hz seismic waves, with short periods of higher frequencies (4–15 Hz) accompanying the high spectral amplitudes of lower frequencies. Following the fifth peak (Figure 7.10C) an extended period of low frequency 1–5 Hz signals continues for *c.* 130 seconds before returning to background levels just prior to a second period of seismic activity (after the second blue line in Figure 7.10C). This second period of activity represents either the

calving of another section from the terminus of Tasman Glacier, or the breakup of one of the large icebergs from the initial event.

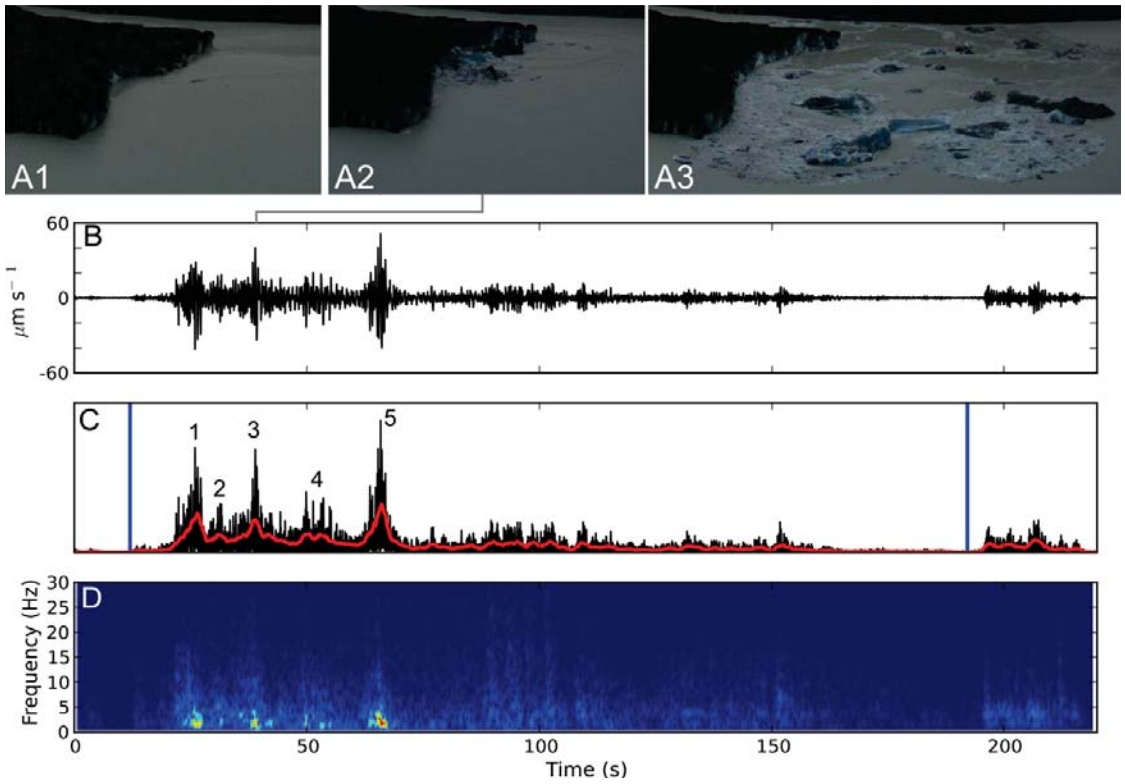

Figure 7.10: Magnitude 14 (1.4×10^6 m^3) buoyancy–driven calving event on the eastern section of the southern ice cliff. A–D are the same data types shown in Figure 7.4. The calving event had a long (*c.* 10 s) onset, increasing steadily over a 5 second period (B) to the first peak in seismic amplitude. In total, five peaks and an extended period of elevated seismic amplitudes occurred throughout the calving event, with a secondary event present after amplitudes had returned to background levels (second blue line in B). High spectral amplitudes in the low frequency 1–3 Hz range dominate the spectrogram of the calving event (D), although high frequency signals (up to 20 Hz) are present throughout. Maximum vertical ground velocity was 51.5 μm s^{-1}. Time zero is UTC 29/04/2012 01:07:30, with calving onset at 01:07:42.0 (first blue vertical line in C).

7.4.2.3 Subaqueous calving

The second largest calving event from the Tasman Glacier terminus was the magnitude 12 subaqueous calving on 02 April 2012. The 1.0×10^6 m^3 of ice calved from the subaqueous section of the terminus in a complex series of events (Figure 7.11B). Two distinct periods can be identified in Figure 7.11B, that relate to an initial period (Figure 7.11C) of activity with two main phases and a second period of higher amplitudes (Figure 7.11D). The first period is shown in Figure 7.11C and encompasses both phases of elevated seismic activity as the signal had not returned to background levels. The initial onset of the signal was long (>20 seconds) and resulted in the gradual increase in signal amplitude through the first major peak at 38 seconds in Figure 7.11C. Seismic amplitude also peaked at 50 seconds before decreasing to almost

background levels. Prior to reaching background levels, amplitude increased again in a second phase of elevated seismic signals. In total this first period lasted 103.5 seconds. In general, seismic amplitudes were dominated by frequencies between 1–3 Hz throughout, with peaks in amplitude in Figure 7.11C2 associated with weak increased spectral amplitudes between 4–10 Hz.

Similarly, the second period of activity (Figure 7.11D) had a long onset (>30 seconds), prior to a spike in seismic amplitude and main frequencies between 3–5 Hz at 35 seconds in Figure 7.11D3. Amplitudes continued to gradually increase until a maximum of 23 μm s^{-1}, localised between 1–5 Hz. The waveform decays after this point, until a final peak in seismic amplitude at 85 seconds in Figure 7.11D2. A protracted coda is evident past this point with the seismic wave form taking 40 seconds to return to background levels.

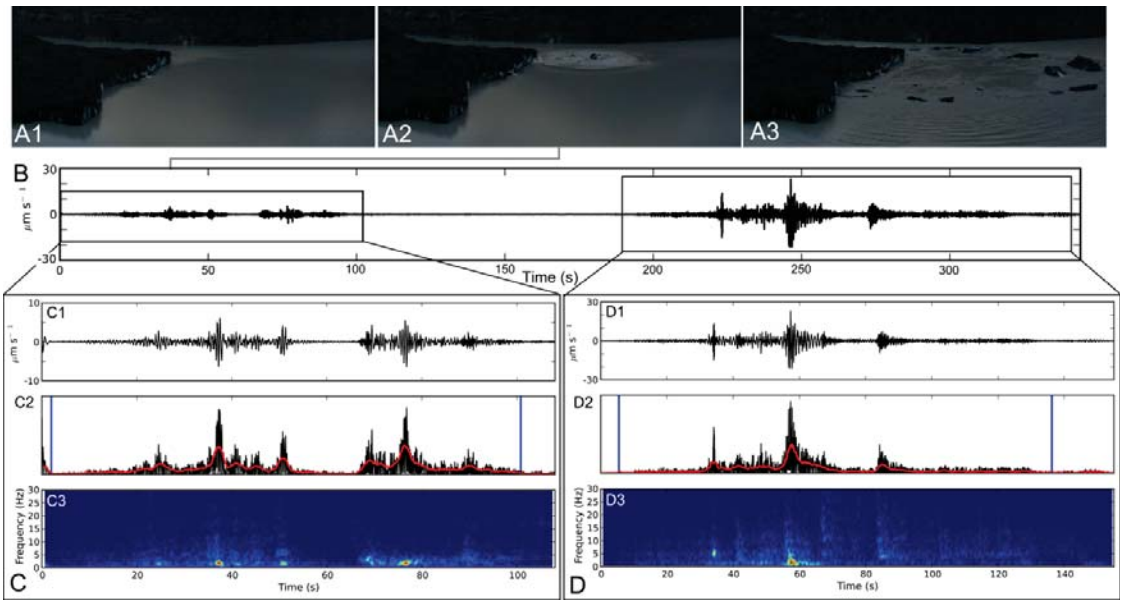

Figure 7.11: Magnitude 12 (1.0×10^6 m^3) subaqueous calving event originating from the base of the southern ice cliff. (A) The pre– (A1), mid– (A2), and post–calving (A3) time–lapse images of the subaqueous calving event. The entire vertical seismic waveform is shown in (B), with inserts (C) and (D) showing the seismic data of two separate periods of activity between the mid– (A2) and post–calving (A3) images. Time zero in (B) is UTC 02/04/2012 05:47:56. Maximum vertical ground velocity across the entire seismic waveform (B) was 23 μm s^{-1}. The data presented in C1–3 and D1–3 is the same as shown in Figure 7.4A–C. Inset boxes (C) and (D) start at 05:47:56 and 05:51:08, respectively. Both periods of activity have long (*c.* 20 s) onsets prior to the first major peak in amplitude.

7.4.3 Common characteristics of calving–generated icequakes

The example calving–induced icequakes presented in section 7.4.2 are a representative sample of the seismicity of calving events recorded at the terminus of Tasman Glacier between February and April 2012. There is clearly a difference in the signal form and duration between

calving events that originate from the subaerial ice cliff (notching and over–steepening events) and those that encompass large sections of both the subaerial and subaqueous ice cliff (buoyancy and subaqueous). However, there are similarities across all calving–generated icequakes. Several seismic parameters (signal form and amplitude, frequency content, signal duration and integrated amplitude) are described below to highlight the similarities and differences in calving–generated icequakes. These seismic parameters are also compared with observed iceberg magnitudes (as a proxy for volume) to assess the possibility for developing a broadly applicable statistical relationship that is able to predict iceberg magnitude (and therefore volume) from seismic data.

7.4.3.1 Signal form

Almost all recorded events had emergent onsets characterised by an initial phase of low amplitude seismic waveform, followed by an increase to higher amplitudes. For subaerial calving events there is a sudden increase (i.e. 'step') in seismic amplitude that can easily be identified and is indicated in example events from the subaerial ice cliff (section 7.4.2.1 and Figure 7.12), with onset to maximum amplitude typically between 1 and 4 seconds. Several other examples of this step in seismic amplitude between 1 to 5 Hz frequencies for subaerial calving events are shown in Figure 7.12. For buoyancy and subaqueous events, the transition from low to high amplitudes is more gradual (Figure 7.13), with amplitudes increasing steadily over a 10 to 20 second period after the initial deviation away from background levels (e.g., Figure 7.10). In both instances (subaerial and buoyancy or subaqueous calving) there is no clear *P*– or *S*–wave arrival.

Maximum amplitude varied across all events (Figure 7.14) with smaller magnitude events (e.g., magnitudes 1–3) tending towards smaller values in maximum amplitudes than higher magnitude events (magnitudes >4). However, maximum amplitude varies significantly within each magnitude increment. Multiple peaks in maximum amplitude can occur during subaerial events (e.g., Figure 7.6), but typically they are more common for buoyancy (Figure 7.10) and subaqueous (Figure 7.11) events. A protracted coda was also evident for all events, with subaerial calving returning to background levels of seismicity between 10 to 20 seconds after maximum amplitudes. This gave all subaerial events a characteristic asymmetric wave form, with a rapid onset and protracted coda. In contrast, buoyancy and subaqueous event seismicity took *c.* 100 seconds to return to background levels. As a result, their associated seismic waveforms had both a slow emergent onset and long protracted coda, distinctly different from subaerial events.

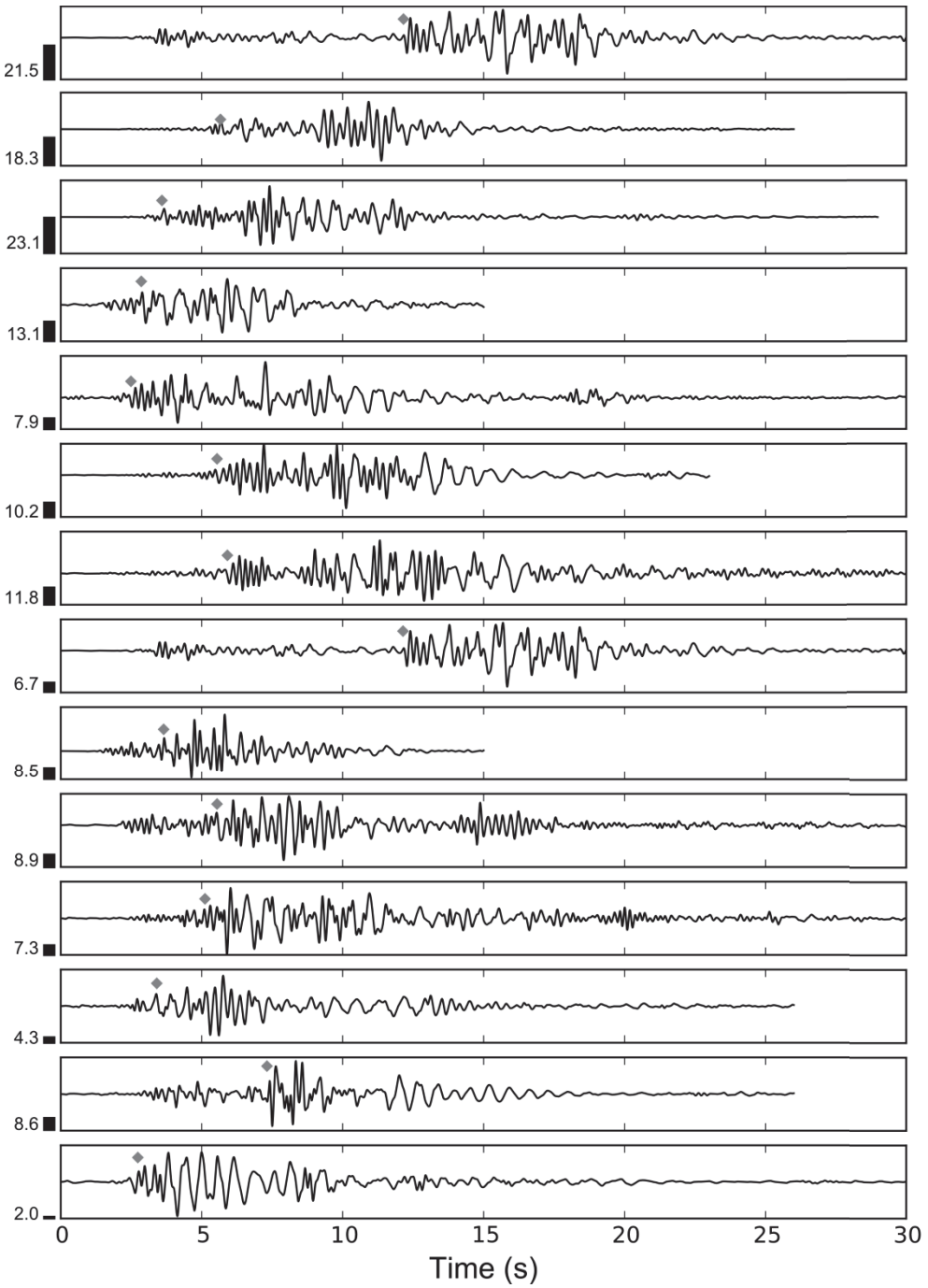

Figure 7.12: Example icequakes generated by subaerial calving identified from the time–lapse imagery record. Seismograms were recorded on the vertical channel and have been filtered between 1 and 5 Hz. The amplitude of all the example icequakes have been normalised, with the relative amplitude of each icequake (in μm s^{-1}) indicated by the height of the vertical bar on the left of the seismogram. The grey diamond indicates the sudden increase (or 'step') in seismic amplitude discussed in section 7.5.1.

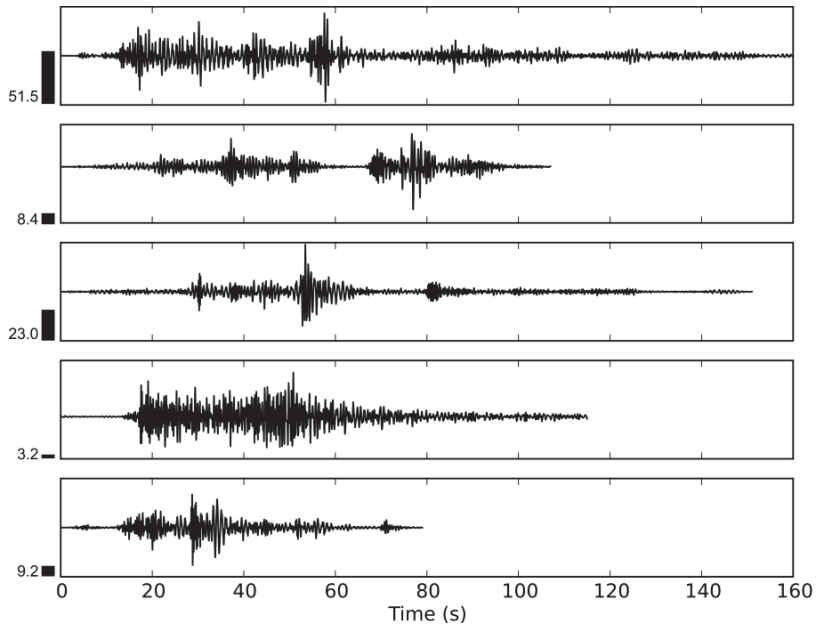

Figure 7.13: Five example icequakes generated by buoyancy or subaqueous calving from the terminus of Tasman Glacier. Seismograms were recorded on the vertical channel and have been filtered between 1 and 5 Hz. The top seismogram is the buoyancy event described in section 7.4.2.2, with the four other calving events subaqueous. The second and third examples are the two successive events in described in section 7.4.2.3. Vertical black bars to the left of the seismic waveforms show the relative maximum amplitude (in μm s^{-1}) of each event.

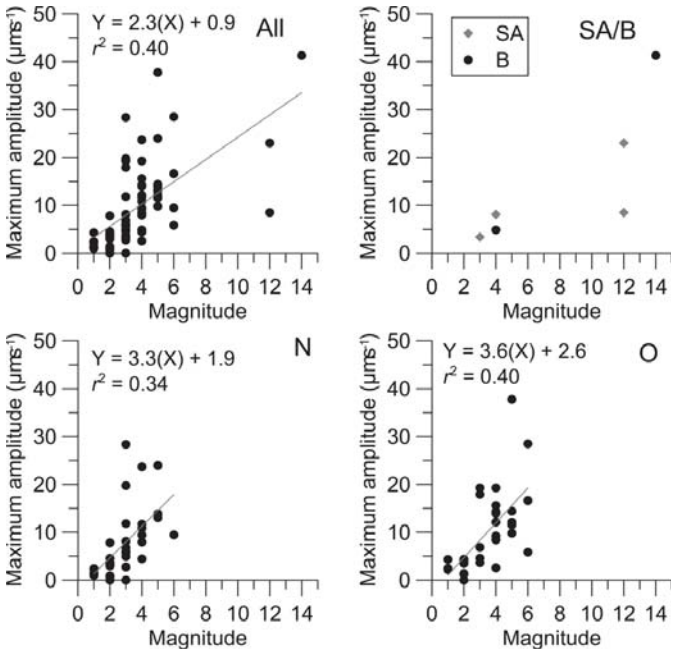

Figure 7.14: Graphs of unfiltered seismic waveform maximum amplitudes (in μm s^{-1}), magnitude, and mechanism of calving. Event maximum amplitude generally increased between magnitude 1 (*c.* 300 m^3 of ice) and 2 (*c.* 1200 m^3 of ice) events, with great scattering of seismic amplitudes between magnitude 3 (*c.* 2700 m^3 of ice) and 6 (*c.* 17000 m^3 of ice). Higher magnitude events (12 and 14) did not necessarily have higher seismic amplitudes, but did tend to be greater than lower magnitude events. Over–steepening (O) and notch–driven (N) events were confined to magnitudes 1 to 6, with buoyancy (B) and subaqueous (SA) calving events typically higher in magnitude. Regression equations and R^2 are also shown for All, N and O events.

7.4.3.2 Frequency content

Similarities in frequency content are evident across all calving events. After an initial onset of a weak power 4 to 16 Hz signal, seismicity within a 1 to 5 Hz frequency band tended to dominated most waveforms. However, the specific peak of frequency within this band varied between events. For example, the first example of an over–steepening event had a peak at *c.* 1.5 Hz, compared to the peak at *c.* 4 Hz for the second over–steepening event. Some example calving events (e.g., Figure 7.7 and Figure 7.8) also contained high spectral amplitudes up to 10 Hz, whilst retaining moderate power between 1 and 5 Hz. However, 80 % of all calving–generated seismic signals had peak frequency between 1 and 5 Hz, similar to previous studies of calving–generated icequakes (e.g., Bartholomaus et al., 2012).

The similarities in the frequency content are independent of calving style, although notch–driven calving events tended to incorporate slightly higher frequencies (between 5 and 8 Hz). There is also no discernable difference in frequency content between the magnitudes of icebergs, with both low (e.g., 1–6) and high (e.g., 12 and 14) magnitude events having similar high amplitude spectral power between 1 and 5 Hz. However, there is a weak tendency for smaller magnitude events to have similar spectral amplitude across a range of frequencies (e.g., Figure 7.4 and Figure 7.7), than larger magnitude events (e.g., Figure 7.10).

7.4.3.3 Signal duration

The seismic parameter that did display differences between calving–generated icequakes relates to the typical time scale of events. Event durations were calculated by identifying the first deviation of the seismic waveform away from background levels to give the start time and the point at which levels returned to pre–event levels for the end time. The mean, maximum, and minimum durations of calving events are shown in Table 7.1. The mean duration of all events was 25.1 ± 31.4 seconds. However, when calving events are broken into the four mechanisms of calving, a clear difference exists. Mean duration for subaerial calving events was 18.2 ± 12.5 seconds for notch–driven and 17.6 ± 9.3 seconds for over–steepening events. In comparison, buoyancy or subaqueous events typically had significantly longer durations in excess of 100 seconds (Table 7.1). The only exception to this is a small buoyancy–driven calving event that had duration of 20.7 seconds.

When durations are broken down by iceberg magnitude (Figure 7.15) there is a general increase in event duration with magnitude. This is unsurprising as the larger the calving event the greater the displacement of ice and the longer it takes for ice to be displaced and seismicity to return to

background levels. However, within each event type there is a large amount of scatter with event duration only showing any sort of relationship when all events are included (Figure 7.15).

Table 7.1: Table showing the duration of calving events in seconds by the mechanism of calving. Mean, minimum, and maximum duration is shown to highlight the similarity of durations between over–steepening (O) and notch–driven (N) events, and buoyancy (B) and subaqueous (SA) events.

Mechanism	No. of events	Mean (s)	Maximum (s)	Minimum (s)
B	2	113.6 ± 131.3	206.4	20.7
N	34	18.2 ± 12.5	77.8	2.3
O	32	17.6 ± 9.3	50.7	3.8
SA	4	99.7 ± 35.2	148.1	72.8
Total	72	25.1 ± 31.4	206.4	2.3

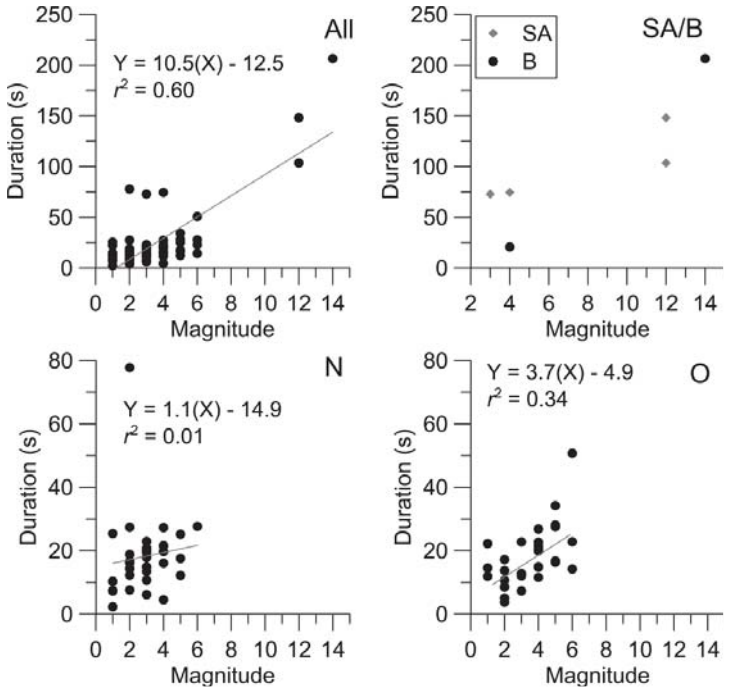

Figure 7.15: Graphs of the duration (in seconds) of seismic waveform, magnitude, and mechanism of calving events from the time–lapse imagery. Event durations generally increased marginally between magnitude 1 (*c.* 300 m^3 of ice) and 6 (*c.* 17000 m^3 of ice), although there is some scattering within each magnitude increment. Higher magnitude events (12 and 14) were longer than lower magnitude events. Over–steepening (O) and notch–driven (N) events were confined to magnitude 1 to 6 events, with buoyancy (B) and subaqueous (SA) calving events typically higher in magnitude and longer in duration.

7.4.3.4 Integrated amplitude

To further attempt to differentiate between calving–generated icequakes and the style or size of events, the integrated amplitude of the data was calculated by integrating over the absolute values of the raw amplitude counts for the entire duration of the seismic signal. This constitutes a measure of the total seismic energy released and is, therefore, a measure to be correlated to event magnitude. Figure 7.16 shows the resulting distribution of integrated amplitude of

calving–induced icequakes. Similar to maximum amplitude and signal duration, there is a general increase in integrated amplitude with respect to the magnitude of calving events. However, unlike maximum amplitude slightly stronger relationships between integrated amplitude and magnitude were found for all events as well as for notch and over–steepening events (Figure 7.16). Buoyancy–driven and subaqueous calving events typically had significantly larger integrated amplitudes than events from the subaerial ice cliff, with the magnitude 14 buoyancy–driven event several orders of magnitude greater than any other events.

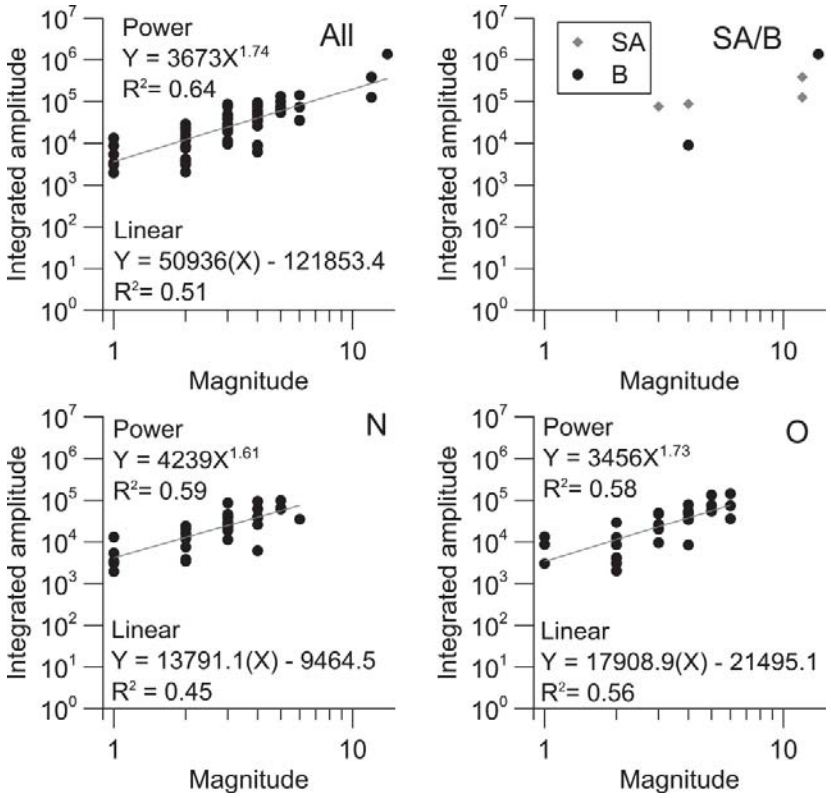

Figure 7.16: Graphs (log–log scale) of integrated amplitude and magnitude (calving size) of calving–generated seismic waveforms. There is scatter of integrated amplitude data, although there is a general increasing trend with respect to magnitude. Over–steepening (O) and notch–driven (N) events were confined to magnitude 1 to 6 events, with buoyancy (B) and subaqueous (SA) calving events typically higher in magnitude. The magnitude 14 buoyancy–driven event is several orders of magnitude greater than all other events. Power–law best fits are shown for All, N, and O events. Linear and power–law regression equations and R^2 are also shown for All, N and O events.

7.4.3.5 Filtered response

Given that several positive, although relatively weak, relationships have been identified between magnitude and maximum amplitude or integrated amplitude, seismograms of calving events were filtered to asses if these relationships could be improved. Filtering the frequency spectra towards lower frequencies decreases possible path effects attenuating higher–frequency signals found within calving–induced icequakes. However, frequency filtering also removes waveforms

that may display characteristics of calving (O'Neel and Pfeffer, 2007). A Butterworth–bandpass filter was applied to the data to filter seismograms between 1–5 Hz and 1–3 Hz, based on the identification that almost all calving–induced icequakes were dominated by frequencies within the 1–5 Hz band (section 7.4.3.2), and that the 1–3 Hz band may contain information relevant to calving (O'Neel et al., 2007). The relationship between maximum amplitude and calving magnitude increased for the 1–5 Hz filtered seismograms (Figure 7.17). The strongest correlation occurs when all iceberg sizes and styles are included. The correlation improves significantly when the signal is filtered between 1–3 Hz (Figure 7.17). The relationship between iceberg size and maximum amplitude in 1–3 Hz range is particularly strong for over–steepening events and plots that include all event data. In contrast, decreasing the frequency range of the signal yields weaker correlation between integrated amplitudes and magnitude for plots of all events and notching events (Figure 7.18). A slight improvement of the empirical fit only occurs for over–steepening calving events (Figure 7.18).

These results indicate that: (1) most of the energy released during the highest amplitude phase is contained within the 1–3 Hz range; (2) the strong correlations for plots including all data and over–steepening events probably occurs because these data sets contain the largest range in volume; (3) the duration of notching events seems to be highly variable and relatively insensitive to iceberg size, in contrast to over–steepening events; and (4) therefore, seismic energy (integrated amplitude over duration) and magnitude are always better correlated for over–steepening events than for notching events.

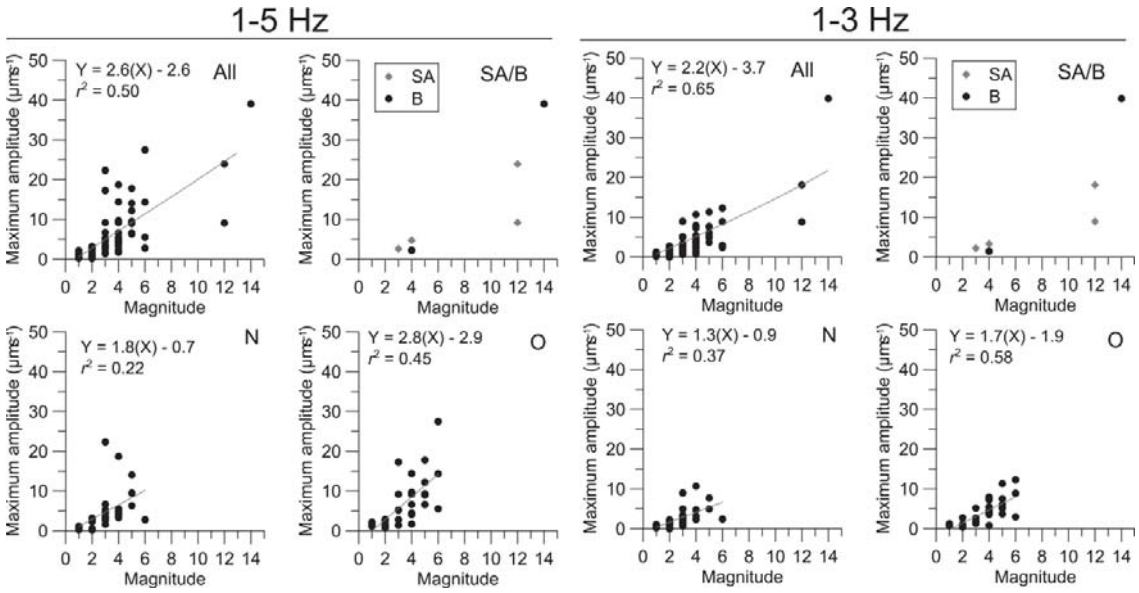

Figure 7.17: Graphs of the 1–5 and 1–3 Hz filtered seismic waveform maximum amplitudes (in μm s^{-1}), magnitude and mechanism of calving. Over–steepening (O), notch–driven (N) and subaqueous and buoyancy (SA/B) events are shown in separate graphs, with 'All' referring to all events. Regression equations and R^2 are also shown for All, N and O events.

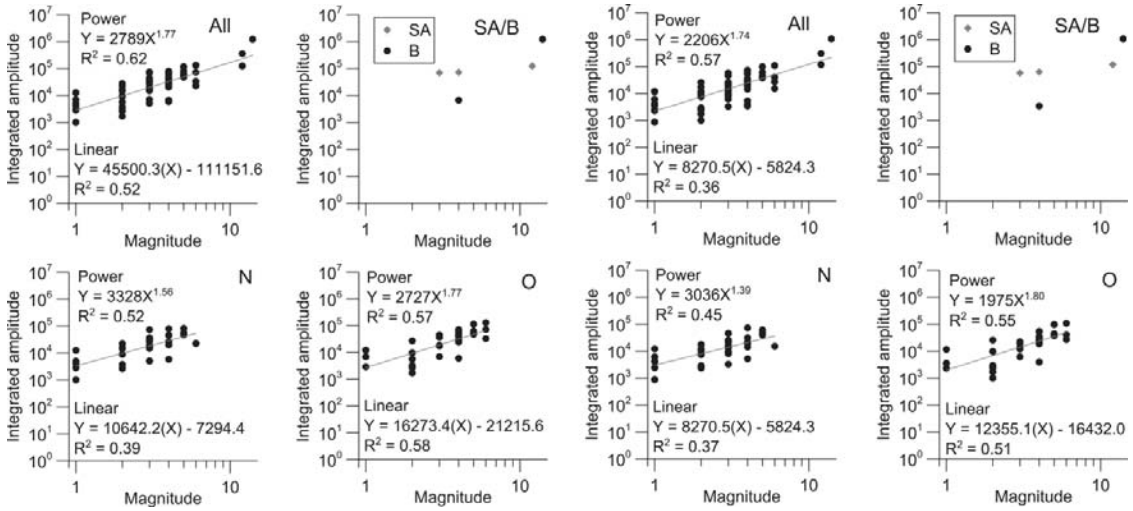

Figure 7.18: Graphs (log–log scale) of integrated amplitude and magnitude (calving size) of calving–generated seismic waveforms filtered between 1–5 Hz and 1–3 Hz. 'All' refers to all events, with over–steepening (O) and notch–driven (N) events in separate graphs. Subaqueous and buoyancy events are presented in the same graph (SA/B). Regression equations (power–law and linear) and R^2 are also shown for All, N and O events.

7.4.3.6 Comparison of calving seismicity at a single location

As calving–generated seismic signals occurred across a range of locations along the terminus of Tasman Glacier, a subset of events is analysed here to identify whether there are any relationships between the common characteristics of calving icequakes and event magnitudes. The general relationship with magnitude has already been described above. Here, a comparison between events of a similar mechanism and location are investigated. The eastern section of the southern ice cliff (Figure 7.19) is used, as a range of event magnitudes between 1 and 6 took place between February and April 2012. Only over–steepening and notching events were included as they have similar characteristics in signal form (section 7.4.2.1).

Figure 7.19: Photograph of the terminus of Tasman Glacier on 02/05/2012 showing the western embayment (WE), eastern embayment (EE), and southern ice cliff (SI). SI–E represents the eastern section of the southern ice cliff along which seismic parameters are compared with calving magnitude.

Comparisons between calving magnitude and the duration, maximum amplitude, and integrated amplitude are shown in Figure 7.20 for the 19 recorded events. For all graphs there is an increase in each of the three variables with respect to magnitude. Reasonable linear fits are found between magnitude and integrated amplitude (R^2 = 0.61), with weaker linear fits between maximum amplitude (R^2 = 0.45) and event durations (R^2 = 0.33). Interestingly the power–law relationship between integrated amplitude and magnitude is weaker for the subset compared to Figure 7.16. For all relationships there is scattering present within each of the magnitude intervals. This indicates that there is a general increase in the duration, maximum amplitude and integrated amplitude with respect to magnitude for events originating from a similar location along the ice cliff. However, as described in sections 7.4.3.1, 7.4.3.3, and 7.4.3.4 when calving events from all regions of the terminus and mechanisms are included the relationship is not so clear.

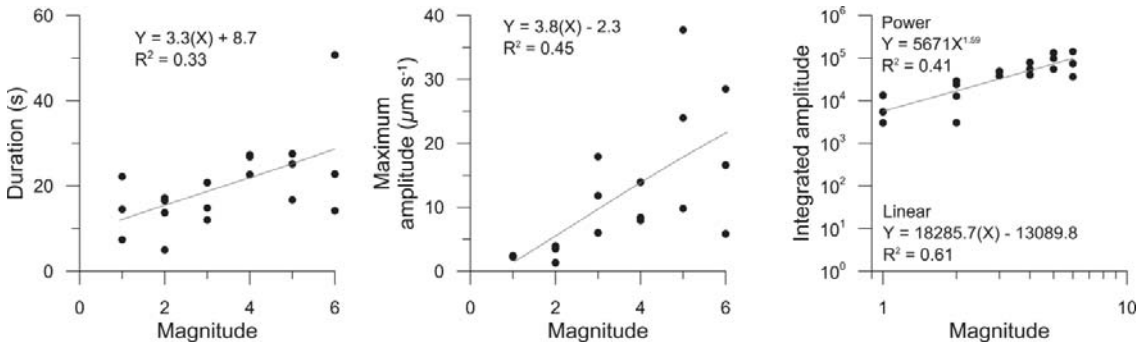

Figure 7.20: Graphs showing the comparison between magnitude and (A) duration, (B) maximum amplitude, and (C) integrated amplitude (log–log scale). Regression equations and R^2 are shown for each graph.

Following on from section 7.4.3.5 the filtered response of the selected events was also investigated (Figure 7.21). Similar to when all events were included, the relationship of calving magnitude and maximum amplitude increased significantly for both the 1–5 Hz and 1–3 Hz filtered data. In comparison, no change in relationship between integrated amplitude of the 1–5 Hz filtered data was found, with a weakening of any relationship with the 1–3 Hz data. As when compared with the entire datasets for the unfiltered data, the relationship between the filtered variables (maximum and integrated amplitude) shows similar trends to the entire dataset, albeit marginally improved.

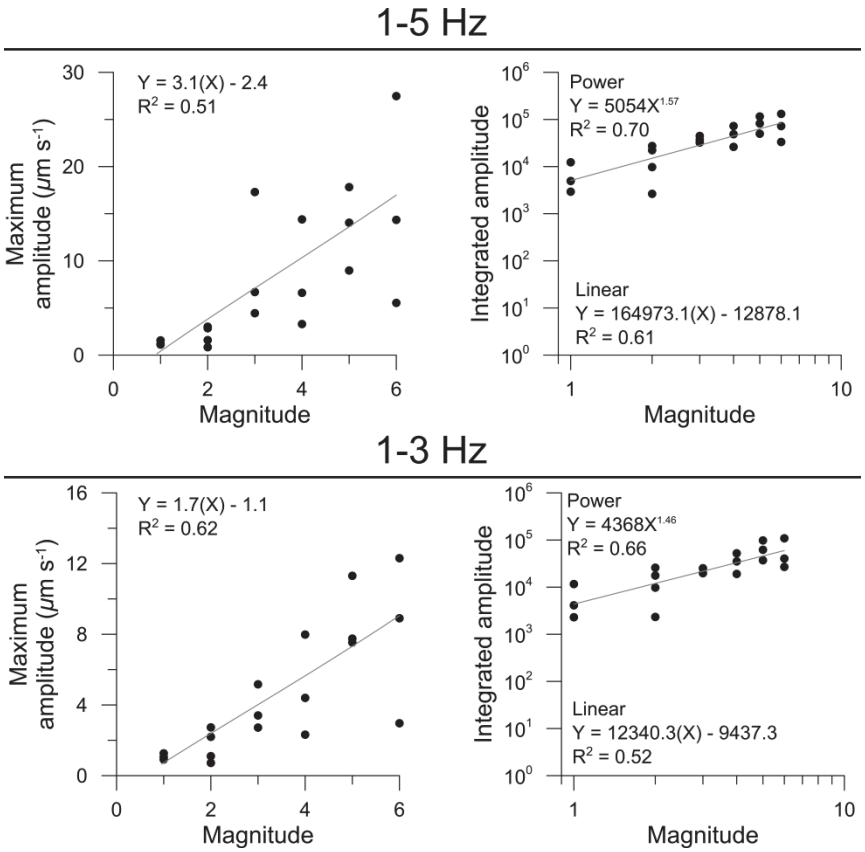

Figure 7.21: Graphs showing the 1–5 Hz and 1–3 Hz filtered comparison of the subset of calving events between iceberg magnitude and maximum amplitude or integrated amplitude (log–log scale) described in section 7.4.3.6. Linear fit, regression equation and R^2 are shown for maximum amplitude. Power–law fit and equation as well as linear regression equation and R^2 is shown for integrated amplitude.

7.4.4 STA/LTA trigger

The characteristics of calving icequakes can be used to develop an automated seismic method for identifying calving events. This is particularly useful for records during night–time and in remote settings. Within earthquake seismology the ratio between the short–term and long–term amplitudes (STA and LTA respectively) is commonly used to automatically detect events. Over a set time window events are marked and catalogued once the STA/LTA ratio exceeds a defined threshold (Figure 7.22). To avoid keeping a long data record in the memory of STA/LTA ratio a recursive STA/LTA (Withers et al., 1998) is used here to automatically identify events. To test whether the recursive STA/LTA event detector (run from within the Obspy toolbox for Python (Beyreuther et al., 2010)) could correctly identify and catalogue calving events, it was run over both a day and month's duration of seismic data. The month of April 2012 was chosen as it had a complete seismic record and a number of well defined calving events across a range of mechanisms and sizes (magnitudes) identified in the time–lapse image record. STA/LTA window lengths of 3 and 40 seconds respectively, were found to provide the best results for

event detection, with the trigger threshold set to a value of 10. However, these settings may differ for different instrument settings.

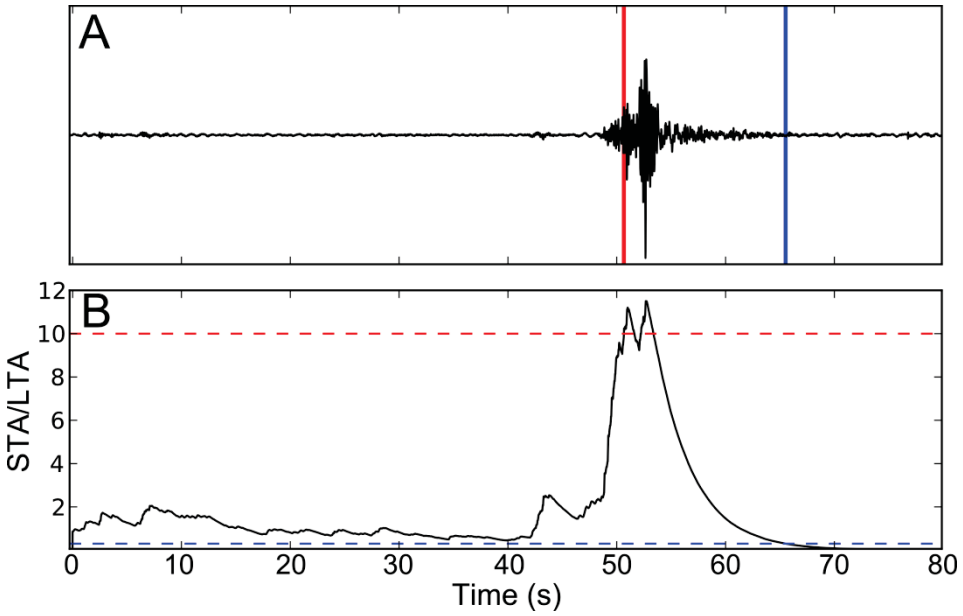

Figure 7.22: Example of the recursive STA/LTA event detector triggering for a magnitude 4 over–steepening calving event. (A) The unfiltered seismic waveform with the timing of the trigger threshold being exceeded (red line) and when the event has returned to near background levels (blue line). (B) The STA/LTA ratio over time showing background levels and the triggering of the event once the threshold of 10 has been met. STA and LTA window lengths are 3 and 40 seconds, respectively. Time zero is UTC 24/04/2012 22:50:30. Note that there is a lag between the onset of the event and the threshold being exceeded.

UTC 24/04/2012 was used in the first instance to test the recursive STA/LTA detector over a 24 hour period that included night time hours. Within this period nine calving events were manually identified in the seismic record (from time–lapse imagery), along with one 4.3 M_L earthquake. The triggered events are shown in Figure 7.23, with the total counts of events reported in Table 7.2. The recursive STA/LTA event detector successfully picked seven out of the nine indentified calving events, with the two unidentified calving events not exceeding the trigger threshold either due to occurring immediately after another event, or not quite exceeding the trigger level (event had a maximum STA/LTA of *c.* 9). If the trigger level is set to lower values (e.g., STA/LTA of 6) to incorporate these events, the total of triggered events increases significantly (hundreds of events in the 24 hour period) as a greater number of non–calving events are able to exceed the trigger threshold. Of the picked calving events the event detector was able to correctly identify the timing of events within 2–3 seconds of the event start times calculated by their deviation away from background levels. However, due to the emergent onset of calving events the event detector consistently delayed the start of an event (e.g., Figure 7.22) compared with the onsets determined for events in section 7.4.3.3, using the method described in section 7.3.2. This resulted in an underestimation of event durations throughout all events.

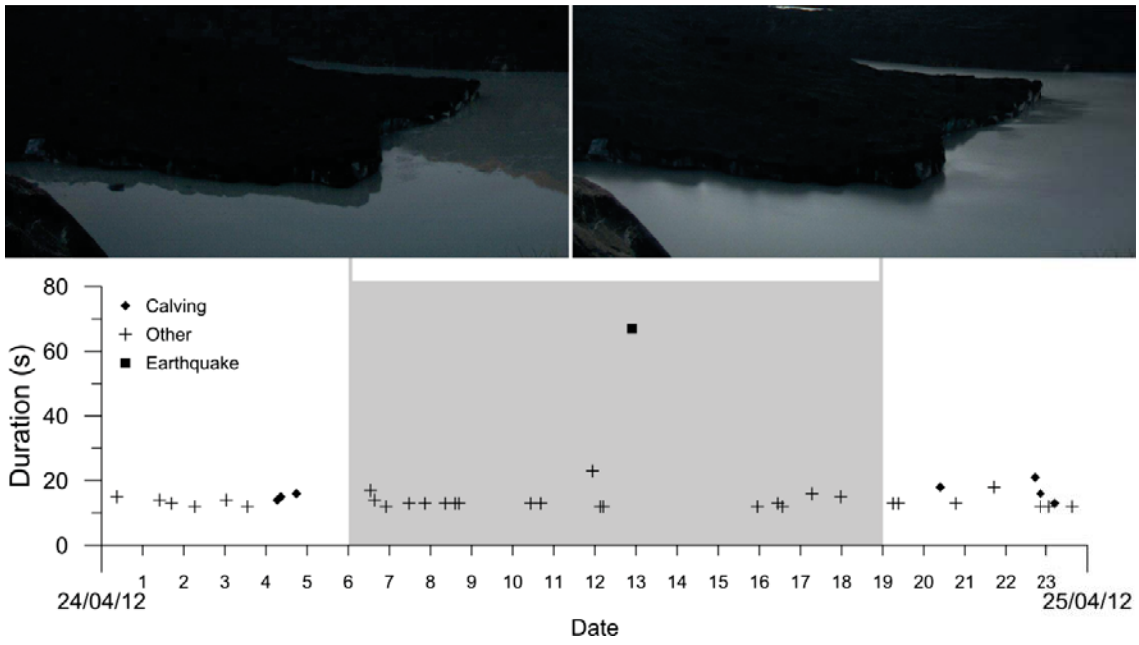

Figure 7.23: The timing and duration of events that exceeded the recursive STA/LTA trigger threshold for the day UTC 24 April 2012. The light grey area indicates night time hours where the time–lapse camera was non operational and no manually identified events occurred. There is no evidence that occurred along the western embayment and southern ice cliff from the time–lapse images bracketing night time hours.

Table 7.2: Number of events that exceed the STA/LTA threshold for 24 April 2012, all of April 2012 and for all data recorded by BB.

Type	24 April 2012	April 2012
Calving events	7 (9[1])	28 (33[1])
Earthquakes[2]	1	30
Other events	24	762
Total	39	819

[1]Number of calving events manually identified in the seismic record from time–lapse imagery.
[2]Earthquake information retrieved from http://geonet.org.nz

Of the non–calving and earthquake events identified by the STA/LTA event detector, a multitude of signal forms were evident. Some signal forms had similar durations and peak seismic amplitudes in similar frequency bands as calving events (e.g., Figure 7.8). However, most triggered events did not have similar signal forms (e.g., Figure 7.25), or had frequency content that were outside those expected for calving–induced seismic waveforms (e.g., Figure 7.26). As a result, triggered events other than those identified in the calving or earthquake record could be characterised as non–calving when their signal waveform and spectrogram where inspected. However, this does not guarantee that all other events are calving in origin without visual confirmation, as signal forms of calving events can be similar to other processes operating within the tectonically active and unstable landscape surrounding Tasman Glacier.

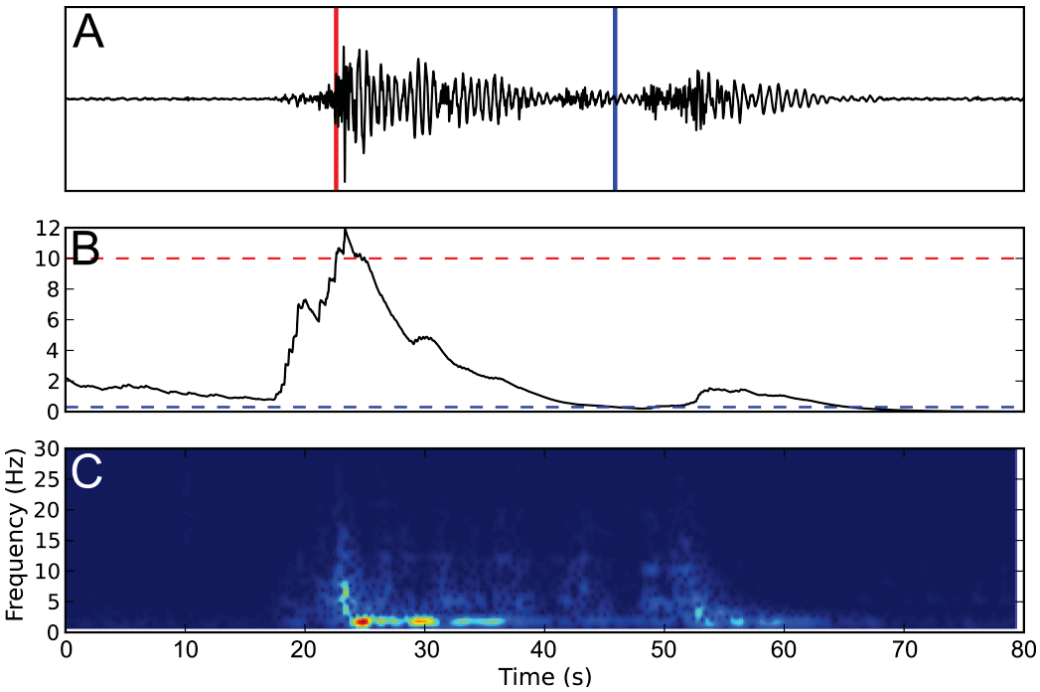

Figure 7.24: Seismic event identified by the STA/LTA trigger during night time hours. The seismic waveform is shown in (A), with the STA/LTA ratio in (B). The spectrogram of the event is shown in (C), with warm (reddish) colours high spectral amplitudes; cold (bluish) colours represent lower amplitudes and background The signal form and frequency content is similar to buoyancy or subaqueous calving events, although there is no evidence for such calving events to have occurred between image pairs in Figure 7.23. Time zero is UTC 24/04/2012 11:56:10. Maximum amplitude in (A) is 3.8 μm s^{-1}.

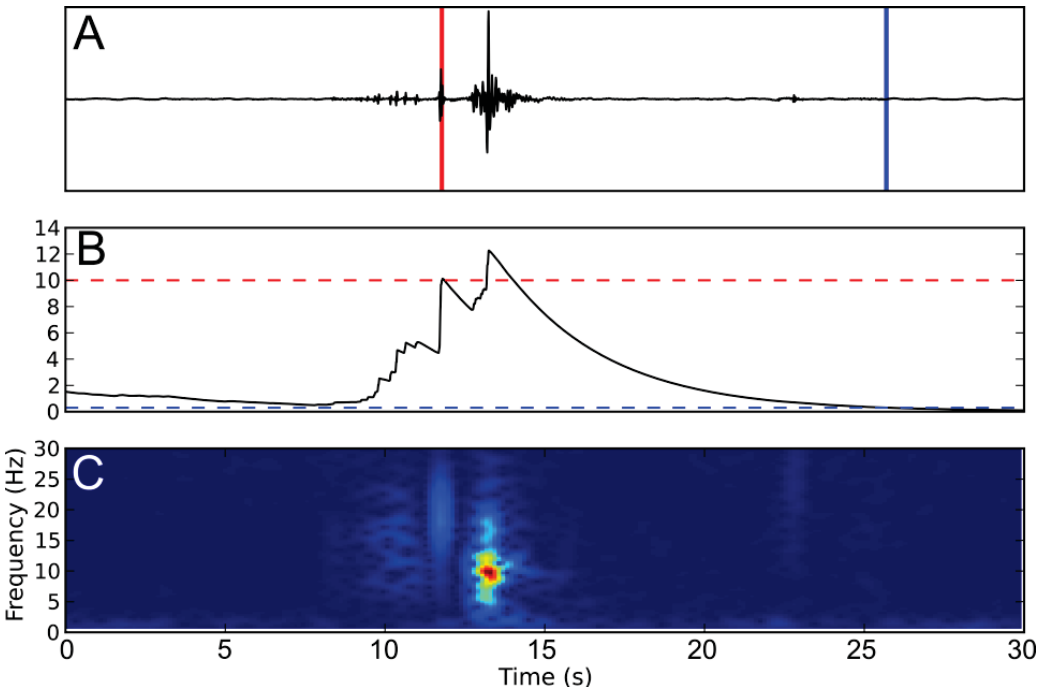

Figure 7.25: Triggered seismic event identified by the STA/LTA event detector. A–C show the same information as described for Figure 7.24. Signal form and frequency content is different to this identified in section 7.4.3. Time zero is UTC 24/04/2012 16:33:30. Maximum seismic amplitude in (A) is 4.4 μm s^{-1}.

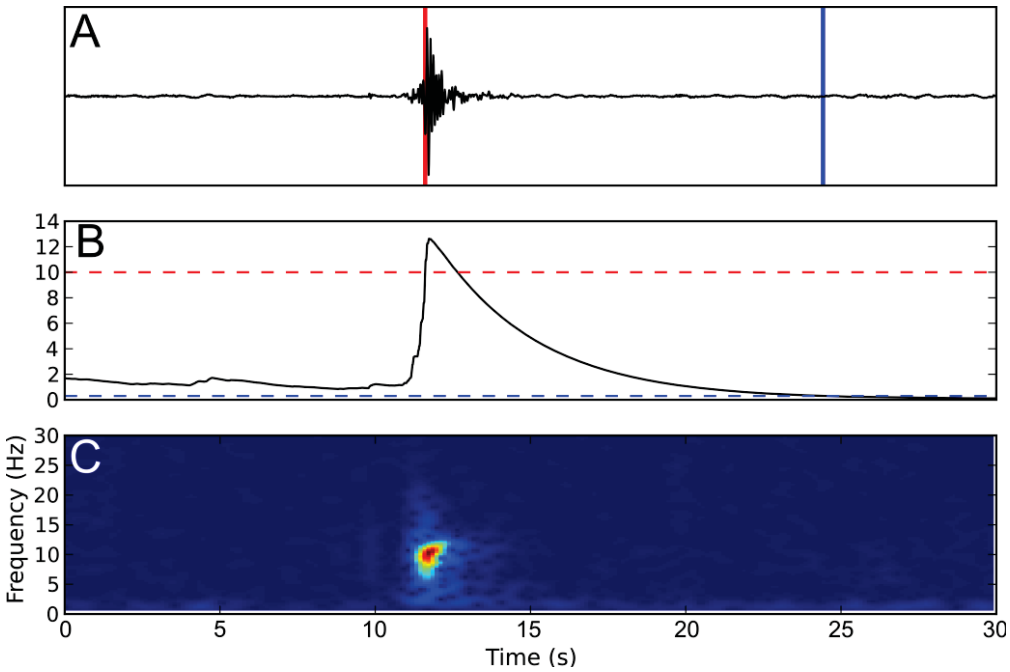

Figure 7.26: Seismic event that triggered the STA/LTA event detector. A–C is the same as Figure 7.24. The event has a frequency content different to calving events and has sudden onset unlike the relatively gradual onset of calving events (e.g., Figure 7.22) Time zero is UTC 24/04/2012 02:16:10. Maximum amplitude in (A) is 2.9 μm s^{-1}.

When the recursive STA/LTA event detector was run across the entire April 2012 seismic dataset, a similar proportion of calving events were correctly identified in the event record (Table 7.2). In total 85 percent of calving events were identified and catalogued, along with 30 earthquakes > 2 $M_{L.}$ A further 762 events were also classified during the month long period. Similar to the day long dataset these events comprised a proportion of triggered events that had similar characteristics to calving events. In summary, the recursive STA/LTA trigger was able to correctly identify at least 80 percent of calving events, but further programmed filters are needed to effectively differentiate between calving events and waveforms produced by other processes (e.g., rock fall) occurring in the Tasman Glacier region.

7.5 Discussion

7.5.1 Calving–induced icequakes

The general characteristics of calving–generated seismicity identified in section 7.4 have indicated that calving events typically have narrow peak frequency content around 1 to 5 Hz, with difference in the duration, maximum amplitude, integrated amplitude, and general signal form. As a result, two groups of events have been identified that comprise similar waveform characteristics: those that originate from the subaerial ice cliff, and buoyancy or subaqueous events. The potential source mechanisms for these two groups of events are discussed here in relation to the observed seismicity at Tasman Glacier and a comparison with similar studies of

calving–induced icequakes (e.g., O'Neel et al., 2007; Amundson et al., 2008; Richardson et al., 2010; Bartholomaus et al., 2012; Walter et al., 2012).

7.5.1.1 Subaerial events

The general characteristics of subaerial calving events from the Tasman Glacier terminus is that they have an emergent onset with weak seismicity above 5 Hz frequencies (e.g., Figure 7.8), followed by a sudden increase ('step') in amplitude when icequakes are filtered between 1 and 5 Hz (Figure 7.12). Over–steepening and notch–driven icequakes have indistinguishable waveforms and frequency content. This is unsurprising, as both over–steepening and notch–driven events destabilise the ice cliff, leading to the detachment of ice from the subaerial ice cliff in similar fashions. The actual detachment of a section of ice from the subaerial ice cliff can occur via the avalanching of ice, ice block slumps, column drops, column rotations, or a combination of all of these processes (O'Neel et al., 2007; Bartholomaus et al., 2012). All of these processes of ice failure and calving have common characteristics, which have been suggested as sources for seismic signals emitted during calving (e.g., Neave and Savage, 1970; Qamar, 1988; O'Neel et al., 2007; Bartholomaus et al., 2012) as the different processes affect the manner by which the calved section of ice fails (either as a single or multiple sections). The actual signal form of subaerial calving events can have subtle differences with respect to the timing and duration of phases within calving–generated seismic wave forms.

Within individual subaerial calving events the primary source of seismic energy, and the cause of the step in the 1–5 Hz amplitude, has been suggested by Bartholomaus et al. (2012) to be the entry of calved ice blocks into the proglacial water–body. Using synchronised video of calving events and seismic data (Welty et al., 2013), Bartholomaus et al. (2012) found that a 'step' in seismic amplitude of calving events at Yahtse Glacier, Alaska, took place at the same time as the calved ice block interacted with the surface of the proglacial water–body. In this situation, seismic signals are generated by a combination of the entry of the ice block into the water (Figure 2.20A), the development of an air cavity (Figure 2.20B), cavity collapse (Figure 2.20C), and 'pinch–off' (Figure 2.20D) which result in the generation of "Worthington" jets (Figure 2.20E). Each step in this process represents a transfer in momentum which can be expressed as compressional seismic waves, particularly the deceleration of the iceberg after impacting the water surface, and the collapse of an air cavity formed if an iceberg descends below the water surface. Such cavity formation and collapse have the potential to form Worthington jets, which are jets of water that emerge at high–speed due to the collapse of cavity walls created by the descending iceberg (Gekle and Gordillo, 2010). Due to the short time period between the impact of an iceberg with the water and the collapse of the resulting cavity, the exact mechanism causing the bulk of seismic energy remains unclear. However, Bartholomaus et al. (2012)

suggest that, due to the forces and timescales involved, either the deceleration of the ice block (Figure 2.20A) or the collapse of the formed cavity (Figure 2.20B) were the two most likely processes. The signal form and frequency content of the example events presented by Bartholomaus et al. (2012) are comparable to those presented in section 7.4.2.1 for subaerial calving events at Tasman Glacier. When coupled with example images from the period preceding the seismic recording, they show a similar 'splash' when ice blocks enter the water (Figure 7.27), meaning that the main source for seismic energy during events at Tasman is considered to be consistent with that found at Yahtse Glacier (Bartholomaus et al., 2012).

Figure 7.27: Cropped time–lapse image on 17/02/2012 showing the splash of water associated with the entry of the calved iceberg into the proglacial water–body. It is this entry into the proglacial water–body and the collapse of a cavity formed by the decelerating ice block that is considered to be the primary source of seismic energy during subaerial calving.

However, there are some differences between several other calving events identified at Tasman Glacier, and those recorded at Yahtse Glacier (Bartholomaus et al., 2012). For example, some subaerial calving events recorded at Tasman Glacier (e.g., Figure 7.7) were dominated by frequencies up to 9 Hz. This may simply represent the inherent variability between calving events, a function of the calving events themselves or path effects. The frequency content of icequakes is thought to increase with respect to the height that an ice block falls (Bartholomaus et al., 2012). For example, Amundson et al. (2010) found that icequakes associated with calving events at Jakobshavn Isbræ, Greenland, had dominant frequencies between 4–6 Hz. This higher frequency content has been attributed to the *c.* 100 m taller ice cliff at Jakobshavn Isbræ than glaciers such as Yahtse Glacier (Bartholomaus et al., 2012). However, Amundson et al. (2010) argue that it is actually a function of icebergs avalanching down the terminus. As Tasman Glacier only has a subaerial ice cliff height of *c.* 25 m it is unlikely that the higher dominant frequencies found within some calving–induced icequakes is a function of the height of calving. Rather they represent the natural variability between calving events. Calving–induced icequakes caused by such events may therefore be characterised more by the fracturing of ice and

avalanching of material down the surface of the subaerial ice cliff than the interaction with the proglacial water–body, although this interaction still comprises a significant portion of the overall signal.

The cause of the higher dominant frequencies (>5 Hz) within some calving events may also provide an explanation for the weak high–frequency gradual onsets identified across all calving events at Tasman Glacier. As with previous studies (e.g., O'Neel et al., 2007; O'Neel and Pfeffer, 2007; Richardson et al., 2010; Bartholomaus et al., 2012), source mechanisms of the weak, higher–frequency, signals during calving–generated icequake onset remains unclear. Nevertheless, fracturing (e.g., Neave and Savage, 1970; Deichmann et al., 2000; Walter et al., 2008; Carmichael et al., 2012) and resonance of water–filled cracks (e.g., O'Neel and Pfeffer, 2007) and the crumbling and impact of ice with the ice cliff during calving (e.g., Amundson et al., 2010; Bartholomaus et al., 2012) are considered to be the most likely source mechanisms. However, the contribution to the overall seismic signal produced during calving is minor compared to the interaction of the calved ice blocks and the proglacial water–body for the majority of calving events.

7.5.1.2 Buoyancy and subaqueous events

Of all events recorded during the operation of the broadband seismometer buoyancy and subaqueous calving were the highest–magnitude and least frequent calving events. These event types involved the loss of up to 1.4×10^6 m^3 of ice during a single event from the terminus of Tasman Glacier taking place over extended periods (>60 seconds) of time. The buoyancy and subaqueous events typically consisted of a long onset (compared to subaerial calving events), followed by a main high amplitude phase that consisted of multiple peaks in seismic amplitude (e.g., Figure 7.10). These multiple peaks in seismic amplitude (Figure 7.10 and Figure 7.11) are comprised of an initial onset of weak high–frequency (>10 Hz) signals, followed by a period of high energy low 1–5 Hz frequency content that tails off until the next peak in amplitude occurs. Such cycles of slow onset and multiple peaks in amplitude have been described at several glaciers globally (e.g., O'Neel et al., 2007; Amundson et al., 2008; Tsai et al., 2008; Amundson et al., 2010; Walter et al., 2010). For example, large (>2.7×10^8 m^3) calving events at Jakobshavn Isbræ, Greenland, are often comprised of a similar gradual onset and multiple peaks in seismic amplitude due to the calving and progressive breakup of a full–thickness calving event (Amundson et al., 2008; Amundson et al., 2010). During these calving events, each peak in amplitude is associated with the rotation and breakup of the calved icebergs. However, in comparison to Tasman Glacier, seismicity continued for an extended period of time (*c.* 10 minutes) due to the transfer of motion to an ice mélange at the terminus (Amundson et al., 2010). At Tasman, the terminus zone is free from such an ice mélange, potentially resulting in

the dissipation of seismic energy faster as the calved icebergs are able to reach equilibrium quicker than with an ice mélange. As a result of these and other observations of similar buoyancy–driven calving events (O'Neel et al., 2007; Amundson et al., 2008; Tsai et al., 2008; Amundson et al., 2010; Walter et al., 2010), the multiple peaks in seismic amplitude observed for the large buoyancy and subaqueous calving events at Tasman Glacier (Figure 7.10) represent not only the initial calving from the terminus, but also the break–up of the calved icebergs.

The calving of such large sections of ice due to buoyant forces therefore involves a variety of mechanisms acting simultaneously throughout calving. Potential source mechanisms include: (1) fracture and resonance within a fluid–filled crack (St Lawrence and Qamar, 1979; Métaxian et al., 2003; O'Neel and Pfeffer, 2007; Winberry et al., 2009); (2) acceleration of the terminus associated with ice loss (Nettles et al., 2008); (3) the scraping of the calved sections with the terminus, other icebergs or the proglacial foreland (Amundson et al., 2008; Tsai et al., 2008; Amundson et al., 2010); and (4) the displacement of water during calving (Bartholomaus et al., 2012). Other source mechanisms suggested for large magnitude events, such as motion of ice mélange near the terminus (Amundson et al., 2010), are not considered to be a factor at Tasman Glacier as no ice melange was present at the time of calving. Given the complex nature of buoyancy–driven calving events and their associated seismic waveforms, a combination of mechanisms 1, 3, and 4 are the more likely sources for the seismicity. For example, the fracturing and overturning of ice and displacement of water during and after calving have been observed for buoyancy and subaqueous calving events at Tasman Glacier (chapter 8) and provided the necessary conditions for the extended period of elevated seismicity after the initial onset of calving. This highlights the complexity of calving events and their associated seismic signals, with the long durations of buoyancy and subaqueous events linked to the time it takes for the calved icebergs to reach equilibrium.

7.5.2 Seismic monitoring of iceberg calving

The monitoring of seismic signals has become an area of increased interest due to the potential to relate calving–generated seismic signal characteristics to the discharge of ice from calving termini and the ability to quantify this mass loss automatically. To date, there has been limited success in relating characteristics with iceberg magnitude and size, with greater success made in the automatic detection of calving events. These tasks are discussed in more detail here in relation to seismicity recorded at Tasman Glacier and similar calving glaciers globally.

7.5.2.1 Iceberg magnitude and seismic characteristics

Several studies (e.g., Qamar, 1988; O'Neel et al., 2007; Bartholomaus et al., 2012) have sought to identify a relationship between seismic parameters and the size of calved icebergs. However,

a broadly applicable relationship has not been found (Bartholomaus et al., 2012), with only event durations found to relate to the discharge of ice from the termini of a calving glacier (O'Neel et al., 2007). Section 7.4.3 introduced several seismic parameters (event duration, maximum amplitude, and integrated amplitude) that indicated a general positive trend between the increase in all unfiltered seismic parameters and event magnitude. Although the error associated with event magnitude is in the order of ± 1 magnitude increment, the general positive trend suggests that a relationship between event magnitude and seismic parameters may be possible. In particular, when only calving events from the subaerial portion of the eastern section of the southern ice cliff are considered integrated amplitude had a better relationship with iceberg magnitude than duration and maximum amplitude (Figure 7.20). The weak relationship between event duration and calving magnitude may be caused by the low seismic amplitudes evident during the protracted coda of calving events. The result of this is an overestimation of event durations due to the method used to identify event ends in this study (section 7.3.2), potentially affecting any relationship between event duration and magnitude. The overestimation of event durations becomes less important for integrated amplitude, potentially leading to an improved relationship when compared to event durations and maximum amplitude alone.

When filtered between 1–5 and 1–3 Hz frequencies, the relationship between maximum amplitude and iceberg magnitude strengthened marginally for the subset of calving events (Figure 7.21). This result was mirrored when the entire dataset is considered (Figure 7.17 and Figure 7.18), suggesting that there is a systematic effect on the relationship between maximum and integrated amplitude. It is unclear why the maximum amplitude relationship with iceberg magnitude increased, while integrated amplitude decreased with the filtering of seismograms. One explanation for this may be that as calving–induced icequakes are typically dominated by frequencies between 1–5 Hz, obtaining the maximum amplitude of events within this band may relate to a process associated with this frequency band (e.g., the impact of a subaerial iceberg into the proglacial water body). Similarly, the reason for the stronger relationship found between integrated amplitude and event magnitude for the unfiltered events may be due to the incorporation of both time and amplitude information in calculations. It therefore represents energy released, so must be related to potential energy, meaning it is comparable to event magnitude. The filtering of events in this situation may remove information that is important for calculations of energy released during calving events from the seismic signal.

However, the relationship of integrated amplitude and event magnitude is also compounded by the incorporation of energy released that is not associated with the initial calving event. For example, high–magnitude buoyancy and subaqueous calving events have greater integrated

amplitudes. This is unsurprising as larger sections of the terminus calved over a longer duration during these events. However, between buoyancy–driven and subaqueous high magnitude calving events there is still a difference between recorded integrated amplitudes. Buoyancy and subaqueous events incorporate not only the calving event itself, but also the resulting rotation and breakup of the calved section (section 7.5.1.2). The two individual subaqueous events shown in Figure 7.11 are a continuation of a single event, and if combined may account for some of the differences found between the similar sized event magnitudes. However, it may also represent a difference in the energy released during the two different types of events. Buoyancy–driven calving events potentially release more energy than the detachment and travel of an iceberg through the water column, as buoyancy events involve the direct contact and transfer of energy to the glacier (e.g., Amundson et al., 2012). This suggests that integrated amplitude may provide a rudimentary approximation of iceberg magnitude (and therefore volume and discharge) for smaller events (less than magnitude 6), but the relationship breaks down at larger magnitudes due to the difficulties in identifying which parts of the seismic signal contribute to recorded seismograms.

A larger dataset that incorporates a greater number of calving event locations and styles is needed to better constrain the relationship of calving event magnitudes and seismic parameters. Such a large dataset may be able to elaborate and better constrain the strongest relationships that have been found at Tasman Glacier. In particular, the relationship between unfiltered integrated amplitude and 1–3 Hz filtered maximum amplitude and iceberg magnitude, may prove to be important seismic parameters for future study. The identification of these parameters at Tasman Glacier is important, as previous studies (e.g., Qamar, 1988; O'Neel et al., 2007; Bartholomaus et al., 2012) have failed to develop any robust relationship between seismic parameters and iceberg magnitude. If these relationships can be analysed in more detail using a wider seismic network to identify sources for icequakes and differentiate path effects (signal attenuation with distance), across a range of glaciers and timescales, a more robust statistical relationship may be found. Such statistical models will provide an important tool for quantifying the mass loss via calving from rapidly retreating freshwater and tidewater glaciers alike (Bartholomaus et al., 2012).

7.5.2.2 Automatic detection of calving icequakes

The automatic detection of calving–generated icequakes independent of visual observations has the potential to be a valuable tool to identify the temporal distribution of calving at a range of calving margins. However, the implementation of such an automatic detector is not straight forward due to the complex and diverse nature of seismic signals. In general, researchers (e.g., O'Neel et al., 2007; Amundson et al., 2010; Walter et al., 2010; Köhler et al., 2012) have

attempted to automatically detect calving events via either time–domain (e.g., STA/LTA) or frequency–domain detectors, with varying degrees of success. At Tasman Glacier, the time–domain recursive STA/LTA event detector was able to correctly identify 85 percent of all calving events identified in the time–lapse imagery record over a month's worth of data. The loss of the initial onset of calving event signals and the inability to correctly pick the event end also represent a flaw in the use of the STA/LTA event detector as the gradual onset of calving–generated icequakes may contain important information on the evolution of both the calving event and calving duration. Also, picking the end of events is particularly difficult when there are multiple peaks or an extended period of elevated seismicity, such as that found with buoyancy–driven calving events. However, the correct identification of the majority of identified calving events indicates that the STA/LTA event detector has the potential to be a powerful tool when coupled with the previously identified relationship between several seismic parameters and calving magnitude at Tasman Glacier.

To further automate the differentiation between calving and non–calving events within the triggered events, additional filters of event waveforms and frequency content are needed. For example, Tasman Glacier is situated within an unstable landscape with ice/snow avalanches, landslides, earthquakes and rock avalanches (Allen et al., 2009b) occurring year around, making the automatic detection of calving–generated icequakes and the differentiation of the icequakes from other signals highly important. Improvements to the automatic detection of calving events at Tasman Glacier could be made by: (1) integrating statistical and unsupervised clustering analysis to STA/LTA event detectors to classify triggered events by their signal characteristics (e.g., West et al., 2010; Köhler et al., 2012); (2) picking and classifying events using a frequency domain detector (e.g., O'Neel et al., 2007; Walter et al., 2010); or, (3) supplementing seismic data with synchronised video (e.g., Bartholomaus et al., 2012) and acoustic monitoring (e.g., Amundson et al., 2010; Richardson et al., 2010) to provide additional sources of information to discriminate between calving and non–calving events. However, as the frequency of calving events at Tasman Glacier recorded in this study is significantly less than rates reported for similar studies of calving–generated seismic signals (*c.* 1 event d^{-1} versus *c.* 20 events h^{-1} (O'Neel et al., 2007)), the combination of time–lapse imagery (or video) and seismic data may be a satisfactory substitute for recording and quantifying calving events over short periods of time (e.g., months).

The ability for automatic calving event detectors to pick and characterise calving events at Tasman Glacier and water–terminating glaciers globally highlights the ongoing importance in the future study of calving at water–terminating margins (e.g., O'Neel et al., 2007; Walter et al., 2010; Köhler et al., 2012). Improvements in their ability to quantify calving will aid in the

remote assessment of the contribution of calving to glacier mass balance, as well as identifying calving related hazards (e.g., calving–generated tsunami). However, to do this, further research improvements are needed in the classification and identification of calving–generated signals, as well as interpreting and constraining of the results (e.g., O'Neel et al., 2007; Walter et al., 2010; Köhler et al., 2012).

7.6 Conclusion

Calving events at Tasman Glacier have been shown to emit seismic signals similar to those found at calving margins globally. All calving events generated seismic signals that had emergent onsets with weak frequencies above 5 Hz, followed by a high amplitude phase with frequency content between 1 and 5 Hz, and a protracted coda. Two groups of calving–induced icequakes were identified: (1) events originating from the subaerial ice cliff; and, (2) higher–magnitude buoyancy and subaqueous calving events. In general, subaerial events had durations between 2 and 30 seconds, and were comprised of a single or double peak in seismic amplitude. In comparison, buoyancy and subaqueous events had long durations (>60 seconds), greater maximum amplitudes, and had multiple peaks in seismic amplitude. The seismic energy released during subaerial calving is associated with the interaction of the calved ice block and the surface of the proglacial water–body, with the fracture and avalanching of material associated with weaker higher frequencies during event onset. Buoyancy and subaqueous event seismicity is associated not only with the fracturing of ice and the interaction with the surface of the proglacial water–body, but also the break–up and scraping of icebergs with the terminus and proglacial foreland. However, at Tasman Glacier, as at other calving margins, the exact mechanisms linked with calving–induced icequakes are not entirely clear, with further research needed to increase the understanding of the dynamic and variable processes involved during iceberg calving.

Greater understanding of the mechanisms that induce seismic waveforms will aid in the development of relationships between the magnitudes (volume) of ice calved during events and seismic parameters. For calving events at Tasman Glacier, positive relationships were found with maximum amplitude, integrated amplitude, and duration. Integrated amplitude appears to provide the best relationship with calving magnitude using unfiltered seismic data. Filtering of seismic events between 1–5 and 1–3 Hz improved the relationship between maximum amplitude and magnitude to a similar level as with unfiltered integrated amplitude. However, filtering weakened the relationship between integrated amplitude's relationships. The presence of several positive relationships is in contrast with previous studies (e.g., O'Neel et al., 2007; Bartholomaus et al., 2012) which have only found duration to roughly approximate calved

volumes. When coupled with any broadly applicable relationships with seismic parameters and calving event volumes, it may also provide a means to quantify ice discharge remotely from inherently dynamic and dangerous termini.

By using a recursive STA/LTA event detector calving events in the time–lapse image record were able to be correctly identified and catalogued. However, given the large number of events catalogued by the STA/LTA event detector which were not calving in origin the use of such an approach in the unstable landscape surrounding Tasman Glacier needs refining. Nevertheless, this study has shown that the combination of seismic data with time–lapse imagery has the potential to provide a means to identify and describe the intra–event characteristics of calving events. This information will extend the growing body of research on the characteristics of calving–generated icequakes, as well as providing information from a glaciological regime (freshwater calving margin) that has not yet received a great deal of attention.

Chapter 8: Buoyancy–driven calving at Tasman Glacier

8.1 Introduction

At Tasman Glacier high–magnitude buoyancy–driven calving events have contributed to the period of rapid retreat between 2007 and 2013 (chapter 4). To understand the spatio–temporal variability in buoyancy–driven calving and the potential triggers, six example calving events are described in this chapter in detail to highlight the characteristics of these high–magnitude episodic events. In particular, the potential for subaqueous calving, lake level fluctuations and coseismic triggers for buoyancy–driven calving events will be discussed. To do this the timing and style of each calving event is outlined, with added high–resolution data (e.g., lake–level, time–lapse imagery, video and seismic data) used to understand inter– and intra–event processes that contribute to mass lost via buoyancy–driven calving at Tasman Glacier.

8.2 Background

The calving of large icebergs from water–terminating glaciers is often caused when upward buoyant forces are applied to the terminus as a result of the density differences between ice and water, resulting in the fracturing of ice (Warren et al., 2001; Benn et al., 2007b; Boyce et al., 2007; Trüssel et al., 2013). Such buoyancy–driven calving events have a significant impact on the transfer of mass between the cryosphere and hydrosphere as large sections of termini can calve in single events (Benn et al., 2007b). For example, large calving events have resulted in the loss of several kilometres of ice from the outlet glaciers of Greenland (e.g., Amundson et al., 2008; Csatho et al., 2008; Walter et al., 2012). Historically, it was thought that tidewater and freshwater calving margins are only able to sustain floating termini for short periods of time (Meier and Post, 1987), due to the presence of highly fractured ice that approaches zero tensile strength near flotation (van der Veen, 1996; O'Neel et al., 2003). However, recent studies at both tidewater (e.g., Walter et al., 2010) and freshwater (e.g., Boyce et al., 2007) glaciers have indicated that they are able to achieve flotation for long durations of years, although they are inherently unstable features. The ability for sections of a glacier terminus to attain flotation for extended periods of time results in a shift in the dominant calving regime from high–frequency,

low–magnitude (relative to the size of the glacier) calving, to low–frequency, high–magnitude calving (e.g., Walter et al., 2010; Trüssel et al., 2013). This transition is initiated by the thinning of the lower glacier due to a combination of decreased ice supply, increased extensional flow at the terminus, increased subaerial ice melt, and subaqueous melt of a cavity formed at the base of the glacier (Benn et al., 2007b; Walter et al., 2010; Motyka et al., 2011; Trüssel et al., 2013).

The duration of flotation for a section of the terminus is controlled by the timing and frequency of high–magnitude buoyancy–driven calving events, as they result in the retreat of the glacier to the grounding–line (Benn et al., 2007b). Such events are episodic, but thus far no distinct time interval has been identified between the point of attaining flotation, and calving. The timing and mechanisms that led to ice fracturing and calving related to buoyancy remain unclear due to the complicated arrangement of forces involved. Mechanisms that have been suggested as contributing to the triggering of buoyancy–driven calving events include: perturbations in proglacial water level (such as tidal flexure at tidewater glaciers (e.g., MacAyeal et al., 2006; Walter et al., 2010) and rain induced lake–level increase at freshwater glaciers (e.g., Boyce et al., 2007)); extensive flow at the terminus, due to effective pressure at the base of the glacier decreasing to zero (e.g., Warren et al., 2001; O'Neel et al., 2005); near–terminus geometry (e.g., Benn et al., 2007b; Walter et al., 2010) and the presence (e.g., van der Veen, 1998a) and development of subaqueous fractures (bottom crevasses), due to torque applied to the terminus as a result of upward bending forces (e.g., Warren et al., 2001).

8.3 Methods

A combination of photographic, video, climate, lake–level and seismic datasets are used to identify and describe six high–magnitude buoyancy–driven calving events from the terminus of Tasman Glacier between 2010 and 2013. The methodologies for recording time–lapse imagery (section 5.3.4), climate (section 5.3.3), lake–level (section 5.3.2), and seismic recording (section 7.3.2) used in this chapter have already been outlined in previous chapters. The location of the camera and data loggers is shown in Figure 5.2 and Figure 7.1 Additional seismic data for the 22 February 2011 event was retrieved from the New Zealand GeoNet program (http://geonet.org.nz).

8.4 Description of calving events

8.4.1 August 2010

The 22 August 2010 calving event occurred over a prolonged period (~50 days) as a 600 m central section of the Tasman Glacier terminus was uplifted out of the water prior to calving

(Figure 8.1 and Figure 8.2). This large section of the terminus was first observed to be emerging sub–aerially on 29 June, as indicated by tilting of thermo–eroisional waterline notches. By 1 July tilting was significant, with the orientation of the thermal–notches increasing to approximately 45º by 17 July (G. Pearson, *pers. comm.*, 2010). Terminus uplift continued until a section on the eastern margin of the tilting peninsula calved on 20 August (Figure 8.1B). Morphological maps (Figure 8.1) produced from oblique photographs show obvious vertical displacement of the peninsula, along with development of transverse crevasses at a hinge–line. Formation and propagation of these crevasses preceded calving of the entire peninsula on 22 August 2010.

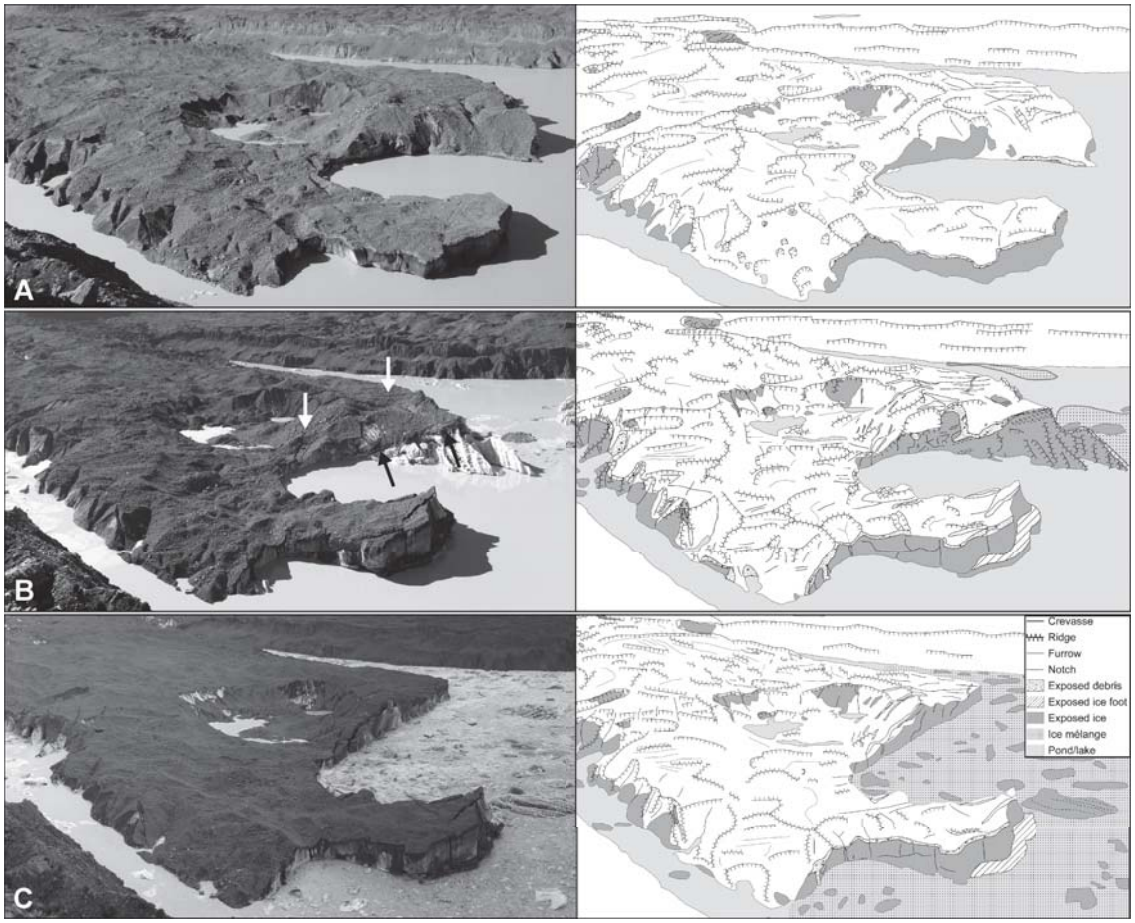

Figure 8.1: Oblique photographs and morphological maps of Tasman Glacier depicting the sequence of events leading up to, and post, calving during August 2010. (A) 22 April. terminus geometry pre–flotation. (B) 20 August, mid–flotation geometry. Black arrows indicate tilted thermo–erosional notches and white arrows indicate the hinge point of calving failure. (C) 22 August. Post calving terminus geometry (sources: D. Callesen and G. Pearson).

Immediately prior to calving, the surface area of the calved section was *c.* 7.9×10^4 m^2, giving an estimated volume of *c.* 24×10^6 m^3 based on the observation that the entire thickness of the glacier calved during this event. However, this is only an estimate of the total calved volume as spot water depth measurements made during September 2009 indicated an extensive subaerial

ice ramp projecting out from the terminus (D. Callesen, *pers. comm.*, 2010). This ramp is visible on the uplifted terminus in Figure 8.1B. The calved icebergs rotated as they separated from the terminus, disintegrating into smaller icebergs tens to hundreds of metres across (Figure 8.1C). A series of smaller slab–calving events followed over the next 24 hours as the glacier readjusted to the new geometry. The second peninsula on the western section of the terminus remained for a number of months after this event; eventually retreating progressively by low magnitude calving events during September and October 2010.

Figure 8.2: Photograph of a section of the calving terminus of Tasman Glacier showing uplifted thermo–erosional notches (arrowed) on 9 August 2010 prior to the 22 August calving event. Maximum height of notches is *c.* 25 m above the waterline in the central section of the terminus. Note the extensive snow cover over the lower glacier surface.

Rainfall between July and August 2010 was dominated by 2 events on 1/2 and 12/13 August, with a total of 261 mm and 134 mm falling at MCV. During August 2010, Tasman Lake sustained an increase in lake level of 0.4 m on the 12/13 of August, in response to 132 mm of rainfall recorded at MCV (Figure 8.3). A large proportion of this rainfall fell as snow above 1000 m (Figure 8.2). This resulted in a sustained rise in lake level due to a lag between the melt of snow fall at higher elevations (>1000 m) and the less efficient routing of meltwater through the englacial and subglacial drainage network. Variability in lake level after this calving event was caused by partial damming of the lake outlet by grounded icebergs from the large calving event on 22 August at the distal (southern) end of the lake.

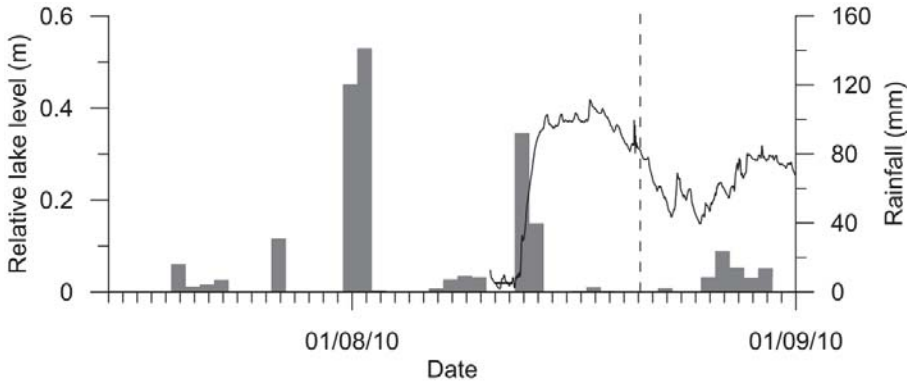

Figure 8.3: Daily rainfall (bars) at MCV and Tasman Lake level (solid line) between July and August 2010. Dotted vertical line indicates calving event.

8.4.2 December 2010

The high magnitude calving event documented on 19 December 2010 was less significant in size than the 22 August 2010 event, but nonetheless resulted in mass loss of a large section of the terminus (Figure 8.4). During December 2010 minor uplift (*c.* 1–2 m) of the central ice cliff was observed (Figure 8.4) prior to calving on 19 December (D. Callesen, *pers. comm.*, 2010), with large transverse crevasses developing in the terminus region. Calving of a large, coherent, section of the central terminus occurred along these fractures on 19 December, as a result of full ice thickness calving of a slab formed along a zone ~ 50 m up–glacier of the terminal cliff. Calving took place during a period of rapid lake level rise (Figure 8.5) associated with rainfall falling within the catchment in the days prior. Based on the post–calving iceberg volume above the waterline, a lower bound estimate of the total volume calved is *c.* 1.8×10^6 m^3.

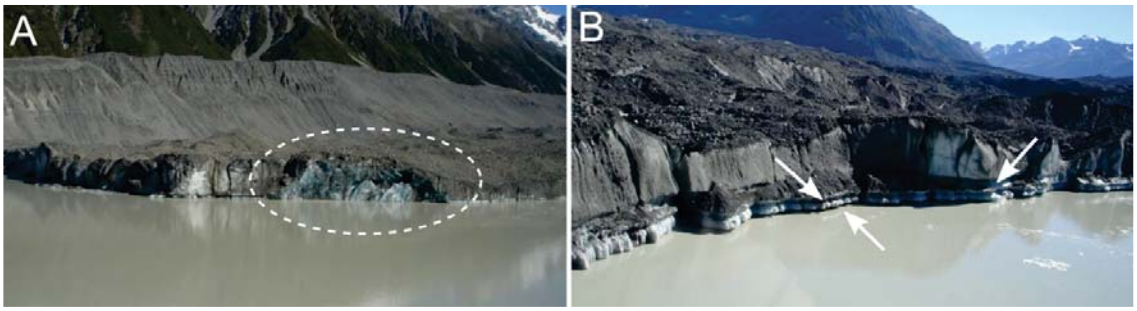

Figure 8.4: Photographs of the Tasman Glacier terminus in the days after the 19 December 2010 calving event. Circle in (A) denotes the area that calved. Evidence for the uplift of the terminus is provided by the exposed thermo–erisional notches above the waterline in (B) (source: D. Callesen).

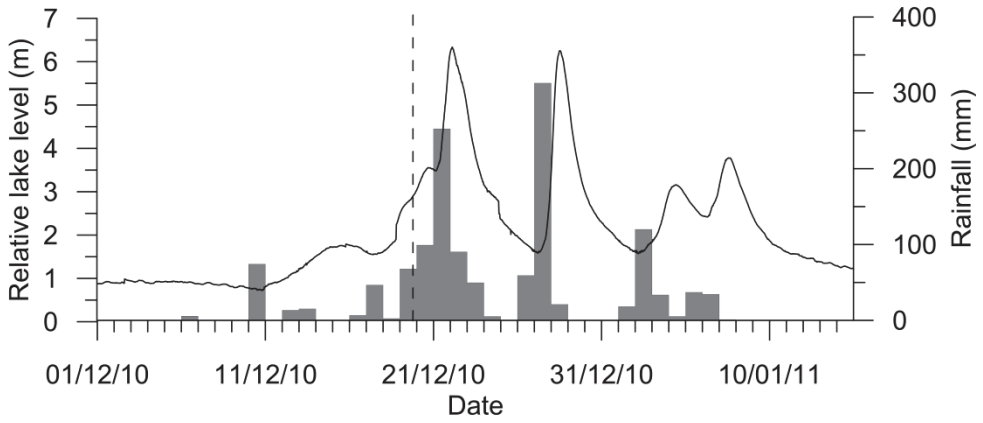

Figure 8.5: Daily rainfall (bars) at MCV and Tasman Lake level (solid line) between December 2010 and January 2011. Dotted vertical line indicates calving event

8.4.3 February 2011

Examination of photographs and video recording (Figure 8.6 and Figure 8.7) of the calving event on 22 February 2011 indicates that bottom out rotation calving failure of the entire glacier thickness (*c.* 4.5×10^6 m^3) commenced at 13:22:46, lasting for *c.* 2 minutes (Figure 8.6). The first sign of calving was the fracturing of ice and the spray of ice particles along the point of failure (Figure 8.7C). The calved section subsequently broke up in the minutes after calving as the iceberg adjusted to its new equilibrium. Water level in supraglacial ponds behind the terminus was observed to fluctuate during the calving event, indicating that they were hydraulically connected to Tasman Lake at the time of calving. The calving event generated a (miniature) 'tsunami' that left a tide–line at *c.* 3.1 m at the southern end of the lake (D. Callesen, *pers. comm.*, 2011).

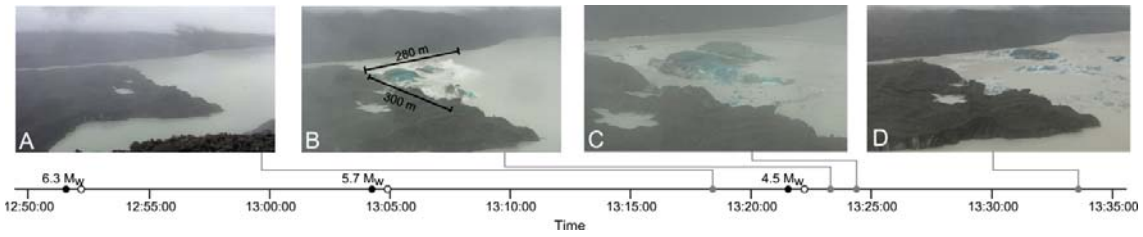

Figure 8.6: Timeline of the 22 February 2011 calving event at Tasman Glacier, showing the timing of earthquakes and the S–wave arrival time at Tasman Glacier as well as the pre– (A), during (B–C), and post–calving (D) images. The approximate dimensions of the calved iceberg are shown in B (source: C. and S. Walter).

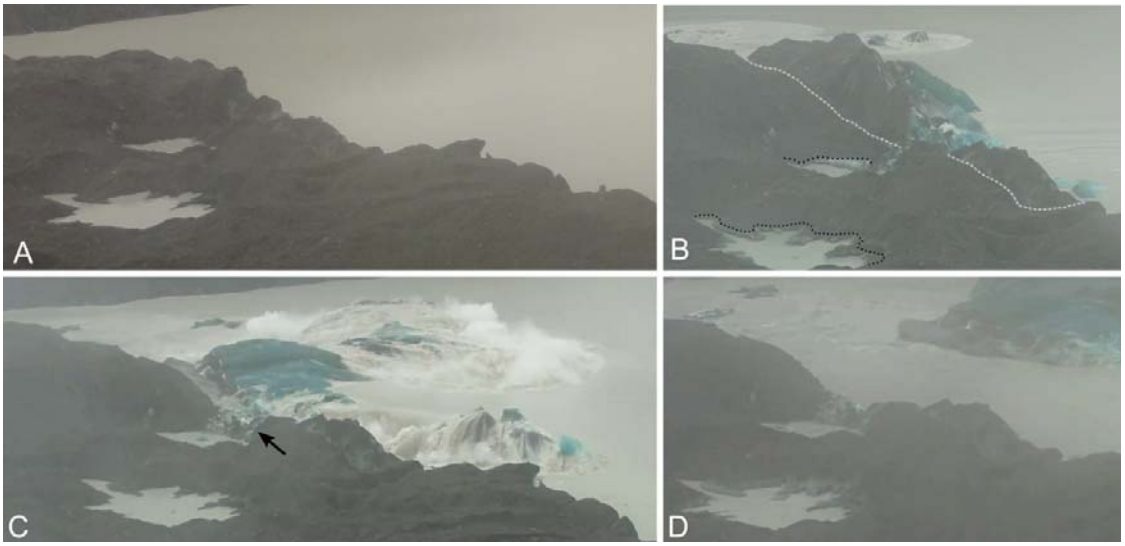

Figure 8.7: Still images from video of calving at the terminus of Tasman Glacier on 22 February 2011. Water level in the ponds behind the terminus can be observed to drop (B) from their initial level (A), increasing again mid–event (C), before lowering again to a level below their original level (D). Dotted black line in B shows the original pond level, with the white dotted line indicating the calved section. Arrow in C indicates ice particles that have sprayed onto the glacier surface (source: C. and S. Walter).

In the hour prior to this large buoyancy–driven calving event at Tasman Glacier, the Christchurch earthquake (M_L 6.3), centred 5 km southeast (Figure 8.8) of Christchurch, New Zealand, occurred at 12:51:42 on 22 February 2011. Significant aftershocks following the initial earthquake occurred at 13:04:19 (M_L 5.7) and 13:21:25 (M_L 4.5). Based on the position of Tasman Glacier, 201 km west of Christchurch (Figure 8.8), shear (S–) waves would have arrived *c.* 59 s after the initial earthquake. This is confirmed by the timing of ground acceleration and S–wave arrival at the Fox Glacier (FOZ) seismic station, 30 km west of Tasman Glacier (Figure 8.8).

Several fluctuations in the level of Tasman Lake were recorded by the water level logger during the period prior to calving. These fluctuations are again associated with rainfall falling within the Tasman Glacier catchment. In the day leading up to 22 February, lake level was increasing in response to 66 mm of rainfall. However, there is a dramatic increase in lake level over the 30 minute period in which the calving event took place. This is attributed to the displacement of the logger due to the tsunami wave. Without the displacement of the logger, increased lake level would have been of a similar amplitude to those recorded in association with rainfall in the weeks prior.

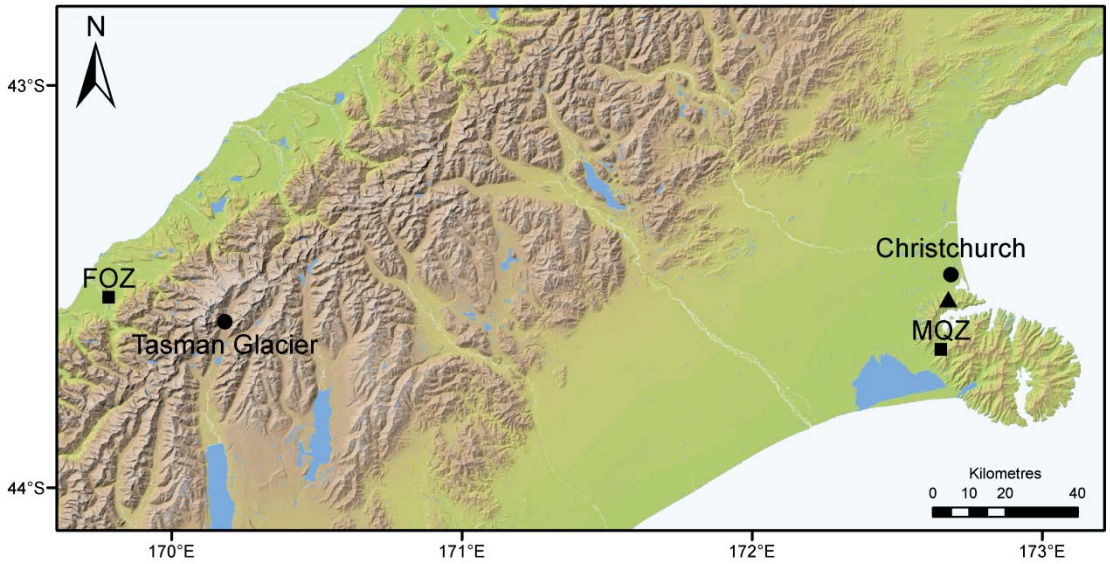

Figure 8.8: Map showing the location of Tasman Glacier, Christchurch, and the epicentre (triangle) of the M_L 6.3 earthquake. Also shown is the location of the McQueen's Valley (MQZ) Fox Glacier (FOZ) seismic station.

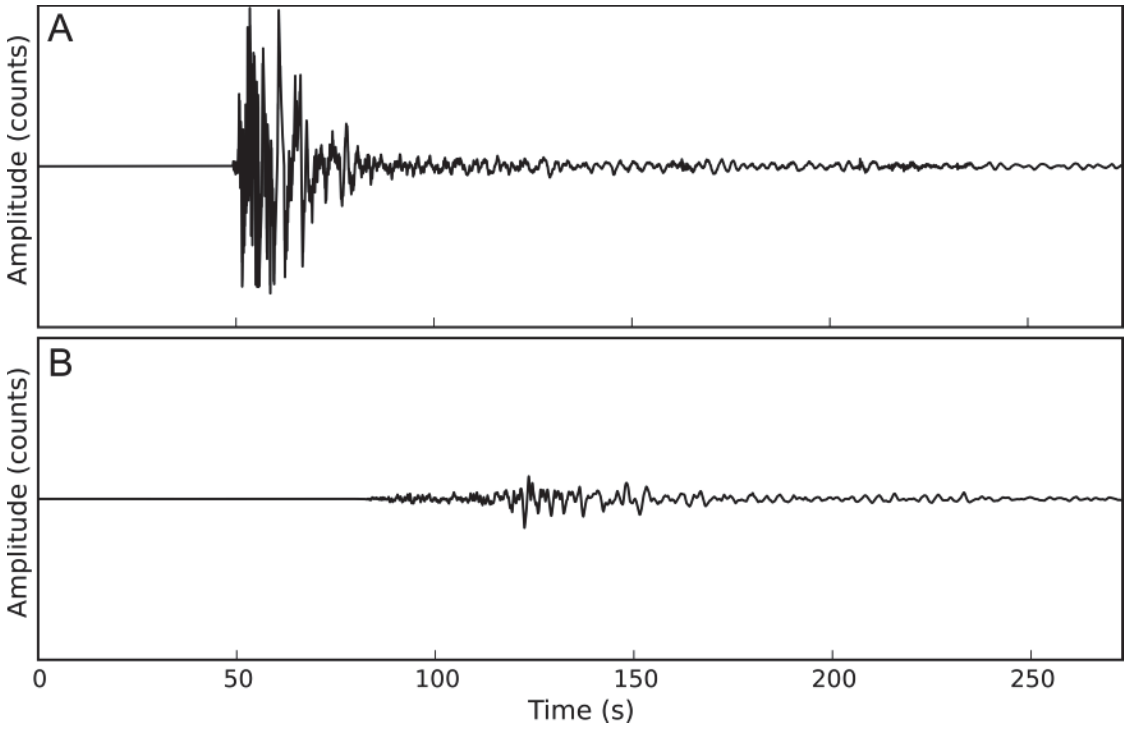

Figure 8.9: Waveform data of the M_L 6.3 Christchurch earthquake at (A) MQZ and (B) FOZ seismic stations. The same amplitude scale is used in (A) and (B). Seismic data retrieved from http://geonet.org.nz.

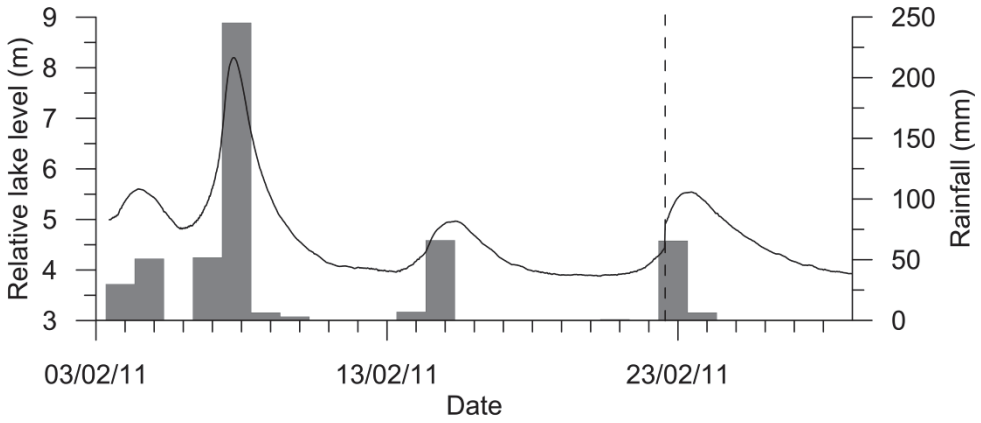

Figure 8.10: Lake–level of Tasman Lake and rainfall data from MCV. Dotted vertical indicates the calving event on 22 February 2011.

8.4.4 January and April 2012

Two large calving events were recorded on 31 January and 29 April 2012 (Figure 5.34). The general characteristics of the two events are discussed in detail in section 5.5.2.3. Similar to previously described buoyancy–driven calving events, uplift of the terminus was evident in the days and weeks prior to calving. However, due to the continuous high–temporal resolution of images bracketing the two it was found that they both were preceded by subaqueous events. In the case of the January 2012, event subaqueous calving in the region of the boundary between the southern ice cliff and the western embayment was recorded in the days prior to calving. On the other hand, the April 2012 event was preceded by a large subaqueous event on 02/04/12. This large subaqueous event affected the stress regime of the terminus resulting in the extensive development of crevasses prior to calving (Figure 5.35). As with several other calving events the icebergs broke up after calving (Figure 8.11).

Figure 8.11: Photograph of the terminus region of Tasman Glacier event on 31 January 2012

8.4.5 February 2013

The largest (*c.* 30 $\times 10^6$ m^3) of all example calving events took place over the night between 22 and 23 February 2013 (Figure 8.12). This calving event encompassed the entire lower section of

the Tasman Glacier terminus, resulting in a retreat of 150 m. Similar to previous events, uplift (up to 5 m in places (B. Anderson, *pers. comm.*, 2013)) of the terminus was observed prior to calving. However, unlike previously described events this 5 m of uplift only occurred on the day prior to calving. A subaqueous calving event took place during the night of the 21/22 February 2013, occurring immediately prior to uplift of the terminus. No obvious transverse crevasses developed across the point of failure during uplift, giving no obvious indication of a high–magnitude calving event prior to the rapid uplift (B. Ward, *pers. comm.*, 2013). The calving event resulted in a typical myriad of small icebergs within Tasman Lake, although the bulk of ice calved remained intact in the form of a single large iceberg (Figure 8.12B). Given that the bulk of the calved ice during the February 2013 event formed a single iceberg, and the rapid onset of the event, limited fractures within the lower glacier must have been present. No lake–level data is available for this calving event. However given the limited amount of rainfall recorded at MCV in the month prior to calving (Figure 8.13), no large increases in lake–level are likely to have occurred immediately prior to the time of calving.

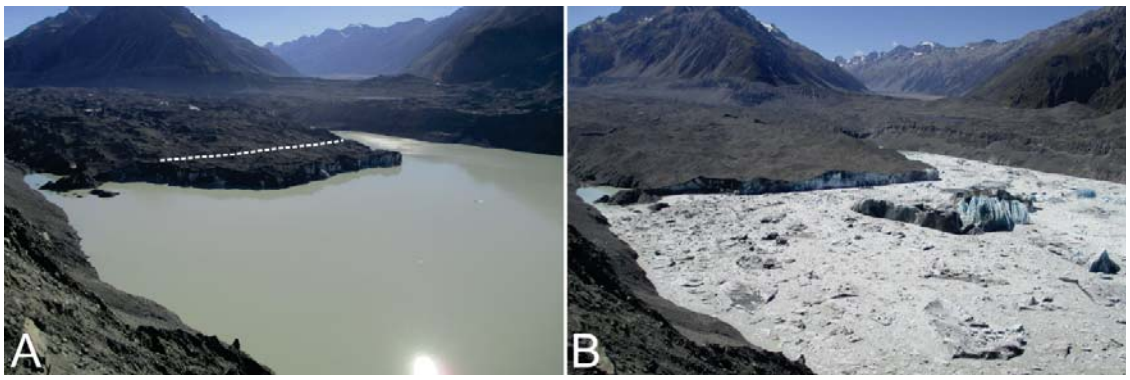

Figure 8.12: Oblique photographs of the terminus of Tasman Glacier before calving on 18/02/2013 (A) and after calving (B) 23/02/2013. Dotted line in (A) indicates the position of the terminus after calving. The single large iceberg formed during this calving event can be seen near the terminus of Tasman Glacier in (B) (source: G. Slatter).

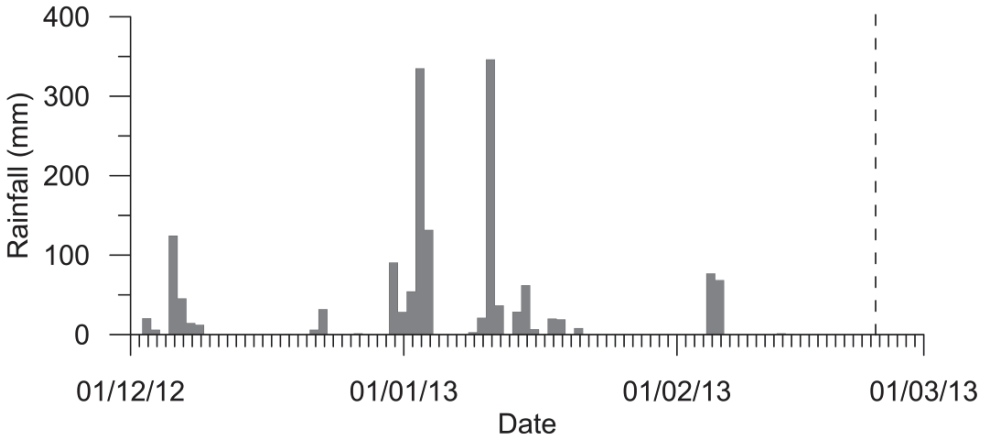

Figure 8.13: Rainfall data from MCV. Dotted vertical indicates the calving event on 22 February 2011.

8.5 Discussion

The susceptibility of the terminus of Tasman Glacier to buoyant forces post–2007 has been clearly demonstrated in section 4.4.2, and is reinforced by the observations that all events presented in this chapter were associated with observed uplift in the days and weeks prior to calving. The general effects of buoyant forces on isolated calving events have also been discussed in section 4.4.2, highlighting that buoyancy driven calving events are primed by the progressive thinning of the Tasman Glacier terminus, subaqueous melt, and the geometry of the terminus effectively isolating sections from lateral support and increasing their susceptibility to buoyant forces. Building on these discussions the six example buoyancy–driven calving events described in this chapter are used to highlight mechanisms that potentially initiate buoyancy–driven calving. The three key mechanisms discussed here are: the importance of the loss of sections of the subaqueous cliff, proglacial water–body fluctuations, and potential coseismic triggers.

8.5.1 Subaqueous ice cliff loss and buoyancy–driven calving

The loss of ice from the subaqueous section of the ice cliff of Tasman Glacier represents not only an important longer–term driver of terminus stability (by adding to the overall thinning of the glacier (e.g., Trüssel et al., 2013)), but also to the initiation of calving via the removal of basal support. Sections of a glacier that are at or exceed the threshold for flotation are inherently unstable features, with any changes increasing buoyant forces contributing to fracture propagation and calving. Subaqueous calving events observed in the days and weeks prior to several other calving events (e.g., section 8.4.5) would have affected the force balance of the near floating sections of the glacier, promoting the development of fractures and the eventual calving of the unstable sections. Such subaqueous calving events remove lateral support from grounded surrounding ice. The loss of lateral support isolates the buoyant section so that it is able to oscillate freely with fluctuations in the proglacial water–body and increased upward buoyant forces. This potential increases stresses applied at the hinge point, resulting in the increased development of bottom crevasses (van der Veen, 1998a). Similarly, the loss of a subaqueous section of the ice cliff via calving (and equally subaqueous melt within a basal cavity) increases stress at the hinge point, by decreasing the ratio between ice cliff height and water depth, introducing greater forces than were already being applied to the buoyant section (Figure 8.14).

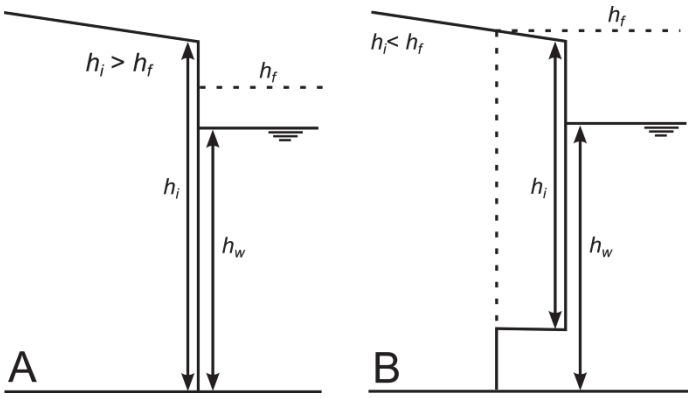

Figure 8.14: Diagram showing the effect that losing a section of the subaqueous ice cliff can have on the flotation thickness of the glacier. (A) Ice thickness (h_i) exceeds flotation thickness (h_f) resulting in stability of the terminus. (B) Ice thickness at the terminus is below flotation thickness due loss of the subaqueous section of the ice cliff, leading to flotation and retreat until h_i equals h_f.

A combination of these two processes resulted in the high–magnitude buoyancy–driven calving events recorded in January and April 2012 and February 2013. In the January 2012 and February 2013 events large sections of the terminus had become susceptible to buoyant forces, with subaqueous calving events in both cases providing the catalyst for initiating rapid uplift and resulting in buoyancy–driven calving events. In particular, prior to the calving event in February 2013 the entire lower 500 m of the terminus was freely fluctuating vertically in response to rainfall within the catchment (H. Horgan, *pers. comm.*, 2013), highlighting that at that point in time (at least) Tasman Glacier was near the point of flotation across the entire lower terminus. As no significant rainfall fell within the Tasman Glacier catchment prior to the calving event (Figure 8.13), limiting perturbations in the level of Tasman Lake, the sudden loss of lateral support or decrease in ice cliff height was enough to destabilise the entire lower terminus to a point where the rapid onset of terminus uplift was sufficient to result in the large buoyancy–driven calving.

8.5.2 Buoyancy–driven calving and lake level fluctuations

Studies of buoyancy–driven calving at temperate–tidewater and freshwater calving margins (e.g., Meier and Post, 1987; van der Veen, 1996; O'Neel et al., 2003; O'Neel et al., 2005) have highlighted the importance of perturbations in water level on buoyancy–driven calving. As is the case at Tasman Glacier, perturbations at freshwater–terminating glaciers are caused by increased meltwater discharge or high rainfall events. Slow perturbations at freshwater calving margins may allow for viscoelastic deformation rather than calving failure (Boyce et al., 2007). However, if upward bending forces in the terminal zone are not accommodated, then tensile stresses at the base of the glacier lead to the development of bottom crevasses (e.g., van der

Veen, 1998a), resulting in the calving of large sections of the glacier at the point of failure (e.g., Warren et al., 2001).

Runoff through the glacial system and perturbations in lake level associated with rainfall are considered to provide a trigger for high magnitude – buoyancy–driven calving events at Tasman Glacier by rapidly (relative to the length of time of flotation) increasing torque at the terminus. To compare lake level fluctuations and the timing of calving events the 22 August and 19 December 2010 calving events are marked on Figure 8.3 and Figure 8.5 for reference. The larger of the two calving events (on 22 August) occurred following gradual increase in lake level due to precipitation in the preceding days. In contrast, the 19 December calving event occurred during a rapid increase in lake level associated with a single high rainfall event.

Prior to calving on 22 August 2010 the Tasman Glacier terminus had uplifted significantly (Figure 8.1) over an extended period of time, being subjected to several fluctuations in lake level and the loss of the eastern margin of the uplifted section two days prior to calving. The cycles of increased water–level would have successively damaged the ice at the hinge point, lowering the tensile strength of ice at the point of failure. These factors had driven the glacier to a point where calving was inevitable, as buoyant forces increased basal tensile stresses. The 0.4 m rise in lake level prior to the 22 August 2010 calving further destabilised the uplifted terminus, leading to the propagation of crevasses and the eventual failure of the entire section. One possible sequence of events is that perturbations in lake level initiated buoyancy–driven calving as lake level dropped, causing the forward rotation of the buoyant section of terminus and increasing tensile stress at the glacier surface (Figure 8.15). Propagation of surface crevasses then occurred in order to accommodate the increase in tensile stress, destabilising the buoyant section. Calving of the buoyant section of the terminus was then initiated along the hinge line as the crevasse propagated to greater depths, potentially aided by the presence of water in the formed crevasses by melt associated with melting snow (Benn et al., 2007a; Mottram and Benn, 2009).

Calving on the 19 December 2010 was preceded by uplift of the terminus, although not to the same extent as the 22 August event (D. Callesen, *pers. comm.*, 2010). Figure 8.5 shows that at the time of calving Tasman Lake level had increased rapidly by 2 m, initiating calving of the already unstable section of the terminus. At this point torque arising from buoyant forces likely caused an upward bending moment (Warren et al., 2001), increasing bottom crevasse propagation at the hinge point. At the time of calving the uplifted section of the terminus could no longer support this bending moment, resulting in the bottom–up calving of the buoyant section of the terminus (Figure 8.15).

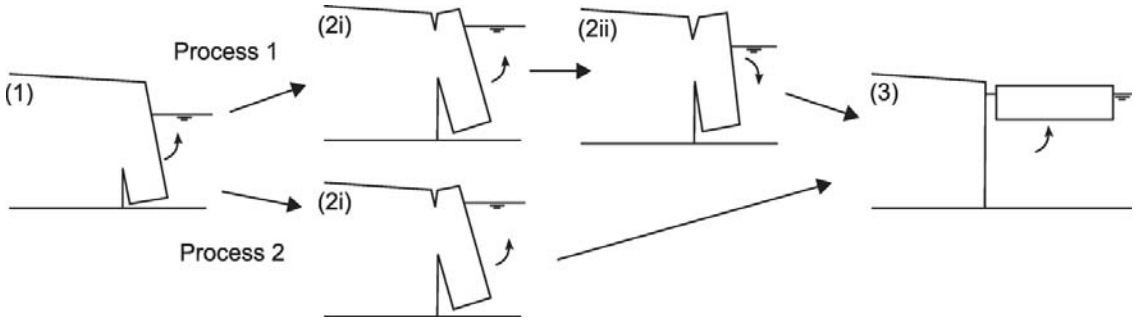

Figure 8.15: Schematic diagram of the processes of buoyancy driven calving for the two described calving events at Tasman Glacier on 22 August (Process 1) and 19 December 2012 (Process 2). In both cases the glacier is subjected to upward buoyant forces (1). Process 1 follows the description of the 22 August calving event where several fluctuations in lake level (2i) damaged the ice at the hinge point until calving was initiated as lake level decreased (2ii). Process 2 describes the 19 December calving event where an increase in (2i) lake level lead to calving (3) due to upward buoyant forces.

Boyce et al. (2007) has also suggested that perturbations in lake–level can initiate calving in their study of Mendenhall Glacier, Alaska, where flotation (initiated by long–term mass wastage) of a section of the glacier was sustained over a two year period by ice creep and lateral support of grounded ice near bedrock margins. Calving of this uplifted section of the terminus occurred in a series of discrete events predominantly associated with a 0.3 m increase in lake level. This is a similar pattern of calving to that at Tasman Glacier, where in the months prior to the 22 August and 19 December calving events, flotation of the terminus occurred in response to downwasting and increased water depth, with calving failure occurring due to lake level perturbations.

The incidence and style of these calving events indicate that perturbations in lake level played an integral component in calving in both instances, highlighting the potential importance of rapid changes in lake level as a trigger of buoyancy–driven calving at an already unstable terminus. However, as the description of the 22 August event indicates, there is not always a direct link between rainfall, fluctuations in lake level, and buoyancy–driven calving, with loss of basal support another potential mechanism through which instability can be introduced into the system.

8.5.3 Coseismic triggering of buoyancy–driven calving events

From analysis of timed video and photo records of the glacier front immediately before, during and after calving on 22 February 2011, it is possible that the Christchurch earthquake (and associated aftershocks) may have initiated instability at Tasman Glacier, leading to the observed buoyancy–driven calving event. Given the available data it is clear that calving on 22 February

did not coincide with the largest s–wave arrival associated with the M_L 6.3 earthquake, but instead the M_L 4.5 aftershock. Based on this observation there are two possible explanations for the temporal proximity of calving to the Christchurch earthquake: (1) the terminus of Tasman Glacier was preconditioned to calving so that the timing of calving with the earthquake aftershocks was coincidental; (2) given the instability of the terminus, s–wave arrival may have activated a pre–existing plane of weakness (crevasse), initiating failure from the free surface of the glacier as the crevasse penetrated the entire glacier thickness.

In order to induce large–scale failure of the frontal part of Tasman glacier in response to an earthquake, an initial crack needs to open in the glacial body and propagate through its entire vertical extent. In the case of a water–terminating glacier two main forces act at any element of glacial ice and affect the maximum critical stress: (1) cryostatic (compressive) forces steadily increase downwards due to the ice weight, while (2) buoyant forces are compressive in the upper half of the glacier and tensile (increasing downwards) below the mid–point due to the buoyant moment of the glacier by the pro–glacial water body (Warren et al., 2001). Warren et al. (2001) considered ice–failing mechanisms in this scenario and argued that initial brittle failure will occur at the base of the glacier, and due to the upwards decrease in maximum tensile stress would propagate catastrophically upwards. If this were the case at Tasman Glacier, catastrophic failure should have occurred during or immediately after arrival of the 6.3 M_L s–wave. It is unclear whether the model assumptions by Warren et al. (2001) are applicable to this situation, or whether (after an initial fracture formation at the base) hydraulic fracturing becomes the dominant mechanism of fracture propagation. In this latter case cryostatic forces (and not only tensile forces; i.e. buoyant bending at glacier base and extension during s–wave propagation) would aid fracturing by transferring compressive force onto water filling the crack and largely increasing fluid pressure at the fracture tip.

There is also an independent line of evidence that calving in response to the 22 February earthquakes may have occurred due to hydraulic fracturing from the free glacier surface downwards. A series of time–stamped photographs of the fracture lineament depicts at least two supra–glacial ponds in close proximity (< 50 m, Figure 8.7) to the later–formed fracture. In between s–wave arrival of the 5.7 M_w and 4.5 M_w earthquakes at Tasman the water level in the ponds decreased visibly. This observation would support the scenario of hydraulic fracturing from top to base with the pond water acting as the hydraulic fluid. A simple model of hydraulic fracture propagation during the high–amplitude phase of all three s–wave phases at Tasman indicates that crack propagation could exceed the local glacier depth of c. 280 m during the third (4.5 M_L) earthquake arrival (Figure 8.16). Crack propagation is modeled after Nye (1957) for an initial dry fracturing during the 6.3 M_L earthquake using Equation (2.1). Strain rate (ε) was

taken as the ratio of s–wave ground velocity and s–wave ground deformation in N–direction at Fox Glacier (FOZ Geonet seismic station). For the 5.7 M_L and 4.5 M_L earthquakes the initially formed fracture is assumed to be completely water–filled leading to ongoing hydraulic fracturing defined by Equation (2.2) (Benn et al., 2007a), where d_w was assumed to be the pre–existing water–filled crack length. Figure 8.16 shows the progressive growth of an initial fracture created during the first earthquake and the final failure during the high–amplitude phase of s–wave propagation of the 4.5 M_w earthquake at Tasman.

From this analysis initial fracturing of ice due to the arrival of the first earthquake initiated fracture propagation from either the base or top of the glacier, with subsequent earthquakes (coupled with hydraulic fracturing) enhancing crack propagation leading to calving failure. However, two other factors contributed to the instability of the terminus of Tasman Glacier: thinning of the glacier causing decreased ice overburden pressure, and perturbations in water level increasing buoyancy induced torque on the terminus (Warren et al., 2001; Boyce et al., 2007). As a result, a clear relationship between earthquake arrival and calving at Tasman Glacier is not possible with the given analysis. However, the analysis presented here does illustrate that in tectonically active areas earthquakes may have an effect on glacier stability, with coseismic–initiated calving having a periodic effect on glacier retreat.

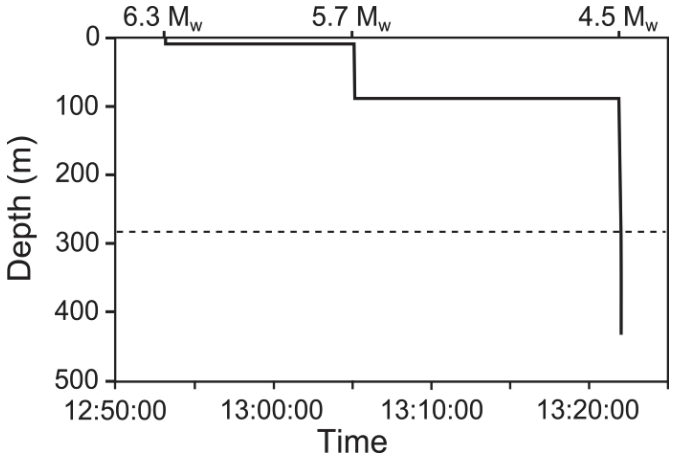

Figure 8.16: Vertical depth of crack propagation described in the scenario of fracture propagation from the surface of the glacier during the three earthquakes. Dotted line indicates glacier thickness.

8.5.4 Flotation and buoyancy–driven calving at freshwater and tidewater glaciers

Buoyancy–driven calving from grounded and floating termini alike, represent some of the largest calving events due to large scale of buoyant forces at glacier–water termini interfaces. At all water–terminating calving margins the controls on flotation and buoyancy–driven calving appear to be similar (Benn et al., 2007b), with variations in ice supply, terminus thinning, basin

morphology and perturbations in proglacial water body levels affecting the timing and duration of flotation and the magnitude and frequency of calving events. However, the degree to which these processes induce buoyant forces at freshwater and tidewater glaciers do differ, resulting in contrasting rates of ice loss due to calving (e.g., Funk and Rothlisberger, 1989; Motyka et al., 2003b; Warren and Kirkbride, 2003; Haresign and Warren, 2005; Benn et al., 2007b; Trüssel et al., 2013). As discussed in section 4.4.2, this is manifested in the duration of flotation observed at freshwater and tidewater glaciers alike (Boyce et al., 2007; Motyka et al., 2011; Trüssel et al., 2013). The cause for this difference remain unknown (Benn et al., 2007b; Trüssel et al., 2013), but the key variables are the contrasting density differences between fresh– and saltwater, resulting in variable buoyant forces as well as subaqueous melt rates, and the frequency in perturbations of proglacial water–level and basin morphology.

However, given the observations and descriptions of buoyancy driven calving events at freshwater and tidewater glaciers, once initiated the evolution of such calving events is similar. For example, high magnitude calving events recorded at the termini of Jakobshavn Isbræ (e.g., Amundson et al., 2008) had the same characteristic bottom–out rotation of large full–thickness calving as observed for the February 2011 calving event at Tasman Glacier. Modelling of the hydrodynamics of such large buoyancy–driven calving events by Amundson et al. (2012) indicates that this type of bottom–out calving is preferential in all events, as a void created during the detachment is more easily filled from underneath rather than from the sides (as would be required in the top out calving events). Buoyancy–driven calving events are also associated with the development of bottom crevasses (e.g., van der Veen, 1998a), meaning that the void in which water would enter is often present prior to calving, likely causing greater buoyant forces at the base of the ice cliff compared to higher in the ice column, where buoyant forces are reduced and are counteracted by cryostatic forces (Warren et al., 2001). The result of these observations is that the forces acting on tidewater and freshwater glaciers are the same and result in similar styles and evolutions of buoyancy–driven calving events, but that the timing and duration of flotation and events is controlled by the contrasting environments that each calving margin is situated in.

8.6 Conclusions

The flotation and uplift of water–terminating calving margins due to buoyant forces, which result from density differences between cryostatic and hydrostatic forces, plays an important role in the stability and retreat of glaciers by initiating high magnitude buoyancy–driven calving events. The triggering of buoyancy–driven calving is inherently related to the processes that initiate uplift (such as terminus geometry and subaqueous melt rates), but is also related to

external variables (such as perturbations in proglacial water–level and near field earthquakes). At Tasman Glacier the importance of buoyancy–driven calving on glacier retreat has increased post–2007. The result of this has been an increase in ice loss via high–magnitude buoyancy–driven calving events triggered by subaqueous calving, perturbations in proglacial water level, or near–field earthquakes. Previous studies at other calving margins have shown that perturbations in proglacial water level can trigger buoyancy–driven calving events, similar to events at Tasman Glacier. The loss of the subaqueous section, on the other hand, has only been identified as a longer term driver of flotation via subaqueous melt, rather than subaqueous calving triggering high–magnitude buoyancy–driven calving events. In contrast, this study represents the first description of a potentially coseismically triggered high–magnitude buoyancy–driven calving event. However, more research is needed to fully understand whether forces associated with the Christchurch earthquake represent a realistic explanation for the timing of calving.

As a result, the six examples presented in this chapter highlight the potential for multiple external and internal variables to trigger buoyancy–driven calving events at Tasman Glacier as well as at calving margins globally. However, a larger number of high–resolution datasets of buoyancy–driven calving events are needed so that not only can the forces involved during flotation and uplift of termini be better understood, but also how different potential triggering mechanisms initiate calving. In particular, continued focus on understanding the processes and rates of fracture propagation, in response to the parameters causing buoyancy–driven calving events, is needed so that, for example, the lag–time between flotation and impending calving events can be better understood.

Chapter 9: Synthesis

9.1 Introduction

The effect of calving and calving processes on the terminus of Tasman Glacier has been described and discussed at multi–annular (chapter 4), sub–annular (chapter 5 and 6), and intra–event (chapters 7 and 8) time–scales. Within each chapter a discussion regarding the five main objectives presented in section 1.2 has been introduced and elaborated on. Those chapters have quantified the extent of Tasman Glacier's retreat. The pattern of retreat since 2000 has also been compared to previous phases of retreat (chapter 4), and it was shown how variations of calving at a sub–annual (chapter 5 and 6) and intra–event (chapter 7 and 8) time–scales can contribute to large–scale retreat. This chapter draws on the results and discussions presented in previous chapters to provide a synthesis of processes affecting calving at Tasman Glacier and the consequences that this has had on contemporary and future retreat. Mechanisms that have controlled ice loss from the terminus are discussed in relation to their overall impact on iceberg calving and glacier retreat rates.

9.2 Conceptual model of calving at Tasman Glacier, 2000–2013

A schematic diagram of processes contributing to calving retreat of Tasman Glacier is presented in Figure 9.1. The evolution of the Tasman Glacier terminus between 2000 and 2013 is indicated by numbers 1 to 3 to highlight the changes in key variables over time. In general, the model diagram elucidates a hierarchy of processes on how calving drives glacier retreat. Firstly, glacier flow controlled the long–term dynamics of the terminus by limiting mass flux at the terminus, leading to stagnation and downwasting. Glacier flow has also remained an important factor post–2007 terminus disintegration, via the distribution of crevasses formed by parabolic and extensional ice flow at the terminus. Second order processes that operate on the terminus are related to glacier melt associated with the proglacial water–body, and buoyant forces as the terminus has approached flotation. The dynamic response of the glacier to these forcings is in close agreement with observations of calving margins globally (Benn et al., 2007b). The following sections outline how the terminus of Tasman Glacier has responded to this hierarchy of processes throughout the documented retreat, including potential dynamics and terminus geometry.

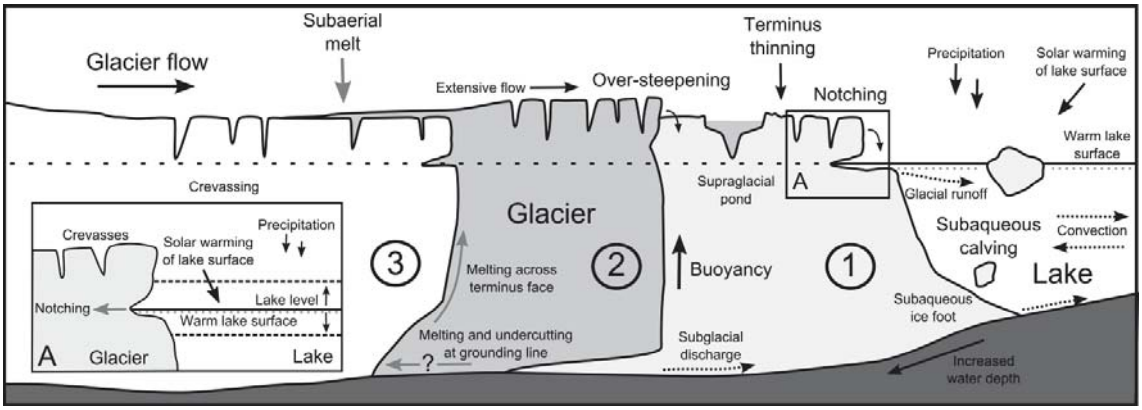

Figure 9.1: Schematic diagram of processes and mechanisms of calving that have contributed to the retreat of Tasman Glacier. Black arrows indicate external inputs into the terminus, with grey arrows indicating melt processes and dotted arrows showing water movement. Numbers 1–3 refer to three potential states Tasman Glacier has been in during retreat between 2000 and 2013. Inset (A) provides greater detail on long term controls of notch–driven calving. Note calving processes (e.g., over–steepening and notch–driven calving) can occur at any time and location along the ice cliff and are not necessarily associated with the hypothesised states.

9.2.1 Terminus dynamics and calving pre–2006

Prior to the disintegration of the lower terminus (pre–2006), conditions at the glacier terminus are indicated by (1) in Figure 9.1. In this configuration, glacier thickness exceeded flotation thickness with limited glacier flow, in combination with glacier melt, being the primary control on mass loss by driving the terminus into disequilibrium through melt beneath debris–cover and ponding of meltwater, as well as affecting calving processes. The limited development of crevasses within the terminus zone pre–2006 gave rise to retreat controlled primarily through over–steepening and notch–driven calving, coupled with subaerial and subaqueous melt. Throughout this phase of retreat at Tasman Glacier, the timing and extent of calving events from the subaerial ice cliff would have been a product of melt at the waterline, and processes that both enhance and suppress waterline melt. Long–term trends in notch–driven calving rates (and calving rates as a whole) presented in chapters 5 and 6 indicate that on a seasonal time–scales notch–driven calving rates (and by extension notch development rates) would have been controlled by changes in lake temperature, with fluctuations in lake level suppressing calving frequencies along the entire terminus length. As a result, glacier flow is considered to be the first order–control on mass loss and calving by providing the preconditions with which waterline melt and notch–driven calving could control retreat over both long–term (inter–annual) and short–term (annual–daily) time–scales. Pre–2006 a subaqueous ice foot was present along sections of the terminus at various points in time, formed due to the retreat of the subaerial ice cliff (e.g., Kirkbride and Warren, 1999; Röhl, 2005; Dykes et al., 2011; Robertson et al., 2012). Furthermore, over longer time–scales decreased glacier flow (in response to long–

term decreased ice supply, coupled with the presence of extensive debris–cover) had a first order control on driving the terminus to a point where disintegration was inevitable.

9.2.2 Present terminus dynamics and calving processes

Continued downwasting of the terminus resulted in the expansion of supraglacial ponds, while increases in water–depth as the glacier receded into deeper water have altered terminus dynamics. This has caused an increase in buoyant forces leading to a transition in dominant calving processes to high–magnitude, low–frequency buoyancy–driven events. This transition is represented by position 2 in Figure 9.1, where buoyant forces acting on the ice margin are shown to increase.

During this phase of retreat, notching and over–steepening events continued, although their contribution to total mass loss was not as significant as at position 1. Glacier flow and the presence of crevasses at the terminus have also provided an important control on calving throughout the observation period as ice velocities have increased through a combination of (1) ice velocity naturally increasing up–glacier and (2) an increase in water–depths adjacent to the terminus. Extensive flow and lateral spreading associated with the unsupported nature of large sections of the glacier are also present at the terminus and have affected the local stress field. This is evident from the distribution of crevasses at the terminus throughout retreat, and particularly over the October 2011 to November 2012 period (Figure 5.41). Crevasses throughout the terminus zone have in part controlled the distribution of calving events by providing loci for calving failure, and also isolating sections of the glacier by cross–cutting fractures and removing lateral support. However, over seasonal time–scales the distribution is still controlled by seasonal warming in the proglacial water–body enhancing waterline melt, moderated over short time–scales by fluctuations in lake level (inset A in Figure 9.1). The contribution of waterline melt and notch–driven calving on the overall volume lost and retreat during this phase is not as significant as pre–2006.

A secondary effect of glacier flow post–2007 has been the extensional flow at the terminus causing thinning of the glacier. In combination with changes in the basin morphology, increasing water–depth has caused the glacier to approach a stage of partial flotation. These processes have contributed to decreasing the stability of the terminus by increasing torque applied to the terminus via upward buoyant forces. For example, the glacier is retreating down a reverse topographic slope into deeper waters (Figure 4.7A), increasing bending forces applied to the terminus by altering the conditions present in Equation (2.3). Together with the continued downwasting, extensional flow of the terminus and the loss of support from the adjacent

sections of the ice cliff, increasing buoyant forces and leading to the increased fracturing of ice (e.g., section 5.5.2.3). Therefore, the terminus has become more susceptible to flotation, resulting in an increase in the frequency and size of high–magnitude buoyancy–driven calving events. At a floating terminus (as depicted in position 2) large buoyancy–driven calving is triggered either through the loss of a subaqueous portion of the ice cliff, perturbations in lake level, or near–field earthquakes (chapter 8). As a result, high–magnitude calving events, initiated by increased buoyant force, constituted the largest contribution to net loss via calving between 2007 and the present (e.g., Figure 5.26).

The result of increased full–thickness buoyancy–driven calving events during the present retreat phase has also caused a change in the morphology of the subaqueous ice cliff. Figure 9.2 shows a large iceberg that calved in February 2011, with evidence of subaqueous melt indicated by the vertical flutes that have formed along the vertical ice cliff. Interestingly, only a small ice 'foot' is evident in Figure 9.2 (c.f. Robertson et al., 2012). Similar features were observed on several large icebergs that calved during the study period. This suggests that in its present state, subaqueous melt and full–thickness buoyancy–driven calving events may be altering the dynamics of the terminus in a way not yet observed throughout the history of research at Tasman Glacier.

Position 3 (Figure 9.1), represents the situation described above, that may now be present (as of 2013). A cavity at the base of the ice cliff may have formed through the exposure of the subglacial section of the terminus through uplift resulting from buoyant forces. This subglacial cavity may be enhancing basal melt rates through increased circulation of meltwater entering Tasman Lake. Cavity development increases buoyant forces at the terminus by decreasing the effective ice cliff height (Figure 8.14). The formation and development of a cavity at the base of Tasman Glacier has not been documented in previous studies of subaqueous morphology (e.g., Robertson et al., 2012). However, since such surveys were carried, out the importance of terminus uplift and buoyancy–driven calving has increased. The morphology of the subaqueous portion of the ice cliff may be in a configuration that promotes cavity development and expansion as the terminus has disconnected from the glacier bed as it approached and exceeded flotation post–2007. The development of a subaqueous cavity has been observed at other freshwater glaciers (e.g., Yakutat Glacier ; Trüssel et al. (2013)) affecting terminus stability and retreat rates. Although this is a feasible state for Tasman Glacier to currently be in (e.g., Trüssel et al., 2013), Tasman Glacier could equally be in a state similar to position 2 in Figure 9.1.

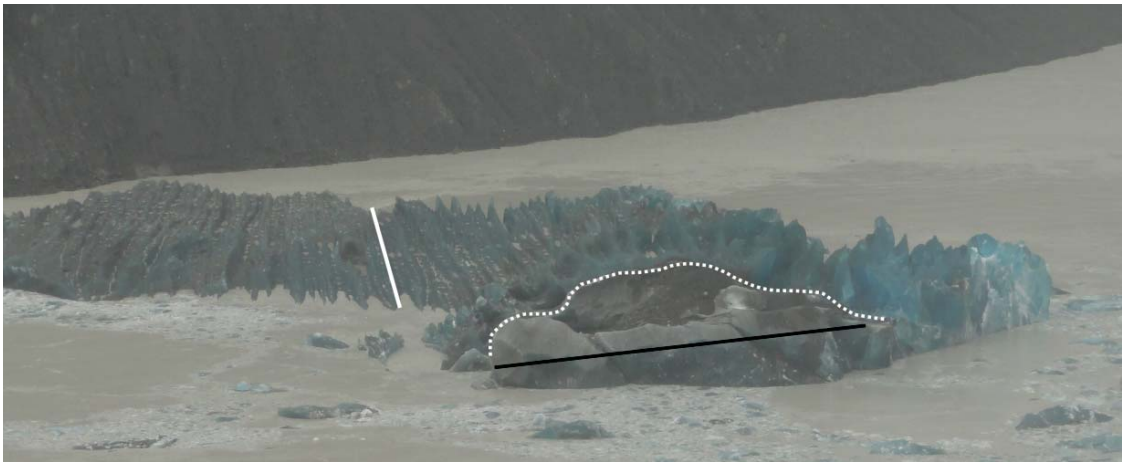

Figure 9.2: Photo showing vertical notches that have formed on a large iceberg that calved from the terminus of Tasman Glacier on 22 February 2011. Black line indicates the original orientation of the iceberg running east to west along the terminus of Tasman Glacier. Dotted white line indicates the waterline along the former subaerial ice cliff, with the white line highlighting the perpendicular orientation of notches extensively formed along the ice cliff. Solid black line is approximately 250 m in length.

9.3 Future response of Tasman Glacier

An important outcome of the analysis of the temporal and spatial patterns of the calving retreat of Tasman Glacier is the ability to better understand and predict future glacier dynamics, be it continued retreat, stability or advance. This is crucial if glacier response to current trends in climate warming can be included in predictions of future SLR (Benn et al., 2007b). However, as is evident in the results presented throughout this study, accounting for and quantifying glacier response to internal and external variables is difficult during accelerated calving retreat. This is echoed by the fact that no current theoretical model of retreat for freshwater–terminating glaciers satisfactorily explains the majority of field observations (e.g., Kirkbride and Warren, 1999; Dykes and Brook, 2010). As a result, empirically–based relationships have represented the primary means of forecasting glacier retreat (Kirkbride and Warren, 1999). However, due to the necessarily simplistic nature of empirically–based relationships, such scenarios have limited use in understanding and predicting retreat. For example, Kirkbride and Warren (1999) indicate that retreat based solely on notch–driven calving would result in the terminus attaining stability by *c.* AD 2200 at approximately the same location as the 2013 terminus position (Figure 9.3). A second scenario incorporating a calving rate and water–depth model resulted in the entire (*c.* 10 km) lower glacier being lost by the year 2008. Similar, updated, results have been replicated by Dykes and Brook (2010).

As shown by prediction of the retreat if Tasman Glacier presented by both Kirkbride and Warren (1999) and Dykes and Brook (2010), the use of simple empirical and mechanistic

relationships to predict the future retreat of Tasman Glacier does not provide satisfactory results over long–term time–scales.

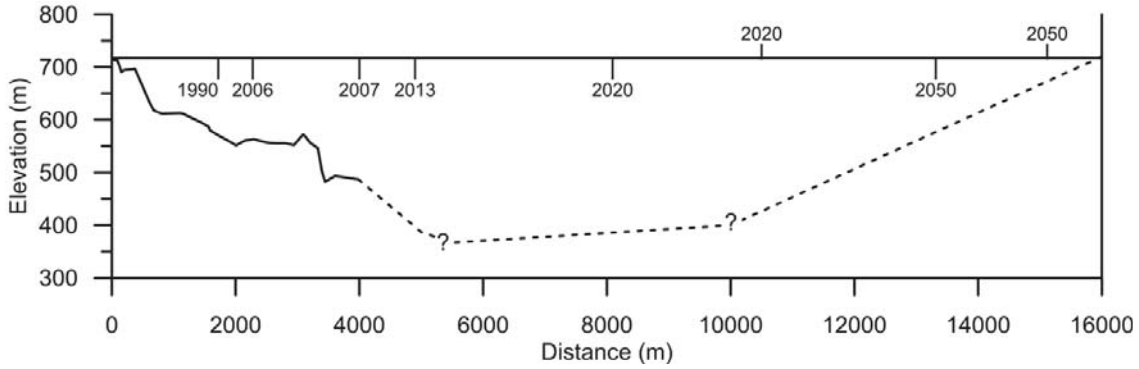

Figure 9.3: Long profile of Tasman Lake along the former centre line of Tasman Glacier from the southern margin moraine dam, with terminus positions derived from satellite imagery. Terminus positions throughout the observed retreat and predicted retreat are shown to indicate the potential rate of glacier retreat. Dates past 2013 below the level of Tasman Lake are based on linear regression equation for post 2007 shown in Figure 4.5. Terminus positions dates above the lake level are based on the power–law regression post 2007 shown in Figure 4.5.

The future response of Tasman Glacier is controlled primarily by a combination of mass flux and bed topography. This is because the terminus will stabilise at a point where either mass flux into and out of the terminus zone equilibrate (i.e. Equation (2.3)), or changes in bed topography result in the glacier receding out of Tasman Lake. Other processes will also contribute to terminus stability, but mass flux and bed topography represent the key parameters that control long term terminus stability. This is indicated by their importance in driving the terminus to transition from melt–controlled to calving–controlled retreat, and the disintegration of the terminus in early 2007.

The continued recession of the glacier through an over–deepened basin has a major impact on the future response of the entire glacier system by potentially leading to the shoaling of the terminus as the valley's bedrock profile eventually intercepts lake level. At this threshold, flotation of the glacier becomes less important, with longitudinal velocity gradients and waterline melt controlling calving (Benn et al., 2007b). Limited bed topography measurements exist for the Tasman Glacier, although interpolation between known glacier thicknesses (Broadbent, 1973; Watson, 1995) indicate that the bed of the glacier will intercept lake level *c.* 15 km up–glacier from the LIA frontal moraines (Kirkbride and Warren, 1999; Dykes and Brook, 2010). This would place the stable terminus just south of the Tasman–Rudolf confluence, indicating that the glacier has the potential to retreat a significant distance from its 2013 position (Figure 9.3) before retreat slows. However, given the current climatic regime this is unlikely to occur, as current ice velocities (Redpath, 2011), and therefore mass flux and

calving rates, are likely to equilibrate in the vicinity of Ball Glacier (Figure 9.4). This does not take into account any future changes in accumulation rates due to continued climatic warming (Herman et al., 2011). As mass flux at the terminus would decrease, retreat of the glacier would continue until it again equilibrates at an unknown point up–glacier. The response of the terminus of Tasman Glacier to such changes in accumulation has historically been considered to be limited, due to the length of Tasman Glacier and the resulting long response time of the glacier as a whole (e.g., Chinn, 1996; Chinn et al., 2012). However, Redpath (2011) has suggested that velocities across the entire glacier surface can fluctuate at up to an annual time–scale. With the position of the Tasman Glacier terminus located at a point where mass flux into and out of the lower glacier is equivalent, a change in velocity up–glacier of the calving terminus could destabilise the lower glacier to the point where retreat is again initiated.

Based on the known bed topography, the likelihood of the terminus equilibrating at any point near Ball Glacier is not high as water depth at this location would still be *c.* 350 m (Figure 9.3). Flotation and buoyancy–driven calving would continue to be a rate controlling process, causing further up–glacier retreat. This is because thinning of the glacier due to continued downwasting and increased extensional flow at the terminus would result in the glacier being at or below the critical flotation thickness, enhancing buoyancy–driven calving and retreat.

Processes other than mass flux and basin morphology will continue to contribute to the retreat of Tasman Glacier, either directly or indirectly. Such mechanisms include: the further development of supraglacial ponds on the lower terminus, affecting buoyancy; the ‘drawdown’ effect of increased calving rate (Kirkbride and Warren, 1999) increasing longitudinal strain (Benn et al., 2007b); and the impact of the increase in the number of crevasses near the terminus (Benn et al., 2007b) as the glacier retreats up–valley nearer the steep, highly crevassed Hochstetter Icefall.

Although no supraglacial ponds were evident in the terminus region in 2013, downwasting and the pooling of meltwater continues to be present further up–glacier. For example, decreases in ice velocities above the Tasman Glacier–Hochstetter icefall confluence (Figure 9.4) reported by Redpath (2011), have given rise to the development of several supraglacial ponds in this zone. If the supraglacial ponds above the Tasman–Hochstetter confluence expand (Röhl, 2008) due to prolonged low velocities, a secondary lake could potentially form in a similar way to the stages described for the original development of Tasman Lake (Figure 4.15). The corollary is that if this does occur, then disintegration of the entire lower glacier could proceed as it would become isolated in terms of ice input, only being fed by ice from the Hochstetter icefall. Although a

worst case scenario, this does provide evidence for the complex interplay of processes that may contribute to the retreat of Tasman Glacier in the near future.

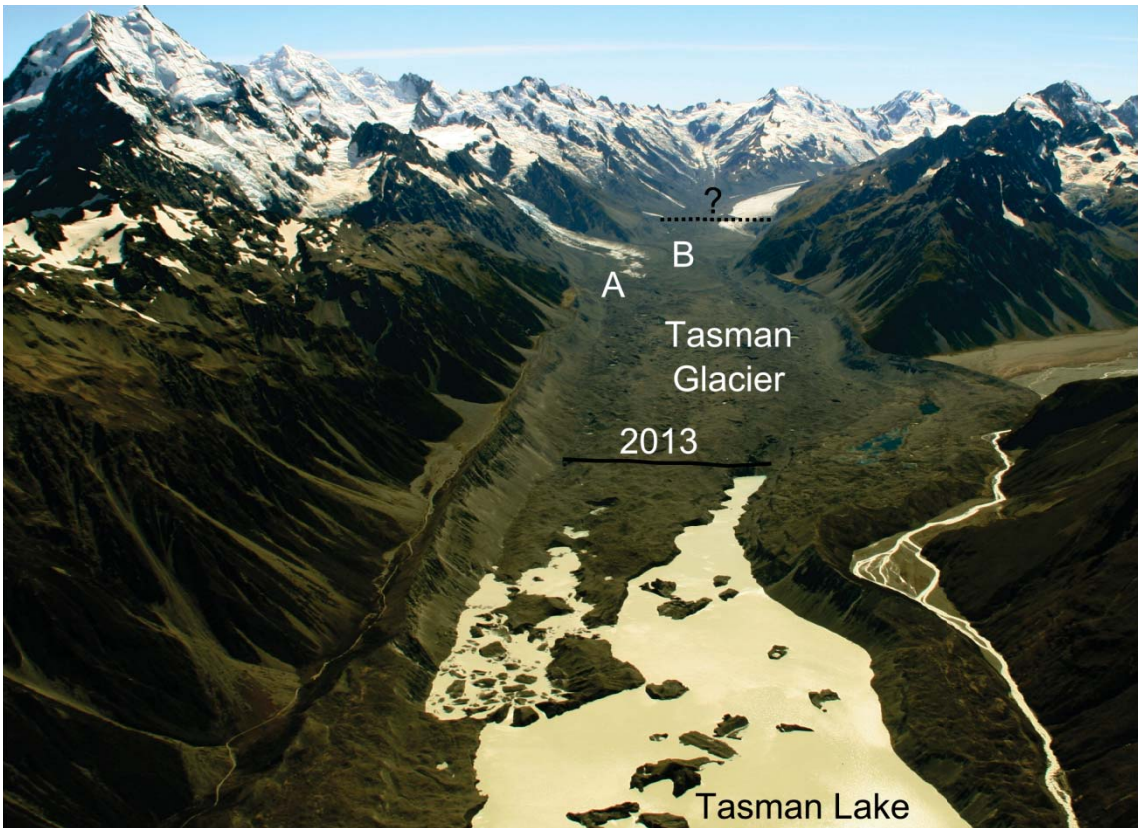

Figure 9.4: Photograph of Tasman Glacier and Tasman Lake in February 2007 showing the approximate location of the 2013 terminus position and the potential terminus position where basin topography intercepts current lake level. The position of the confluences of Ball Glacier (A) and the Hochstetter ice fall (B) with Tasman Glacier are also shown. (Source: S. Winkler, 2007).

The timing with which the processes described in this section will affect Tasman Glacier is unknown. Based on current rates of retreat post–2006 (138 m a^{-1}; Table 4.1), the glacier may retreat to the point where basin topography intercepts the current lake level (*c.* 10 km from the current terminus position) within 80 years (Figure 9.3). However, if conditions are favourable (i.e. increased water–depth and terminus flotation), retreat of the terminus to this upper limit of lake development may occur in less than 50 years. For example, if the current rates of accelerated lake expansion identified in Figure 4.5 continue, the terminus of the glacier will retreat to a point where it would exit the lake around 2050 (Figure 9.3). Equally, Tasman Glacier may stabilise at an unknown point. More research is needed to better constrain factors affecting Tasman Glacier (such as bed topography) so that a fully quantitative predictive model can be generated and applied.

9.4 Comparison of calving at Tasman Glacier with calving margins globally

9.4.1 Comparison of the evolution of Tasman Glacier with debris–covered glaciers globally

The development and evolution of a proglacial lake at the termini of debris–covered–glaciers has affected the dynamics and retreat of glaciers within the *Aoraki*/Mount Cook National Park, as well as other regions of the world (e.g., the Himalayas). The transition from solely melt under debris–cover to calving–dominated ablation regimes has been identified as an important stage in conditioning the rapid retreat at Tasman Glacier. In particular, the development and expansion of supraglacial ponds and the development of a transverse ice cliff have controlled not only the initial development of Tasman Lake, but also the continued retreat through triggering disintegration of the lower terminus in early 2007.

Tasman Glacier follows a consistently similar pattern of processes of lake development and expansion has been repeatedly described for other debris–covered glaciers throughout the *Aoraki*/Mount Cook National Park (Robertson, 2012). However, when compared to similar debris–covered glaciers located within the Himalayas (e.g., Komori, 2008; Thompson et al., 2012), the timing and extent to which proglacial lake development has affected Tasman Glacier is significantly greater (Figure 9.5). In particular, the timing of rapid lake expansion at Tasman Glacier in the early 1990s is greatly delayed in comparison to similar Himalayan glaciers, which all entered into a phase of lake expansion throughout the 1960s. However, once all of the Himalayan lakes entered a phase of lake expansion the percentage of lake growth accelerated at a similar rate, albeit slightly slower than observed at Tasman Glacier and the other *Aoraki*/Mount Cook National Park glaciers (Figure 4.14).

The primary difference between *Aoraki*/Mount Cook National Park and the Himalayan debris–covered glaciers is the rapid nature of the transition from solely melt–dominated ablation regimes through to calving–dominated retreat observed at Tasman Glacier. Within the Himalayas, Komori (2008) notes that debris–covered glaciers in the Bhutan Himalaya advanced through stages of lake development similar to those described in Figure 4.15 over a period of at least a 40 years. This extended transition has also been found in other areas of the Himalayas (e.g., Sakai, 2012; Thompson et al., 2012). However, New Zealand debris–covered glaciers have advanced through stages 1 to 3 over a period of between 8 to 30 years (Robertson, 2012), with several glaciers (especially Tasman Glacier) accelerating rapidly.

It can be concluded that the processes operating at Tasman Glacier are globally representative, but that Tasman Glacier has progressed through the stages of proglacial lake development and glacier retreat more rapidly than observed elsewhere globally. This may be due in part to the size of Tasman Glacier and the extent to which water–depth and other factors that control calving rates are able to be applied to the terminus. For example, water–depth at the terminus of Tasman Glacier exceeds *c.* 300 m, compared to the relatively shallower lakes for other debris–covered glaciers in the *Aoraki*/Mount Cook National Park and the Himalayas. This has meant that an extended period of flotation and buoyancy–driven calving has been able to dominate calving rates at Tasman Glacier. In comparison calving processes at other debris–covered glaciers are typically confined to low–magnitude, high–frequency calving and ice melt (e.g., Benn et al., 2012; Sakai, 2012; Robertson et al., 2013).

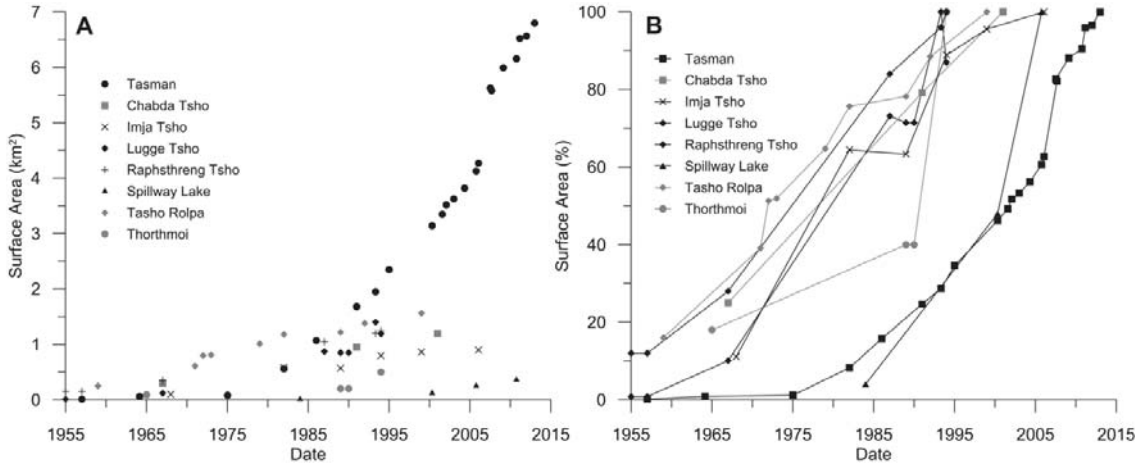

Figure 9.5: Comparison between the growth of Tasman Lake and proglacial lakes in the Himalaya throughout the 20th century (lake areas from Thompson et al. (2012), after Komori et al. (2008); Sakai et al. (2009b)).

Nevertheless, Tasman Glacier and similar debris–covered termini within New Zealand and the Himalayas have progressed along similar evolutionary trajectories, with only the timing and extent of retreat differing. The stages of lake development and expansion identified in Figure 4.15 that have been proposed for the New Zealand debris–covered glaciers also appear to be applicable to other debris–covered glaciers globally. The difference in the timing and duration of the transition between stages within different regions is likely to be related to the more dynamic response of New Zealand glaciers compared to their higher altitude, less maritime Himalayan counterparts. In particular, variations between the two regions are associated with: differences between the continental and mid–latitude climate affecting precipitation and temperature, glacier gradients and velocities, basin morphologies, and the influence of calving on retreat (Sakai et al., 2000; Röhl, 2005; Komori, 2008; Benn et al., 2012; Robertson, 2012;

Thompson et al., 2012). Indeed, New Zealand debris–covered glaciers are more dynamic in their response compared to those of the Himalaya (Figure 9.5).

9.4.2 Comparison of calving frequencies and magnitudes

The rapid nature of retreat of Tasman Glacier observed between 2000 and 2013, and calving styles and processes can also be compared with non–debris–covered and tidewater calving margins. Given the contrasting frequencies of calving events between the relatively slow rate at Tasman Glacier and more frequent events at tidewater glaciers, the contribution of calving events on the total loss of ice from termini differs. At Tasman Glacier, low magnitude, high–frequency, calving events did not contribute largely to the total volume of ice lost, with intermittent high–magnitude (relative to the size of Tasman Glacier) calving events dominating total ice loss. A similar situation has been observed at tidewater glaciers, where high–magnitude calving events have resulted in the loss of several kilometres of the terminus in a single event (e.g., O'Neel et al., 2007) as a glacier approaches flotation. This indicates that where water–terminating glaciers are grounded (limiting the potential for large buoyancy–driven calving events) the frequency of calving events can provide a good approximation of ice loss (e.g., Amundson et al., 2008).

However, where a terminus approaches flotation the frequency of events becomes less important than individual calving events (e.g., Walter et al., 2010). Such a transition has been observed at Tasman Glacier, with retreat pre–2006 dominated by higher–frequency, low–magnitude calving events initiated by waterline melt. The importance of calving frequency has, therefore, decreased post–2007 as large sections of the glacier have been lost by buoyancy–driven calving events. Similar transitions have also been observed at tidewater glaciers in recent years (such as Columbia Glacier (Walter et al., 2010)), indicating that although the frequency of calving events between tidewater and freshwater glaciers can be explained by a variety of factors, the response of both glacier types to flotation and the importance of calving frequency on recession are similar.

Frequency differences between high–magnitude calving events at freshwater (approximately yearly; e.g., chapter 8) and tidewater calving margins (approximately monthly during spring and summer) are related to processes that lead to high–magnitude calving events (Trüssel et al., 2013). In particular, subaqueous melt rates are a key control on the contrasting rates of high–magnitude calving events. At tidewater glaciers subaqueous melt rates can exceed 1 m d^{-1} (e.g. Motyka et al., 2003a; Motyka et al., 2011), far in excess of those found at freshwater glaciers which are in the order of 4–8 m a^{-1} (e.g., Hochstein et al., 1995; Röhl, 2005). The increased

subaqueous melt enhancing glacier thinning through the development of a subglacial cavity at the base of the ice cliff (Trüssel et al., 2013), coupled with a lower effective pressure due to density differences between fresh and saline water (van der Veen, 2002), destabilises the terminus at tidewater glaciers. These processes operate over short time–scales at tidewater glaciers, with tidal flexure and extensional thinning initiating calving on a daily or weekly basis (Benn et al., 2007b). In comparison, lower melt rates and intermittent fluctuations in the level of the proglacial water–body at freshwater margins increase the time between buoyancy–induced calving events, as flexure at the point of failure does not occur as regularly as at tidewater margins (Boyce et al., 2007). This may explain why at Tasman Glacier large–buoyancy driven calving events occur at periods of many months to years, compared to the higher frequency occurrence typical of tidewater glaciers (Trüssel et al., 2013). Nevertheless, at Tasman Glacier buoyancy–driven calving events appear to occur more frequently than at other well–studied freshwater–terminating glaciers (e.g., Boyce et al., 2007). This may be due to the current state of the glacier (e.g., terminating in water depths >300 m) and the variety of triggering mechanisms present.

Chapter 10: Conclusions

10.1 Objectives revisited

The primary aim of the study was to improve understanding of calving processes at Tasman Glacier, as calving from the terminus has become an important mass loss mechanism, controlling terminus retreat. In order to do this, the temporal evolution of Tasman Glacier since the formation of proglacial Tasman Lake until the present was quantified. This was completed through observations of retreat and calving processes at inter–annual, sub–annual and intra–event time–scales. This data was used to characterise the impact and variability of calving in driving the retreat of Tasman Glacier and to highlight the interplay of glacier dynamics and external variables at a water–terminating glacier. Revisiting the aims and objectives of the study, the major research questions were:

1. What are the long–term kinematic (decadal) characteristics of glacier retreat since the initial formation of Tasman Lake, and how can they be explained?
2. How does the contemporary phase of retreat (2000–2013) of Tasman Glacier compare with previous phases of retreat and what forces current changes in ice loss behaviour?
3. What is the natural variability in magnitude, frequency and style of iceberg calving at freshwater–terminating glaciers and is there any time–dependent pattern to them?
4. What is the relative impact of high–frequency, low–magnitude and low–frequency, high–magnitude calving on the overall ice loss budget and is the occurrence of small and large calving events linked?
5. Do external parameters directly control iceberg calving and can they be used to model and forecast the probability of calving events?
6. Can seismic methods, successfully applied to calving margins at tidewater glaciers, be deployed at freshwater–terminating glaciers to reliably detect and possibly quantify the frequency, magnitude and style of iceberg calving?

In response, the main conclusions from the thesis are as follows:

- Tasman Glacier lost 3.51 km^2 of surface area throughout the 13 year study period (2000–2013), resulting in the up–glacier retreat of the terminus by 1.2 km. However, significant spatial and temporal variations in ice loss were present, controlled by changes in glacier dynamics (e.g., ice velocities) and external parameters (e.g., water

depth at the terminus) that influenced the extent to which iceberg calving contributed to mass loss.

- A significant transition in retreat rates was observed in early 2007 as the entire lower section of the terminus disintegrated in response to increased buoyant forces resulting from greater water depth at the terminus and the extensive development of supraglacial ponds. Ice loss and glacier retreat increased from *c.* 50 m a^{-1} prior to disintegration, to *c.* 138 m a^{-1} post–2007. The disintegration event was the largest loss of ice in a single event from the terminus since the formation of Tasman Lake, involving an area of 1.36 km^2. On a global scale, this event represents one of the largest observed ice losses from debris–covered, freshwater–terminating glaciers.

- Acceleration in the growth of Tasman Lake since formation has occurred at an average rate of 0.37 km^2 a^{-1}, taking place in three phases: (1) the development and expansion of supraglacial ponds between the 1950s and 1990; (2) accelerated lake expansion between 1990 and 2006 due to increased calving and glacier melt; and (3) terminus disintegration in early 2007. This has been followed by continued rapid retreat conditioned by flotation and buoyancy–driven calving. The intervals between these phases of lake expansion and retreat can be categorised into a generalised four–stage model.

- High–magnitude, low–frequency, buoyancy–driven calving events dominated retreat post–2007, accounting for over half of all volume lost via calving. This is in contrast to the low–magnitude, high–frequency, subaerial calving events initiated by waterline melt that were the primary driver of calving pre–2006. The transition to high–magnitude buoyancy–driven calving has been caused by continued thinning and retreat of Tasman Glacier into deeper waters of Tasman Lake, leaving the glacier more susceptible to buoyant forces. Triggering of buoyancy–driven calving events was via subaqueous calving, perturbations in water level and near–field earthquakes. Coseismic triggering of buoyancy–driven calving presented in this study appears unique, illustrating that in tectonically–active areas near–field earthquakes can have a periodic effect on retreat.

- At a sub–annual time–scale there is a strong seasonal trend in calving, with the frequency of events reaching a maximum during spring and summer months (December to April). Seasonal trends in calving are related to fluctuations in low–magnitude, high–frequency, thermo–erosional notch–driven and over–steepening calving events,

accounting for 93 percent of all events. Seasonal frequency of calving events closely follows annual cycles in lake temperature, with increased water temperatures resulting in increased calving events.

- The frequency of calving events is relatively insensitive to the specific location along the terminus. However, the occurrence of high–magnitude buoyancy–driven styles shows a strong spatial localisation and is concentrated in areas of deepest water depth.

- A proportional hazards Weibull renewal model was developed to quantitatively relate the calving event distribution to external parameters. This highlighted the importance of lake temperature in enhancing calving rates, suppression of calving due fluctuations in lake level, and the observation that there is no time–dependency in calving event volumes. The probability of a particular calving style changes with respect to time. There is a tendency for calving to cluster and for subsequent events to be of the same style as the preceding event.

- Passive seismic methods can be used to reliably detect calving events at Tasman Glacier and to distinguish them from non–calving events. Characteristics of the amplitude and frequency spectra of calving icequakes were used to establish an automatic STA/LTA event detector for remote calving detection. These characteristics can also be used to distinguish between subaerial (notch–driven and over–steepening) and high–magnitude, buoyancy–driven and subaqueous calving events.

- Seismic analysis revealed that the magnitude of calved icebergs can be related to the duration, maximum amplitude and energy of seismic waveforms. Of these seismic parameters, energy (integrated amplitude) provided the best relationship with calving magnitude using unfiltered seismic data, and could potentially be used as a universal proxy at research sites elsewhere.

- The automatic identification of calving events using a recursive STA/LTA event detector has the potential to become a powerful tool for identifying and quantifying calving at Tasman Glacier. Results from day and month long tests showed that the event detector was able to be correctly catalogue the majority of calving events identified in time–lapse imagery. However, it was unable to differentiate reliably between several calving and non–calving sources.

10.2 Future work

From this study several avenues for future research at Tasman Glacier and other calving margins have emerged:

- Continued monitoring of Tasman Glacier would allow a more complete understanding of the key patterns and processes of calving retreat. Continued long–term monitoring of terminus position from satellite imagery, repeat ground surveys, and terrestrial time–lapse imagery would assist. This may be coupled with the derivation of flow fields of Tasman Glacier through the use of algorithms applied to satellite imagery (e.g., Redpath et al., 2013) to better understand the evolution of the terminus response to continued monitoring of external variables (e.g., climate and lake characteristics).

- Investigations into the vertical kinematics of the Tasman Glacier terminus could be carried out to determine if it is floating or grounded and the implications for future retreat. Continuous GPS units could be placed across the lower surface to record how the terminus is responding to changes in lake level (e.g., due to rainfall events). Continuous GPS units would also allow monitoring of terminus ice velocities to calibrate and validate satellite remote sensing–measured velocities.

- Undertaking more comprehensive surveys of the bed topography (using gravity surveying or active seismics) of Tasman Glacier would better constrain current estimates of the subglacial bedrock long profile. This is of particular importance for forecasting and understanding the multi–decadal future calving retreat.

- Limnological characteristics of Tasman Lake (e.g., water–temperature, circulation, lake level) have had an effect on the retreat of Tasman Glacier, enhancing both subaqueous melt and calving rates. A combination of techniques such as temperature and pressure loggers (e.g., Robertson, 2012) or the use of conductivity–temperature–depth (CTD) casts (e.g., Bartholomaus et al., 2013) throughout Tasman Lake would create useful datasets. Limnological data could be combined with high–frequency multi–beam sonar (Turner et al., 2012) and remotely operated vehicles (e.g., Motyka, 1997) to map the subaqueous portion of the calving ice cliff and account for subaqueous ice loss rates.

- High resolution observations of retreat and calving processes across all glaciers of the *Aoraki*/Mount Cook National Park will assist in predicting future calving retreat. Bathymetric surveys (e.g., Classen, Grey/Maud, and Godley glacial lakes) should be updated and new surveys undertaken at newly–formed lakes (e.g., Murchison) to better

constrain parameters that are affecting retreat. Robertson (2012) has taken the initial steps (at Hooker and Mueller proglacial lakes) towards accomplishing this goal through proving that accurate mapping of subaqueous portions of calving termini can be achieved.

- More spatially and temporally extensive studies of calving–generated icequakes at a broad range of calving margins would be advantageous. This should include the use of seismic arrays and water–based hydrophones, coupled with high–resolution video datasets to automate the detection of calving events. Indeed, integrated seismic recording and time synchronised video (e.g., Bartholomaus et al., 2012; Welty et al., 2013) are just emerging. Specifically, developing the pseudo–energy (integrated amplitude) relationship and pseudo–energy of the onset to the point of maximum amplitude would be useful. Improving this relationship and incorporating statistical and clustering analysis into STA/LTA event detectors and frequency domain detectors will advance the automatic detection of calving events and their contribution to glacier retreat.

10.3 Concluding remarks

This study has quantified and described the retreat of Tasman Glacier and the effect that calving processes have had on this retreat. Processes that controlled calving at inter–annual, sub–annual and intra–event time–scales have also been identified, contributing to the global dataset of calving margin mass loss. Calving processes generate seismic energy, so can be used to better characterise mechanisms and rates of calving. Hence, the study has direct implications for calving contributions to mass loss from freshwater glaciers, and indirect implications for tidewater glaciers.

References

Akaike, H., 1977. On entropy maximization principle. In: P.R. Krishnaiah (Editor), Applications of Statistics. North-Holland, Amsterdam, pp. 27-41.

Allen, S., Cox, S. and Owens, I., 2011. Rock avalanches and other landslides in the central Southern Alps of New Zealand: a regional study considering possible climate change impacts. Landslides, 8: 33-48.

Allen, S., Gruber, S. and Owens, I., 2009a. Exploring steep bedrock permafrost and its relationship with recent slope failures in the Southern Alps of New Zealand. Permafrost and Periglacial Processes, 20: 345-356.

Allen, S., Schneider, D. and Owen, I., 2009b. First approaches towards modelling glacial hazards in the Mount Cook region of New Zealand's Southern Alps. Natural Hazards and Earth System Sciences, 9: 481-499.

Alley, R.B., Dupont, T.K., Parizek, B.R. and Anandakrishnan, S., 2005. Access of meltwater to beds of sub-freezing glaciers: preliminary insights. Annals of Glaciology, 40(1): 8-14.

Alley, R.B. et al., 2008. A simple law for ice-shelf calving. Science, 322: 1344.

Amundson, J. et al., 2010. Ice mélange dynamics and implications for terminus stability, Jakobshavn Isbræ, Greenland. J. Geophys. Res, 115: F01005.

Amundson, J.M., 2010. Iceberg calving dynamics of Jakobshavn Isbrae, Greenland. PhD Thesis, University of Alaska Fairbanks, Fairbanks.

Amundson, J.M., Burton, J.C. and Correa-Legisos, S., 2012. Impact of hydrodynamics on seismic signals generated by iceberg collisions. Annals of Glaciology, 53(60): 106-112.

Amundson, J.M. and Truffer, M., 2010. A unifying framework for iceberg-calving models. Journal of Glaciology, 56(199): 822-830.

Amundson, J.M. et al., 2008. Glacier, fjord and seismic response to recent large calving events, Jakobshavn Isbrae, Greenland. Geophysical Research Letters, 35: L22501.

Anandakrishnan, S. and Alley, R.B., 1997. Tidal forcing of basal seismicity of ice stream C, West Antarctica, observed from far inland. Journal of Geophysical Research, 102: 15183-15196.

Anandakrishnan, S. and Bentley, C.R., 1993. Micro-earthquakes beneath Ice Streams B and C, West Antarctica: observation and implications. Journal of Glaciology, 39(133): 455-462.

Anderton, P.W., 1975. Tasman Glacier 1971-73, Ministry of Works and Development, Wellington.

Aniya, M. and Wakao, Y., 1997. Glacier variations in Hielo Patagonico Norte Chile, Between 1944\45 and 1995\9. Bulletin of Glacier Research 15: 11-18.

Bamber, J. and Payne, A.J., 2004. Mass balance of the cryosphere: observations and modelling of contemporary and future changes. Cambridge Universty Press, Cambridge.

Bartholomaus, T., Larsen, C.F. and O'Neel, S., 2013. Does calving matter? Evidence for significant submarine melt. Earth and Planetary Science Letters, 380: 21-30.

Bartholomaus, T., Larsen, C.F., O'Neel, S. and West, M., 2012. Calving seismicity from iceberg-sea surface interactions. Journal of Geophysical Research, 117(F4029).

Bassis, J., Coleman, R., Fricker, H. and Minster, J., 2005. Episodic propagation of a rift on the Amery Ice Shelf, East Antarctica. Geophysical Research Letters, 32(6).

Bassis, J.N., 2011. The statistical physics of iceberg calving and the emergence of universal calving laws. Journal of Glaciology, 57(201): 3-16.

Bebbington, M.S., 2008. Incorporating the eruptive history in a stochastic model for volcanic eruptions. Journal of Volcanology and Geothermal Research, 175(3): 325-333.

Bebbington, M.S., 2013. Models for temporal volcanic hazard. Stastistics in Volcanology, 1: 1-24.

Benn, D.I. et al., 2012. Response of debris-covered glaciers in the Mount Everest region to recent warming, and implications for outburst flood hazards. Earth-Science Reviews, 114(1-2): 156-174.

Benn, D.I. and Evans , D.J.A., 2010. Glaciers and Glaciation (2nd ed). Hodder Education, London.

Benn, D.I., Hulton, N.R.J. and Mottram, R.H., 2007a. 'Calving laws', 'sliding' and the stability of tidewater glaciers. Annals of Glaciology, 46: 123-130.

Benn, D.I., Kirkbride, M.P., Owen, L.A. and Brazier, V., 2003. Glaciated Valley Landsystems. In: D.J.A. Evans (Editor), Glacial Landsystems. Arnold, London.

Benn, D.I. and Warren, C.R., 2002. Reply to the comments of J.P. Keanneally on "buoyancy-driven lacustrine calving, Glacier Nef, Chilean Patagonia" by D. Benn and C.R. Warren. Journal of Glaciology, 48(163): 630.

Benn, D.I., Warren, C.R. and Mottram, R.H., 2007b. Calving processes and the dynamics of calving glaciers. Earth-Science Reviews, 82: 143-179.

Benn, D.I., Wiseman, S. and Hands, K.A., 2001. Growth and drainage of supraglacial lakes on the debris-mantled Ngozumpa Glacier, Khumbu Himal, Nepal. Journal of Glaciology, 47(159): 626-638.

Beyreuther, M. et al., 2010. ObsPy: a python toolbox for seismology. Seismological Research Letters, 81(3): 530-533.

Bindschadler, R.A., King, M.A., Alley, R.B., Anandakrishnan, S. and Padman, L., 2003. Tidally controlled stick-slip discharge of a West Antarctic Ice Stream. Science, 301: 1087-1089.

Blair, R.W., 1994. Moraine and valley wall collapse due to rapid deglaciation in Mount Cook National Park, New Zealand. Mountain Research and Development, 14(4): 347-358.

Bolch, T., Buchroithner, M., Kunert, A. and Kamp, U., 2007. Automated delineation of debris-covered glaciers based on ASTER data, Geoinformation in Europe (Proc. of 27th EARSel Symposium, 04-07 June 2007), Bozen, Italy, pp. 403-410.

Bolch, T. et al., 2012. The state and fate of Himalayan glaciers. Science, 336(6079): 310-314.

Boyce, E., 2006. Instability and retreat of a lake-calving terminus, Mendenhall Glacier, southeast Alaska. MSc Thesis, University of Alaska Fairbanks, Fairbanks.

Boyce, E., Motyka, R.J. and Truffer, M., 2007. Flotation and retreat of a lake-calving terminus, Mendenhall Glacier, southeast Alaska, USA. Journal of Glaciology, 53(181): 211-223.

Broadbent, M., 1973. A preliminary report on seismic and gravity surveys on the Tasman Glacier 1971-2, Geophysics division, DSIR, Wellington.

Brodrick, T.N., 1891. Report on the Tasman Glacier. Journals of the House of Representatives of New Zealand, C1-A, Appendix 4: 39-43.

Brown, C.S., Meier, M.F. and Post, A., 1982. Calving speed of Alaska tidewater glaciers, with application to Columbia Glacier. U.S. Geological Survey Professional Paper 1258-C: 13.

Canassy, P.D. et al., 2011. Hazard assessment investigations due to recent changes in Triftgletscher, Bernese Alps, Switzerland. Natural Hazards Earth System Science, 11: 2149-2162.

Carmichael, J.D., Pettit, E.C., Hoffman, M., Fountian, A. and Hallet, B., 2012. Seismic multiplet response triggered by melt at Blood Falls, Taylor Glacier, Antarctica. Journal of Geophysical Research, 117: F03004.

Cenderelli, D.A. and Wohl, E.E., 2003. Flow hydraulics and geomorphic effects of glacial-lake outburst floods in the Mount Everest Region, Nepal. Earth Surface Processes and Landforms, 28: 385-407.

Chamberlain, C.P., Poage, M.A., Craw, D. and Reynolds, R.C., 1999. Topographic devlopment of the Southern Alps recorded by the isotopic compisition of authigenic clay minerals, South Island, New Zealand. Chemical Geology, 155: 279-294.

Chapuis, A., Rolstad, C. and Norland, R., 2010. Interpretation of amplitude data from a ground-based radar in combination with terrestrial photogrammetry and visual observations for calving monitoring of Kronebreen, Svalbard. Annals of Glaciology, 51(55): 34-40.

Chapuis, A. and Tetzlaff, T., in press. The variability of tidewater-glacier calving: origin of event-size and interval distributions. Journal of Glaciology.

Chen, X., Shearer, P.M., Walter, F. and Fricker, H.A., 2011. Seventeen Antarctic seismic events detected by global surface waves and a possible link to calving events from satellite images. Journal of Geophysical Research: Solid Earth, 116(B6): B06311.

Chikita, K., Jha, J. and Yamada, T., 1999. Hydrodynamics of a Supraglacial Lake and Its Effect on the Basin Expansion: Tsho Rolpa, Rolwaling Valley, Nepal Himalaya. Arctic, Antarctic, and Alpine Research, 31(1): 58-70.

Chinn, T.J.H., 1995. Glacier Fluctuations in the Southern Alps of New Zealand determined from snowline elevations. Arctic and Alpine Research, 27(2): 187-198.

Chinn, T.J.H., 1996. New Zealand glacier responses to climate change of the past century. New Zealand Journal of Geology and Geophysics, 39: 415-428.

Chinn, T.J.H., 1999. New Zealand glacier response to climate change of the past 2 decades. Global and Planetary Change, 22: 155-168.

Chinn, T.J.H., Fitzharris, B.B., Willsman, A. and Salinger, M.J., 2012. Annual ice volume changes 1976-2008 for the New Zealand Soutthern Alps. Global and Planetary Change, 92-93: 105-118.

Cichowicz, A., 1983. Icequakes and glacier motion: the hans Glacier, Spisbergen. Pure and Applied Geophysic, 121(1): 27-38.

Clague, J.J. and Evans, S.G., 2000. A review of catastrophic drainage of moraine-dammed lakes in British Columbia. Quaternary Science Review, 19: 1763-1783.

Claridge, D., 1983. A geophysical study of the termini of the Mount Cook National Park glacier. MSc thesis Thesis, University of Auckland, Auckland.

Clayton, L., 1964. Karst topography on stagnant glaciers. Journal of Glaciology, 5: 107-112.

Corporation, O.C., 2006. HOBO U20 Water Level Logger (Part # U20-001-01). Onset Computer Corporation.

Cox, S., Allen, S. and Ferris, B., 2008. Vampire rock avalanches, Aoraki/Mount Cook National Park, New Zealand., GNS Science Report 2008/10. Institue of Geological and Nuclear Sciences, Lower Hut, New Zealand.

Cox, S.C. and Allen, S., 2009. Vampire rock avalanches of Januray 2008 and 2003, Southern Alps, New Zealand. Landslides, 6: 161-166.

Cox, S.C. and Barrell, D.J.A., 2007. Geology of the Aoraki area. Institute of Geological and Nuclear Science, Lower Hutt, New Zealand.

Cox, S.C. and Findlay, R.H., 1995. The Main Divide Fault Zone and its role in formation of the Southern Alps, New Zealand. New Zealand Journal of Geology and Geophysics, 38: 489-499.

Crary, A.P., 1955. A brief study of ice tremors. Bulletin of the Seismological Society of America, 45(1-9).

Cronin, S.J., Bebbington, M.S. and Lai, C.D., 2001. A probabilistic assessment of eruption recurrence on Tavenuni volcano, Fiji. Bulletin of Volcanology, 63: 274-288.

Csatho, B., Schenk, T., van der Veen, C.J. and Krabill, W., 2008. Intermittent thinning of Jakobshavn Isbrae, West Greenland, since the Little Ice Age. Journal of Glaciology, 54(184): 131-144.

Cuffey, K.M. and Paterson, W.S.B., 2010. The physics of glaciers (4th ed.). Butterworth-Heinemann/Elsevier, Burlington, MA.

Dalban Canassy, P., Faillettaz, J., Walter, F. and Huss, M., 2012. Seosmic activity and surface motion of a steep temperate glacier: a study on Triftgletscher, Switzerland. Journal of Glaciology, 58(209): 513-528.

Deichmann, N. et al., 2000. Evidence for deep icequakes in an Alpine glacier. Annals of Glaciology, 31: 85-89.

Dowdeswell, J., 1989. On the nature of Svalbard icebergs. Journal of Glaciology, 35: 224-234.

Drewry, D., 1986. Glacial Geologic Processes. Edward Arnold, London.

Duck, R.W. and Mcmanus, J., 1985. Short-term bathymetric changes in an ice-contact proglacial lake. Norsk Geografisk Tidsskrift, 39: 39-45.

Dykes, R.C. and Brook, M., S., 2010. Terminus recession, proglacial lake expansion and 21st century calving retreat of Tasman Glacier, New Zealand. New Zealand Geographer, 66: 203-217.

Dykes, R.C., Brook, M., S., Robertson, C.M. and Fuller, I., C., 2011. Twenty-first century calving retreat of Tasman Glacier, Southern Alps, New Zealand. Arctic, Antarctic, and Alpine Research, 43(1): 1-10.

Eijpen, K., Warren, C. and Benn, D., 2003. Subaqueous melt rates at calving termini: a laboratory approach. Annals of Glaciology, 36(1): 179-183.

Ekström, G., Nettles, M. and Abers, G.A., 2003. Glacial Earthquakes. Science, 302: 622-624.

Etzelmuller, B., 2000. Quantification of thermo-erosion in proglacial areas - examples from Svalbard. Zeitschrift fur Geomorphologie, 44(3): 343-361.

Fischer, M.P. and Powell, R.D., 1998. A simple model for the influence of push-morainal banks on the calving and stability of glacial tidewater termini. Journal of Glaciology, 44: 31-41.

Fitzharris, B.B., Lawson, W. and Owens, I., 1999. Research on glaciers and snow in New Zealand. Progress in Physical Geography, 23(4): 469-500.

Fujita, K., Sakai, A., Nuimura, T., Yamaguchi, S. and Sharma, R.R., 2009. Recent changes in Imja Glacial Lake and its damming moraine in the Nepal Himalaya revealed by in situ surveys and multi-temporal ASTER imagery. Environmental Research Letters, 4: 045205.

Funk, M. and Rothlisberger, H., 1989. Forecasting the effects of a planned reservior which will partially flood the tongue of Unteraargletscher in Switzerland. Annals of Glaciology, 13(76-81).

Gekle, S. and Gordillo, J.M., 2010. Generation and breakup of Worthington jets after cavity collapse. Part 1. Jet formation. Journal of Fluid Mechanics, 663: 293-330.

Gellatly, A.F., 1984. The use of rock weathering-rind thickness to redate moraines in Mount Cook National Park, New Zealand. Arctic and Alpine Research, 16(2): 225-232.

Gellatly, A.F., 1985. Historical records of glacier fluctuations in Mt Cook National Park, New Zealand: a century of change. The Geographical Journal, 151(1): 86-99.

Glasser, N.F., Hambrey, M.J., Etienne, J.L., Jansson, P. and Petterson, R., 2003. The origion and significance of debris-charged rides at the surface of Storglaciaren, northern Sweden. Geografiska Annaler. Series A, Physical Geography, 85(2): 127-147.

Górski, M., 1997. Seismicity of the Hornsund region, Spitsbergen: icequakes and earthquakes. Polska Akademia Nauk. Instytut Geofizyki, Warsaw.

Green, R.M., Bebbington, M.S., Cronin, S.J. and Jones, G., 2013. Geochemical precursors for eruption repose length. Geophysical Journal International, 193: 855-873.

Griffiths, G.A. and McSaveney, M.J., 1983. Distribution of mean annual precipitation across some steepland regions of New Zealand. New Zealand Journal of Science, 26: 197-209.

Hagen, J., Melvold, K., Pinglot, F. and Dowdeswell, J., 2003. On the Net Mass Balance of the Glaciers and Ice Caps in Svalbard, Norwegian Arctic. Arctic, Antarctic, and Alpine Research, 35(2): 264-270.

Hallet, B., Hunter, L. and Bogen, J., 1996. Rates of erosion and sediment evacuation by glaciers: A review of field data and their implications. Global and Planetary Change, 12(1-4): 213-235.

Hambrey, M.J., 1994. Glacial Environments. UCL Press, London.

Hambrey, M.J. and Ehrmann, W., 2004. Modification of sediment characteristics during glacial transport in high-alpine catchments: Mount Cook area, New Zealand. Boreas, 33: 300-318.

Hanson, B. and Hooke, R.L., 2000. Glacier calving: a numerical model of forces in the calving-speed/water-depth relation. Journal of Glaciology, 46(153): 188-196.

Hanson, B. and Hooke, R.L., 2003. Buckling rate and overhang development at a calving face. Journal of Glaciology, 49: 577-586.

Haresign, E.C., 2004. Glacio-limnological interactions at lake-calving glaciers. PhD Thesis, University of St Andrews, St Andrews.

Haresign, E.C. and Warren, C.R., 2005. Melt rates at calving termini: a study at Glaciar Leon, Chilean Patagonia. In: C. Harris and J.B. Murton (Editors), Cryospheric Systems: Glaciers and Permafrost. Geological Society, London, Special Publications, 242, London, pp. 99-109.

Harrison, S. et al., 2006. A glacial lake outburst flood associated with recent mountain glacier retreat, Patagonia Andes. The Holocene, 16(4): 611-620.

Hart, J.K., Rose, K.C., Waller, R.I., Vaughan-Hirsch, D. and Martinez, K., 2011. Assessing the catastrophic break-up of Briksdalsbreen, Norway, associated with rapid climate change. Journal of the Geological Society, 168(3): 673.

Hastie, T., Tibshirani, R. and Friedman, J., 2001. The elements of statistical learning. Springer-Verlag, New York.

Hatherton, T. and Evison, F.F., 1962. A special mechanism for some Antarctic earthquakes. New Zealand Journal of Geology and Geophysics, 5: 864-873.

Healy, T.R., 1975. Thermokarst - a mechanism of de-icing ice-cored moraines. Boreas, 4(1): 19-23.

Herman, F., Anderson, B. and Leprince, S., 2011. Mountain glacier velocity variation during a retreat/advance cycle quantified using sub-pixel analysis of ASTER images. Journal of Glaciology, 57(202): 197-207.

Hochstein, M.P. et al., 1995. Downwasting of the Tasman Glacier, South Island, New Zealand: changes in the terminus region between 1971 and 1993. New Zealand Journal of Geology and Geophysics, 38: 1-16.

Hochstein, M.P., Watson, M.I., Malengreau, B., Nobes, D.C. and Owens, I., 1998. Rapid melting of the terminal section of the Hooker Glacier (Mt Cook National Park, New Zealand). New Zealand Journal of Geology and Geophysics, 41: 203-218.

Holdsworth, G., 1973. Ice calving into the proglacial Generator Lake, Baffin Island, N.W.T, Canada. Journal of Glaciology, 12(65): 235-250.

Houghton, J. et al., 2001. Climate change 2001: the scientific basis. Cambridge University Press, Cambridge.

Howarth, P. and Price, R., 1969. The Proglacial Lakes of Breiđamerkurjökull and Fjallsjökull, Iceland. The Geographical Journal, 135(4): 573-581.

Howat, I.M., Joughin, I., Tulaczyk, S. and Gogineni, S., 2005. Rapid retreat and acceleration of Helheim Glacier, east Greenland. Geophysical Research Letters, 32: L22502.

Huggel, C., Kääb, A. and Salzmann, 2004. GIS-based modelling of glacial hazards and the interactions using Landsat-TM and IKONOS imagery. Norsk Geografisk Tidsskrift, 58: 61-73.

Hughes, T., 1986. The Jakobshanvs effect. Geophysical Research Letters, 13: 46-48.

Hughes, T., 1989. Calving ice walls. Annals of Glaciology, 12: 74-80.

Hughes, T., 1992. Theoretical calving rates from glaciers along ice walls grounded in water of variable depths. Journal of Glaciology, 38(129): 282-294.

Hughes, T., 1996. Can ice sheets trigger abrupt climatic change? Arctic and Alpine Research, 28: 448-465.

Hughes, T., 2002. Calving bays. Quaternary Science Reviews, 21(1-3): 267-282.

Hughes, T. and Nakagawa, M., 1989. Bending shear: the rate-controlling mechanism for calving ice walls. Journal of Glaciology, 35(120): 260-266.

Hunter, L.E. and Powell, R.D., 1998. Ice foot development at temperate tidewater margins in Alaska. Geophysical Research Letters, 25: 1923-1926.

Iken, A., 1977. Movement of a large ice mass before breaking off. Journal of Glaciology, 19: 595-605.

IPCC, 2007. The Physical Science Basis. Contribution of Working Group 1 to the Fourth Assessment Report of the Intergovernmental Panel on Climate Change. University Press, Cambridge, Cambridge.

Jacobs, S., Hellmer, H., Doake, C., Jenkins, A. and Frolich, R., 1992. Melting of ice shelves and the mass balance of Antarctica. Journal of Glaciology, 38(130): 375–387.

Jansson, P., Hock, R. and Schneider, T., 2003. The concept of glacier storage: a review. Journal of Hydrology, 282(1-4): 116-129.

Josbergerm, E.G. and Neshyba, S., 1980. Iceberg melt-driven convection inferred from field measurements of temperature. Annals of Glaciology, 1: 113-117.

Joughin, I. et al., 2008a. Ice-front variation and tidewater behavior on Helheim and Kangerdlugssuaq Glaciers, Greenland. Journal of Geophysical Research, 113: F01004.

Joughin, I. et al., 2008b. Continued evolution of Jakobshavn Isbrae following its rapid speedup. Journal of Geophysical Research, 113: F04006.

Joughin, I. and MacAyeal, D., 2005. Calving of large tabular icebergs from ice shelf rift systems. Geophysical Research Letters, 32(2): L02501.

Kääb, A., 2002. Monitoring high-mountain terrain deformation from repeated air- and spacebourne optical data: examples using digital aerial imagery and ASTER data. Journal of Photogrammetry and Remote Sensing, 57: 39-52.

Kattelmann, R., 2003. Glacial lake outburst floods in the Nepal, Himalaya: a manageable hazard? Natural Hazards, 28: 145-154.

Kenneally, J.P. and Hughes, T.J., 2002. The calving constraints on inception of Quaternary ice sheets. Quaternary International, 95-96: 43-53.

Kennett, M., Laumann, T. and Kjoellmoen, B., 1997. Predicted response of the calving glacier Svartisheibreen, Norway, and outbursts from it, to the future changes i clmate and lake level. Annals of Glaciology, 24: 16-20.

Kershaw, J.A., Clague, J.J. and Evans, S.G., 2005. Geomorphic and sedimentological signiture of a two-phase outburst flood from moraine-dammed Queen Bees Lake, British Columbia, Canada. Earth Surface Processes and Landforms, 30: 1-25.

Kirkbride, M.P., 1989. The influence of sediment budget an geomorphic activity of the Tasman Glacier, Mount Cook National Park, New Zealand. PhD thesis Thesis, University of Canterbury, Christchurch.

Kirkbride, M.P., 1993. The temporal significance of transitions from melting to calving termini at glaciers in the central Southern Alps of New Zealand The Holocene, 3(3): 232-240.

Kirkbride, M.P., 1995a. Ice flow vectors on the debris-mantled Tasman Glacier, 1957-1986. Geografiska Annaler. Series A, Physical Geography, 77(3): 147-157.

Kirkbride, M.P., 1995b. Relationships between temperature and ablation on the Tasman Glacier, Mount Cook National Park, New Zealand. New Zealand Journal of Geology and Geophysics, 38: 17-27.

Kirkbride, M.P., 2000. Ice marginal geomorphology and Holocene expansion of debris-covered Tasman Glacier, New Zealand. In: M. Nakawo, C.F. Raymond and A. Fountain (Editors), Debris-Covered Glaciers. IAHS Publication 264. Wallingford, Oxfordshire, pp. 211-218.

Kirkbride, M.P. and Brazier, V., 1998. A critical evaluation of the use of glacier chronologies in climatic reconstruction, with reference to New Zealand. Quaternary Proceedings, 6: 55-64.

Kirkbride, M.P. and Spedding, N., 1996. The influence of englacial drainage on sediment transport pathways and till texture of temperate valley glaciers. Annals of Glaciology, 22: 160-166.

Kirkbride, M.P. and Sugden, D.E., 1992. New Zealand loses its top. Geographical Magazine, 64(7): 30-34.

Kirkbride, M.P. and Warren, C.R., 1997. Calving processes at a grounded ice cliff. Annals of Glaciology, 24: 116-121.

Kirkbride, M.P. and Warren, C.R., 1999. Tasman Glacier, New Zealand: 20th-century thinning and predicted calving retreat. Global and Planetary Change, 22: 11-28.

Köhler, A., Chapuis, A., Nuth, C., Kohler, J. and Weidle, C., 2012. Autonomous detection of calving-related seismicity at Kronebreen, Svalbard. The Cryosphere, 6: 393-406.

Komori, J., 2008. Recent expansions of glacial lakes in the Bhutan Himalayas. Quaternary Internation, 184: 177-186.

Krimmel, R.M., 1997. Documentaion of the retreat of Columbia Glacier, Alaska. In: C.J. van der Veen (Editor), Calving glaciers: reports of a workshop, Feb 28 - March 2, 1997. Byrd Polar Research Center, The Ohio State University, Columbas, pp. 105-108.

Krimmel, R.M. and Vaughn, B.H., 1987. Columbia Glacier, Alaska: changes in velocity 1977-1986. Journal of Geophysical Research, 92(B9): 8961-8968.

Lamont, G.N., Chinn, T.J.H. and Fitzharris, B.B., 1999. Slopes of glacier ELAs in the Southern Alps of New Zealand in relation to atmospheric circulation patterns. Global and Planetary Change, 22: 209-219.

Larour, E., Rignot, E. and Aubry, D., 2004. Modelling of rift propagation on Ronne Ice Shelf, Antarctica, and sensitivity to climate change. Geophysical Research Letters, 31(16): L16404.

Laumann, T. and Wold, B., 1992. Reactions of a calving glacier to changes in water level. Annals of Glaciology, 16: 158-162.

Lejeune, Y., Bertrand, J., Wagnon, P. and Morin, S., 2013. A physically based model of the year-round surface energy and mass balance of debris-covered glaciers. Journal of Glaciology, 59(214): 327-344.

Lingle, C. et al., 1993. Bering Glacier surge and iceberg-calving mechanism at Vitus Lake, Alaska, USA. Journal of Glaciology, 39(133): 722-727.

Lundstrom, S., McCafferty, A. and Coe, J., 1993. Photogrammetric analysis of 1984-89 surface altitude change of the partially debris-covered Eliot Glacier, Mount Hood, Oregon, USA. Annals of Glaciology, 17: 167-170.

MacAyeal, D. et al., 2006. Transoceanic wave propagation links iceberg calving margins of Antarctica with storms in tropics and Northern Hemisphere. Geophysical Research Letters, 33.

MacAyeal, D.R., Okal, E.A., Aster, R.C. and Bassis, J.N., 2008. Seismic and hydroacoustic tremor generated by colliding icebergs. Journal of Geophysical Research, 113: F03011.

MacAyeal, D.R., Okal, E.A., Aster, R.C. and Bassis, J.N., 2009. Seismic observations of glaciogenic ocean waves (micro-tsunamis) on icebergs and ice shelves. Journal of Glaciology, 55(190): 193-206.

MacAyeal, D.R., Scambos, T.A., Hulbe, C.L. and Fahnestock, M.A., 2003. Catastrophic ice-shelf break-up by an ice-shelf-fragment-capsize mechanism. Journal of Glaciology, 49: 22-36.

Mangerud, J. et al., 2004. Ice-dammed lakes and rerouting of the drainage of northern Eurasia during he Last Glaciation. Quaternary Science Review, 23: 1313-1332.

Mathews, J.B. and Quinlan, V.A., 1975. Seasonal characteristics of water masses in Muir Inlet, a fjord with tidewater glaciers. Journal of the Fisheries Research Board of Canada, 32(10): 1693-1703.

Mathieu, R., Chinn, T.J.H. and Fitzharris, B.B., 2009. Detchting the equilibrium-line altitudes of New Zealand glaciers using ASTER satellite images. New Zealand Journal of Geology and Geophysics, 52: 209-222.

McKillop, R.J. and Clague, J.J., 2007a. A procedure for making objective preliminary assessments of outburst flood hazard from moraine-dammed lakes in southwestern British Columbia. Natural Hazards, 41: 131-157.

McKillop, R.J. and Clague, J.J., 2007b. Statistical, remote sensing-based approach for estimating the probability of catastrophic drainage from moraine-dammed lakes in southwestern Britsh Columbia. Global and Planetary Change, 56: 153-171.

McSaveney, M., 2002. Recent rockfalls and rock avalanches in Mount Cook National park, New Zealand. In: S.G. Evans and J.V. Degraff (Editors), Catastrophic Landslides: Effects, Occurrence and Mechanisms. Geological Society of America Reviews in Engineering Geology, Boulder, Colorado, pp. 35-70.

Meier, M.F., 1994. Columbia Glacier during rapid retreat: interaction between glacier flow and iceberg calving dynamics. In: N. Reeh (Editor), Report of a workshop on "The calving rate of the West Greenland glaciers in response to climate change', Copenhagen, 13-15 September, 1993. Danish Polar Center, Copenhagen, pp. 63-83.

Meier, M.F., 1997. The iceberg discharge process: observations and inferences drawn from the study of Columbia Glacier. In: C.J. van der Veen (Editor), Calving glaciers: report of a workshop, February 28-March 2, 1997. Byrd Polar Research Center, The Ohio State University, Columbas, pp. 109-114.

Meier, M.F. and Post, A., 1987. Fast tidewater glaciers. Journal of Geophysical Research, 92(B9): 9051-9058.

Métaxian, J., Araujo, M. and Lesage, P., 2003. Seismicity related to the glacier Cotopaxi Volcano, Ecuador. Geophysical Research Letters, 30(9): 1483.

Moon, T. and Joughin, I., 2008. Changes in ice front position on Greenland's outlet glaciers from 1992 to 2007. Journal of Geophysical Research, 113: F02022.

Mottram, R.H., 2008. Processes of crevasse formation and the dynamics of calving glaciers: a study at Breiðamerkurjökull. PhD Thesis, University of St Andrews, St Andrews.

Mottram, R.H. and Benn, D.I., 2009. Testing crevasse-depth models: a field study at Breiethamerkurjokull, Iceland. Journal of Glaciology, 55: 746-752.

Motyka, R.J., 1997. Deep water calving at Le Conte Glacier, Southeast Alaska. In: C.J. van der Veen (Editor), Calving Glaciers: report of a workshop, Feb. 28-March 2, 1997. Byrd Polar Research Center, The Ohio State University, Columbus, pp. 115-118.

Motyka, R.J., Hunter, L.E., Echelmeyer, K.A. and Connor, C.L., 2003a. Submarine melting at the terminus of a temperate tidewater glacier, LeConte Glacier, Alaska, U.S.A. Annals of Glaciology, 36(57-65).

Motyka, R.J., O'Neel, S., Connor, C.L. and Echelmeyer, K.A., 2003b. Twentieth century thinning of Mendenhall Glacier, Alaska, and its relationship to climate, lake calving, and glacier run-off. Global and Planetary Change, 35(1-2): 93-112.

Motyka, R.J. et al., 2011. Submarine melting of the 1985 Jakobshavn Isbræ floating tongue and the triggering of the current retreat. Journal of Geophysical Research: Earth Surface, 116(F1): F01007.

Mullen, A.B., Stuart, S.J., Hadfield, M.G. and Smith, M.J., 2010. Report on the Review of NIWA's 'Seen -Station' Temperature Series. NIWA Information Series N. 78: 175pp.

Naito, N., Nakawo, M., Kadota, T. and Raymond, C.F., 2000. Numerical simulation of recent shrinkage of Khumbu Glacier, Nepal Himalayas. In: M. Nakawo, C.F. Raymond and A. Fountain (Editors), Debris-Covered Glaciers. IAHS Publication 264. Wallingford, Oxfordshire, pp. 245-254.

Nakawo, M. and Rana, B., 1999. Estimate of ablation rate of glacier ice under a supraglacial debris layer. Geografiska Annaler. Series A, Physical Geography, 81(4): 695-701.

Nakawo, M. and Young, G., 1981. Field experiments to determine the effect of a debris layer on ablation of glacier ice. Annals of Glaciology, 2: 85-91.

Naruse, R. and Skvarca, P., 2000. Dynamic features of thinning and retreating Glacier Upsala, a lacustrine calving glacier in Southern Patagonia. Arctic, Antarctic, and Alpine Research, 32(4): 485-491.

Neave, K.G. and Savage, J.C., 1970. Icequakes on the Athabasca Glacier. Journal of Geophysical Research, 75(8): 1351-1362.

Nettles, M. and Ekström, G., 2010. Glacial earthquakes in Greenland and Antarctica. Annual Review of Earth and Planetary Sciences, 38: 467-491.

Nettles, M. et al., 2008. Step-wise changes in glacier flow speed coincide with calving and glacial earthquakes at Helheim glacier, Greenland. Geophysical Research Letters, 35: L24503.

Nicholson, L. and Benn, D.I., 2006. Calculating ice melt beneath a debris layer using meteorological data. Journal of Glaciology, 52(178): 463-470.

Nick, F.M. and Oerlemans, J., 2006. Dynamics of tidewater glaciers: comparison of three models. Journal of Glaciology, 52: 183-190.

Nick, F.M. et al., 2013. Future sea-level rise from Greenland's main outlet glaciers in a warming climate. Nature, 497: 235-238.

Nienow, P.W. et al., 2005. Hydrological controls on diurnal ice flow variability in valley glaciers. Journal of Geophysical Research, 110(F04002).

Nye, J.F., 1957. The distribution of stress and velocity in glacier and ice sheets. Proceedings of the Royal Society of London, Series A 239: 113-133.

O'Leary, M. and Christoffersen, P., 2012. Calving on tidewater glaciers amplified by submarine frontal melting. The Cryosphere Discuss., 6(4): 3287-3316.

O'Neel, S., 2000. Motion and calving at LeConte Glacier, Alaska. MSc Thesis, University of Alaska Fairbanks, Fairbanks, Alaska.

O'Neel, S., Echelmeyer, K.A. and Motyka, R.J., 2001. Short-term flow dynamics of a retreating tidewater glacier: LeConte Glacier, Alaska, U.S.A. Journal of Glaciology, 49(159): 567-578.

O'Neel, S., Echelmeyer, K.A. and Motyka, R.J., 2003. Short-term variations in calving of a tidewater glacier: LeConte Glacier, Alaska, U.S.A. Journal of Glaciology, 49(167): 587-598.

O'Neel, S., Marshall, H.P., McNamara, D.E. and Pfeffer, W.T., 2007. Seismic detection and analysis of icequakes at Columbia Glacier, Alaska. Journal of Geophysical Research, 112: F03S23.

O'Neel, S. and Pfeffer, W.T., 2007. Source mechanics for monochromatic ice quakes produced during iceberg calving at Columbia Glacier, AK. Geophysical Research Letters, 34: L22502.

O'Neel, S., Pfeffer, W.T., Krimmel, R.M. and Meier, M.F., 2005. Evolving force balance at Columbia Glacier, Alaska, during its rapid retreat Journal of Geophysical Research, 110: F03012.

Oerlemans, J. and Nick, F.M., 2006. Modelling the advance-retreat cycle of a tidewater glacier with simple sediment dynamics. Global and Planetary Change, 50: 148-160.

Østrem, G., 1959. Ice melting under a thin layer of moraine, and the existance of ice cores in moraine ridges. Geografiska Annaler, 4: 228-230.

Otero, J., Navarro, F.J., Martin, C., Cuadrado, M.L. and Corcuera, M.I., 2010. A three-dimentsional calving modal: numerical experiments on Johnsons Glacier, Livingston Island, Antarctica. Journal of Glaciology, 56(196): 200-214.

Paterson, W.S.B., 1994. The Physics of Glaciers. Pergamon, Oxford.

Pelto, M.S. and Warren, C.R., 1991. Relationship between tidewater glacier calving velocity and water depth at the calving front. Annals of Glaciology, 15: 115-118.

Pfeffer, W.T., 2007. A simple mechanism for irreversible tidewater glacier retreat. Journal of Geophysical Research, 112.

Pfeffer, W.T., Harper, J.T. and O'Neel, S., 2008. Kinematic constraints on glaicer contributions to 21st century sea-level rise. Science, 321: 1340-1343.

Posamentier, H.W., 1977. A new climatic model for glacier behaviour in the Austrian Alps. Journal of Glaciology, 18(78): 57-65.

Powell, R., 1983. Glacial-marine sedimentation processes and lithofacies of temperate tidewater glaciers, Glacier Bay, Alaska. In: B.F. Molnia (Editor), Glacial-marine sedimentation. Plenum Press, New York, pp. 185–232.

Pralong, A. and Funk, M., 2005. Dynamic damage model of crevasse opening and application to glacier calving. Journal of Geophysical Research-Solid Earth, 110(B1): B01309.

Pralong, A., Funk, M. and Luthi, M., 2003. A description of crevasse formation using continuum damage mechanics. Annals of Glaciology, 37(1): 77-82.

Purdie, H., Anderson, B., Lawson, W. and Mackintosh, A., 2011a. Controls on spatial variability in snow accumulation on glaciers in the Southern Alps, New Zealand; as revealed by crevasse stratigraphy. Hydrological Processes, 25(1): 54-63.

Purdie, H., Mackintosh, A., Lawson, W. and Anderson, B., 2011b. Synoptic Influences on Snow Accumulation on Glaciers East and West of a Topographic Divide: Southern Alps, New Zealand. Arctic, Antarctic, and Alpine Research, 43(1): 82-94.

Purdie, H.L., Brook, M., S. and Fuller, I., C., 2008. Seasonal variation in Ablation and surface velocity on a temperate maritime glacier: Fox Glacier, New Zealand. Arctic, Antarctic, and Alpine Research, 40(1): 140-147.

Purdie, J. and Fitzharris, B.B., 1999. Processes and rates of ice loss at the terminus of Tasman Glacier, New Zealand. Global and Planetary Change, 22(79-91).

Qamar, A., 1988. Calving icebergs: a source of low-frequency seismic signals from Columbia Glacier, Alaska. Journal of Geophysical Research, 93(B6): 6615-6623.

Quincey, D.J. and Glasser, N.F., 2009. Morphological and ice-dynamical changes on the Tasman Glacier, New Zealand 1990-2007. Global and Planetary Change, 68: 185-197.

Quincey, D.J. et al., 2005. Optical remote sensing techniques in high-mountain environments: application to glacial hazards. Progress in Physical Geography, 29(4): 475-505.

Rahmstorf, S., 2007. A semi-emprircal approach to projecting future sea-level rise. Science, 315: 368-370.

Redpath, T., 2011. Utilising optical satellite imagery to derive multi-temporal flow-fields for the Tasman Glacier, New Zealand. MSc Thesis, University of Otago, Dunedin.

Redpath, T., Sirguey, P., Fitzsimons, S. and Kääb, A., 2013. Accuracy assessment for mapping glacier flow velocity and detecting flow dynamics from ASTER satellite imagery: Tasman Glacier, New Zealand. Remote Sensing of Environment, 133: 90-101.

Redpath, T., Thomas, D., Sirguey, P., Fitzsimons, S. and Kääb, A., 2012. A tale of two glaciers: Contrasting behaviour of the Tasman and Murchison glaciers, 2006-2009, SIRG 2012, Twizal, New Zealand.

Reeh, N., 1968. On the calving of ice from floating glaciers and ice shelves. Journal of Glaciology, 7(50): 215-232.

Reeh, N., 1994. Calving from Greenland glaciers: observations, balance estimates of calving rates, calving laws. In: N. Reeh (Editor), Workshop on the Calving rate of West Greenland Glaciers Response to climate Change, Sept 13-15 1993. Danish Polar Centre, University of Copenhagen, pp. 85-102.

Reid, J. and Callender, E., 1965. Origin of debris-covered icebergs and mode of flow of ice into 'Miller Lake', Martin River Glacier, Alaska. Journal of Glaciology, 5(40): 497–503.

Reynolds, J.M., 2000. On the formation of supraglacial lakes on debris-covered glaciers. In: M. Nakawo, C.F. Raymond and A. Fountain (Editors), Debris-Covered Glaciers. IAHS Publication 264. Wallingford, Oxfordshire, pp. 187-197.

Reznichenko, N., Davies, T. and Alexander, D.J., 2011. Effects of rock avalanches on glacier behaviour and moraine formation. Geomorphology, 132: 327-338.

Reznichenko, N., Davies, T., Shulmeister, J. and McSaveney, M.J., 2010. Effects of debris on ice-surface melting rates: an experimental study. Journal of Glaciology, 56(197): 384-394.

Richardson, J., Waite, G., FitzGerald, K. and Pennington, W., 2010. Characteristics of seismic and acoustic signals produced by calving, Bering Glacier, Alaska. Geophysical Research Letters, 37(3): L03503.

Richardson, J., Waite, G., Pennington, W., Turpening, R. and Robinson, J., 2012. Icequake locations and discrimination of source and path effects with small aperture arrays, Berring Glacier terminus, AK. Journal of Geophysical Research, 117(F04013): 1-19.

Richardson, S.D. and Reynolds, J.M., 2000. Degradation of ice-cored moraine dams: implications for hazard development. In: M. Nakawo, C.F. Raymond and A. Fountain (Editors), Debris-Covered Glaciers. IAHS Publication 264. Wallingford, Oxfordshire, pp. 187-197.

Rignot, E. and Kanagaratnam, P., 2006. Changes in the velocity structure of the Greenland Ice Sheet. Science, 311: 986-990.

Rignot, E., Koppesm, M. and Velicogna, I., 2010. Rapid submarine melting of the calving faces of West Greenland glaciers. Nature Geoscience, 3: 187-191.

Rivera, A., Corripio, J., Bravo, C. and Cisternas, S., 2012. Glaciar Jorge Montt (Chilean Patagonia) dynamics derived from photos obtained by fixed cameras and satellite image feature tracking. Annals of Glaciology, 53(60): 147.

Robertson, C.M., 2012. Temporal evolution of the termini and subaqueous morphologies of lake-calving glaciers in the Aoraki/Mount Cook National Park, New Zealand. PhD Thesis, Massey University, Palmerston North.

Robertson, C.M., Benn, D.I., Brook, M.S., Fuller, I.C. and Holt, K.A., 2012. Subaqueous calving margin morphology at Mueller, Hooker and Tasman glaciers in Aoraki/Mount Cook National Park, New Zealand. Journal of Glaciology, 58(212): 1037-1046.

Robertson, C.M., Brook, M.S., Holt, K.A., Fuller, I.C. and Benn, D.I., 2013. Calving retreat and proglacial lake growth at Hooker Glacier, Southern Alps, New Zealand. New Zealand Geographer, 69(1): 14-25.

Robin, G., 1974. Depth of water-filled crevasses that are closely spaced. Journal of Glaciology, 13(69): 543.

Rogerson, R., Olson, M. and Branson, D., 1986. Medial moraines and surface melt on glaciers of the Torngat Mountains, Northern Labrador, Canada. Journal of Glaciology, 32: 350-354.

Röhl, K., 1999. Sedimentation processes in the proglacial Tasman Lake. Dissertation Thesis, University of Otago, Dunedin.

Röhl, K., 2005. Terminus disintegration of debris-covered, lake-calving glaciers. PhD Thesis, University of Otago, Dunedin.

Röhl, K., 2006. Thermo-erosional notch development at fresh-water-calving Tasman Glacier, New Zealand. Journal of Glaciology, 52(177): 203-213.

Röhl, K., 2008. Characteristics and evolution of supraglacial ponds on debris-covered Tasman Glacier, New Zealand. Journal of Glaciology, 54(188): 867-880.

Rothlisberger, H., 1955. Studies on glacier physics on the Penny Ice Cap, Baffin Island 1953, 3: Seismic soundings. Journal of Glaciology, 2: 539-552.

Rothlisberger, H. and Lang, H., 1987. Glacial hydrology. In: A.M. Grunell and M.J. Clark (Editors), Glacio-fluvial Sediment Transfer. Wiley, New York, pp. 207-284.

Rott, H., Stuefer, M., Siegel, A., Skvarca, P. and Eckstaller, A., 1998. Mass fluxes and dynamics of Moreno glacier, southern Patagonia icefield. Geophysical Research Letters, 25(9): 1407-1410.

Roux, P., Marsan, D., Métaxian, J., O'Brien, G. and Moreau, L., 2008. Microseismic activity within a serac zone in an alpine glacier (Glacier d'Argentiére, Mont Blanc, France). Journal of Glaciology, 54(184): 157-168.

Ruddell, A.R., 1995. Recent glacier and climate change in the New Zealand Alps. PhD thesis Thesis, University of Melbourne, Melbourne.

Russell-Head, D.S., 1980. The melting of free-drifting icebergs. Annals of Glaciology, 1: 119-122.

Sakai, A., 2012. Glacial lakes in the Himalayas: A review on formation and expansion processes. Global Environmental Research, 16: 23-30.

Sakai, A., Fujita, K., Nakawo, M. and Yao, T., 2009a. Simplification of heat balance calculation and its application to the glacier runoff from the July 1st Glacier in northwest China since the 1930s. Hydrological Processes, 23(4): 585-596.

Sakai, A., Nishimura, K., Kadota, T. and Takeuchi, N., 2009b. Onset of calving at supraglacial lakes on debris-covered glaciers of the Nepal Himalaya. Journal of Glaciology, 55: 909-917.

Sakai, A., Takeuchi, N., Fujita, K. and Nakawo, M., 2000. Role of supraglacial ponds in the ablation process of a debris-covered glacier in the Nepal Himalayas. In: M. Nakawo, C.F. Raymond and A. Fountain (Editors), Debris-Covered Glaciers. IAHS Publication 264. Wallingford, Oxfordshire, pp. 119-130.

Salinger, M.J., Hay, J., McGann, R. and Fitzharris, B.B., 1993. Southwest Pacific temperatures: diurnal and seasonal trends. Geophysical Research Letters, 20: 935-938.

Salinger, M.J. and Mullen, A.B., 1999. New Zealand climate: temperature and precipitation variations and their links with atmospheric circulation 1930-1994. International Journal of Climatology, 19(10): 1049-1071.

Scambos, T.A., Hulbe, C., Fahnestock, M. and Bohlander, J., 2000. The link between climate warming and break-up of ice shelves in the Antarctic Peninsula. Journal of Glaciology, 46: 516-530.

Schmeltz, M., Rignot, E. and MacAyeal, D., 2002. Tidal flexure along ice-sheet margins: comparison of InSAR with an elastic-plate model. Annals of Glaciology, 34(1): 202-208.

Schytt, V., 1967. A Study of "ablation gradient". Geografiska Annaler. Series A, Physical Geography, 49(2/4): 327-332.

Sciascia, R., Straneo, F., Cenedese, C. and Heimbach, P., accepted. Seasonal variability of submarine melt rate and circulation in an East Greenland fjord. Journal of Geophysical Research: Oceans.

Siegert, M.J. and Dowdeswell, J.A., 2004. Numerical reconstructions of the Eurasian Ice Sheet and climate during the Late Weichselian. Quaternary Science Review, 23: 1273-1283.

Sikonia, W.G., 1982. A two-dimensional dynamic finite-element glacier flow model applied to columbia Glacier, Alaska. U.S. Geological Survey Professional Paper 1258-B.

Simpson, G.D.H., Cooper, A.F. and Norris, R.J., 1994. Late Quaternary evolution of the Alpine Fault Zone at Paringa, South Westland, New Zealand. New Zealand Journal of Geology and Geophysics, 37: 49-58.

Singh, P., Kumar, N., Ramasatri, K.S. and Singh, Y., 2000. Influence of a fine debris layer on the melting of snow and ice on a Himalayan glacier. In: M. Nakawo, C.F. Raymond and A. Fountain (Editors), Debris-Covered Glaciers. IAHS Publication 264. Wallingford, Oxfordshire, pp. 63-70.

Skinner, B.E., 1964. Measurement of Twenthieth Century ice loss on the Tasman Glacier, New Zealand. New Zealand Journal of Geology and Geophysics, 7: 796-803.

Skvarca, P., De Angelis, H., Naruse, A., Warren, C.R. and Aniya, M., 2002. Calving rates in fresh-water: new data from southern Patagonia. Annals of Glaciology, 34: 379-384.

Squire, V., 2007. Of ocean waves and sea-ice revisited. Cold Regions Science and Technology, 49(2): 110-133.

St Lawrence, W.S. and Qamar, A., 1979. Hydraulic transients: a seismic source in volcanoes and glaciers. Science, 203(4381): 654-656.

Stokes, C.R. and Clark, C.D., 2004. Evolution of late glacial ice-marginal lakes on the northwestern Canadian Shield and their influence on the location of the Dubawnt Lake palaeo-ice stream. Palaeogeography, Paleoclimatology, Paleoecology, 215: 155-171.

Strong, D., 2008. Patterns and processes of ice loss at Tasman Glacier: an evlauation using historic data sources and remotely sensed imagery. MSc Thesis, University of Otago, Dunedin.

Stuart, G., Murray, T., Brisbourne, A., Styles, P. and Toon, S., 2005. Seismic emissions from a surging glacier: Bakaninbreen, Svalbard. Annals of Glaciology, 42: 151-157.

Sutherland, D.A. and Straneo, F., 2012. Estimating ocean heat transports and submarine melt rates in Sermilik Fjord, Greenland, using lowered acoustic Doppler current profiler (LADCP) velocity profiles. Annals of Glaciology, 53(60): 50-28.

Syvitski, J., 1989. On the deposition of sediment within glacier-influenced fjords: oceanographic controls. Marine Geology, 85(2-4): 301-329.

Theakstone, W.H. and Knudsen, N.T., 1986. Recent Changes of a Calving Glacier, Austerdalsisen, Svartisen, Norway. Geografiska Annaler. Series A, Physical Geography, 68(4): 303-316.

Thompson, S.S., Benn, D., Dennis, K. and Luckman, A., 2012. A rapidly growing moraine-dammed glacial lake on Ngozumpa Glacier, Nepal. Geomorphology, 145-146: 1-11.

Tippett, J.M. and Kamp, P.J.J., 1995. Geomorphic evolution of the Southern Alps, New Zealand. Earth Surface Processes and Landforms, 20(2): 177-192.

Trüssel, B.L., Motyka, R., Truffer, M. and Larsen, C.F., 2013. Rapid thinning of lake-calving Yakutat Glacier and the collapse of the Yakutat Icefield, southeast Alaska, USA. Journal of Glaciology, 59(213): 149-161.

Tsai, V.C. and Ekström, G., 2007. Analysis of glacial earthquakes. Journal of Geophysical Research, 112: F03S22.

Tsai, V.C., Rice, J.R. and Fahnestock, M., 2008. Possible mechanisms for glacial earthquakes. Journal of Geophysical Research, 113: F03014.

Tsutaki, S., Sugiyama, S., Nishimura, D. and Funk, M., 2013. Acceleration and flotation of a glacier terminus during formation of a proglacial lake in Rhonegletscher, Switzerland. Journal of Glaciology, 59(215): 559-570.

Turner, A.J. et al., 2012. Geophysical surveys of the sediments of Loch Ness, Scotland: implications for the deglaciation of the Moray Firth Ice Stream, Britsh-Irish Ice Sheet. Journal of Quaternary Science, 27(2): 221-232.

Vacco, D.A., Alley, R.B. and Pollard, D., 2010. Glacial advance and stagnation caused by rock avalanches. Earth and Planetary Science Letters, 294: 123-130.

van der Veen, C.J., 1996. Tidewater calving. Journal of Glaciology, 42(141): 375-385.

van der Veen, C.J., 1997. Controls on the position of iceberg-calving fronts. In: C.J. van der Veen (Editor), Calving Glaciers: Report of a Workshop, Februrary 28 - March 2, 1997. Byrd Polar Research Center, The Ohio State University, Columbus, pp. 163-172.

van der Veen, C.J., 1998a. Fracture mechanics approach to penetration of bottom crevasses on glaciers. Cold Regions Science and Technology, 27(3): 213-223.
van der Veen, C.J., 1998b. Fracture mechanics approach to penetration of surface crevasses on glaciers. Cold Regions Science and Technology, 27(1): 31-47.
van der Veen, C.J., 1999. Fundamentals of Glacier Dynamics. A. A. Balkema Publishers, Rotterdam.
van der Veen, C.J., 2002. Calving glaciers. Progress in Physical Geography, 26(1): 96-122.
Vaughan, D.G. and Doake, C.S.M., 1996. Recent atmospheric warming and retreat of ice shelves on the Antarctic Peninsula. Nature, 379: 328-331.
Veitch, S.A. and Nettles, M., 2012. Spatial and temporal variations in Greenland glacial-earthquake activity, 1993-2010. Journal of Geophysical Research: Earth Surface, 117(F4): F04007.
Venteris, E.R., 1999. Rapid tidewater glacier retreat: a comparison between Columbia Glacier, Alaska and Patagonia calving glaciers. Global and Planetary Change, 22: 131-138.
Venteris, E.R., Whillans, I.M. and van der Veen, C.J., 1997. Effect of extension rate on terminus position, Columbia Glacier, Alaska, USA. Annals of Glaciology, 24: 49-53.
Vieli, A., Funk, M. and Blatter, H., 2000. Tidewater glaciers: frontal flow acceleration and basal sliding. Annals of Glaciology, 31(217-221).
Vieli, A., Funk, M. and Blatter, H., 2001. Flow dynamics of tidewater glaciers: a numerical modelling approach. Journal of Glaciology, 47(159): 595-606.
Vieli, A., Jania, J. and Kolondra, L., 2002. The retreat of a tidewater glacier: observations and model calculation on Hansbreen, Spitsbergen. Journal of Glaciology, 48(163): 592-600.
von Lendenfeld, R., 1884. Der Tasman-Gletscher und seine Umrandung. Erganzungsheft No. 75 'Petermanns Mitteilungen': 1-80.
Walter, F. et al., 2012. Analysis of low-frequency seismic signals generated during a multiple-iceberg calving event at Jakobshavn Isbræ, Greenland. Journal of Geophysical Research, 117(F1): F01036.
Walter, F. et al., 2009. Moment tensor inversions of icequakes on Gornergletscher, Switzerland. Bulletin of the Seismological Society of America, 99(2A): 852-870.
Walter, F., Deichmann, N. and Funk, M., 2008. Basal icequakes during changing subglacial water pressures beneath Gornergletscher, Switzerland. Journal of Glaciology, 54(186): 511-521.
Walter, F. et al., 2010. Iceberg calving during transition from grounded to floating ice: Columbia Glacier, Alaska. Geophysical Research Letters, 37(15): L15501.
Warren, C.R., 1992. Iceberg calving and the glacioclimatic record. Progress in Physical Geography, 16(3): 253-282.
Warren, C.R., 1999. Calving speed in freshwater at Glacier Ameghino, Patagonia. Zeitschrift fuer Gletscherkunde und Glazialgeologie, 35(1): 21-34.
Warren, C.R. and Aniya, M., 1999. The calving glaciers of Southern America. Global and Planetary Change, 22: 59-77.
Warren, C.R., Benn, D.I., Winchester, V. and Harrison, S., 2001. Buoyancy-driven lacustrine calving, Glaciar Nef, Chilean Patagonia. Journal of Glaciology, 47(156): 135-146.
Warren, C.R. et al., 1995a. Characteristics of tidewater calving at Glaciar San Rafael, Chile. Journal of Glaciology, 41: 273-289.
Warren, C.R., Greene, D.R. and Glasser, N.F., 1995b. Glacier Upsala, Patagonia: rapid calving retreat in fresh water. Annals of Glaciology, 21: 311-316.
Warren, C.R. and Kirkbride, M.P., 1998. Temperature and bathymetry of ice-contact lakes in Mount Cook National Park, New Zealand. New Zealand Journal of Geology and Geophysics, 41: 133-143.
Warren, C.R. and Kirkbride, M.P., 2003. Calving speed and climate sensitivity of New Zealand lake-calving glaciers. Annals of Glaciology, 36: 173-178.
Watson, M.I., 1995. Geophysical and glaciological studies of the Tasman and Mueller Glaciers. MSc Thesis, University of Auckland, Auckland.
Weeks, W.F. and Campbell, W.J., 1973. Icebergs as a fresh-water source: an appraisal. Journal of Glaciology, 12(65): 207-233.

Weertman, J., 1973. Can water filled crevasses reach the bottom surface of a glacier? IAHS Publication, 95: 139-145.

Welty, E., Bartholomaus, T., O'Neel, S. and Pfeffer, W.T., 2013. Cameras as clocks. Journal of Glaciology, 59(214): 275-286.

West, M., Larsen, C., Truffer, M., O'Neel, S. and LeBlanc, L., 2010. Glacier microseismicity. Geology, 38(4): 319-322.

Willsman, A., Chinn, T.J.H. and Lorrey, A., 2012. Glacier snowline survey 2011. Technical report, National Institute for Water and Atmospheric Research Ltd., Christchurch, New Zealand.

Winberry, J.P., Anandakrishnan, S. and Alley, R.B., 2009. Seismic aobservations of transient subglacial water-flow beneath MacAyeal Ice Stream, West Antarctica. Geophysical Research Letters, 36(11): L11502.

Winkler, S., 2000. The 'Little Ice Age' maximum in the Southern Alps, New Zealand: preliminary results at Mueller Glacier. The Holocene, 10(5): 643-647.

Winkler, S., 2005. The Schmidt hammer as a relative-age dating technique: potential and limitations of its application of Holocene moraines in Mt Cook National Park, Southern Alps, New Zealand. New Zealand Journal of Geology and Geophysics, 48: 105-116.

Withers, M. et al., 1998. A comparison of select trigger algorithms for automated global seismic phase and event detection. Bulletin of Seismological Society of America, 88(1): 95-106.

Wolf, L.W. and Davies, J.N., 1986. Glacier-generated earthquakes from Prince William Sound, Alaska. Bulletin of the Seismological Society of America, 76(2): 367-379.

Xu, Y., Rignot, E., Fenty, I., Menemenlis, D. and Flexas, M.M., 2013. Subaqueous melting of Store Glacier, west Greenland from three-dimensional, high-resolution numerical modeling and ocean observations. Geophysical Research Letters, 40: 1-6.

Xu, Y., Rignot, E., Menemenlis, D. and Koppes, M.N., 2012. Numerical experiments of subaqueous melting of Greenland tidewater glaciers in response to ocean warming and enhanced subglacial discharge. Annals of Glaciology, 53(60): 229-234.

Zweck, C. and Huybrechts, P., 2003. Modeling the marine extent of Northern Hemisphere ice sheets during the last glacial cycle. Annals of Glaciology, 37: 173-180.

Appendix A: Contents of the DVD

A DVD accompanies the thesis and is stored in a pocket at the rear. The DVD contains the following files:

A time-lapse video created from the time-lapse images recorded between 27 October 2011 and 20 November 2012. The video resolution has been down-sampled from the original resolution of the images recorded by the time-lapse camera. A total of 25 610 images are included in the video at a frame rate of 40 fps. Degradation in image quality throughout the video is caused primarily by kea (*Nestor notabilis*) scratching the lens cover of the camera (filename: TG_time-lape_Oct11-Nov12.avi, length: *c.* 10 minutes).

Calving events identified in time-lapse imagery of Tasman Glacier between 27 October 2011 and November 2012. Details for each recorded calving event are included for the parameters discussed in chapters 5 and 6 (file name: calving_events_Oct11-Nov12.xlsx).

Seismic parameters retrieved for calving events record by time-lapse imagery between 20 February and May 2012 (file name: seismic_calving_events_Feb12-May12.xlsx).

Appendix A: Contents of the DVD

Appendix B: Coverage and sources of satellite imagery

This appendix outlines the satellite images that were used to determine terminus positions and proglacial lake extents of Tasman Glacier and Tasman Lake which are incorporated into chapters 4 and 5. The date, type, coverage, and cloud cover of satellite imagery used are indicated in Table B.1.

Table B.1: The date, types, coverage, and cloud cover for satellite images used throughout the study. Advanced Spaceborne Thermal Emission and Reflection Radiometer (ASTER) imagery was sourced from Wolfgang Rack at the University of Canterbury, New Zealand via the Global Land Ice Measurements from Space (GLIMS) project. Where cloud cover is indicated, the clouds present did not hinder identification of the terminus of Tasman Glacier.

Date (NZST)	Type	Coverage	Cloud cover
30/04/2000	ASTER	Complete	Nil
08/04/2001	ASTER	Complete with two scenes	Nil
30/01/2002	ASTER	Complete	Nil
01/01/2003	ASTER	Complete	Nil
05/02/2004	ASTER	Complete	Partial
10/09/2005	ASTER	Lower Tasman	Nil
25/01/2006	ASTER	Complete	Nil
09/04/2007	ASTER	Complete	Nil
07/12/2007	ASTER	Complete	Nil
18/02/2009	ASTER	Complete	Nil
10/04/2010	ASTER	Complete	Nil
03/02/2011	ASTER	Complete with two scenes	Nil
01/01/2012	ASTER	Complete with two scenes	Nil
23/03/2012	ASTER	Complete	Partial
22/04/2012	ASTER	Complete	Nil
24/05/2012	ASTER	Complete	Extensive
11/06/2012	ASTER	Complete	Nil
01/01/2013	ASTER	Complete	Partial

Appendix B: Coverage and sources of satellite imagery

Appendix C: Geophones and data loggers

In combination with the broadband seismometer deployed on the terminus of Tasman Glacier two XIAN CHINA SN4-10 (10 Hz peak response) single component geophones connected to an AFM board (to filter, amplify and divided data into a high-gain and low-gain form) and data logger with GPS time clocks, were deployed. The data loggers and ARM boards were designed and built specifically for the recording of seismic signal emanating from the terminus of Tasman Glacier at a high (*c.* 100 Hz) sampling rate. The geophones were positioned down (GD) and up-glacier (GU) from the broadband seismometer (Figure 7.1) with the initial intent to use the array to provide an indication of directionality for recorded seismic signals. Memory and equipment issues were also encountered during deployment, resulting in the sampling rate having to be reduced from 100 to 1 Hz in February 2012. The resulting data recorded by the two geophones only provided a means of describing seismic signals generated by calving events on a general scale (due to the low sampling rate), but not original direction of source as was originally intended. As a result, they did not add any addition useful information for the analysis of calving-generated seismic signals and were not included in the analysis presented in chapter 7.

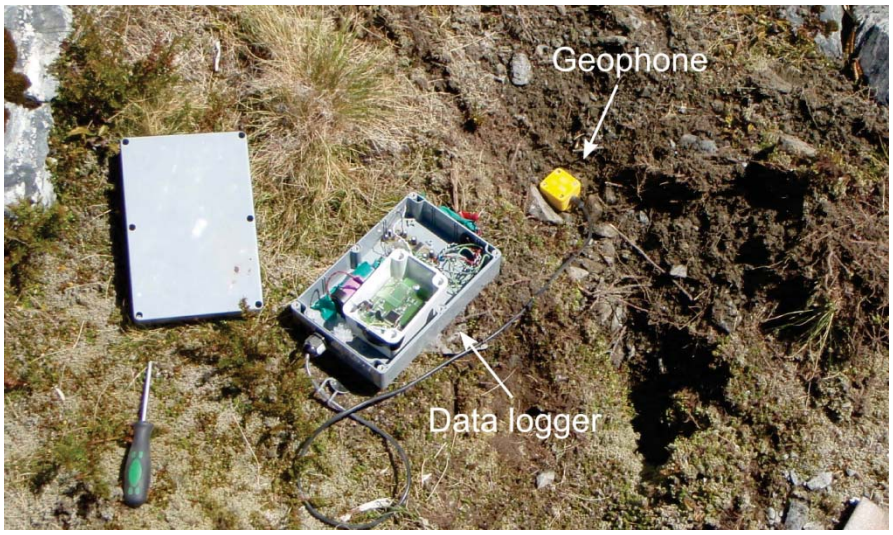

Figure C.1: Photograph showing the geophone and data logger during a pre-deployment test during fieldwork carried out at Hooker Glacier in November 2009.